Weak gravitational lensing in the Red-sequence Cluster Survey 2

Edo van Uitert

Weak gravitational lensing in the Red-sequence Cluster Survey 2

Proefschrift

ter verkrijging van
de graad van Doctor aan de Universiteit Leiden,
op gezag van de Rector Magnificus prof. mr. P. F. van der Heijden,
volgens besluit van het College voor Promoties
te verdedigen op dinsdag 29 mei 2012
klokke 13:45 uur

door

Edo van Uitert
geboren te Groningen
1984

Promotiecommissie

Promotor:	Prof.dr. K. H. Kuijken
Co-Promotor:	Dr. H. Hoekstra
Overige leden:	Prof.dr. M. Franx Prof.dr. J. Schaye Prof.dr. P. Schneider (Argelander-Institut für Astronomie, Bonn) Prof.dr. H. K. C. Yee (University of Toronto)

Voor saba&safta, opa&oma

Energie doet overwinnen (C. van Uitert, 1984)

Cover design: Redmar van Leeuwen en Edo van Uitert

Contents

1 Introduction

In this first chapter, we set the scene for the research projects presented in this thesis. We begin with a brief description of the standard model of cosmology, ΛCDM, and describe its main components. To study these observationally, a large variety of techniques has been developed. The one central to the studies in this thesis is weak gravitational lensing. We therefore provide a short description of how this method works, and give some examples of its applications. We also provide a short overview of the other chapters.

1.1 The ΛCDM framework

For millennia, people believed that the Earth was the centre of the Universe, with the Sun, the planets and all the stars revolving around it. Almost 500 years ago, this ancient world view started to change, and it has been subject to change ever since. Due to the work of, amongst others, Nicolaus Copernicus and Galileo Galilei, it became clear that our Sun did not revolve around the Earth, but that the Earth and the planets moved around the Sun. At the same time, Giordano Bruno proposed that the stars in our sky were actually very distant suns like our own, although it took more than two centuries before their distances from us could be determined. With the help of his telescope, Galileo Galiliei found that the faint band of light that crossed our nocturnal sky actually consisted of many small stars our eyes could not discern. This large collection of stars was called our Galaxy, and at the beginning of the twentieth century it was a hot topic of debate whether or not other galaxies similar to ours existed outside our own. In the 1920s, Edwin Hubble measured the distances to some faint nebulae in the sky whose origin was uncertain. These distance measures conclusively showed that these objects had to reside far outside our Galaxy, and therefore had to be galaxies themselves. Subsequent observations showed that the Universe was filled with uncountable galaxies - currently, it is estimated that there are more than 100 billion of them.

Soon after the discovery of the existence of other galaxies, another important one followed. A few years earlier, in 1912, Slipher had already measured the spectra of these faint clouds that turned out to be nearby galaxies, and determined that almost all of them were recessing from us at high speeds. Combining these velocity measurements with the distance measurements, Edwin Hubble and others soon discovered that the more distant a galaxy was located from our galaxy, the faster it was moving away from us. The interpretation was as simple

as it was astonishing: it could only mean that all galaxies were moving away from each other, hence the Universe was expanding. Until then, the Universe had been thought to be static. If it was expanding, it meant that it had a beginning as well. This moment when everything was created has become famous as the Big Bang (the name was coined by Fred Hoyle in 1949, who believed in a static Universe and invented the term to sarcastically express his dislike in the theory - although according to his reading, the term only served to highlight the differences between the theories). The fact that people had great difficulties in believing in a Universe that was not static but expanding was demonstrated by one of the greatest minds of all times, Albert Einstein. In his work on General Relativity a few years earlier, he added a constant to one of his equations so that it would enforce a static Universe rather than an expanding one (the largest error of his career, he later confessed, as he could have predicted the expansion of the Universe before it was observed).

Another change of our world view was initiated in the 1930s by the work of Fritz Zwicky on groups of galaxies (galaxy clusters), but only became widely known after the work of Vera Rubin and her collaborators in the 1960s. Zwicky studied the orbital velocities of galaxies in the Coma cluster, and inferred from their large velocities that 'missing' mass had to be present to prevent these galaxies from flying off. Rubin studied rotation curves[1] of nearby spiral galaxies and deduced the total mass enclosed within a certain radius using standard Newtonian physics. The total mass exceeded the mass that could be accounted for by the sum of stars, gas and dust (the baryons). Hence another component had to be present, exerting gravity, but invisible to the eye: dark matter. Nowadays, the presence of dark matter has been confirmed by various observations, including the stellar dynamics in nearby galaxies, the kinematics of satellite galaxies in clusters, and by observations of hot X-ray emitting gas. These observations support the view that the galaxies and galaxy clusters we observe are embedded in giant dark matter structures. One of the most convincing observations supporting the existence of dark matter has been made by Clowe et al. (2006) in a system called the Bullet Cluster. In this work, two galaxy clusters are studied just after they crashed into each other. The hot gas from both galaxy clusters, which constitutes the major part of the ordinary baryonic matter, collided violently and slowed down, whilst emitting a huge amount of X-ray radiation. The dark matter, however, which only interacts through gravitation, did not collide and moved on after the collision, forming two separate clumps, clearly offset from the gas.

At about the same time of the first observations of galaxy rotation curves, Penzias and Wilson, two radio engineers working for Bell Labs, measured a source of radio noise at millimeter wavelengths coming from all directions in the sky. Radiation in this wavelength regime had already been predicted in 1948 by Gamow, Alpher and Herman as a relic of the Big Bang. Shortly after the Big Bang, the Universe consisted of one giant immensely dense and hot soup of elementary particles and radiation. After approximately 380 000 years of expansion and cooling, the conditions in the Universe allowed protons and electrons to recombine and form hydrogen atoms. During this process, photons were emitted with an energy of 13.6 eV, i.e. with a frequency peaking in the ultraviolet.

[1] a rotation curve depicts the orbital velocity of stars as a function of distance from the galactic centre

Most of these photons traversed the Universe ever since, although the expansion of the Universe redshifted their frequency to the millimeter regime. This radiation, known as the Cosmic Microwave Background Radiation (CMBR), was exactly what Penzias and Wilson observed. The CMBR is found to be extremely homogeneous, and is very well described by a black-body spectrum with a temperature of 2.71 K, with fluctuations of the order 10^{-5} K. The observation of the CMBR at exactly the expected wavelength regime is considered as one of the strongest proofs that the Big Bang actually happened. Detailed observations of the CMBR pattern across the sky with, amongst others, the Wilkinson Microwave Anisotropy Probe (WMAP) space telescope (Bennett et al. 2003; Jarosik et al. 2011) revealed a wealth of information about the structure of the Universe (e.g. that space appears flat rather than curved). It also provided constraints on the total amount of matter in the Universe, as well as strong evidence that a large fraction of the matter in the Universe has to be in a non-baryonic form (i.e. dark matter). The extreme homogeneity of the CMBR is commonly attributed to a period just after the Big Bang when the Universe expanded extremely rapid - exponentially - for a short timespan, which is called inflation. During inflation, the tiny quantum fluctuations in the Universe were blown up, and formed the seeds of the structure that formed afterwards.

In 1998, two independent research groups, called the *high-z SN search*[2] and the *Supernova Cosmology Project*[3] determined the distance to very distant galaxies by studying the light of exploding stars (supernovae; Riess et al. 1998; Perlmutter et al. 1999). This lead to the discovery that these distant galaxies are actually more distant than predicted for a Universe that expands at a constant rate. The only explanation again changed our world view radically - not only is the Universe expanding, but the expansion is actually accelerating! This conclusion has been disputed over the years, but the evidence supporting this view is increasing. For example, the CMBR observations show that the Universe is practically flat, which means that the average density in the Universe is close to a particular value (the critical density). Combining this with the constraints on the total amount of matter in the Universe, it follows that an additional form of energy has to be present. Also, studies of the growth of structure point in the same direction (e.g. Schrabback et al. 2010). What is causing this acceleration is not clear, but it is attributed to a hypothetical form of energy: dark energy. The nature of dark energy is not understood at all. Attempts have been made to relate it to the ground state energy of the quantum field that pervades space, but the discrepancy between the theoretical value and the value that follows from cosmological observations is an incredible factor of 10^{-120}, which serves as a perfect illustration of our ignorance. These four components, i.e. the baryons, radiation, dark matter and dark energy, are currently believed to make up the Universe.

Parallel to all these observations, astronomers have developed countless models to describe our Universe and the way it evolves. Most of these models were discarded at some point as observations proved them wrong. One of them, however, has managed to stand the test of time so far, and is currently the most favoured model by the majority of the astronomical society. The model is called ΛCDM. The "CDM" stands for Cold Dark Matter, where the "Cold"

[2]http://cfa-www.harvard.edu/cfa/oir/Research/supernova/home.html
[3]http://supernova.lbl.gov/

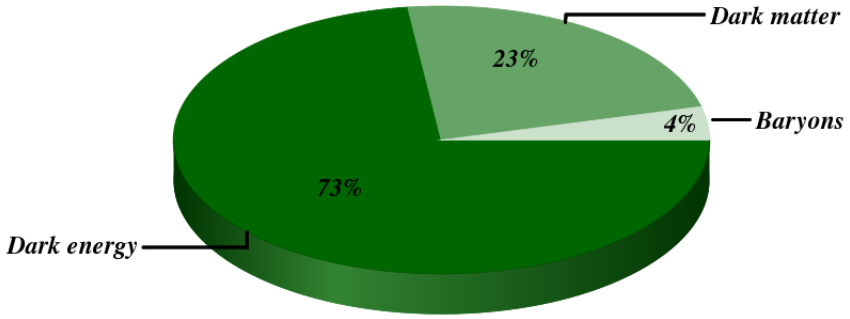

Figure 1.1: Contribution to the total energy density of the Universe by the three main components of ΛCDM.

indicates that the dark matter particles have relatively high masses and move at low speeds (as opposed to Hot Dark Matter, where the particles are assumed to move with relativistic speeds). The Λ refers to the constant Einstein added to his equations to enforce a static Universe, which he considered a mistake, but ironically has been reintroduced as the most natural description for dark energy. The ΛCDM model describes how the Universe, starting from a very hot and dense state, expanded, gradually cooled and eventually formed stars and galaxies. The strength and beauty of ΛCDM is that from a modest number of initial conditions and ingredients, it has the ability to predict with great precision a large variety of observations, ranging from the observations of density peaks in the cosmic microwave background radiation, to the cosmic abundances of the light elements (hydrogen, helium, deuterium and lithium), to the clustering of galaxies in the current day Universe. In ΛCDM, hot dark matter is also present in the form of neutrino's, but they only make up a small fraction of the total energy budget.

In our Universe, the baryons only make up a very modest part of the total content, as is depicted in Figure 1.1. The two dark components, dark matter and dark energy, dominate the energy density, but their nature is poorly understood at best. The majority of current research in cosmology is aimed at improving our understanding of these components: how are they distributed in the Universe, what are they made of, how do they interact, etc.

These efforts can be roughly divided into two main streams: numerical simulations and observations. In the first stream, the evolution and formation of structure in a certain volume of the Universe is simulated with computers. This field has rapidly expanded over the last two decades, propelled by the enormous growth of computational power. In recent simulations such as the Millennium Simulation (Springel et al. 2005), the movements of ten billion particles were traced from the moment of the formation of hydrogen (recombination) up to the current-day Universe, which is already an incredible achievement. The main difficulty with simulations is the correct incorporation of the baryons: baryonic physics is notoriously difficult, as many different processes such as supernova explosions and AGN[4] activity are important, but they are intertwined as well.

These processes play, however, a very significant role in the formation of structure, and need to be incorporated accurately. If the implementation of these processes is not correct, neither will be the predictions from the simulations.

Although simulations improve our understanding of the evolution of our Universe, how it came to be as we observe it today, they need to be constrained by observations. For example, when we compare simulations with different implementations of supernova feedback to observations, we can learn which scenario is more likely than the other. But the opposite is true as well: for a given set of observations, we need simulations to help interpret what we see. Comparing observations with the results from simulations is generally complicated. Observations are distorted by all sorts of processes in the intergalactic medium, the atmosphere and the telescope, for which we have to correct. Simulations, however, offer a simplification of reality, as not all the processes that occur in the real Universe are accounted for. To match the observations to simulations and vice versa, we have to translate the one into the other, and herein lies the difficulty. Nonetheless, it is worth the effort as only through the combination of both we can improve our understanding of the Universe.

This thesis is part of the observational effort to study how dark matter is distributed in and around galaxies and galaxy clusters, and how it traces the baryons. The main technique we have used in our studies is gravitational lensing, which we introduce in the following section.

1.2 Gravitational lensing

As light emitted by distant galaxies (sources) travels through the Universe towards our telescopes, it is deflected by the gravitational pull of massive galaxies and galaxy clusters (lenses) that it passes on its way. Rather than in straight lines, each lightray follows a wiggly path through space. This effect is known as gravitational lensing. A sketch of a gravitational lens system is shown in Figure 1.2. A galaxy at a distance D_s from us that resides in the source plane emits light rays, that travel towards Earth (depicted by the thick solid line). After traveling the distance D_ds, the lightray is deflected by a massive structure in the lens plane, and travels the remaining D_d in a direction that is different from its original path towards the observer on Earth. This deflection of a lightray is described by the following geometrical relationship:

$$\vec{\beta} = \vec{\theta} - \vec{\alpha}(D_\mathrm{d}\vec{\theta})\frac{D_\mathrm{ds}}{D_\mathrm{s}}, \tag{1.1}$$

with $\vec{\beta}$ the angular position of the source, $\vec{\theta}$ the angular position of the image, and $\vec{\alpha}(D_\mathrm{d}\vec{\theta})$ the deflection angle. Introducing the angular coordinate $\vec{\xi} = D_\mathrm{d}\vec{\theta}$, the deflection angle is given by

$$\vec{\alpha}(\vec{\xi}) = \frac{4G}{c^2}\int d^2\xi' \Sigma(\vec{\xi'})\frac{\vec{\xi} - \vec{\xi'}}{|\vec{\xi} - \vec{\xi'}|^2} \tag{1.2}$$

[4]Active Galactic Nuclei refer to the centre of galaxies that harbour a massive black hole that actively accretes matter. An enormous amount of energy is released during this process through the expulsion of material in jets with speeds that near the speed of light.

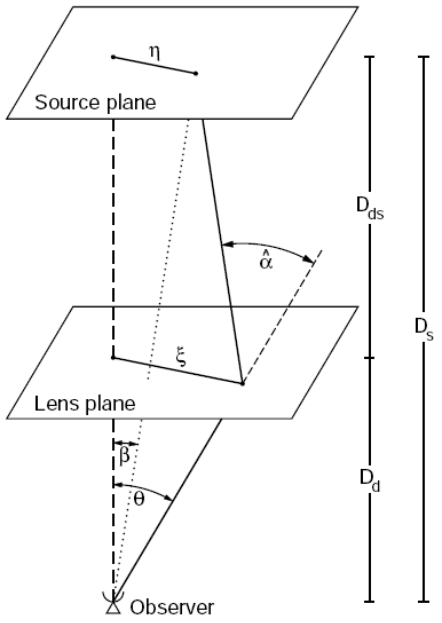

Figure 1.2: Sketch of a gravitational lens system (Bartelmann & Schneider 2001)

with $\Sigma(\vec{\xi'})$ the surface mass density and $\vec{\xi}$ the impact parameter (Bartelmann & Schneider 2001).

Gravitational lensing affects our observations in several ways. Firstly, the observed location of source galaxies is different from their real positions on the sky. Since we do not know their positions beforehand, we cannot measure this effect. Secondly, if the lens is very massive, the lightrays are bent around different sides of the lens towards Earth. As a result, we may observe more than one image of the same source galaxy. The length of the path that the light travels before it reaches us generally differs between the images. Therefore, when the light emitted by the source suddenly changes (for example due to a supernova explosion), this 'news' arrives at Earth for each image at a different moment. These so-called time delays can be used to study the rate of expansion of the Universe (Refsdal 1964), and constrain several cosmological parameters (Coe & Moustakas 2009).

From Equation (1.2) it can be observed that the deflection depends on the impact parameter; photons that pass the lens at different distances are deflected by different amounts. This differential deflection of the lightrays leads to a remapping of the background sky. Consequently, the total amount of light of the sources is magnified, and their shapes are distorted. If the source galaxy image is small compared to the angular scale on which the lens properties change, the deflection of the lightrays can locally be described by the deflection matrix. The deflection matrix relates the intrinsic (unlensed) surface-brightness of the source

$I(x, y)$ to the observed one, $I'(x', y')$. It is given by:

$$\begin{pmatrix} x' \\ y' \end{pmatrix} = (1-\kappa) \begin{pmatrix} 1-g_1 & -g_2 \\ -g_2 & 1+g_1 \end{pmatrix} \begin{pmatrix} x \\ y \end{pmatrix} \tag{1.3}$$

with (x, y) the observed coordinates and (x', y') the undistorted ones. κ is the convergence, defined as

$$\kappa = \frac{\Sigma(\vec{\xi})}{\Sigma_{\rm crit}} \;\; ; \;\; \Sigma_{\rm crit} = \frac{c^2}{4\pi G} \frac{D_{\rm s}}{D_{\rm d} D_{\rm ds}}, \tag{1.4}$$

with $\Sigma_{\rm crit}$ the critical surface mass density. The weak lensing regime is defined as the regime where $\kappa \ll 1$ holds; if $\kappa \geq 1$, Equation (1.1) can have multiple solutions, resulting in multiple images of a single source for particular lens-source configurations. $g_1, g_2 \equiv (\gamma_1, \gamma_2)/(1-\kappa)$ is the reduced shear and (γ_1, γ_2) the shear. The shear describes the stretch of the image of the source due to the gravitational potential of the lens. Its effect on a round source is illustrated in Figure 1.3. The quantity we measure from the source ellipticities is the reduced shear, however. In weak lensing, $\kappa \ll 1$, and therefore $g \approx \gamma$, hence the reduced shear is approximately equal to the shear. If the distortion is small, it can be shown that the ellipticities of source galaxies change as follows:

$$e_i^{\rm obs} = e_i^{\rm int} + g_i, \tag{1.5}$$

with $e_i^{\rm obs}$ one of the two components of the observed ellipticity, and $e_i^{\rm int}$ the intrinsic ellipticity of the source. The shear can be retrieved in a certain part of the sky by averaging the ellipticities of a large number of sources: $\langle g_i \rangle \approx \langle e_i^{\rm obs} \rangle$. The fundamental assumption made here is that the intrinsic ellipticities of galaxies have random orientations; the intrinsic part of the observed ellipticities averages out, leaving us with the average shear imprinted on those sources. This assumption is actually not correct as neighbouring galaxies that are or have been subject to the same large-scale gravitational field may have correlated ellipticities, an effect known as intrinsic alignments (e.g. Hirata et al. 2004, 2007). This affects studies that rely on the correlation of the ellipticities, but not the studies where the ellipticities are correlated with the *location* of the lenses as the lensing signal is generally averaged over large numbers of sources, and the effect averages out.

If a spherically symmetric lens lenses a source, the shape of the source is stretched tangentially, i.e. in the direction perpendicular to the vector that connects the lens with the source projected onto the plane of the sky. To understand this qualitatively, trace the lightrays back past the lens to the source. The lightrays that passed the lens at small impact radii (close to the lens) were deflected more than the lightrays that passed it at larger radii, hence the real image of the source is stretched radially compared to the image we observed. Vice versa, the observed image is stretched tangentially with respect to the real image. This process is illustrated in Figure 1.4.

A commonly used method to extract the shear from the shapes of the sources is therefore by measuring the source ellipticity components in the direction tangent to the line that connects the lens and the source, hence the direction in which they were distorted. The quantity we measure is the tangential shear (also known as the galaxy-mass cross-correlation function),

$$\gamma_{\rm t} = -[\gamma_1 \cos(2\theta) + \gamma_2 \sin(2\theta)], \tag{1.6}$$

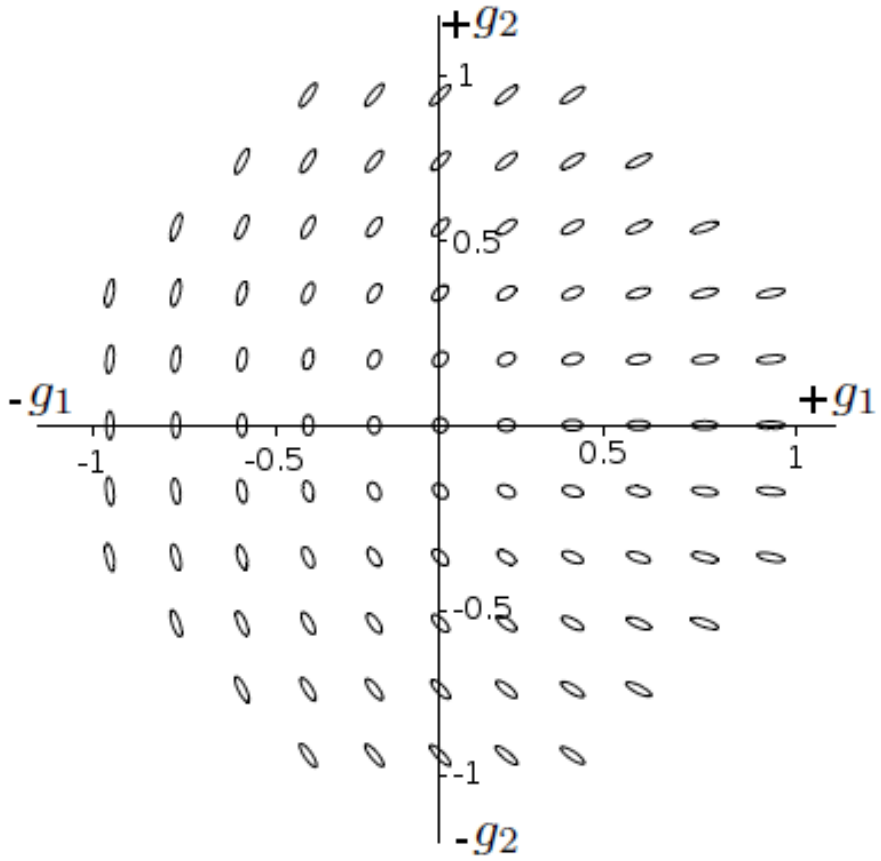

Figure 1.3: Gravitational shear applied on an intrinsically round source. If g_1 is positive (negative), the source is stretched horizontally (vertically); if g_2 is positive (negative), the source is stretched in the $x = y$ ($x = -y$) direction (source: D. Clowe).

with θ the angle between the horizontal axis and the vector between the lens and the source. By measuring the tangential shear in concentric rings centred on the lens, the radial shear pattern of the lens can be studied.

To determine whether galaxy-galaxy lensing produces a tangential shear that is positive or negative, we imagine a round source galaxy that lies on the horizontal axis that passes through the centre of the lens, hence $\cos(2\theta) = 1$. The distortion of its shape is in the tangential direction: the source is stretched vertically. In Figure 1.3 we find that this corresponds to a negative γ_1. Therefore, the tangential shear is positive.

The tangential shear is a convenient way to quantify the lensing signal, because it can be directly related to the differential surface mass density:

$$\langle \gamma_{\rm t}(\xi) \rangle = \frac{\Delta\Sigma(\xi)}{\Sigma_{\rm crit}}, \tag{1.7}$$

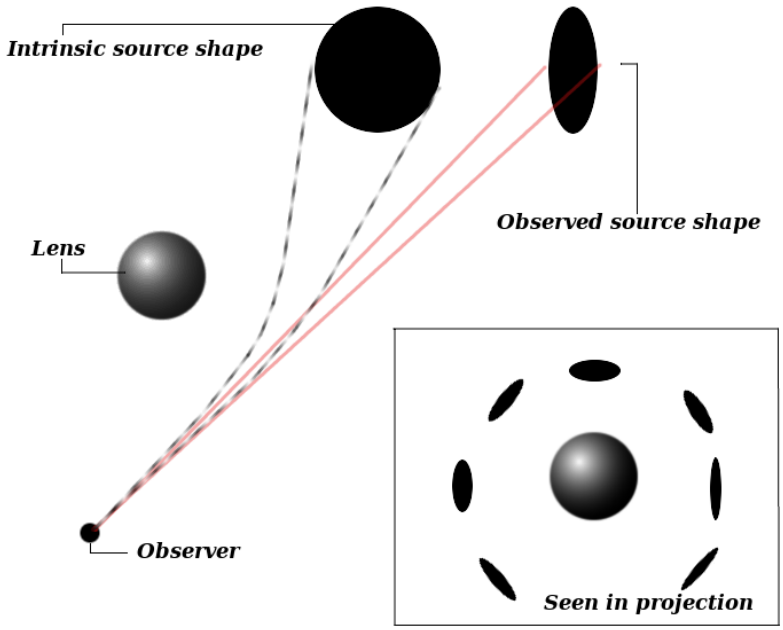

Figure 1.4: Cartoon of galaxy-galaxy lensing. Lightrays of a source passing the lens at different impact parameters are bent by different amounts. As a consequence, the shape of the source becomes elongated in the direction perpendicular to the lens-source separation. When seen in projection on the sky, a coherent shear pattern is formed around the lens when there are multiple sources at different positions behind the lens.

where $\Delta\Sigma(\xi) = \bar{\Sigma}(< \xi) - \bar{\Sigma}(\xi)$ is the difference between the mean projected surface density enclosed by ξ and the mean projected surface density on a circle at ξ. Since we only measure the difference between projected densities, and not the projected density itself, we can in principle not determine the mass of the lenses, unless we know the value of the projected density at a certain position in the lens plane. In other words, if we were to increase the density uniformly across the lens plane, the tangential shear in the weak lensing regime ($\kappa \ll 1$) would not change, but the mass obviously would – this problem is known as the mass-sheet degeneracy (Falco et al. 1985; Schneider & Seitz 1995). The most common solution to this problem is to assume a certain two-dimensional profile for the density (e.g. based on results from numerical simulations), and fit the corresponding lensing signal to the observed shear. Amongst the most popular models are the Singular Isothermal Sphere (SIS) profile, and the Navarro-Frenk-White (NFW) profile (Navarro et al. 1996). The total mass is then obtained by integrating the density in an area where the density is larger than a certain threshold value.

Another consequence of differential deflections is that the source galaxies are magnified, which leads to an increase of their flux. This cannot be measured for individual objects, as their brightnesses are not known a priori. However,

if the luminosity function[5] of a certain sample of sources is accurately known, the effect is measurable (e.g. Hildebrandt et al. 2011). The systematic errors of shear and magnification are different, mainly because different quantities are measured: for shear, we measure the shapes of galaxies, whilst for magnification we measure their total flux. Particularly for high-redshift lenses magnification is expected to complement shear in constraining the dark matter distribution, because for magnification more faint and high-redshift sources can be used as the flux of a (faint) source is more easy to determine than its shape (van Waerbeke 2010).

The distortion of the background sky leads only by approximation to a stretch of the sources; the actual change of shape is more complex. The source galaxies are slightly bent as well, in such a way that the total deformation gives the sources the appearance of a banana. These higher-order distortions are called flexion, and they can be measured on small projected scales close to the lens (e.g. Goldberg & Natarajan 2002; Goldberg & Bacon 2005; Bacon et al. 2006; Velander et al. 2011). Flexion is particularly sensitive to substructures in the lens, which makes it a useful complement to shear. If the distortion is very strong, for example close to a massive cluster of galaxies, the image of a source can be stretched into long arcs, and in exceptional cases even into rings (Einstein rings). This is the regime of strong lensing.

Shear, flexion and magnification are part of weak gravitational lensing. So far, most weak lensing studies have utilised the shape distortions by measuring the shear. The science chapters presented in this thesis are based on shear measurements too, and we discuss this further in the next section. Please note that in the forthcoming, when references are made to 'weak lensing', we generally mean the shear, unless explicitly stated otherwise.

1.2.1 Shear measurement

To measure the weak lensing signal, the ellipticities of a large number of source galaxies need to be accurately determined. In practice, this is a difficult task. When we observe galaxies from Earth, the images are distorted by the atmosphere, telescope and camera optics, changing the observed ellipticities of the galaxies and hence the shear we would infer from them. Since the gravitational lensing signal is very small, we have to correct for these distortions to a high level of accuracy. Any residual ellipticity pattern that is not due to gravitational lensing, but still present in the data, may be misinterpreted as real shear, which could bias the science results. Note that besides the technical difficulties, there are also physical complications (e.g. intrinsic alignments), which have to be properly accounted for when interpreting the observed lensing signal.

A large variety of methods has been developed since the 90s of last century, aimed at recovering the unconvolved shapes (i.e. the images before they entered Earth's atmosphere) of the galaxies as precisely as possible. Their performance has been tested on artificial survey images that contain large numbers of galaxies whose morphologies mimic those of real galaxies (Heymans et al. 2006; Massey et al. 2007; Bridle et al. 2010). The best can measure the gravitational distortion with the precision of a few percent, which already enables

[5] The luminosity function describes the number density of galaxies as a function of luminosity.

a wealth of science projects. A lot of work is currently invested in developing methods that can reach an even higher precision, with subpercent errors on the measured shear values. This requires the understanding and control of ever smaller subtleties in the data, a difficult task but certainly worth the effort.

1.2.2 Galaxy-galaxy/cluster lensing

In this thesis, we study the shear profile around (the positions of) lenses. If these lenses are other galaxies, this is called galaxy-galaxy lensing; if these lenses are clusters, this is called cluster lensing. As the shear of a lens is typically 10-100 times smaller than the intrinsic ellipticities of source galaxies, we generally cannot measure the tangential shear of a single lens. Only for massive low-redshift clusters the shear can be large enough to be detected for an individual system. For less massive clusters, and in the case of galaxy-galaxy lensing, the lensing signal has to be averaged over many lenses, as that reduces the noise caused by the intrinsic ellipticities of the sources. Even for small and low-mass lens galaxies, the lensing signal can be measured as long as we stack a sufficiently large number of lenses. The downside of stacking is that individual properties of galaxies cannot be studied; however, when we stack lenses of a certain type or brightness, we can still learn about the average properties, which is very interesting and useful.

It is clear from the definition of $\Sigma_{\rm crit}$ in Equation (1.4) that the magnitude of the lensing signal depends on the distances from us to the lens, to the source, and between the lens and the source. We measure a small signal at a given physical scale if either the lens is very close to us ($D_{\rm d}$ is small), or if the lens is very close to the source ($D_{\rm ds}$ is small). When the lens is roughly halfway between the source and the observer, the ratio of the distances, called the lensing efficiency, is optimal for lensing. To convert the tangential shear to $\Delta\Sigma$, we need to know either the individual redshifts of all galaxies involved, or the redshift distribution of the lenses and sources, and use the average distances. If no individual redshifts are available, the redshifts distributions can usually be obtained from public photometric redshift catalogues, to which identical selection criteria can be applied as was done for the lenses and sources.

In practice, there are various other issues that have to be accounted for: galaxies that were selected as sources may actually be physically associated to the lens; the ellipticity estimates of the sources may be inaccurate due to a variety of reasons; residual false shear patterns may still be present in the data. These complications have to be addressed and, when necessary, corrected. We will not go into detail here, as they are discussed when they come along in the following chapters.

1.3 Applications of weak gravitational lensing

Gravitational lensing is a unique tool in observational cosmology as it is the only method that directly probes the projected matter density distribution around lenses. Furthermore, since lensing does not depend on visible tracers, it can be used to measure the projected distribution of matter over a huge range of scales, from a few tens of kpc to a few Mpc. In contrast, other methods rely on

the availability of visible tracers such as planetary nebulae or satellite galaxies that orbit the lenses, which limit their applicability to small scales (for planetary nebulae) or to particular types of lens galaxies (only central galaxies in satellite kinematic studies). Still other methods have to make assumptions on the physical state of the object (such as hydrostatical equilibrium of hot gas in X-ray measurements), which makes them less robust.

A broad variety of research topics can be studied with weak lensing. On large scales, weak lensing can be used to study the large-scale distribution of matter. Lensing by the large-scale distribution imprints coherent shear patterns on the ellipticities of galaxies, which can be studied by correlating the ellipticities of galaxies in a certain patch of the sky. These measures provide us with estimates of the statistical properties of the distribution of matter (e.g. Huff et al. 2011). When we have redshift information available for the galaxies, we can split the galaxies in redshift slices, and learn how these correlation functions – and hence the distribution of matter – change with time. These changes are on the one side due to gravity, which makes the distribution more clumpy as material is pulled towards each other. Acting in the opposite direction is dark energy, causing an accelerated expansion of the Universe, which pulls space - and therefore the matter that is embedded - apart. Hence by studying the variations of these correlation functions with time, we can measure how dark energy impacts the growth of structure, and therefore study properties of dark energy itself (Schrabback et al. 2010).

When we measure the lensing signal around galaxies, we can compare the matter distribution to the light distribution. This reveals where the dark matter is residing, how much there is of it and how it is distributed (e.g. Gavazzi et al. 2007). By splitting the lenses as a function of type, environment, and redshift, we learn which types of galaxies host most of the dark matter, how this depends on the environment and how this has evolved over time (e.g. van Uitert et al. 2011; Leauthaud et al. 2012). This knowledge is crucial for understanding how galaxies form and evolve. Such studies also provide insights on the properties of dark matter (e.g. about its clumpiness), which may eventually lead to clues about the nature of dark matter.

Similarly to galaxies, we can also measure the lensing signal around groups of galaxies and galaxy clusters. This enables us to calibrate their masses without the need to make assumptions about the physical state of the cluster (e.g. hydrostatical equilibrium in X-ray measurements, or virial equilibrium in satellite kinematic studies). This is particularly useful for low-mass clusters, which have fewer tracers of the mass and are typically not in equilibrium. Measuring the mass as a function of the number of cluster members (e.g. Sheldon et al. 2009), and of redshift (e.g. see Chapter 6), leads to important insight into the formation and evolution of clusters, and hence into the physics that govern these processes.

In short, the observational constraints obtained from lensing provide crucial information on the relation between dark matter and baryons, the formation of structure and the evolution of the Universe. The expected arrival of high quality imaging data from upcoming surveys, in combination with the expected improvement of the methods used for lensing, leads to the believe that weak lensing is a particularly promising way to study dark energy in comparison to other methods (Albrecht et al. 2006).

1.4 This thesis

In this thesis we study the distribution of matter around galaxies and galaxy clusters with weak gravitational lensing. Amongst the questions we attempt to answer are the following: how massive are the dark matter haloes of galaxies? Do some type of galaxies have more dark matter than others? What is the relation between the baryonic properties of galaxies (e.g. the total amount of light emitted, or the total mass in stars) and the total amount of dark matter of their haloes? Which of the baryonic tracers is most closely related to the halo mass of a galaxy? Are the dark matter haloes triaxial or not, and can we detect that with gravitational lensing? Does that depend on the type of galaxy? How massive are galaxy clusters, and how does the mass scale with their richness (total number of member galaxies)? Does the relation between mass and richness evolve with redshift?

We study these questions using the imaging data from the Red Sequence Cluster Survey 2 (RCS2), which is a 900 square degree imaging survey in the $g'r'z'$-bands. With a median seeing in the r'-band of $0.7''$, and a depth of $\sim$24.3 in $m_{r'}$, this survey enables many unique (lensing) studies that cannot be performed with any other currently available imaging data set. In **Chapter 2**, we discuss the details of the RCS2, and highlight the differences between the RCS2 and the other imaging surveys that have been used for lensing studies. We detail on the image reduction we have performed, and outline the steps that led to the creation of the galaxy shape catalogues. The shape catalogues, which contain the ellipticities of all the galaxies in the survey, are at the core of the science studies worked out in further chapters. We have performed various checks to ensure that the quality of the catalogues is at the desired level, and the results of these checks are presented.

The RCS2 overlaps with various other surveys, including $\sim$300 square degrees with the Sloan Digital Sky Survey (SDSS; York et al. 2000). The combination of spectroscopic coverage and photometry in five optical bands (u, g, r, i, z) in the SDSS provides a wealth of information on galaxies that is not available for the RCS2 alone. We use this information, but also benefit from the improved lensing quality of the RCS2, by matching the shape catalogues from the RCS2 with various catalogues of the SDSS. This results in 17 000 matching galaxies with a spectroscopic redshift, and many other galaxy properties such as stellar mass, velocity dispersion and luminosity. These galaxies form the lens sample of **Chapter 3** and **Chapter 4**.

In **Chapter 3**, we study the relation between the baryonic properties of galaxies and their dark matter haloes. As this relation depends on galaxy type, we split the 17 000 matching galaxies in an elliptical (early-type) and spiral (late-type) sample. These samples are further divided in bins of either luminosity, stellar mass or dynamical mass, and the lensing signal of the lenses in each bin is measured. To model the lensing signal accurately, we have to account for the fact that a fraction of the lenses are satellite of a larger system. At large projected separations, these larger systems contribute significantly to the lensing signal, which has to be taken into account. For that purpose, we implement a halo model, which enables us to study both the mass and the clustering properties of the lenses. We study how the average luminosity and stellar mass relate to the total halo mass. Furthermore, we determine the satellite fraction of

the lens samples, and study how it depends on luminosity and stellar mass. We derive mass-to-luminosity ratios and baryonic fractions of the lens galaxies, and study their dependence on luminosity and stellar mass, respectively. Finally, we divide the lens bins into redshift slices, in order to study potential evolutionary trends in the relation between baryons and dark matter.

In **Chapter 4** we use a subsample of the lenses from **Chapter 3** to address the question: which observable property of galaxies is most closely related to the lensing signal? We compare three properties: the stellar mass, the spectroscopic velocity dispersion and the model velocity dispersion, which is an alternative estimate of the spectroscopic velocity dispersion of galaxies. The calculation of the model velocity dispersion is based on the results of Taylor et al. (2010), who demonstrated that the dynamical mass and stellar mass are linearly related if one accounts for the structure of a galaxy. As the model velocity is calculated using quantities that are generally better determined than the spectroscopic velocity dispersion, it is believed that the former is a more robust velocity dispersion estimator. Comparing the model velocity dispersion to the spectroscopic velocity dispersion, we find that they correlate well for de Vaucouleur-type galaxies at redshifts $z < 0.2$, and these are the galaxies that form the lens sample. To determine which galaxy property is most closely related to the lensing signal, we measure how the lensing signal depends on each of them. We cannot directly interpret the measurements, however, because the three galaxy properties are correlated. To account for this, we remove the dependence of the lensing signal on either stellar mass or velocity dispersion, and study whether there is a residual dependence on the other property. Comparing these residuals enables us to determine which property of galaxies is most closely related to the lensing signal.

Weak gravitational lensing is not only a useful tool to determine the total masses of galaxies and their relative correlation with respect to the underlying dark matter distribution, but it can also be used to study the shapes of the dark matter haloes of galaxies. This is the subject of **Chapter 5**. Numerical simulations predict that matter collapses in triaxial haloes. If the orientation of galaxies and dark matter haloes are correlated (so either aligned or oriented at a 90° angle, i.e. anti-aligned), the lensing signal around galaxies becomes anisotropic. Hence by studying anisotropies in the weak lensing signal we can learn about the average projected dark matter halo ellipticity of galaxies. We use the imaging data from the RCS2 to select the lenses and sources, and perform the lensing analysis on the whole survey area. We select massive low-redshift galaxies as lenses to optimize the lensing signal-to-noise and to minimize potential systematic contributions. To study potential environmental dependencies, we divide the lens sample in an isolated and a clustered part, and analyse them separately. There are several complications that could change the anisotropy of the lensing signal. We address the impact of a few of them: PSF residual systematics in the galaxy shape catalogues, additional lensing by foreground structures, clustering and magnification. We set up a number of idealised simulations to estimate the impact of these complications on our measurements. To interpret the observed anisotropy of the shear in terms of the average halo ellipticity of galaxies, we need to account for the intrinsic scatter in the position angles between galaxies and their dark matter hosts. Recent studies suggest that the scatter is large, with a value in the range 20°-40°. We present estimates of the impact of this scatter on the observed anisotropy of the lensing

signal.

Finally, we move our attention to larger structures and study the largest gravitationally bound systems in the Universe, galaxy clusters, in **Chapter 6**. Cluster evolution has been one of the main science goals of the RCS2, and the survey design was chosen such as to optimize the detection of clusters up to a redshift $z \sim 1$. Nearly 30 000 galaxy clusters have been detected using the cluster red sequence method, a detection method that utilizes the property that the early-type galaxies in a cluster have very similar colours. These clusters are spread over a large range of optical richnesses (number of cluster members) and have redshifts in the range $0.2 < z < 1.2$. To learn about the growth and evolution of clusters, we can study how various properties of clusters are related as a function of redshift. One of the relations of interest is the one between the mass of a cluster and the richness. A careful calibration of the mass-richness relation is also crucial for studies aimed at constraining cosmological parameters using cluster number counts. To determine the evolution of the mass-richness relation, we divide the cluster sample into bins of richness and redshift, and measure the lensing signal in each bin to determine the average cluster mass. We end the chapter by measuring the excess galaxy number density around the clusters, and outline how we can use it to improve the modeling of the lensing signal.

Bibliography

Albrecht, A., Bernstein, G., Cahn, R., et al. 2006, [arXiv:astro-ph/0609591]

Bacon, D. J., Goldberg, D. M., Rowe, B. T. P., & Taylor, A. N. 2006, MNRAS, 365, 414

Bartelmann, M. & Schneider, P. 2001, Phys. Rep., 340, 291

Bennett, C. L., Halpern, M., Hinshaw, G., et al. 2003, ApJS, 148, 1

Bridle, S., Balan, S. T., Bethge, M., et al. 2010, MNRAS, 405, 2044

Clowe, D., Bradač, M., Gonzalez, A. H., et al. 2006, ApJ, 648, L109

Coe, D. & Moustakas, L. A. 2009, ApJ, 706, 45

Falco, E. E., Gorenstein, M. V., & Shapiro, I. I. 1985, ApJ, 289, L1

Gavazzi, R., Treu, T., Rhodes, J. D., et al. 2007, ApJ, 667, 176

Goldberg, D. M. & Bacon, D. J. 2005, ApJ, 619, 741

Goldberg, D. M. & Natarajan, P. 2002, ApJ, 564, 65

Heymans, C., Van Waerbeke, L., Bacon, D., et al. 2006, MNRAS, 368, 1323

Hildebrandt, H., Muzzin, A., Erben, T., et al. 2011, ApJ, 733, L30

Hirata, C. M., Mandelbaum, R., Ishak, M., et al. 2007, MNRAS, 381, 1197

Hirata, C. M., Mandelbaum, R., Seljak, U., et al. 2004, MNRAS, 353, 529

Huff, E. M., Eifler, T., Hirata, C. M., et al. 2011, MNRAS, submitted [arXiv:1112.3143]

Jarosik, N., Bennett, C. L., Dunkley, J., et al. 2011, ApJS, 192, 14

Leauthaud, A., Tinker, J., Bundy, K., et al. 2012, ApJ, 744, 159

Massey, R., Heymans, C., Bergé, J., et al. 2007, MNRAS, 376, 13

Navarro, J. F., Frenk, C. S., & White, S. D. M. 1996, ApJ, 462, 563

Perlmutter, S., Aldering, G., Goldhaber, G., et al. 1999, ApJ, 517, 565

Refsdal, S. 1964, MNRAS, 128, 307

Riess, A. G., Filippenko, A. V., Challis, P., et al. 1998, AJ, 116, 1009

Schneider, P. & Seitz, C. 1995, A&A, 294, 411

Schrabback, T., Hartlap, J., Joachimi, B., et al. 2010, A&A, 516, A63
Sheldon, E. S., Johnston, D. E., Scranton, R., et al. 2009, ApJ, 703, 2217
Springel, V., White, S. D. M., Jenkins, A., et al. 2005, Nature, 435, 629
Taylor, E. N., Franx, M., Brinchmann, J., van der Wel, A., & van Dokkum, P. G. 2010, ApJ, 722, 1
van Uitert, E., Hoekstra, H., Velander, M., et al. 2011, A&A, 534, A14
van Waerbeke, L. 2010, MNRAS, 401, 2093
Velander, M., Kuijken, K., & Schrabback, T. 2011, MNRAS, 412, 2665
York, D. G., Adelman, J., Anderson, Jr., J. E., et al. 2000, AJ, 120, 1579

2

Data reduction of the RCS2

In this chapter we present the weak lensing analysis of the Red Sequence Cluster Survey 2 (RCS2). The shape catalogues that result from this analysis are used in all science chapters of this thesis. We begin with a description of the survey specifications, then discuss the reduction steps, and detail the creation of the shape catalogues. Finally, we describe a number of basic tests we have performed to ensure the robustness of the results.

2.1 Introduction

The rise of weak gravitational lensing studies has been closely related to the ability to accurately measure the shapes of large numbers of galaxies. With the advent of mosaic CCD cameras that imaged several square degrees of sky, the conditions were set to extract the lensing signal from the data and use it for science. From the first detection of the lensing signal by Tyson et al. (1990), the field has rapidly expanded and has proven to be of great use in a wide variety of research areas, ranging from the study of galaxy formation and evolution using galaxy-galaxy lensing, to the testing of cosmological models through the measurement of the lensing properties of the large scale structure (LSS). One of the main propellants of the rapid progress of the field has been the continuous inauguration of ever larger cameras and telescopes with larger fields of view and improved image quality, and the resulting mapping of ever larger parts of the sky to greater depths. As a result, the number of galaxies whose shapes has been reliably determined has increased by orders of magnitudes (from a few thousands to tens of millions in the most recent surveys), and so has the signal-to-noise of the lensing measurements.

To date, a broad variety of imaging surveys has been used for lensing. We show in Table 2.1 a list of the most recent surveys and their main characteristics relevant for weak lensing studies. In any survey, the observation time can either be used to image a large patch of sky, but shallow, or to image a small area to great depths. The weak lensing science that can be extracted strongly depends on this choice. The wide but shallow surveys (e.g. SDSS) contain many objects at low redshift, and the stacked lensing signal of low-redshift lenses (galaxies, galaxy groups and/or clusters) provides tight constraints on the distribution of matter in the nearby universe (e.g. Mandelbaum et al. 2006; Sheldon et al. 2009). In addition, these surveys are particularly suited for studying the lensing signal of low-mass galaxies (as there are many of them), and for studies of the

Table 2.1: The characteristics of current large imaging surveys relevant for weak lensing studies

Survey	Size	Depth	Bands	PSF size
(1)	(2)	(3)	(4)	(5)
SDSS	10 000	22	$ug\boldsymbol{r}iz$	1.5
RCS2	900	24.3	$g'\boldsymbol{r'}(i')z'$	0.7
CFHTLS-WIDE	171	24.8	$u^*g'r'\boldsymbol{i'}z'$	0.7
RCS1	90	25.2	$\boldsymbol{R_c}z'$	0.8
CTIO	90	23.5	$\boldsymbol{R}$	1.05
CFHT12K-VIRMOS	17	24.5	BVR**I**	0.75
COSMOS	1.64	28.6	$\boldsymbol{I}g$	0.09

(1) name of the survey; (2) area of the survey [deg^2]; (3) depth of the band used for lensing (note that different definitions have been utilized); (4) wavelength coverage (PI imaging, the lensing band in bold font); (5) median size of the PSF in the band used for lensing [arcsec].

intrinsic alignment of galaxies (e.g. Hirata et al. 2004), which can occur if the galaxies are subject to the same large-scale gravitational field, e.g. during their time of formation. Finally, if the PSF[1] is small, these surveys can be used for constraining cosmological parameters (Amara & Réfrégier 2007). The galaxies in a small but deep survey (e.g. COSMOS) are spread over a large range of redshifts, which makes those surveys particularly suited for evolutionary studies, e.g. to study how the stellar mass-to-halo mass relation evolves (Leauthaud et al. 2012) or how the universe expands (Schrabback et al. 2010). For deep surveys it is also possible to measure the lensing signal from individual massive low-redshift clusters (e.g. Okabe et al. 2010).

With a size of 900 deg^2 and a depth of 24.3 in the r'-band, the RCS2 fills the gap between these two survey strategy extremes of width and depth. The survey was specifically designed to optimize the detection of clusters from $z \sim 0.1$ to 1 via the red sequence method (Gladders & Yee 2000), a technique that takes advantage of the fact that the early-type galaxies belonging to a given cluster have very similar colours, and their positions are clustered. The main goals of the survey are to use the cluster catalogue to constrain the cosmological parameters Ω_M and σ_8, to study the evolution of clusters, to define a large sample of strong lensing clusters and to perform weak lensing studies. Thanks to its combination of size, depth and seeing, the RCS2 is well suited for a large range of lensing studies, as we demonstrate in this thesis.

In this chapter, we will discuss the characteristics of the RCS2 in Section 2.2. The reduction we have performed is described in Section 2.3. In Section

[1]The Point Spread Function (PSF) describes the observed shape of a point source (e.g. a star) across the field-of-view of the camera. The shape and size of the PSF are mainly determined by the optics of the telescope and the conditions in the atmosphere. The observed galaxies in an image have been convolved with the PSF, and their shapes need to be corrected for this convolution before they can be used in lensing studies. If the PSF is small and round, this correction is generally more accurate, which is crucial for lensing studies that rely on the correlation of galaxy ellipticities.

2.4 we detail the creation of the shape catalogues. We have performed some basic tests to ensure that no errors occurred in the reduction process that, if unnoticed, could affect our science results. This is presented in Section 2.5. Note that various details of the survey have already been described in Gilbank et al. (2011) and van Uitert et al. (2011). This chapter is intended to provide more details on the steps carried out to construct the catalogues with shape measurements. In particular, the various quality checks discussed in Section 2.5 have not been described in these papers.

2.2 Red Sequence Cluster Survey 2

The RCS2 is a nearly 900 square degree multicolour imaging survey, carried out with the Canada-France-Hawaii Telescope (CFHT), a 3.6m telescope located at the top of Mauna Kea, Hawaii. With a median seeing of $0.7''$ in the r'-band, this site is exceptionally suited for deep surveys that require a good resolution. The camera that has been used is the wide field imager MegaCam (Boulade et al. 2003), which consists of 36 2048×4612 pixel CCD chips, placed in 4 rows and 9 columns. The lay-out of the chips, and the variation of the pixel size across the sky, are shown in Figure 2.1. The pixel size variation is the result of small non-linearities in the camera optics. MegaCam covers about 1×1 degree on the sky, properly sampling the PSF with an average pixel size of $0.186''$. The size of the camera enables the surveying of large parts of the sky in a reasonable amount of time.

The survey consists of two parts: the primary survey, which covers about 740 square degrees, is divided into 13 well-separated patches on the sky (including the uncompleted patch 1303), each with an area ranging from 20 to 100 square degrees. The second part is formed by the CFHT Legacy Survey Wide, comprising of 171 square degrees of imaging data in $u^\star$, g', r', i' and z'. In this thesis we have only used data from the primary survey area. If references are made to 'the survey' from here on, we implicitly mean the primary survey. The location of the various patches on the sky are shown in Figure 2.2. The lay-out of the exposures within the patch CDE2338 is shown in Figure 2.3 as an example. A number of these patches coincide with other surveys, including the Sloan Digital Sky Survey (SDSS) (York et al. 2000) and the WiggleZ Dark Energy Survey (Blake et al. 2008). Combining data from these surveys is advantageous, as it enables science projects that cannot be performed on either of the data sets individually, as we demonstrate in Chapters 3 and 4.

The observations of the survey were performed in three filters (g', r' and z'). About half of the survey area is observed in the i'-band as part of the Canada-France High-z quasar survey (Willott et al. 2005), and was made available for the RCS2 through a data exchange agreement. Details of the observations in each of these bands can be found in Table 2.2. Note that the depth of the r'- and z'-band were chosen to detect $M^* + 1$ red-sequence cluster galaxies at a redshift $z \sim 1$.

The survey is observed in single exposures, since the observations are deep enough for the survey objectives, and valuable CCD read-out time is saved (≈2 minutes per read-out). As a result, small gaps in the surveyed area are present due to the separation between the chips, but they cause no limitations to the science projects. A disadvantage of single exposures is that the removal of cos-

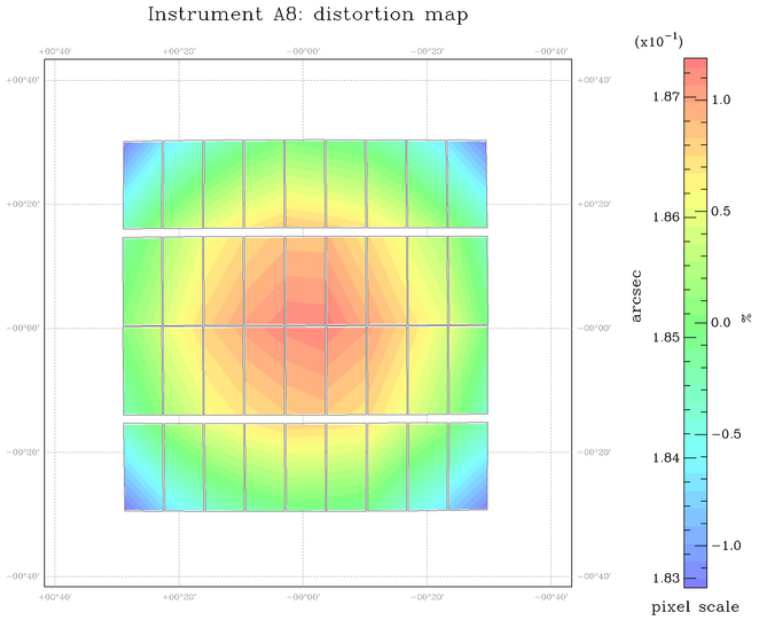

Figure 2.1: The variation of the pixel size in the MegaCam camera, also known as the camera distortion, induced by slight non-linearities in the camera optics. The colour bar indicates the size of the pixels in arcsec, and their relative size with respect to the mean. The pixel size is largest in the centre of the camera. The lay-out of the individual chips is clearly discernible. The variation is smooth and constant over time; the small jumps in the pattern between the central chips are caused by a lack of stars to trace the relative astrometry. The camera distortion generates a false shear signal, which has been corrected for in the lensing analyses. This image is a product of the THELI pipeline (Erben et al. 2005, 2009).

mic rays is more difficult, especially those that hit galaxies and stars. However, they introduce no bias in the analyses, but only act as a minor source of noise.

To quantify the image quality, the variation of the PSF is measured across the field in each exposure. The images of the stars are used for this purpose because they are essentially point sources. For each star, the Full Width Half Maximum (FWHM) is determined, which is the distance from the star's centre where the flux reaches half of its maximum value. The median stellar FWHM is a measure of the quality of the PSF; the larger it is, the more the observed images of galaxies are smeared out, which causes them to appear rounder. Correcting the observed shapes for this smearing becomes increasingly difficult for larger PSF sizes, particularly for small and faint galaxies. Additionally, the depth of the images decreases if the PSF is large, as very faint galaxies are smeared out such that they become buried in the background noise. Weak lensing studies therefore require observations with small PSF sizes.

The median stellar FWHM of the primary survey images in each band is

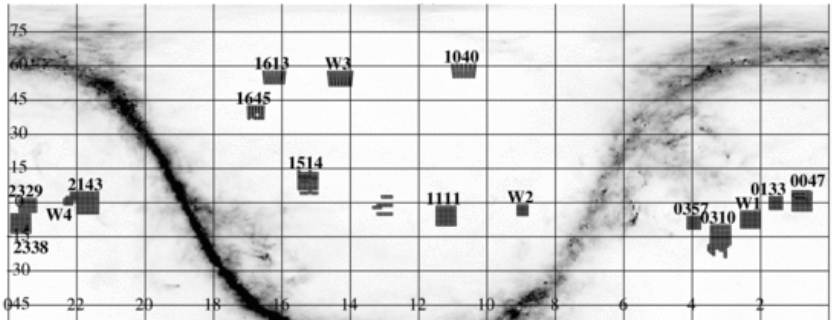

Figure 2.2: The location of the RCS2 patches on the sky in Cartesian projection, as a function of right ascension and declination. The grey scale denotes the dust maps from Schlegel et al. (1998). The labels indicate the name of the patches. The name-less patch in the centre is the uncompleted patch 1303, for which no photometric catalogues exist because of its non-contiguous nature (image courtesy: David Gilbank).

Table 2.2: Details on the various observing bands of the RCS2 (PI data)

Band	Area [deg^2]	t_{exp} [sec]	m_{lim}[(a)]	Median seeing
g'	740	240	24.4	$0.79''$
r'	740	480	24.3	$0.71''$
i'	400	500	23.7	$0.53''$
z'	740	360	22.8	$0.67''$

(a) the 5σ point source limiting magnitude, averaged over all chips

given in Table 2.2. It differs between the observing bands due to the difference of the atmospheric conditions during the observations. The distribution of the FWHMs in the r'-band, the band used for the lensing analysis, is shown in Figure 2.4. The values of the FWHM range from $0.5''$ to $1.0''$, and have a median value of $0.71''$. This is exceptionally good for a ground-based survey (e.g. compare Table 2.1.)

In November 2004, when approximately 20% of the primary survey area had been observed, the lens L3 was accidentally mounted incorrectly after the wide-field corrector had been disassembled. This surprisingly led to a significant improvement in the PSF pattern, and the new configuration was kept. The dramatic improvement of the PSF pattern is demonstrated by plotting the stellar ellipticity vectors across the camera in Figure 2.5; prior to that moment, the PSF showed a strong pattern, with ellipticities reaching up to 15% in the corners of the images. After this moment, no clear PSF pattern could be discerned, and the amplitude of the PSF ellipticity was significantly reduced. The FWHM distribution of the two sets are shown in Figure 2.4. We note, however, that none of the area observed prior to November 2004 has been discarded, as we correct for the potential residual systematics that may result from the very elliptical PSF (detailed in Section 2.5.4).

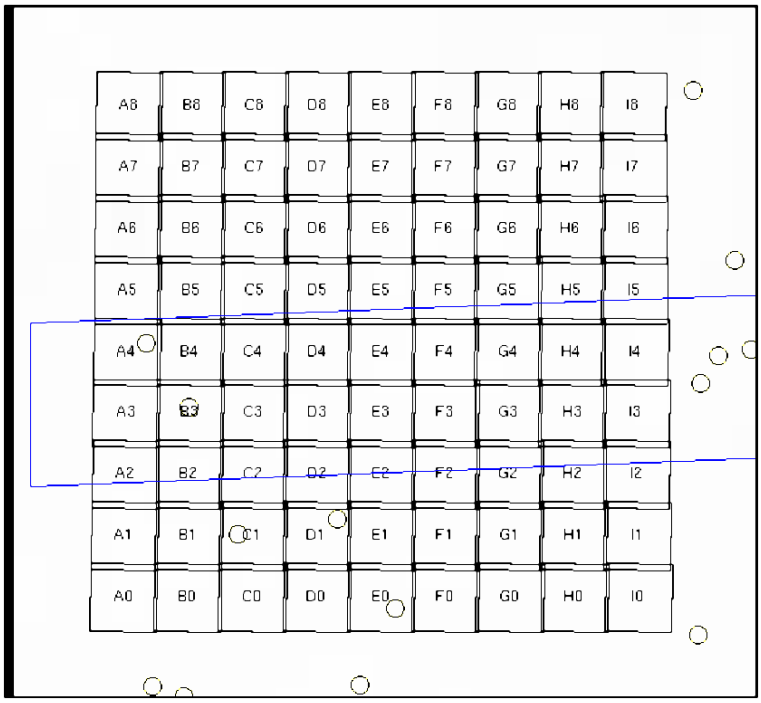

Figure 2.3: The location of the 81 exposures in the patch 2338, as a function of right ascension (horizontal axis) and declination (vertical axis). The circles denote the location of bright stars from the Bright Star Catalogue 4, with a magnitude between 4 and 6. The blue box shows the overlap with the SDSS (image courtesy: rcs2.org)

2.3 Data reduction

The basic reduction of the images is performed with Elixir[2] at the CFHT. Elixir consists of a collection of programs that is used for the instant assessment of the image quality of telescope data, and also contains programs to perform the basic image reduction. The goal of this reduction is to remove the instrumental signature from the data, so that the images can be used for science. This reduction corrects for the positive offset of the detector of the camera, for the dark current (the electrons that are occasionally released in the CCD due to thermal motions instead of photons), for the unequal sensitivity of the pixels in the CCD, and for the presence of fringes, which are caused by thin-film interference effects in the detector. Once this basic reduction has been performed, objects are detected with `SExtractor` (Bertin & Arnouts 1996). The locations of the detections are compared to the USNO 1.0 star catalogue to calculate the astrometric solution, such that the (x, y)-locations of the pixels can be translated into sky coordinates. Finally, by comparing the observed photon counts of these stars to their known magnitudes, zero points, that is the conversion factor between counts and apparent magnitude, are calculated for each image.

[2] http://www.cfht.hawaii.edu/Instruments/Elixir/

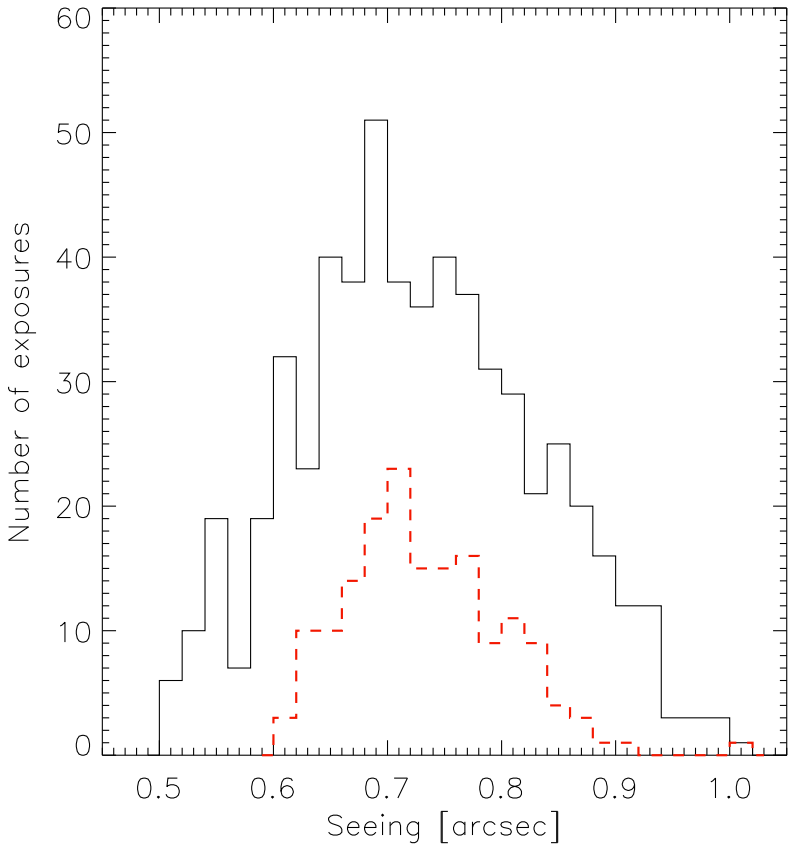

Figure 2.4: The distribution of the FWHM of the stars in the 739 r'-band images in the primary survey area of the RCS2. The solid black (dashed red) line shows the distribution for the images observed after (before) the change of the lens configuration.

Using the zero points, we can determine the apparent magnitudes of all detected objects in the image.

We retrieve the Elixir processed images from the Canadian Astronomy Data Centre (CADC) archive[3]. We use the THELI pipeline (Erben et al. 2005, 2009) to subtract the image backgrounds, create weight maps that we use in the object detection phase, and to identify satellite and asteroid trails. To obtain a more accurate astrometric solution, we run `SCAMP` (Bertin 2006) on the images, which enables us to match our catalogues to other catalogues, including the photometric catalogues from Gilbank et al. (2011), and the spectroscopic catalogues from the SDSS. Additionally, we use the polynomial coefficients from `SCAMP` that describe the mapping from image to sky coordinates to calculate the systematic shear that results from the camera distortion, and for which we have to correct.

[3]http://www1.cadc-ccda.hia-iha.nrc-cnrc.gc.ca/cadc/

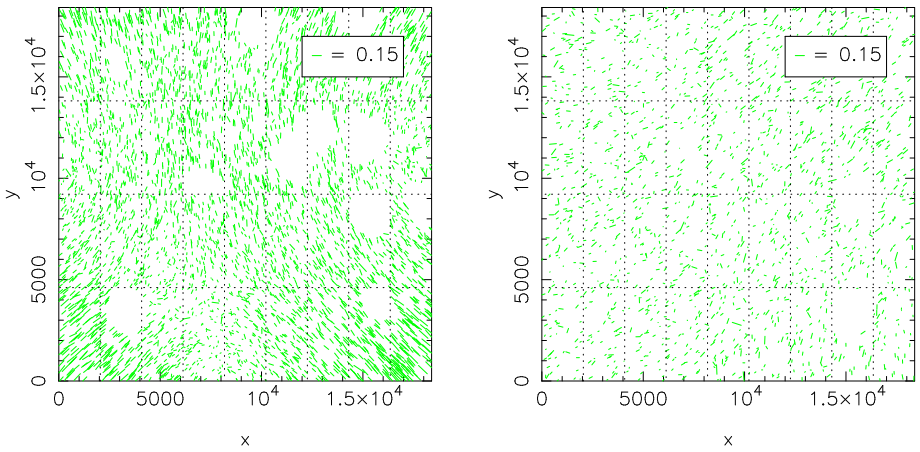

Figure 2.5: The ellipticities of the stars in two exposures as a function of position in the mosaic. The green sticks indicate the size and orientation of the ellipticities of the stars that are used for modeling the PSF (note that only half of the total number of stars is plotted for clarity). The dashed lines approximately denote the chip boundaries. On the left-hand side, we show the stellar ellipticities in the field 2143H6, which was observed before the lens configuration changed. The PSF shows a clear pattern, and is very elliptical in the corners of the image. On the right-hand side, we show the stellar ellipticities in 1613A2, which was observed after the lens-configuration change. No pattern is observed in the PSF, and the PSF ellipticity is small across the image.

Each exposure contains areas where the photometry is affected by the reflection haloes of large stars, diffraction spikes, satellite and asteroid trails, and other anomalies. Excluding such areas in lensing studies is important, as the shape measurement of galaxies in those areas is unreliable, and may contaminate the lensing signal. For that purpose, we create image masks for our lensing analyses by combining the masks from the automated masking routines from THELI with the RCS2 masks, as neither of these masks individually works sufficiently well for our purposes. The THELI mask poorly covers the large stellar reflections, potentially because we run the pipeline on individual chips. The RCS2 masks covers these large stellar reflections well, but misses many satellite and asteroid trails that are properly masked by THELI. To exclude the contaminated areas that are not covered by either mask, we inspect all masks by eye, and manually improve them where necessary.

An additional advantage of the visual inspection of the data was the discovery of various problematic exposures that were not flagged by the standard image quality checks. Two sets of these exposures are discussed in the last two paragraphs of the next section.

2.3.1 Problematic exposures

For a number of exposures, problems occurred either during the observations or the image reduction. Consequently, some images had to be excluded from

the science analysis. We describe the problems of these fields below.

During parts of the observing run 05BQ03, the upper half of the camera (chips 18 to 36) was not read out due to a failure in the power supply in the South controller. The four RCS2 r'-band images that were taken in this run have been discarded.

The read-out of chip 5 failed for the twenty-one r'-band exposures taken in observing runs 03BQ06 and 03BQ07. This did not affect the other chips, and the exposures were included.

The r'-band exposures of the patches 0047F8, 2338I1 and 2338I8 exhibit a strange feature; faint horizontal and vertical trails emerge from the bright stars, which are most likely caused by an electronic problem during the read-out. As it is not clear how this anomaly depends on the brightness, nor whether stars and galaxies are affected in an equivalent way, these three exposures have been removed from the science analyses.

Finally, the central pixels of the bright stars in chip 28 to 36 in the observing runs 04BQ02 and 04BQ03 have negative values. This problem was caused by a failure of the video board in the South controller, which resulted in the amplifier saturating at 32K instead of the usual 65K. All the problematic stars are masked, as to make sure they are not used to model the PSF. The exposures have been included in the science analyses.

2.4 Catalogue creation

We use `SExtractor` (Bertin & Arnouts 1996) to detect the objects in the images. From the object catalogues we select the stars, which are used for modeling the PSF variation across the images. An accurate model of the local size and shape of the PSF is essential, as the measured galaxy images have to be corrected for the smearing of the PSF to obtain their unconvolved shapes. Hence we require a clean star catalogue, that contains many stars distributed over the entire image in order to sample the spatial variation of the PSF. To separate the stars from the galaxies, we first identify the locus of the stellar branch in a size-magnitude diagram. We select the non-saturated objects close to the stellar branch with a S/N ratio larger than 30 and with no `SExtractor` flags raised. To remove small galaxies that have been misidentified as stars, and stars that have been affected by cosmic rays, we fit a second-order polynomial to both the size and the ellipticity of these star-candidates as a function of their position in the chip, and discard all 3-sigma outliers. We clean the stellar selection even further in the shape measurement pipeline by removing shape parameter outliers. All objects larger than 1.2 times the local size of the PSF are classified as galaxies, and passed on to the shape measurement pipeline. Smaller objects are not included as they consist of a mixture of stars and galaxies. The resulting effective galaxy number density is 11.6 arcmin^{-2}. Two diagnostic plots of the star-galaxy separation are shown in Figure 2.6. The separation has been fully automated, but as a precaution we inspect the diagnostic plots for all exposures by eye. The separation fails only for a few chips that have either very few stars or a PSF with a large FWHM, and we manually adjust those. As neighbouring patches overlap by ~ 1 arcminute, we remove all galaxies within 35 arcseconds from the image edges in order to avoid duplicating the objects in our analysis.

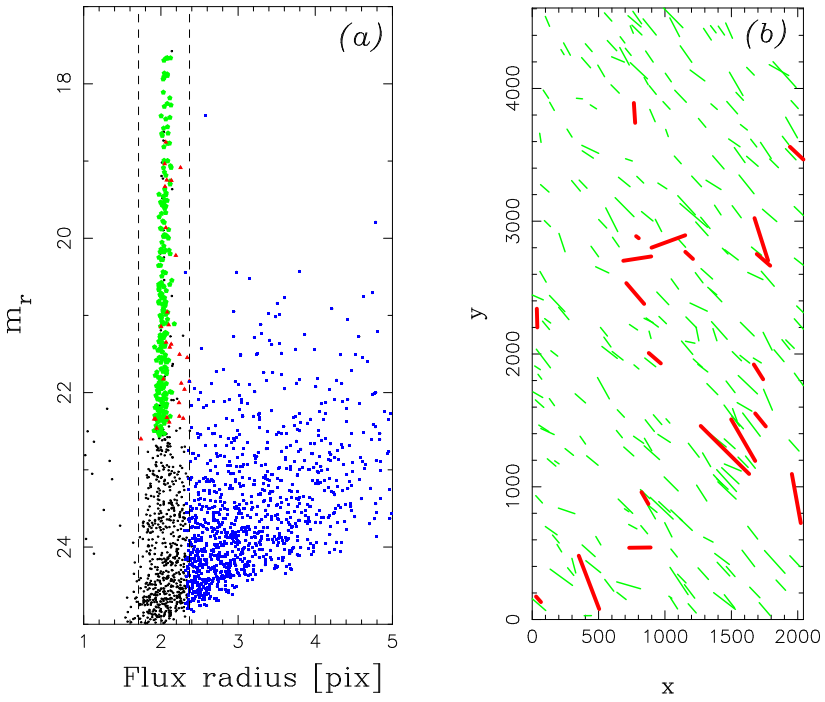

Figure 2.6: In panel (a), we show the size-magnitude diagram of one of the chips in a randomly picked exposure. The black dots are the `SExtractor` detections, the green pentagons are the selected stars, the red triangles are the 3-sigma outliers, and the blue squares are the selected galaxies. The dashed lines indicate the location of the stellar branch. Thanks to the good image quality the stars are easily separated from the galaxies. In panel (b), we show the location of the same stars and their ellipticity vectors as a function of position in the chip. The 3-sigma outliers are indicated by the thick red lines.

Elixir provides approximate zero-points for each pointing, which we use to measure the r'-band apparent magnitudes of the objects in the images. We correct the magnitudes for galactic extinction using the dust maps from Schlegel et al. (1998). We asses the quality of the photometry in Section 2.5.

2.4.1 Weak lensing analysis

For our lensing analysis we measure the shapes of galaxies with the KSB method (Kaiser et al. 1995; Luppino & Kaiser 1997; Hoekstra et al. 1998), using the implementation described by Hoekstra et al. (1998, 2000). There are several alternative methods to measure shapes of galaxies. We use the KSB method because it measures the shapes of galaxies accurately in simulations (see Section 2.5), and because it has been extensively used and tested on real data. Finally, the method is fast.

In KSB, galaxy shapes are defined by the raw pseudo ellipticities, which we

call polarizations from here on:

$$\epsilon_1 = \frac{Q_{11} - Q_{22}}{Q_{11} + Q_{22}}; \epsilon_2 = \frac{Q_{12}}{Q_{11} + Q_{22}}, \tag{2.1}$$

where Q_{ij} is the weighted moment of the brightness distribution $B(\mathbf{x})$:

$$Q_{ij} = \int d^2\mathbf{x}\, B(\mathbf{x}) W(x) x_i x_j, \tag{2.2}$$

with $W(x)$ a Gaussian weight function. The weight function and the integral are centered at the galaxy. To convert the measured galaxy polarizations into ellipticities, the polarizations have to be corrected for the circularization by the weight function, and for smearing by the PSF. These corrections are described by complex formula that can be found in the original papers. To correct for the PSF, we need to determine the smear susceptibility tensor, $P^{\mathrm{sm}\star}$, which describes how the PSF affects the galaxy polarizations. $P^{\mathrm{sm}\star}$ is estimated by the combination of various higher-order moments of the brightness distribution of the stars in a chip. The components of the tensor are interpolated at the location of the galaxies using a polynomial that is third-order in y and second-order in x (the length of the chip in the y-direction is more than twice the length in the x-direction), fitted to each chip separately.

The PSF correction has a limited accuracy in practice. One of the reasons is that in the KSB formalism, it is assumed that the brightness distribution of stars can be described by an isotropic profile convolved with a small anisotropic kernel. The PSF is generally more complicated which may lead to biases. To study the magnitude of these biases, this implementation of KSB has been tested on simulations with a variety of PSFs, which we will discuss in Section 2.5.2.

The ellipticities of the galaxies are also affected by slight non-linearities in the mapping between the sky coordinates and the CCD pixels in the camera, an effect which is called camera distortion. We calculate the shear induced by this distortion using the polynomial coefficients from `SCAMP` that describe how the image coordinates are mapped onto the sky coordinates. The camera shear of MegaCam is shown in Figure 2.7. The images of both the stars and the galaxies are sheared, with a value reaching 1.5% at the corners of the images. At large lens-source separations, where the gravitational lensing signal is small, the camera shear dominates the observed lensing signal. Hoekstra et al. (1998, 2000) demonstrate that the observed shear is the sum of the gravitational shear and the camera shear. We therefore simply subtract the camera shear from the observed ellipticities of the galaxies to correct for it, after correcting the galaxy shapes for smearing by the PSF.

In real data, there is always shear present to some level that is not produced by gravitational lensing (systematic shear), due to imperfect PSF corrections, biases in the shape measurement pipeline, the image masks and the survey layout. When we measure the mean lensing signal around galaxies or clusters of galaxies on small scales, these systematic contributions average out since we generally average over a large number of lens-source orientations. On larger scales, however, we cannot average over many orientations, because we perform the lensing analysis on single exposures. We do this because including source galaxies from neighbouring exposures to the analysis barely improves the lensing signal-to-noise on small scales, which is the regime we are interested in in

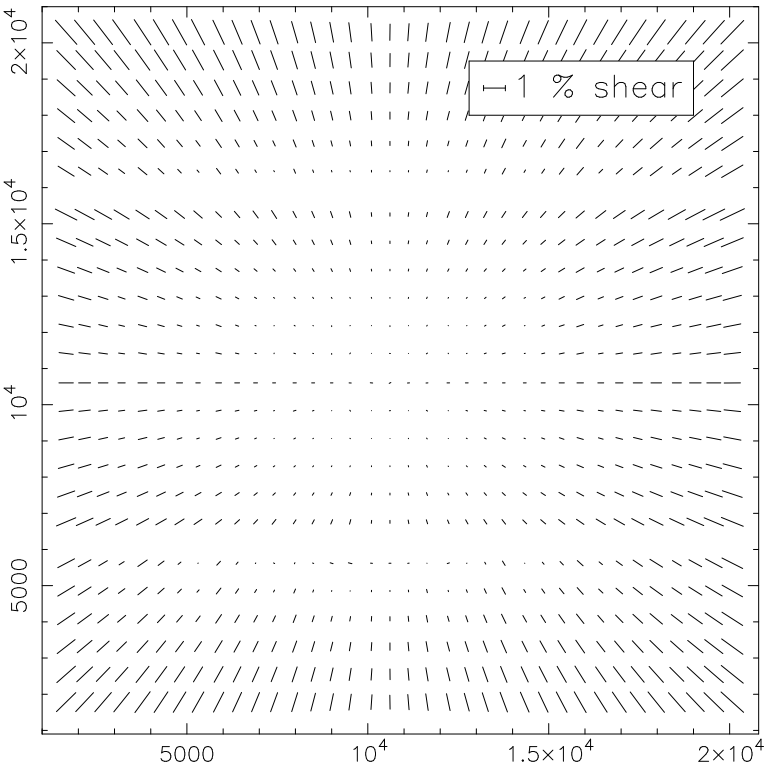

Figure 2.7: Shear induced by camera distortion in the MegaCam imager. The camera shear is largest in the corners of the mosaic, with values up to 1.5%. As the observed shear is the sum of the gravitational shear and the camera shear, we simply subtract the camera shear from the observed galaxy ellipticities to correct for it.

the studies of this thesis. Hence the source galaxies at large separations always reside in the corners. Consequently, there is systematic contribution to the real shear. To remove this signal, we measure the lensing signal around a catalogue of random lens positions. In the absence of systematic shear in the shape catalogues, the shear signal around random lenses is zero, but if systematic shear is present, the random signal and the real signal are equally affected. We use 40 000 random lenses per image, roughly 20 times the number of real lenses used at most per image in the science analyses. The random lensing signal is measured using the same binning, and subtracted from the real lensing signal. We test the correction in the next section.

2.5 Quality Checks

We perform various tests to assess the quality of the photometry and the shape measurements. Furthermore, we study the fidelity of our corrections for camera shear and systematic shear. These tests are done to ensure that no major systematics remain in the catalogues that may bias the science results.

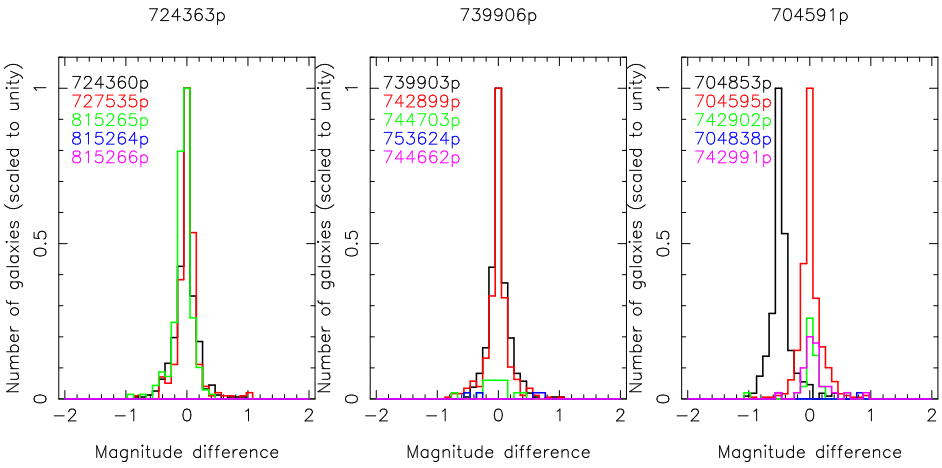

Figure 2.8: Internal comparison of the r'-band magnitudes of galaxies that reside in the areas that overlap with neighbouring exposures. Each overlapping exposure is indicated by a different colour, and their names shown in the top-left corners. The photometry of the majority of exposures agrees well internally, as the histograms are centered on zero and have a small width. Only a few exposures have erroneous zero-points. We show one example in the right-hand panel, where the zero-point of the image 704853 is off by ∼0.5 magnitude.

2.5.1 Photometry

As a check of internal consistency, we compare the magnitudes of the galaxies from different exposures that reside in the overlapping areas. Depending on its location in the patch, an exposure may overlap with up to 8 neighbours. We match the galaxies from adjacent fields, and make histograms of the difference in r'-band magnitudes. A few examples are shown in Figure 2.8. These histograms show that for nearly all exposures, the zero-points between neighbouring fields are consistent as the histograms are centered close to zero. Only for a few exposures, the histograms are significantly shifted from zero, which indicates that in either one of the exposures the zero-point is far off. As the exposures generally overlap with more than one neighbour, the fields with erroneous photometry are easily identified.

Next, we compare the 'raw' dust-corrected r'-band magnitudes of the galaxies to the more accurately calibrated ones from Gilbank et al. (2011). For each exposure we make a histogram of the difference in magnitudes. A few examples are shown in Figure 2.9. The histograms demonstrate that the magnitudes agree well for the majority of galaxies. The fields with an erroneous zero-point as revealed by the internal comparison are easily identified from these histograms as well since they are significantly shifted from 0. None of the histograms are Gaussian, but they all show a tail at $m_{r'} - m_{r',\mathrm{Gilbank}} < 0$. This is likely due to the fact that different apertures have been used in the measurements. In one exposure, the histograms are offset by $\Delta m_r \approx 2$, indicating that a major error occurred in one of the photometric solutions. On average, however, the magnitudes agree well, and differ in the r'-band by $\langle m_{r'} - m_{r',\mathrm{Gilbank}} \rangle = 0.00 \pm 0.26$. The scatter is dominated by faint galaxies; when we limit the comparison to

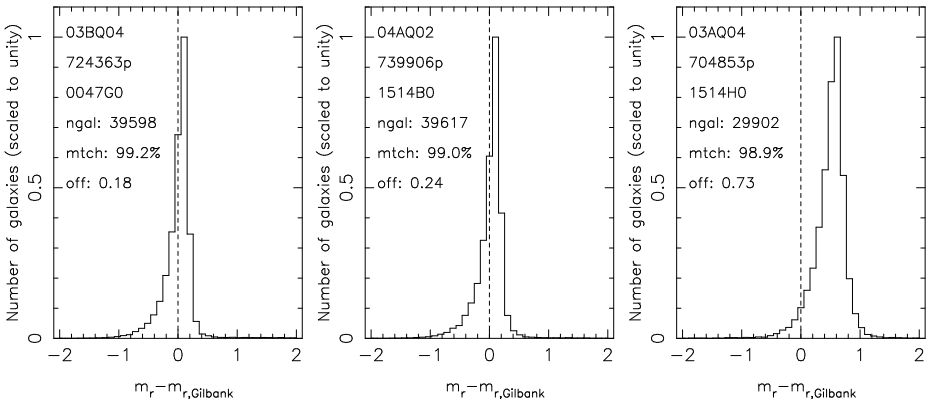

Figure 2.9: Comparison of the r'-band magnitudes of galaxies with the photometric catalogues from Gilbank et al. (2011) for three exposures. The left-hand and middle panel show the same exposures as in Figure 2.8, the right-hand panel shows the exposure with image number 704583 whose zero-point was found to be off, which is again confirmed. The top-left corner of each plot shows the observing run number, the image name, the patch name, the number of galaxies, the percentage of matched galaxies and the mean offset. For the majority of exposures, the magnitudes agree well. The non-Gaussian shapes of the histograms are likely due to a difference in the size of the aperture used for measuring the flux.

galaxies with $m_{r'} < 23$, we find $\langle m_{r'} - m_{r',\mathrm{Gilbank}} \rangle = 0.01 \pm 0.14$.

In the whole thesis we use the photometric catalogue from Gilbank et al. (2011), except in Chapter 3, as the photometric catalogue was not available at the time of writing. However, in Chapter 3 the 'raw' Elixir magnitudes are only used to select the source galaxy sample and for this purpose they are sufficiently accurate.

2.5.2 Galaxy shapes

The implementation of the KSB method we use has been tested on the Shear Testing Programme (STEP) simulations (the HH method in Heymans et al. 2006; Massey et al. 2007). The STEP simulations are used for the blind testing and comparison of shape measurement methods. These simulations consist of an artificial set of survey images, containing a large number of galaxies whose morphologies mimic those of real galaxies. To these galaxies a shear is applied which is constant, but differs from image to image. The images are then convolved with a variety of PSFs, to test the reliability of methods under different observing conditions. The goal of any of the tested methods is to determine as accurately as possible the value of the input shear. Its values is not known beforehand to avoid tweaking of the methods. The performance of each method is determined by two numbers, m_i and c_i, the multiplicative bias and the shear calibration bias, defined as

$$\langle \tilde{\gamma}_i \rangle - \gamma_i^{\mathrm{input}} = m_i \gamma_i^{\mathrm{input}} + c_i, \tag{2.3}$$

where i denotes the different components, $\gamma_i^{\rm input}$ is the input shear and $\langle\tilde{\gamma}_i\rangle$ is the averaged measured shear. A non-zero m_i indicates that the method does not respond one-to-one to shear, and a non-zero c_i generally indicates that the PSF has not been properly corrected for. For STEP1, the HH method has an average multiplicative bias of $\langle m\rangle = -0.015 \pm 0.006$, and a mean calibration bias $\langle c\rangle$ that is consistent with shot noise at the 0.1% level. For STEP2, the average $\langle m\rangle$ is -0.01, and the mean $\langle c\rangle$ is consistent with zero. Note, however, that for the simulations with a highly elliptical PSF (simulation set D and E in STEP2), all tested shape measurement pipelines (including the HH method) have a significant non-zero shear calibration bias. This is not a major concern in this thesis for a number of reasons. First of all, the area with a highly elliptical PSF in the RCS2 is very small compared to the total survey area; potentially biased galaxy shapes will not contribute much to the total signal. Furthermore, most of the systematics will average out since we measure the lensing signal around galaxies and galaxy clusters for a large number of random lens-source orientations. Finally, by subtracting the random lensing signal from the signal computed with real lenses, we remove PSF residuals from the galaxy-mass cross-correlation function at large-scales that are still present because we do not have enough lens-source orientations to average over. Note that in the measurement of the correlation between the ellipticities of galaxies, as is done in cosmic shear studies, or in cluster mass reconstruction studies, PSF residuals can introduce a significant bias in the result. The areas with a highly elliptical PSF should be excluded from such analyses. In conclusion, the results of the STEP simulations indicate that the HH method is a shape measurement method accurate and robust enough for the scientific purposes of this thesis, and suggest that the shear measured in the RCS2 data is underestimated by 1–2 % at most.

As for the photometry, we make an internal comparison of the ellipticity estimates using the galaxies in the areas that overlap with neighbouring exposures. Histograms of the differences in the e_2 ellipticity components are shown in Figure 2.10. The histograms are all centered on zero. Combining all the overlapping regions, we find that the average spread has a value 0.09, which decreases to 0.05 and 0.03 if we only compare galaxies with $m_{r'} < 23$ and $m_{r'} < 22$, respectively. The average galaxy polarization errors for these selections are 0.05, 0.02 and 0.01. The average *ellipticity* error of these galaxies is larger, however, due to uncertainties in the PSF correction. Additionally, we compare galaxies close to the sides of the image, where the PSFs pattern differs most between the images. Hence the values for the average spread are reasonable, which demonstrates that the method is stable, and the ellipticity estimate for a galaxy is robustly measured in the RCS2.

The shapes of galaxies in the RCS2 have been measured independently with the shapelet method (Refregier 2003; Refregier & Bacon 2003), using the implementation of Kuijken (2006). This shape measurement technique provides independent estimates of the ellipticity of galaxies. We compare the ellipticity components of 450 000 galaxies in Figure 2.11. For small ellipticities, the ellipticity components agree well. For galaxies with $e_i > 0.15$, the ellipticities measured with KSB are slightly larger than those measured with shapelets. This discrepancy might be caused by the rapid radial decline of the shapelets basis functions. Consequently, shapelets have difficulties in fitting galaxies with flat surface brightness profiles, and very elliptical galaxies, leading to biases in the ellipticity measurement.

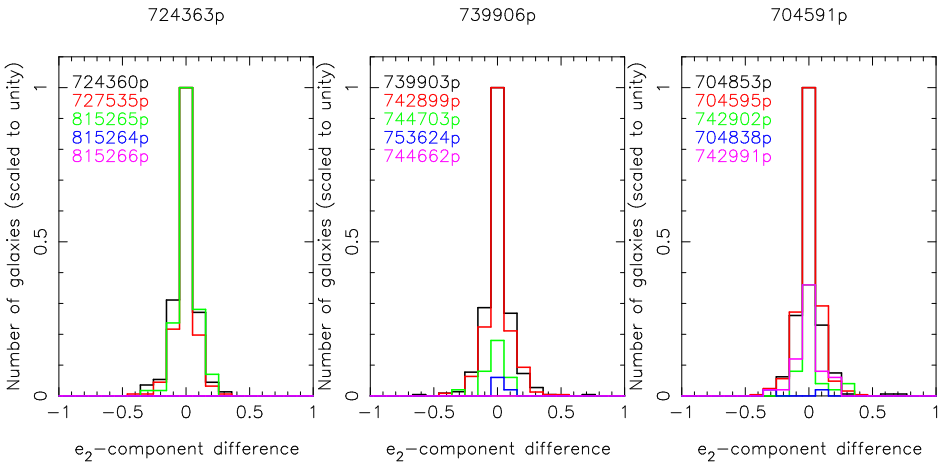

Figure 2.10: Three examples of the comparison of the e_2 ellipticity component of the galaxies that reside in the areas that overlap with neighbouring exposures. Each overlapping exposure is indicated by a different colour, and their names shown in the top-left corners. Both the e_1 and e_2 ellipticity component agree well internally, as all histograms are narrow and centered on zero. This demonstrates that the ellipticities of galaxies are robustly determined with the KSB method.

Another standard test performed in gravitational lensing is the measurement of the so-called cross shear. Gravitational lensing only produces 'tangential' distortions – the shapes of source galaxies are stretched in the direction perpendicular to the lens-source separation. The cross shear measures the shear component that is rotated by 45 degrees with respect to the lens-source separation vector. A non-zero cross shear indicates the presence of systematics in the shape catalogues. If the cross shear is zero, however, the shape catalogues are not necessarily free of systematics. The cross shear and the tangential shear are measured simultaneously in the science analyses. In all the lensing measurements we perform throughout this thesis, we find that the cross shear signal is consistent with zero. As an example, we refer the interested reader to Figure 3.5 in Chapter 3.

2.5.3 Camera shear correction

The camera shear results from slight non-linearities in the mapping between the sky coordinates and the CCD pixels. It is calculated by taking the gradient of the polynomial fits from `SCAMP` that describe the mapping between image to sky coordinates. The camera shear pattern is mainly radial, as can be seen in Figure 3.4 in Chapter 3. To check whether we properly remove the camera shear, we measure the tangential shear around the centre of the images, using the corrected and uncorrected galaxy ellipticities. The result of this test is shown in Figure 2.12. When we do not correct for camera shear, we observe that the measured signal turns negative towards the edges of the images. After the correction, the effect is reduced but some residual is still present. We attribute this to residual PSF systematics, as we demonstrate in the next section.

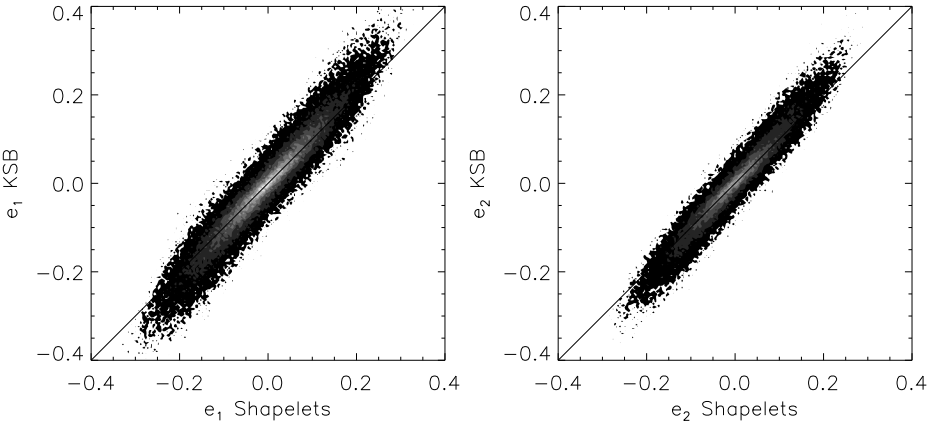

Figure 2.11: Comparison of the ellipticity components of 450 000 galaxies measured with the KSB method and with the shapelets method, for e_1 in the left-hand panel, and for e_2 in the right-hand panel. The ellipticities agree well for $e_i < 0.15$, but for larger ellipticities KSB measures larger values.

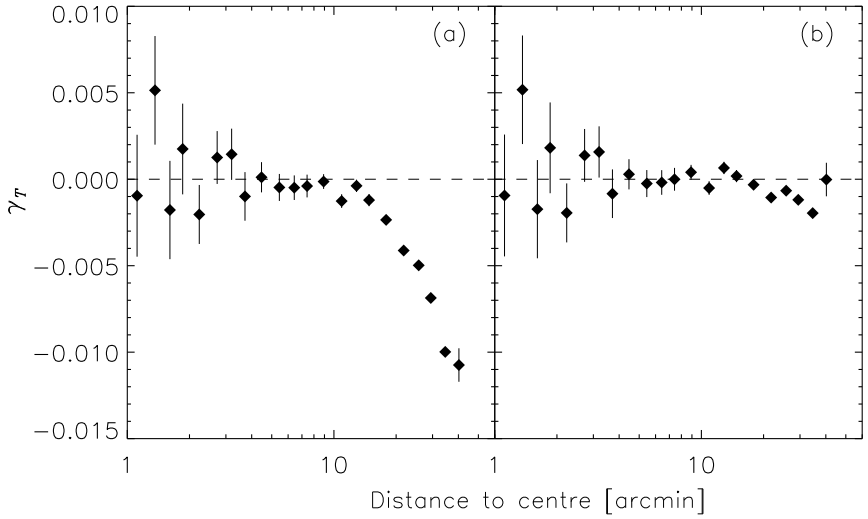

Figure 2.12: The shear around the centre of the camera. In panel (a), the correction for camera shear has not been applied. Consequently, the signal becomes negative at scales >10 arcmin as the camera distortion is mainly radial. We apply the camera shear correction in panel (b), which strongly suppresses the large-scale negative signal. A small residual negative signal is left, which is caused by imperfect PSF corrections of the galaxy shapes. In lensing measurements, the subtraction of the signal around random lenses corrects for this.

2.5.4 Random catalogues

For each image, a large number of random lens positions are generated. The lenses that reside inside the masked regions are removed. We measure

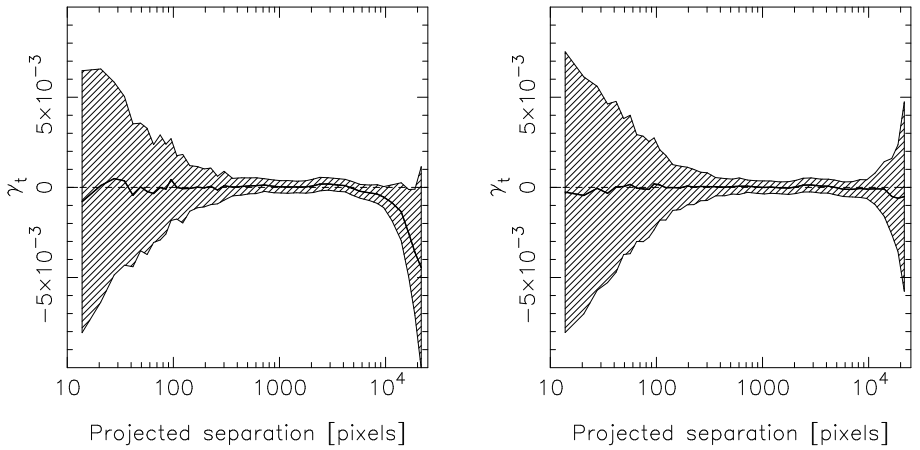

Figure 2.13: The signal of the random lens catalogues for the exposures taken prior to the lens-configuration change (left-hand panel), and the exposures observed afterwards (right-hand panel), after applying the correction for camera shear. The thick line shows the average, the hatched area shows the scatter between the exposures. The random signal of the left-hand panel turns negative at large scales, which indicate the presence of PSF residual systematics in the shape catalogues.

the lensing signal using 40 000 random lenses per image, and show the average signal in Figure 2.13 (after applying the correction for camera shear). The left panel shows the random signal for the 160 exposures taken prior to the change of the orientation of the lens, which took place in November 2004. The right panel shows the random signal for the 600 exposures taken after that moment. In both cases, the random signal on small scales is consistent with zero, since the signal is averaged over many lens-source orientations. At large scales, the random shear signal of the images observed before the lens configuration change turns negative. This residual pattern is due to imperfect PSF corrections of the galaxies that reside near the edges and corners of the images, where the PSF was found to be very elliptical (see Figure 2.5).

To demonstrate how the random signal impacts the lensing measurements, we measure the tangential shear around 1.6×10^6 lenses with magnitudes in the range $19.5 < m_{r'} < 21.5$, using 14×10^6 source galaxies with $22 < m_{r'} < 24$. We perform the measurement both with and without subtracting the random lensing signal, and show both results in Figure 2.14. Without correcting for the random signal, the shear increases from $\sim$6 to $\sim$10 arcminutes, after which it rapidly decreases and turns negative. Correcting the shear with the random signal removes this odd bump and negative signal. The corrected signal is smooth, suggesting that the correction for systematic contributions works well.

Bibliography

Amara, A. & Réfrégier, A. 2007, MNRAS, 381, 1018

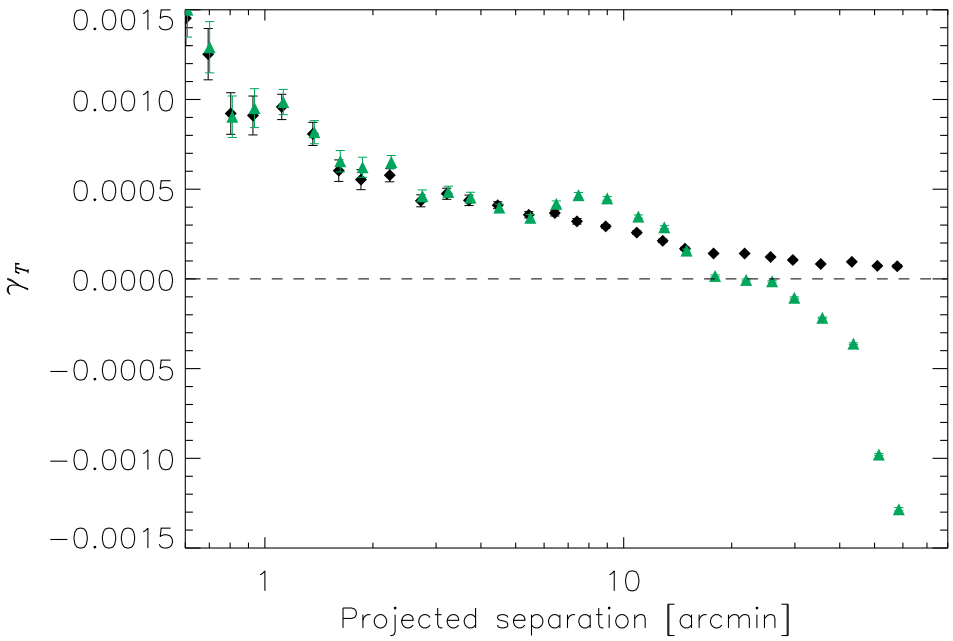

Figure 2.14: The stacked tangential shear around 1.6×10^6 magnitude-selected lenses ($19.5 < m_r < 21.5$) measured using 14×10^6 source galaxies with $22 < m_{r'} < 24$. The green triangles show the signal that has not been corrected for the random lensing signal, and is slightly negative at lens-source separations larger than 20 arcmin. Note that the effect is about ten times smaller than the camera shear. The black diamonds show the corrected signal, which is smoother at large scales and does not become negative. We did not use neighbouring exposures to measure the lensing signal in this figure, because this more clearly illustrates the main source of the systematic signal, i.e. imperfect PSF corrections in the corners of the images.

Bertin, E. 2006, in Astronomical Society of the Pacific Conference Series, Vol. 351, Astronomical Data Analysis Software and Systems XV, ed. C. Gabriel, C. Arviset, D. Ponz, & S. Enrique, 112

Bertin, E. & Arnouts, S. 1996, A&AS, 117, 393

Blake, C., Brough, S., Couch, W., et al. 2008, Astronomy and Geophysics, 49, 050000

Boulade, O., Charlot, X., Abbon, P., et al. 2003, in Society of Photo-Optical Instrumentation Engineers (SPIE) Conference Series, Vol. 4841, Society of Photo-Optical Instrumentation Engineers (SPIE) Conference Series, ed. M. Iye & A. F. M. Moorwood, 72–81

Erben, T., Hildebrandt, H., Lerchster, M., et al. 2009, A&A, 493, 1197

Erben, T., Schirmer, M., Dietrich, J. P., et al. 2005, Astronomische Nachrichten, 326, 432

Gilbank, D. G., Gladders, M. D., Yee, H. K. C., & Hsieh, B. C. 2011, AJ, 141, 94

Gladders, M. D. & Yee, H. K. C. 2000, AJ, 120, 2148

Heymans, C., Van Waerbeke, L., Bacon, D., et al. 2006, MNRAS, 368, 1323

Hirata, C. M., Mandelbaum, R., Seljak, U., et al. 2004, MNRAS, 353, 529
Hoekstra, H., Franx, M., & Kuijken, K. 2000, ApJ, 532, 88
Hoekstra, H., Franx, M., Kuijken, K., & Squires, G. 1998, ApJ, 504, 636
Kaiser, N., Squires, G., & Broadhurst, T. 1995, ApJ, 449, 460
Kuijken, K. 2006, A&A, 456, 827
Leauthaud, A., Tinker, J., Bundy, K., et al. 2012, ApJ, 744, 159
Luppino, G. A. & Kaiser, N. 1997, ApJ, 475, 20
Mandelbaum, R., Seljak, U., Kauffmann, G., Hirata, C. M., & Brinkmann, J. 2006, MNRAS, 368, 715
Massey, R., Heymans, C., Bergé, J., et al. 2007, MNRAS, 376, 13
Okabe, N., Takada, M., Umetsu, K., Futamase, T., & Smith, G. P. 2010, PASJ, 62, 811
Refregier, A. 2003, MNRAS, 338, 35
Refregier, A. & Bacon, D. 2003, MNRAS, 338, 48
Schlegel, D. J., Finkbeiner, D. P., & Davis, M. 1998, ApJ, 500, 525
Schrabback, T., Hartlap, J., Joachimi, B., et al. 2010, A&A, 516, A63
Sheldon, E. S., Johnston, D. E., Scranton, R., et al. 2009, ApJ, 703, 2217
Tyson, J. A., Wenk, R. A., & Valdes, F. 1990, ApJ, 349, L1
van Uitert, E., Hoekstra, H., Velander, M., et al. 2011, A&A, 534, A14
Willott, C. J., Delfosse, X., Forveille, T., Delorme, P., & Gwyn, S. D. J. 2005, ApJ, 633, 630
York, D. G., Adelman, J., Anderson, Jr., J. E., et al. 2000, AJ, 120, 1579

3

On the relation between baryons and dark matter in galaxies in the Red Sequence Cluster Survey 2

We present the results of a study of weak gravitational lensing by galaxies using imaging data that were obtained as part of the second Red Sequence Cluster Survey (RCS2). In order to compare to the baryonic properties of the lenses we focus here on the ∼300 square degrees that overlap with the DR7 of the SDSS. The depth and image quality of the RCS2 enables us to significantly improve upon earlier work for luminous galaxies at $z \geq 0.3$. Comparison with dynamical masses from the SDSS shows a good correlation with the lensing mass for early-type galaxies. For low luminosity (stellar mass) early-type galaxies we find a satellite fraction of ∼40% which rapidly decreases to < 10% with increasing luminosity (stellar mass). The satellite fraction of the late-types has a value in the range 0-15%. We find that early-types with a r-band luminosity in the range $10^{10} < L_r < 10^{11.5}\ h_{70}^{-2} L_\odot$ have virial masses that are about five times higher than those of late-type galaxies and that the mass scales as $M_{200} \propto L^{2.34^{+0.09}_{-0.16}}$. We also measure the virial mass-to-light ratio, and find for early-types that have a total luminosity within the virial radius of $L_{200} < 10^{11}\ h_{70}^{-2} L_\odot$ a value of $M_{200}/L_{200} = 42 \pm 10\ h_{70} M_\odot/L_\odot$, which increases for higher luminosities to values that are consistent with those observed for groups and clusters of galaxies. For late-type galaxies we find a lower value of $M_{200}/L_{200} = 17 \pm 9\ h_{70} M_\odot/L_\odot$. Our measurements also show that early- and late-type galaxies have comparable halo masses for stellar masses $M_* < 10^{11}\ h_{70}^{-1} M_\odot$, whereas the virial masses of early-type galaxies are higher for higher stellar masses. Finally, we determine the efficiency with which baryons have been converted into stars. Our results for early-type galaxies suggest a variation in efficiency with a minimum of ∼10% for a stellar mass $M_{*,200} = 10^{12}\ h_{70}^{-1} M_\odot$. The results for the late-type galaxies are not well constrained, but do suggest a larger value.

E. van Uitert, H. Hoekstra, M. Velander, D.G. Gilbank, M.D. Gladders, H.K.C. Yee, A&A accepted (ref. AA/2011/17308);

3.1 Introduction

There is now overwhelming evidence that galaxies are surrounded by dark matter haloes. Studying the global properties of the haloes, such as their virial masses or density profiles, however, has proven difficult due to a lack of reliable tracers of the gravitational potential at large distances. Improving observational constraints is important because the details of galaxy formation are not completely clear, even though significant progress has been made in recent years (e.g. Bower et al. 2010; Kim et al. 2009). The relation between the baryons and the dark matter in galaxies has been studied using numerical simulations (e.g. Wang et al. 2006; Croton et al. 2006; Somerville et al. 2008; Moster et al. 2010) and it is important to confront the predictions with observations. This requires reliable estimates of both the dark matter and the baryonic content of galaxies.

Several observables can be used to trace the baryons, such as the luminosity of a galaxy, which is readily available. It is also possible to derive stellar masses by fitting stellar synthesis models to either the spectral features of a galaxy (Kauffmann et al. 2003; Gallazzi et al. 2005) or to its colours (Bell & de Jong 2001; Salim et al. 2007). The stellar mass estimates are tightly correlated to various other important global properties of galaxies (colour, metallicity, luminosity, environment, see e.g. Grützbauch et al. 2011, and references therein) and they are therefore considered a useful tracer of the baryonic content of a galaxy.

Numerical simulations suggest that the dark matter haloes of massive galaxies extend out to hundreds of kiloparsecs (e.g. Springel et al. 2005), which is supported by observations (e.g. Hoekstra et al. 2004). For nearby galaxies it is possible to study the dark matter distribution using the dynamics of planetary nebulae (e.g. Napolitano et al. 2009). In addition, studies of satellite galaxies around central galaxies (e.g. More et al. 2011; Conroy et al. 2007) have provided constraints on the relation between baryons and dark matter. Unfortunately these studies require spectroscopy of large numbers of objects, which makes them rather expensive. Furthermore, the observations are limited to small scales due to the requirement of having optical tracers, which complicates the determination of the virial mass of the haloes galaxies reside in, unless one is willing to extrapolate the measurements.

Fortunately it is possible to probe the matter distribution on large scales, thanks to an effect called weak gravitational lensing; we can measure the distortion of the shapes of faint background galaxies (sources) caused by the bending of light rays by intervening mass concentrations (lenses). The distortion is independent of the type of matter in the lenses, and so the projected mass of the lens is measured without any assumption on the physical state of the matter at scales from a few kiloparsec to a few megaparsec.

The weak lensing signal around a single galaxy is too weak to detect since it is 10-100 times smaller than the intrinsic ellipticities of galaxies. Therefore the galaxy-galaxy signal has to be averaged over many lenses to decrease the shape noise. Although individual galaxies cannot be studied in this way, their average properties can be determined (e.g. Brainerd et al. 1996; Fischer et al. 2000; Hoekstra et al. 2004). Only more recently has it become possible to study lenses as a function of properties such as type, luminosity, stellar mass, etc., because early studies lacked the ancillary data needed to subdivide the lenses into subsamples. For instance Hoekstra et al. (2005) used nearly 34 square degrees

of the Red Sequence Cluster Survey (RCS) (Gladders & Yee 2005) for which photometric redshifts were available (Hsieh et al. 2005), to study the relation between the virial mass and baryonic contents of isolated galaxies in the redshift range $0.2 < z < 0.4$, and derived star formation efficiencies for early- and late-type galaxies. Thanks to the wealth of ancillary data, the Sloan Digital Sky Survey (SDSS; York et al. 2000) has had a major impact on galaxy-galaxy lensing studies (e.g. Guzik & Seljak 2002; Mandelbaum et al. 2006). This is evidenced by Mandelbaum et al. (2006) who used nearly 5000 square degrees of the SDSS DR4 (Adelman-McCarthy et al. 2006) to study galaxies in the redshift range $0.02 < z < 0.35$ as a function of galaxy type and environment, and constrained the stellar mass to virial mass relation, the luminosity to virial mass relation and the satellite fractions of the lens samples.

Currently no survey can surpass the precision that can be achieved by the SDSS at low redshift ($z < 0.3$) because of the large survey area and the availability of spectroscopic data. We note, however, that complementing the SDSS data with deeper imaging by the Panoramic Survey Telescope & Rapid Response System[1] (Pan-STARRS; Kaiser et al. 2002) will provide a major improvement, as is demonstrated by the results we present here. For lenses with $z > 0.3$ it is possible to achieve a significant improvement over the SDSS results by surveying a smaller area with deeper data and good image quality; it allows us to use sources at higher redshifts. This is important because the amplitude of the lensing signal scales proportionally to the ratio of the angular diameter distance between the lens and the source and the distance between the observer and the source. The signal decreases rapidly when the lens redshift approaches the peak of the source redshift distribution, which occurs around $z \sim 0.35$ for the SDSS.

In this paper we use data from the second generation Red Sequence Cluster Survey (RCS2) to measure the weak lensing signal around galaxies that are observed in the SDSS. The RCS2 is a nearly 900 square degree imaging survey carried out by the Canada-France-Hawaii-Telescope (CFHT), and is $\sim$2 magnitudes deeper than the SDSS in r'. The increase in depth combined with a median seeing of $0.7''$, which is a factor of two smaller than the seeing in the SDSS, results in a source galaxy number density that is about five times higher, and a source redshift distribution that peaks at z$\sim$0.7.

We use the overlapping area between the two surveys, which amounts to approximately 300 square degrees, in order to assign the spectroscopic redshifts, luminosities, stellar masses and dynamical masses from the SDSS to the lenses. The lensing analysis itself is performed on the RCS2 data. Even though the overlap between the surveys is modest, the loss in survey area is outweighed by the gain in the number density of source galaxies and the improvement of the lensing efficiency. This enables us to improve the measurements of the lensing signal around the most massive galaxies, which mostly reside at redshifts where the SDSS lensing is not very sensitive.

In this paper we describe the lenses in Section 3.2. The weak lensing analysis is discussed in Section 3.3. The halo model that we have implemented is introduced in Section 3.4. In Section 3.5 we compare the weak lensing mass to the dynamical mass. We describe the luminosity results in Section 3.6, and the stellar mass results in Section 3.7. We summarize our conclusions in Section 3.8. Throughout the paper we assume a WMAP5 cosmology (Komatsu et al.

[1] http://pan-starrs.ifa.hawaii.edu/public/

2009) with $\sigma_8 = 0.8$, $\Omega_\Lambda = 0.73$, $\Omega_M = 0.27$, $\Omega_b = 0.045$ and the dimensionless Hubble parameter $h = 0.7$. All distances quoted are in physical (rather than comoving) units unless explicitly stated otherwise.

3.2 Lens Sample

The SDSS has imaged roughly a quarter of the entire sky, and has observed the spectra for about one million galaxies (Eisenstein et al. 2001; Strauss et al. 2002). The combination of spectroscopic coverage and photometry in five optical bands (u, g, r, i, z) in the SDSS provides a wealth of galaxy information that is not available for the RCS2. To use this information, but also benefit from the improved lensing quality of the RCS2, we use the 300 square degrees overlap between the surveys for our analysis. We match the RCS2 catalogues to the DR7 (Abazajian et al. 2009) spectroscopic catalogue, to the MPA-JHU DR7[2] stellar mass catalogue and to the NYU Value Added Galaxy Catalogue (NYU-VAGC)[3] (Blanton et al. 2005; Adelman-McCarthy et al. 2008; Padmanabhan et al. 2008) which yields the spectroscopic redshift, luminosity, stellar mass, and the dynamical mass of 1.7×10^4 galaxies. These form the lens sample of this work; we study the distortion these galaxies imprint as a function of their baryonic content on the shapes of the background galaxies.

As the relation between dark matter and baryons depends on galaxy type, we split the lens sample into early- and late-type galaxies using the $frac\_deV$ parameter included in the SDSS photometric catalogues. This parameter is determined by simultaneously fitting $frac\_deV$ times the best-fitting De Vaucouleur profile plus (1-$frac\_deV$) times the best-fitting exponential profile to an object's brightness profile. This has been done in the g, r and i band, and we use the average value. We classify galaxies with $frac\_deV > 0.5$ as early-types, and galaxies with $frac\_deV < 0.5$ as late-types. The classification of early-types is at least 96% complete and 76% reliable (96% of all early-type galaxies are in the early-type sample, while 76% of all the galaxies in the early-type sample are actually early-types), and the classification of late-types is at least 55% complete and 90% reliable (Strateva et al. 2001; Mandelbaum et al. 2006).

We visually inspect the brightest and most massive early- and late-type galaxies of our lens sample using our RCS2 imaging data. We find that about 30 of the 100 most massive late-types (with a stellar mass in the range $10^{11.4}-10^{12.5}$ $h_{70}^{-1} M_\odot$) actually consists of multiple objects with small separations. These galaxies reside at a redshift of ~ 0.4, and are not well resolved in the SDSS. They are not removed from the analysis as that may introduce a selection bias. More importantly, including them facilitates a comparison to the literature. As a test, we excluded these lenses, and found that the results did not significantly change (note, however, that due to the low number of massive late-type lenses, the errors are large).

3.2.1 Luminosities & Stellar Masses

The MPA-JHU stellar mass catalogue contains about 7×10^5 unique galaxies, and provides the r-band absolute magnitudes and the stellar mass estimates of

[2] http://www.mpa-garching.mpg.de/SDSS/DR7/
[3] http://sdss.physics.nyu.edu/vagc/

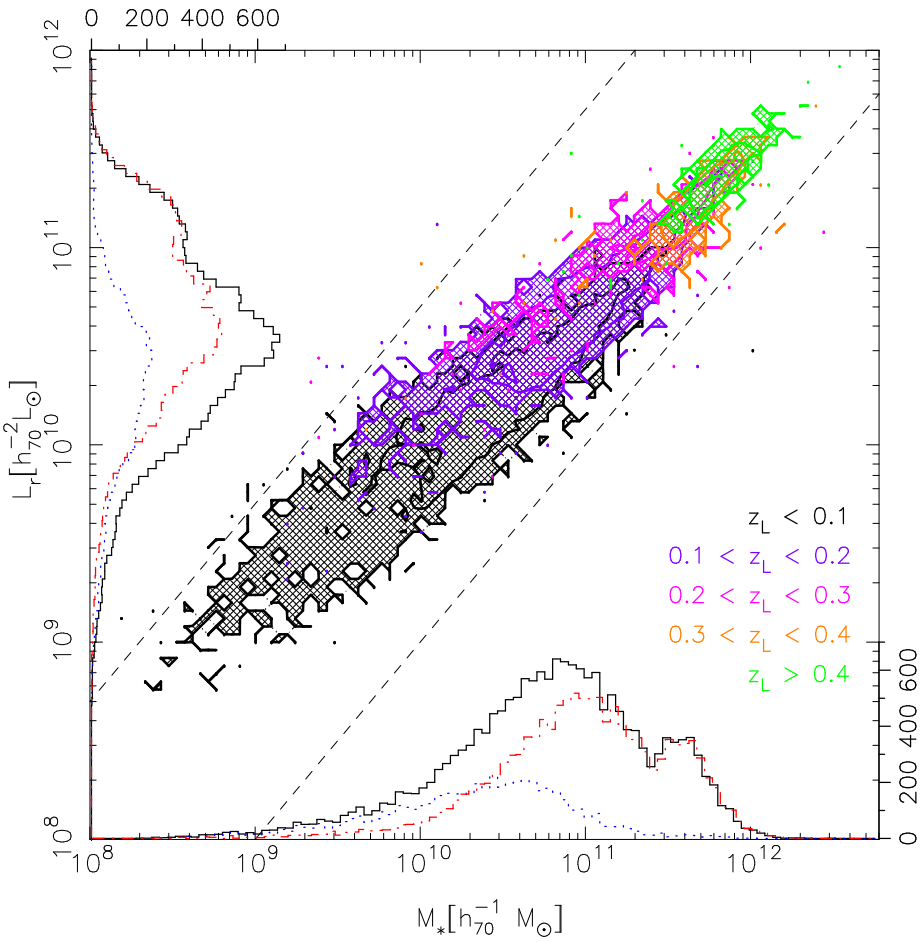

Figure 3.1: Stellar mass versus luminosity of the lens sample. The colour coding represents the redshift of the galaxies as denoted in the lower right-hand corner. The histograms for all galaxies (black solid line), the early-types (red dot-dashed line) and the late-types (blue dotted line), as a function of stellar mass and luminosity are also shown, and are drawn slightly offset for clarity. The dashed diagonal lines indicate the additional mass-to-light ratio cuts we have applied (objects with M_*/L_r between 0.2 $h_{70}M_\odot/L_\odot$ and 10 $h_{70}M_\odot/L_\odot$ have been selected) to remove outliers that may contaminate the lensing signal.

our lenses. The absolute magnitudes that are used to compute the luminosities and stellar masses are based on the Petrosian apparent magnitudes from the SDSS. The Petrosian apparent magnitude measures the flux within a circular aperture whose radius depends on the azimuthally averaged brightness profile in the r-band. It does not include the flux at very large radii from a galaxy, and therefore underestimates the total flux by typically a few tenths of a magnitude (Blanton et al. 2001). Although we do not correct for the missing flux as it would complicate a comparison with previous observational work, this should be kept in mind when comparing our results to predictions from numerical simulations.

The absolute magnitudes have been corrected for extinction using the dust maps from Schlegel et al. (1998), the k-corrections have been calculated to $z = 0.0$ using the `KCORRECT` v4_2 code (Blanton et al. 2003; Blanton & Roweis 2007), and the distance modulus is determined with $h = 0.7$. We convert the absolute magnitudes into solar luminosities using the absolute AB magnitude in the SDDS r-band of $M_{solar} = 4.65$ for $z = 0.0$. We account for passive evolution by dividing the luminosities of the early-type galaxies by $(1 + z)$. The luminosity evolution of late-type galaxies can in principle be computed if the star formation histories (SFHs) are accurately known. The SFHs are generally uncertain, however, since they depend on many parameters such as the stellar mass, environment, assembly history, and AGN activity of a galaxy. Hence the luminosity evolution is difficult to determine and the correction highly uncertain. We therefore do not correct the luminosites of late-type galaxies for evolution.

The stellar masses have been estimated by fitting a library of Bruzual & Charlot (2003) stellar population models to the u, g, r, i, z photometry of the galaxies in the SDSS. The initial mass function (IMF) was taken to be a Kroupa (2001) IMF and the modelling methodology follows Salim et al. (2007).

Nearly all galaxies with a spectroscopic redshift from DR7 are present in the stellar mass catalogue. Figure 3.1 shows the stellar mass versus luminosity for the matched galaxies. The different colours represent galaxies at different redshifts. The most massive and luminous galaxies in our sample reside in the highest redshift range, and are almost exclusively early-type galaxies. Also shown are the histograms of the stellar masses and of the luminosities on respectively the horizontal and vertical axis. The dashed lines indicate the additional $0.2 < M_*/L_r < 10\ h_{70} M_\odot/L_\odot$ cut we apply to minimize the outlier contamination of the lensing bins.

3.2.2 Dynamical Masses

The motions of stars in a galaxy provide an alternative way to estimate the mass of a galaxy at small radii, and constrain the scaling relations between baryons and dark matter. Spectroscopic observations are required to measure the velocity dispersion, which is converted into a dynamical mass estimate via the scalar virial theorem, taking into account projection effects and assumptions on the structure of the stellar orbits:

$$GM_{\rm dyn} = K_V(n)\sigma^2_{\rm los} R_e, \tag{3.1}$$

with $\sigma_{\rm los}$ the line-of-sight velocity dispersion of the galaxy, R_e the effective radius (containing 50% of the light of the best fit Sérsic model), and $K_V(n)$ a

term that includes the effects of structure on stellar dynamics, which can be approximated by (Bertin et al. 2002):

$$K_V(n) \cong \frac{73.32}{10.465 + (n - 0.94)^2} + 0.954, \tag{3.2}$$

with n the Sérsic index (Sérsic 1968).

Using the dynamical mass as a tracer for the total mass of a galaxy has various complications. Firstly, it is implicitly assumed that the velocity dispersion in Equation 3.1 is only generated by the radial motions of the stars, and the $K_V(n)$ term is derived under the assumption that the mass distribution is spherical, dynamically isotropic, and non-rotating. In reality, however, the rotation of a galaxy contributes to the measured velocity dispersion as well, and this effect is particularly important in late-type galaxies. The majority of the early-type galaxies in our study are massive and luminous. They are expected to rotate slowly (e.g. Emsellem et al. 2007), so their dynamical mass estimates are less affected. The dynamical masses of late-type galaxies, however, are potentially overestimated. A second complication arises from the fact that the spectroscopic fibre within which the velocity dispersion is measured has a fixed size. Therefore, the physical region over which the velocity dispersion is averaged depends on the redshift of a galaxy, and hence it probes different regions for galaxies at different redshifts. If the velocity dispersion changes with radius, we would effectively assign different dynamical masses to the same galaxy depending on its redshift. Thirdly, the dynamical mass is measured within the effective radius. The effective radius is a rather arbitrary point, as it depends on parameters such as the shape, the brightness profile and the orientation of a galaxy, and the distribution of dust within the galaxy. Even if a galaxy is spherical and isotropic, it is not clear whether the effective radius marks a special point in relation to the total mass content of a galaxy, given that the dark matter does not follow the distribution of stars. This is most obvious in the outer regions of a galaxy, where most of the matter is dark.

To calculate the dynamical mass of our lenses, we retrieve the velocity dispersions from the SDSS spectroscopic catalogue. As it is complex to estimate the velocity dispersion of galaxies whose spectra are dominated by multiple components, e.g. galaxies with different stellar populations or different kinematic components, the SDSS only provides estimates for spheroidal systems whose spectra are dominated by red stars. At low redshift, the selection also includes the bulges of late-type galaxies because their spectra are similar to the spectra of early-type galaxies. The Sérsic index and the effective radius are obtained from the NYU-VAGC. The sizes and fluxes are underestimated 10% and 15% respectively for large galaxies and galaxies with high Sérsic indices (Blanton et al. 2005), whereas the Sérsic index itself is underestimated by ~ 0.5 to ~ 1.3 for galaxies with high Sérsic indices. It is shown in Guo et al. (2009) that these biases arise from background overestimation and subtraction. As a result, the dynamical mass estimates for these galaxies may be slightly biased, but we do not account for it since we do not know the correction for each galaxy. To ensure that the dynamical mass is computed in approximately the rest-frame r-band, we split the sample according to redshift. For galaxies at $z < 0.2$ we use the Sérsic index and effective radius in the r-band, for galaxies between $0.2 < z < 0.4$ we use the values in the i-band, and for galaxies at $z > 0.4$ we average the values of the i- and z-band.

3.3 Lensing analysis

3.3.1 The RCS2

The lensing signal can be detected with high significance at low redshifts ($z < 0.3$) using SDSS data only. At higher redshifts, the significance decreases rapidly, because of the limited imaging depth and image quality of the SDSS. To improve the lensing signal-to-noise ratio at $z \geq 0.3$, we use the deep imaging data from the Red Sequence Cluster Survey 2 (RCS2) (Gilbank et al. 2011) instead. The RCS2 is a nearly 900 square degree imaging survey in three bands (g', r' and z') carried out with the Canada-France-Hawaii Telescope (CFHT) using the 1 square degree camera MegaCam. The primary survey area is divided into 13 well-separated patches on the sky (including the uncompleted patch 1303), each with an area ranging from 20 to 100 square degrees [4]. Since the RCS2 consists of single exposures only, it is difficult to identify cosmic rays, especially those that hit stars and galaxies. However, only a small fraction of objects is hit by a cosmic ray, and the affected objects do not bias the measurements, but act as a negligible source of noise (Hoekstra et al. 2004). We perform the weak lensing analysis in the SDSS and RCS2 overlap using the 8 minute exposures of the r'-band (r'_{lim} ∼24.8), which is best suited for lensing as it has a median seeing of $0.7''$.

3.3.2 Image processing

We retrieve the Elixir[5] processed images from the Canadian Astronomy Data Centre (CADC) archive[6]. We use the THELI pipeline (Erben et al. 2005, 2009) to subtract the image backgrounds, to create weight maps that we use in the object detection phase, and to identify satellite and asteroid trails. To obtain accurate astrometry, we run `SCAMP` (Bertin 2006) on the images, which enables us to match our catalogues to the SDSS. The polynomial coefficients from `SCAMP` describing the mapping from image to sky coordinates are used to calculate the camera distortion. We use the automated masking routines from the THELI pipeline to generate image masks and to combine them with the RCS2 masks in order to omit image regions that contaminate the lensing signal (e.g. saturated stars, satellite trails). All masks are inspected by eye, and manually improved where necessary.

We use `SExtractor` (Bertin & Arnouts 1996) to detect the objects in the images. To select the stars for modelling the PSF variation across the images, we first identify the locus of the stellar branch in a size-magnitude diagram. We select the non-saturated objects close to the stellar branch with a signal to noise ratio larger than 30 and with no `SExtractor` flags raised. To remove small galaxies that have been misidentified as stars, and stars that have been affected

[4] The CFHT Legacy Survey Wide, comprising of 171 square degrees of imaging data in $u^\star$, g', r', i' and z', is also included in the RCS2, but is not used in this study.

[5] http://www.cfht.hawaii.edu/Instruments/Elixir/

[6] http://www1.cadc-ccda.hia-iha.nrc-cnrc.gc.ca/cadc/

by cosmic rays, we fit a second-order polynomial to both the size and the ellipticity of these star-candidates, and discard all 3-sigma outliers. We clean the stellar selection even further in the shape measurement pipeline by removing shape parameter outliers. All objects larger than 1.2 times the local size of the PSF are classified as galaxies.

In Figure 3.2 we illustrate the star-galaxy separation. It has been fully automated, but as a precaution we inspect all size-magnitude diagrams by eye. The separation fails for a few chips that have either very few stars or a PSF with a large FWHM, and we manually adjust those. As neighbouring patches overlap by $\sim$1 arcminute, we remove all galaxies within 35 arcseconds from the image edges in order to avoid duplicating the lenses and sources in our analysis.

Elixir provides approximate zeropoints for each pointing, which we use to measure the r'-band magnitudes of the objects in the images. We correct the magnitudes for galactic extinction using the dust maps from Schlegel et al. (1998). These magnitudes are not as accurately calibrated as those from Gilbank et al. (2011), and differ in the r'-band on average by -0.01 ± 0.32. Our calibration is, however, sufficiently accurate to select the source galaxy sample. For the calculation of the luminosity overdensity, which is discussed in Section 3.6.1, we use the catalogues from Gilbank et al. (2011) instead.

3.3.3 Contamination correction

A fraction of the galaxies in the source catalogue is physically associated with the lenses. Since we lack redshifts for the sources, we are unable to remove them. These objects are not lensed, and therefore dilute the lensing signal. To estimate this contamination we measure $f_{cg}(r)$, the excess source number density around the lenses. We show the overdensity around the lenses which have been divided into seven stellar mass bins (defined in Table 3.3) as a function of lens-source separation in Figure 3.3. The error bars are computed assuming that the number of source galaxies in each radial bin follows a Poisson distribution. The contamination increases with stellar mass, as massive galaxies reside in denser environments and therefore have more satellite galaxies. Although the overdensity is shown independently of the lens galaxy type in Figure 3.3, we measure it for the early- and late-types separately in the science analysis presented in Section 3.5, 3.6 and 3.7. Assuming that the satellite galaxies have random orientations, we correct for the contamination by boosting the lensing signal with a factor $1 + f_{cg}(r)$. Note, however, that the contamination correction may be too small if satellite galaxies are preferentially radially aligned in the direction of the lens. This type of intrinsic alignment has been studied with seemingly different results; some authors (e.g. Agustsson & Brainerd 2006; Faltenbacher et al. 2007) who determined the galaxy orientation using the isophotal position angles, have observed a stronger alignment than others (e.g. Hirata et al. 2004; Mandelbaum et al. 2005a) who used galaxy moments. Siverd et al. (2009) and Hao et al. (2011) attribute the discrepancy to the different definitions of the position angle of a galaxy. As we measure the shapes of source galaxies using galaxy moments, we expect that intrinsic alignment only has a minor impact on the correction factor and hence can be safely ignored.

Gravitational lenses do not only shear the images of the source galaxies, but also magnify the background sky. As a result, the flux of the sources is magnified, and the source galaxy number density is diluted. These combined effects

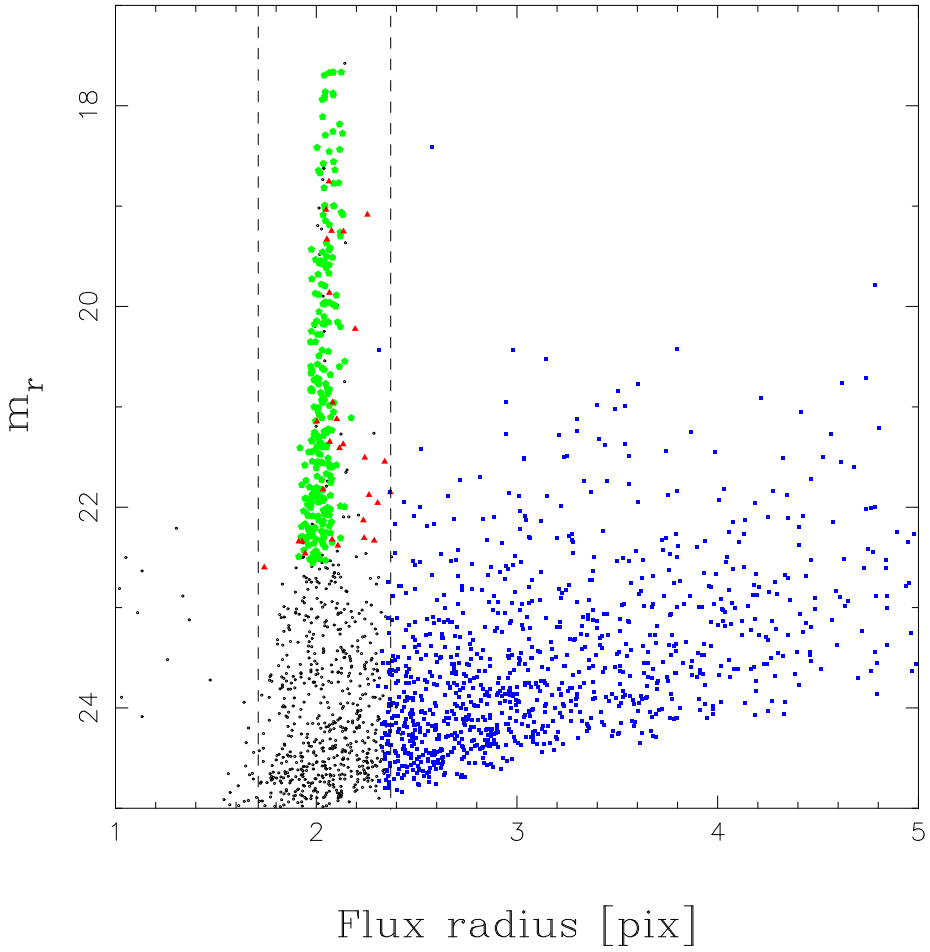

Figure 3.2: Size-magnitude diagram of one of the chips in a randomly picked exposure. The black dots are the `SExtractor` detections, the green pentagons are the selected stars, the red triangles are the 3-sigma outliers, and the blue squares are the selected galaxies. The dashed lines indicate the location of the stellar branch. Thanks to the good image quality the stars are easily separated from the galaxies.

are known as magnification bias, and it changes the source density around the lenses. The effect is negligible for the lensing study presented here.

3.3.4 Shape measurement

The measurement of the shapes of galaxies is central to any weak lensing analysis. The accuracy that is required depends on the science goal. For example, in cosmic shear studies aimed at constraining cosmological parameters, it is necessary to accurately correct the measured galaxy shapes for the anisotropic smearing of the PSF since the signal is small and very sensitive to any PSF residual systematic. In contrast, in the case of galaxy-galaxy lensing the signal is averaged over many lens-source pairs with random orientations, which

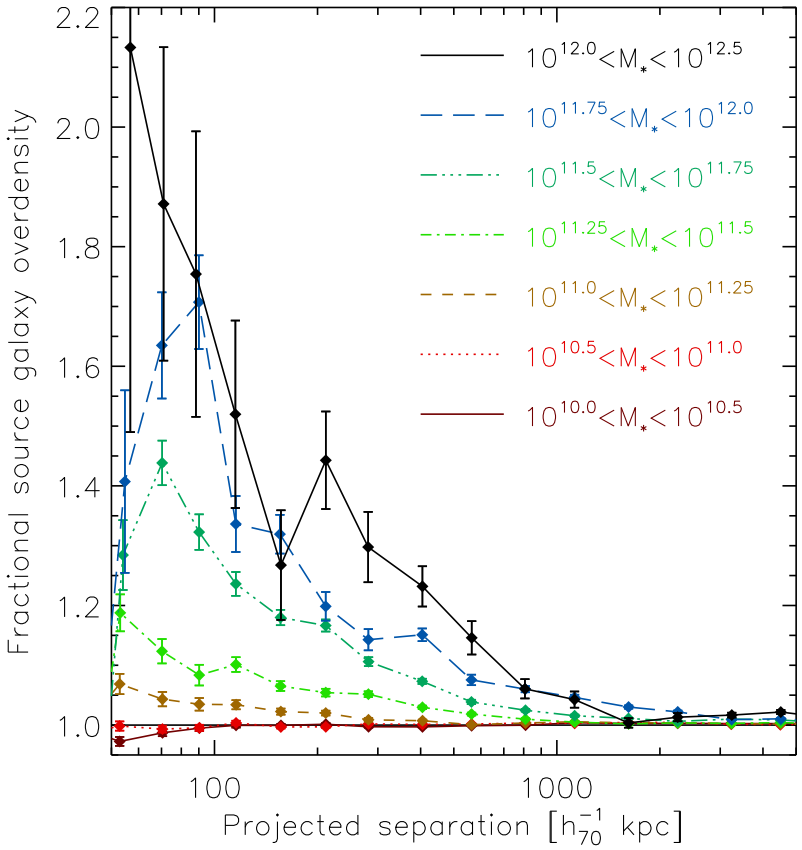

Figure 3.3: Source galaxy overdensity as a function of distance from the lenses for the different stellar mass bins. The overdensity increases with stellar mass. Massive galaxies reside on average at higher redshifts and live in denser environments with more satellite galaxies.

removes most of the PSF systematics on small scales.

For our lensing analysis we measure the shapes of galaxies with the KSB method (Kaiser et al. 1995; Luppino & Kaiser 1997; Hoekstra et al. 1998), using the implementation described by Hoekstra et al. (1998, 2000). The measured galaxy shapes are corrected for smearing by the PSF under the assumption that the brightness distribution of stars can be described by an isotropic profile convolved with a small anisotropic kernel. Generally, the PSF is more complicated which may lead to biases. The version of KSB we use has been tested on simulated images as part of the Shear Testing Programme (STEP) 1 and 2 (the 'HH' method in Heymans et al. (2006) and Massey et al. (2007) respectively). These tests have shown that the correction scheme works well for a variety of PSFs; in STEP2, the HH method underestimates the shear on average by 1-2% only.

The mapping between the sky coordinates and the CCD pixels is slightly non-linear due to the camera optics, which causes an additional shear that needs

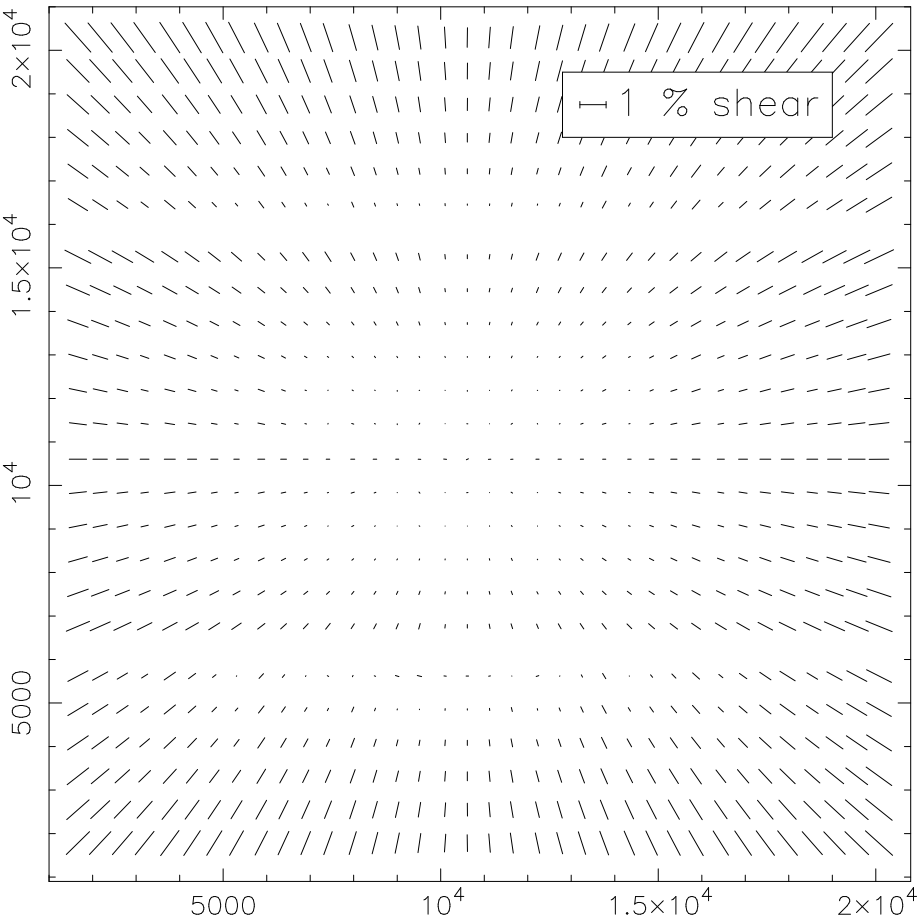

Figure 3.4: Shear induced by camera distortion in the MegaCam imager. The camera shear is largest in the corners of the mosaic, with values up to 1.5%. As the observed shear is the sum of the gravitational shear and the camera shear, we simply subtract the camera shear from the observed galaxy ellipticities to correct for it.

to be corrected. We calculate the shear induced by this distortion using the polynomial coefficients from `SCAMP` describing the mapping from image to sky coordinates. The camera shear of MegaCam is shown in Figure 3.4. The images of both the stars and the galaxies are sheared, with a value reaching 1.5% at the corners of the images. At large lens-source separations, where the gravitational lensing signal is small, the camera shear dominates the observed lensing signal. Hoekstra et al. (1998, 2000) demonstrate that the observed shear is the sum of the gravitational shear and the camera shear. We therefore simply subtract the camera shear from the observed ellipticities of the galaxies to correct for it.

To demonstrate the excellence of the RCS2 as a lensing survey, we measure the galaxy-mass cross-correlation function in the exposures that significantly overlap with the SDSS (defined as having more than 30 matching objects). 301 exposures of the total overlapping 350 meet this requirement, which after

masking and exclusion of the image boundaries leads to an effective area of approximately 260 square degrees. The galaxy-mass cross-correlation function measures the correlation between the galaxies and the surrounding distribution of (predominantly dark) matter. We compute it by measuring the azimuthally averaged tangential shear as a function of radial distance from the lens:

$$\langle\gamma_t\rangle(r) = \frac{\Delta\Sigma(r)}{\Sigma_{\rm crit}}, \tag{3.3}$$

where $\Delta\Sigma(r) = \bar{\Sigma}(< r) - \bar{\Sigma}(r)$ is the difference between the mean projected surface density enclosed by r and the mean projected surface density in an annulus at r, and $\Sigma_{\rm crit}$ is the critical surface density

$$\Sigma_{\rm crit} = \frac{c^2}{4\pi G}\frac{D_s}{D_l D_{ls}}, \tag{3.4}$$

with D_l, D_s and D_{ls} the angular diameter distance to the lens, the source, and between the lens and the source respectively.

Since we do not have redshifts for all galaxies we separate the lenses from the sources using magnitude cuts (see e.g. Hoekstra et al. 2004). Objects with $19.5 < m_{r'} < 21.5$ are defined as lenses, and objects with $22.0 < m_{r'} < 24.0$ are sources. We discard objects with ellipticities larger than 1, and objects that have a `SExtractor` flag raised. Using these selection criteria we find 7.3×10^5 lenses and 5.9×10^6 sources. The corresponding effective source number density is 6.3 arcmin^{-2}, which is five times higher than the source density of 1.2 arcmin^{-2} used in the SDSS analysis (Mandelbaum et al. 2005a). To obtain the approximate redshift distribution of the lenses and sources, we apply identical magnitude cuts to the photometric redshift catalogues of the Canada-France-Hawaii-Telescope Legacy Survey (CFHTLS) "Deep Survey" fields (Ilbert et al. 2006). We stack the signals of all the lenses in the RCS2, and azimuthally average them in radial bins. To remove the contributions of systematic shear (from, e.g., the image masks), we subtract the signal computed around random lenses from the signal around the real lenses. We measure the source galaxy overdensity as a function of lens-source separation, and boost the signal to correct for the contamination as outlined in Section 3.3.3. Figure 3.5 shows the tangential shear, and the inset shows the signal at small scales using a linear vertical scale.

We also measure the cross shear around the lenses by rotating the background galaxies 45° and repeating the measurement. Gravitational lensing does not produce cross shear, and a non-zero signal indicates the presence of residual systematics in the catalogues. We indicate the cross shear with the red symbols in the inset in Figure 3.5, and note that it is consistent with zero on all scales.

For reference, we fit a singular isothermal sphere (SIS) and a Navarro-Frenk-White (NFW) profile (Navarro et al. 1996) to the tangential shear on scales between 0.2 and 0.6 arcminutes (∼60-180 h_{70}^{-1}kpc at the median lens redshift $z_{\rm med} = 0.34$). The SIS signal is given by

$$\gamma_{t,\rm SIS}(r) = \frac{r_E}{2r} = \frac{4\pi\sigma^2}{c^2}\frac{D_{ls}}{D_s}\frac{1}{2r}, \tag{3.5}$$

where r_E is the Einstein radius and σ the velocity dispersion. We indicate the best fit SIS model with the dashed line in Figure 3.5. The NFW density profile

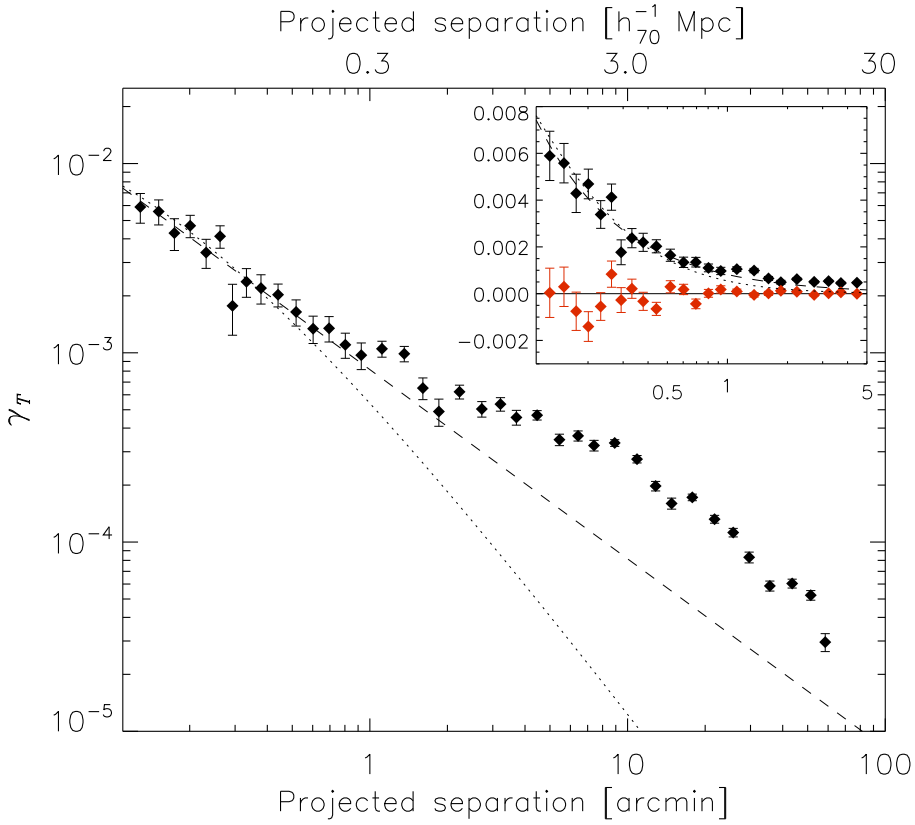

Figure 3.5: Galaxy-mass cross-correlation function around 7.3×10^5 apparent magnitude selected lenses measured with 5.9×10^6 sources. The black symbols are the tangential shear, the red symbols are the cross shear. The top axis shows the projected separation in physical units for the median lens redshift $z_{\rm med}$=0.34. The inset shows the signal on a linear scale for small separations. The signal has been corrected for contributions from systematic shear, and boosted to account for source galaxy contamination. The dashed (dotted) line shows the best fit SIS (NFW), fitted to the shear on scales between 0.2 and 0.6 arcminutes. The clustering of galaxies causes excess shear at scales >1 arcminutes.

is given by

$$\rho(r) = \frac{\delta_c \rho_c}{(r/r_s)(1+r/r_s)^2}, \tag{3.6}$$

with δ_c the characteristic overdensity of the halo, ρ_c the critical density for closure of the universe, and $r_s = r_{200}/c_{\rm NFW}$ the scale radius, with $c_{\rm NFW}$ the concentration parameter. The NFW profile is specified by two free parameters: the mass and the concentration parameter. Since numerical simulations have shown that the concentration depends on the mass and redshift of the halo, we can reduce the number of free parameters in the fit by adopting a mass-

concentration relation. We use the mass-concentration relation from Duffy et al. (2008), which is based on numerical simulations using the best fit parameters of the WMAP5 cosmology. It is given by

$$c_{\rm NFW} = 5.71 \left(\frac{M_{200}}{2 \times 10^{12} h^{-1} M_{\odot}}\right)^{-0.084} (1+z)^{-0.47}, \tag{3.7}$$

with M_{200} the mass in units of $h^{-1}M_{\odot}$. M_{200} is defined as the mass inside a sphere with radius r_{200}, the radius where the density is 200 times the critical density ρ_c. We use the median lens redshift $z_{\rm med} = 0.34$ for the stacked lenses in the NFW fit, and calculate the tangential shear profile using the analytical expressions provided by Bartelmann (1996) and Wright & Brainerd (2000). The best fit NFW profile is indicated by the dotted line in Figure 3.5.

It is clear that both the SIS and NFW profiles underestimate the signal at scales larger than ∼1 arcminute, which corresponds to ∼300 h_{70}^{-1}kpc at the median lens redshift. The majority of galaxies live in clustered environments, and with gravitational lensing we measure the shear induced by neighbouring galaxy haloes as well. This excess lensing signal complicates a straightforward analysis of the data. The problem could be avoided by studying the lensing signal on small scales around isolated galaxies (following Hoekstra et al. 2005), but this requires the availability of redshifts for all galaxies, which we do not have in the RCS2. Alternatively, the lensing signal can be modelled taking the clustering of the lenses into account, which enables the simultaneous study of the mass and of the clustering properties of the galaxies. This is inherent in the halo model (Seljak 2000; Cooray & Sheth 2002), which we will use here.

The lenses in a bin generally have a range of masses. The correct interpretation of the signal therefore requires knowledge of the distribution of the masses of the lens galaxies, an issue we return to at the end of Section 3.4.

3.4 Halo model

Galaxies form in the gravitational potential of dark matter haloes and therefore trace the large scale distribution of matter in the universe. The quantity that describes the relation between galaxies and dark matter is referred to as galaxy biasing. The description of galaxy biasing is non-trivial as the physics governing galaxy formation is complex, and the bias may depend on the dark matter halo mass, environment, scale and redshift (e.g. Cresswell & Percival 2009; Coupon et al. 2011; Kovač et al. 2011). To gain insight into the relation between galaxies and dark matter the weak lensing signal around galaxies can be used, as it measures the correlation between the galaxies and the surrounding dark matter distribution. These lensing measurements provide constraints for models of the large scale distribution of matter, which are commonly described with the power spectrum of the density fluctuations (e.g. Peacock & Dodds 1996; Smith et al. 2003). For a given power spectrum, the lensing signal can be computed directly (Guzik & Seljak 2001):

$$\begin{aligned}\gamma_t(\theta) = 6\pi^2 \left(\frac{H_0}{c}\right)^2 \Omega_M \int_0^{\infty} {\rm d}\chi W_1(\chi) \frac{f(\chi)}{a(\chi)} \\ \times \int {\rm d}k k P(k,\chi) J_2(kr(\chi)\theta),\end{aligned} \tag{3.8}$$

with $r(\chi)$ the angular comoving distance, χ the radial distance (in a flat universe, $r(\chi) = \chi$ and $\chi = a^{-1}\ D_A$ with a the scale factor and D_A the angular diameter distance), $W_1(\chi)$ the normalized radial distribution of the lenses, $f(\chi) = \int_\chi^\infty \mathrm{d}\chi' g(\chi, \chi') W_2(\chi')$, with $W_2(\chi')$ the radial distribution of the sources, and

$$g(\chi, \chi') = \frac{D_l D_{ls}}{D_s a(z_l)}. \tag{3.9}$$

$P(k)$ is the power spectrum under consideration, and J_2 is the second Bessel function of the first kind. Instead of using a single power spectrum to describe the distribution of matter in the universe, it is beneficial to consider the various components that contribute, as is done in the halo model. This allows a simultaneous study of the halo masses of galaxies and of their clustering properties.

In the halo model the mass distribution in the universe is described as a distinct number of dark matter haloes that are clustered. As the large scale spatial distribution of haloes is unlikely to affect the physics inside individual haloes, and vice versa, the description of the model can be separated into two steps: the halo mass function and the bias at large scales, and the halo occupation distribution at small scales.

The large scale distribution of haloes can be described by the halo number density. In the Press-Schechter approach (Press & Schechter 1974) the dark matter haloes are assumed to form by spherical collapse. This, however, leads to a halo number density that overestimates the abundance of galaxies below the non-linear mass scale. Better agreement with numerical simulations of hierarchical structure formation comes from the assumption of ellipsoidal rather that spherical collapse (Sheth et al. 2001). The number density of bound objects is generally written as

$$n_h(M, z) dM = \frac{\bar{\rho}}{M} f(\nu) d\nu, \tag{3.10}$$

where $n_h(M, z)$ is the halo mass function which depends on the halo mass M and redshift z, and $\bar{\rho}$ is the mean matter density of the universe at redshift z. Unless explicitly stated otherwise we use $M = M_{200}$. The peak height ν is given by

$$\nu = \left(\frac{\delta_{sc}(z)}{\sigma(M, z)} \right)^2, \tag{3.11}$$

with $\delta_{sc}(z)$ the critical overdensity required for spherical collapse at redshift z, and $\sigma(M, z)$ the rms of the density fluctuation field on the scale $R = (3M/4\pi\bar{\rho})^{1/3}$, extrapolated to z using linear theory. In the case of ellipsoidal collapse, $f(\nu)$ is given by (Sheth et al. 2001)

$$f(\nu) = A\ (1 + (a\nu)^{-p})\ \nu^{-1/2} e^{-a\nu/2}, \tag{3.12}$$

with $a = 0.707$, $p = 0.3$, and $A = 0.13683$ a constant that is determined by requiring $\int f(\nu) d\nu = 1$ (i.e. mass conservation).

How the haloes trace the mass is given by the halo-to-mass bias, which is defined as the ratio of the power spectrum of the halo distribution to the power spectrum of the matter distribution. We use an analytical formula for the bias

as given by Sheth et al. (2001), but incorporate the adjustments described in Tinker et al. (2005):

$$b(\nu) = 1 + \frac{1}{\sqrt{a}\delta_{sc}} \times \left[\sqrt{a}(a\nu) + \sqrt{a}b(a\nu)^{1-c} - \frac{(a\nu)^c}{(a\nu)^c + b(1-c)(1-c/2)}\right], \tag{3.13}$$

with $a = 0.707$, $b = 0.35$ and $c = 0.80$. The scale dependence of the bias is given by

$$b^2(\nu, r) = b^2(\nu)\frac{[1 + 1.17\xi_m(r)]^{1.49}}{[1 + 0.69\xi_m(r)]^{2.09}}, \tag{3.14}$$

where $\xi_m(r)$ is the matter correlation function, which in turn is the Fourier transform of the non-linear power spectrum $P_{\rm NL}(k)$ from Smith et al. (2003), and r is the distance to the centre of the halo.

To describe how the galaxies and dark matter are distributed within the haloes, we closely follow the approach outlined in Guzik & Seljak (2002) and Mandelbaum et al. (2005b). Galaxies living inside dark matter haloes are divided into two classes; they are either a central galaxy located in the central halo, or a satellite galaxy located in a subhalo inside the central halo. The fraction of satellites in a certain sample of galaxies is denoted by α. The number of satellites in a central halo is described by the halo occupation distribution (HOD). Galaxy formation simulations (e.g. Zheng et al. 2005; Kravtsov et al. 2004) show that the HOD is well approximated by a powerlaw $N_s(M) \propto M^\epsilon$ with $\epsilon = 1$, which is cut off below a certain minimal halo mass. Rather than this steep cut off, we follow Mandelbaum et al. (2005b) and assume a more gradual transition, and use $\epsilon = 2$ for halo masses smaller than $M_{\rm char}$, whilst $\epsilon = 1$ for halo masses larger than $M_{\rm char}$, where $M_{\rm char} = 3M_h$. M_h is the typical halo mass of a certain set of galaxies (for example the galaxies selected in a luminosity bin). The amplitude is determined by normalizing to the total number of satellites in the set.

3.4.1 Lensing signal from the halo model

We now proceed to explain how the lensing signal is computed. The ensemble averaged tangential shear is the sum of the signal around central galaxies and satellites, since we cannot distinguish between them. We compute each contribution separately, starting with the signal around central galaxies. It is assumed that the central galaxies are located at the centre of the dark matter haloes. Two terms contribute to the lensing signal around central galaxies: the signal coming from the halo where the galaxy resides ($\gamma_{t,\rm cent}^{1h}$), and the signal from nearby haloes ($\gamma_{t,\rm cent}^{2h}$). Hence the total signal around central galaxies is given by

$$\gamma_{t,\rm cent} = \gamma_{t,\rm cent}^{1h} + \gamma_{t,\rm cent}^{2h}. \tag{3.15}$$

The density profiles of the central haloes are assumed to be NFW, which we compute using the mass-concentration relation from Duffy et al. (2008) given by Equation (3.7). By picking a central halo mass we can thus compute the tangential shear of the central halo term directly, as spectroscopic redshifts are

available for all lenses.

The calculation of $\gamma_{t,\mathrm{cent}}^{2h}$ requires the power spectrum describing the correlation between the galaxy in the central halo and the dark matter of nearby haloes:

$$P_{\mathrm{cent}}^{2h}(k, M_h, r) = b_g(M_h, r)\frac{P_{\mathrm{NL}}(k)}{(2\pi)^3} \times \int_0^{M_{\mathrm{lim}}} \mathrm{d}\nu f(\nu) b(\nu, r) y_{\mathrm{dm}}(k, M), \tag{3.16}$$

with $b_g(M_h, r)$ the bias of the central galaxy, $P_{\mathrm{NL}}(k)$ the non-linear power spectrum from Smith et al. (2003), and $y_{\mathrm{dm}}(k, M)$ the radial Fourier transform of the central halo density profile divided by mass:

$$y_{\mathrm{dm}}(k, M) = \frac{1}{M}\int_0^{r_{200}} \mathrm{d}r 4\pi r^2 \rho_{\mathrm{dm}}(r, M)\frac{\sin(kr)}{kr}, \tag{3.17}$$

which we calculate using the analytical formula given in Pielorz et al. (2010).

The dark matter profiles of adjacent haloes cannot overlap, which is prevented by implementing halo exclusion. Different approaches to halo exclusion have been used in the literature. For example, Cacciato et al. (2009) set the two-halo correlation function to zero below r_{180}, which leads to a sharp truncation in the halo models. We follow the approach of Tinker et al. (2005), which leads to a more natural smooth cut-off: the integral in Equation (3.16) is cut off for masses greater than M_{lim} which is chosen such that the r_{200} of the central halo does not overlap with the r_{200} of nearby haloes: $r_{200}(M_h)+r_{200}(M_{\mathrm{lim}}) = r$. It should be noted that this choice, as any other halo exclusion approach, is an approximation. Ultimately, numerical simulations should be used to provide improved estimates for P_{cent}^{2h}. Note that $P_{\mathrm{cent}}^{2h}(k, M_h, r)$ not only depends on the wavenumber but also on the projected separation r, because of the scale dependence of the bias and the implementation of halo exclusion.

The contribution of the satellites to the lensing signal consists of three terms: the signal from the subhalo where the satellite resides ($\gamma_{t,\mathrm{sat}}^{\mathrm{trunc}}$), the signal from the central halo in which the subhalo resides ($\gamma_{t,\mathrm{sat}}^{1h}$), and the signal from nearby haloes ($\gamma_{t,\mathrm{sat}}^{2h}$). Hence the total signal around satellites is given by

$$\gamma_{t,\mathrm{sat}} = \gamma_{t,\mathrm{sat}}^{\mathrm{trunc}} + \gamma_{t,\mathrm{sat}}^{1h} + \gamma_{t,\mathrm{sat}}^{2h}. \tag{3.18}$$

First we compute the lensing signal of the subhalo, $\gamma_{t,\mathrm{sat}}^{\mathrm{trunc}}$, following Mandelbaum et al. (2005b). The density profile is assumed to follow an NFW profile in the inner regions. The outer regions of the subhalo are tidally stripped of its dark matter by the central halo. Due to this stripping the lensing signal is proportional to r^{-2} at radii larger than the truncation radius. Based on good agreement with numerical simulations, Mandelbaum et al. (2005b) chose a truncation radius of $0.4r_{200}$, and we use the same. This choice corresponds to roughly 50% of the dark matter being stripped from the subhalo.

To compute the lensing signal induced by the halo where the subhalo resides, we calculate the power spectrum describing the correlation between the subhalo and the dark matter profile of the central halo:

$$P_{\mathrm{sat}}^{1h}(k, M_h) = \frac{1}{(2\pi)^3\bar{n}}\int \mathrm{d}\nu f(\nu) N_s(M, M_h) \times y_{\mathrm{dm}}(k, M) y_{\mathrm{g}}(k, M), \tag{3.19}$$

with $\bar{n}$ the mean galaxy number density, which can be determined using $\bar{n} = \bar{\rho} \int \mathrm{d}\nu f(\nu) \frac{N_s(M,M_h)}{M}$, and y_g the radial Fourier transform of the radial distribution of satellites around the central halo. We assume that the radial distribution of satellites follows an NFW profile with a concentration c_g, given by the mass-concentration relation from Duffy et al. (2008). To asses the sensitivity to the shape of the radial distribution of the satellites, we also calculate the $\gamma_{t,\mathrm{sat}}^{1h}$ term using a c_g that is varied by a factor of two. We find that this change mainly impacts the model signal at small scales: for a larger (smaller) concentration, the signal increases (decreases). At scales larger than a few hundred kpc, the change of the model signal is negligible. When we fit these adjusted models to the data, we find that the best fit model parameters do not change significantly. We conclude that the signal-to-noise of our data currently does not enable us to discriminate between halo models with different radial distributions of satellite galaxies.

Finally we compute the contribution from nearby haloes to the lensing signal around satellite galaxies:

$$\begin{aligned} P_\mathrm{sat}^{2h}(k, M_h, r) = \frac{P_\mathrm{NL}(k)}{(2\pi)^3} \int_0^{M_\mathrm{lim}} \mathrm{d}\nu f(\nu) b(\nu, r) y_\mathrm{dm}(k, M) \\ \times \frac{\bar{\rho}}{\bar{n}} \int \mathrm{d}\nu f(\nu) b(\nu, r) \frac{N_s(M, M_h)}{M} y_\mathrm{g}(k, M). \end{aligned} \tag{3.20}$$

The three power spectra are converted into their respective shear signals using Equation (3.8), and the contributions from the central galaxies and satellites are combined to yield

$$\gamma_t = (1 - \alpha)\, \gamma_{t,\mathrm{cent}} + \alpha\, \gamma_{t,\mathrm{sat}}, \tag{3.21}$$

where α is the fraction of satellites of the sample. The resulting model is compared to the data.

The lens sample is selected to cover a range in an observable, such as luminosity or stellar mass, as the relation between the mean observable and the lensing mass is a useful constraint for simulations. The dark matter haloes of the lenses from such a sample have different masses, however, and it is therefore important to account for the scatter in the observable-halo mass relation. If the halo mass distribution is well-known, this can be done by integrating the models over the distribution of halo masses. Unfortunately, the distribution is generally not accurately known as the lenses span a considerable range in observable, redshift and environment. A simpler approach is to study how the lensing mass is related to the mean halo mass for a given halo mass distribution. This approach, which was proposed by Mandelbaum et al. (2006), provides the leading-order correction for the scatter, and we use it in this paper.

3.5 Comparison with dynamical mass

The dynamical mass traces the gravitational potential of a galaxy at small scales, and typically provides estimates of the total mass enclosed by the effective radius, which is of the order of a few kpc. Comparison to the mass derived from strong lensing shows that both estimates agree well for early-type galaxies

(Bolton et al. 2008). In contrast, weak lensing traces the gravitational potential at much larger scales, and the mass is usually determined within r_{200}, whose values range between a few tens to a few hundreds of kpc. To study how the dynamical mass is related to the weak lensing mass, we measure the lensing signal for galaxies divided into seven dynamical mass bins, as detailed in Table 3.1. The lensing signal of the stacked galaxies in each bin is shown in Figure 3.6. We fit our halo model to the lensing signal in the distance interval between 50 h_{70}^{-1}kpc and 2 h_{70}^{-1}Mpc. At scales smaller than 50 h_{70}^{-1}kpc the lensing signal is very noisy, since we do not have many sources at small separations, and lens light contamination might bias the shear signal. At scales larger than 2 h_{70}^{-1}Mpc we measure the lensing signal using mainly sources that reside at the edge of the images, where the PSF ellipticity is large for the data taken prior to a change in the MegaCam configuration[7](up to 15%), and the residual PSF systematics noticeably bias the lensing signal. We fit for the central halo mass and the satellite fraction, and use Equation (3.13) to compute the bias because the lensing signal is not well constrained at scales >3 h_{70}^{-1}Mpc.

We impose two priors on the fits. Firstly, we do not fit halo masses that are lower than the mean stellar mass of the galaxies in the bin. This prior could introduce a bias if the assumed IMF is significantly different from the true one, leading to stellar mass estimates that are too high, but this is not expected to be the case. The second prior we impose is on the satellite fraction, which is not well constrained by the data for the most massive galaxies and is anti-correlated with the best fit halo mass (see Appendix 3.C for details). To prevent this from biasing the halo mass low, we limit the range of fitted satellite fractions to be less than 20% in the three highest dynamical mass bins as they contain galaxies that are expected to be nearly exclusively centrals. The best fit halo model for each bin is also shown in Figure 3.6. We find that the model fits the data well. The resulting best fit halo masses for the early- and late-type galaxies are shown in Figure 3.7, and detailed in Table 3.1. The error bars on the best fit halo mass (satellite fraction) indicate the 1σ deviations determined by marginalizing over the satellite fraction (halo mass).

For the early-type galaxies, we find that the dynamical mass correlates well with the halo mass. The halo mass is ∼10 times larger than the mean dynamical mass for $M_{\rm dyn} < 1 \times 10^{11}\ h_{70}^{-1} M_{\odot}$, which increases to a factor ∼50 for the highest dynamical mass bins, as the galaxy dark matter haloes extend far beyond the effective radius. To establish whether we can scale the dynamical mass to the lensing mass, we replace R_e with the best fit lensing r_{200} in Equation (3.1). We find that the rescaled dynamical masses are 8 times larger than the best fit lensing masses for D1 and D2, but the difference decreases for the more massive bins: the rescaled dynamical mass is only 40% larger than the best fit lensing mass for D7. We therefore cannot simply rescale the mean dynamical mass to the lensing mass. Note that at the high mass end, galaxies predominantly live in groups and clusters. With lensing we fit the halo mass of the entire structure, whereas the dynamical mass is determined for the individual galaxy only.

We observe that for the late-type galaxies the halo mass does not correlate

[7]In November 2004, the lens L3 was accidentally mounted incorrectly after the wide-field corrector had been disassembled. As this surprisingly led to a significant improvement in the image quality for the u^*-, g'-,and r'-band, the new configuration was kept. About 20% of the RCS2 survey was obtained prior to this change.

Table 3.1: Dynamical mass results

Sample	$\log(M_{\rm dyn})$	$n_{\rm lens}$	$\langle z\rangle$	$\langle M_{\rm dyn}\rangle$	$f_{\rm late}$	$M_h^{\rm early}$	$\alpha^{\rm early}$	$M_h^{\rm late}$	$\alpha^{\rm late}$
	(1)	(2)	(3)	(4)	(5)	(6)	(7)	(8)	(9)
D1	$[10.00, 10.50]$	2 011	0.08	1.96	0.44	$2.86^{+4.84}_{-2.64}$	$0.24^{+0.11}_{-0.09}$	$7.00^{+6.91}_{-5.19}$	$0.17^{+0.11}_{-0.09}$
D2	$[10.50, 11.00]$	4 752	0.10	5.91	0.35	$5.69^{+3.37}_{-2.80}$	$0.41^{+0.07}_{-0.06}$	$1.06^{+3.16}_{-1.04}$	$0.11^{+0.12}_{-0.08}$
D3	$[11.00, 11.25]$	2 762	0.13	13.2	0.25	$25.4^{+7.66}_{-7.86}$	$0.14^{+0.07}_{-0.07}$	$6.10^{+8.50}_{-5.39}$	$0.19^{+0.15}_{-0.12}$
D4	$[11.25, 11.50]$	2 281	0.16	23.6	0.16	$40.3^{+11.0}_{-10.7}$	$0.31^{+0.09}_{-0.08}$	$45.1^{+17.3}_{-17.6}$	$0.00^{+0.09}_{-0.00}$
D5	$[11.50, 11.75]$	1 715	0.22	41.7	0.07	$150^{+24.4}_{-37.1}$	$0.20^{+0.00}_{-0.09}$	$12.7^{+27.0}_{-12.7}$	$0.00^{+0.39}_{-0.00}$
D6	$[11.75, 12.00]$	935	0.32	72.5	0.05	$421^{+96.7}_{-107}$	$0.20^{+0.00}_{-0.20}$	$4.96^{+66.1}_{-4.94}$	$0.00^{+0.20}_{-0.00}$
D7	$[12.00, 12.50]$	380	0.39	137.4	0.07	669^{+184}_{-351}	$0.20^{+0.00}_{-0.20}$	313^{+320}_{-300}	$0.20^{+0.00}_{-0.20}$

(1) the dynamical mass range of the bin in units of $h_{70}^{-1}M_\odot$; (2) the number of lenses; (3) the mean redshift; (4) the mean dynamical mass in units of $10^{10}\ h_{70}^{-1}M_\odot$; (5) the fraction of late type galaxies; (6) the best fit halo mass for the early types in units of $10^{11}h_{70}^{-1}M_\odot$; (7) the best fit satellite fraction for the early types; (8) the best fit halo mass for the late types in units of $10^{11}h_{70}^{-1}M_\odot$; (9) the best fit satellite fraction for the late types.

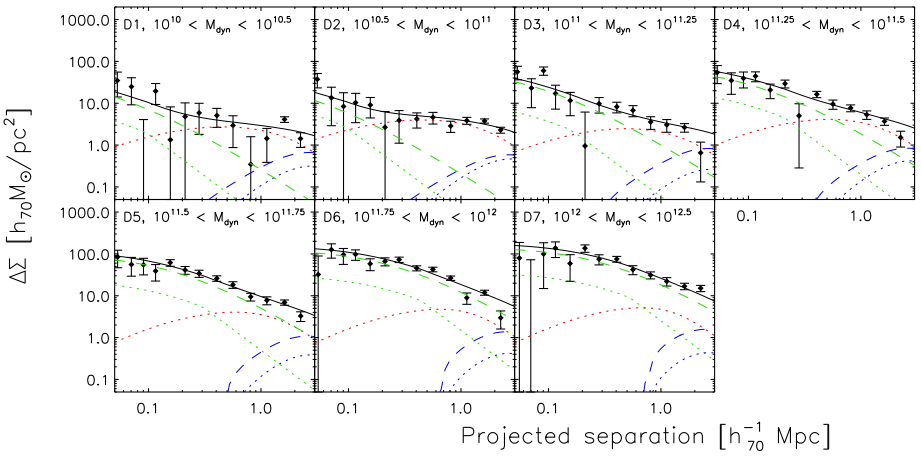

Figure 3.6: Lensing signal $\Delta\Sigma$ for each dynamical mass bin as a function of physical distance from the lens. The green dashed line shows the $\gamma_{t,\mathrm{cent}}^{1h}$ term, the blue dashed line the $\gamma_{t,\mathrm{cent}}^{2h}$ term, the green dotted line the $\gamma_{t,\mathrm{sat}}^{\mathrm{trunc}}$ term, the red dotted line the $\gamma_{t,\mathrm{sat}}^{\mathrm{1h}}$ term, the blue dotted line the $\gamma_{t,\mathrm{sat}}^{\mathrm{2h}}$ term, and the black line shows the sum of the terms. The $\gamma_{t,sat}^{1h}$ term causes a prominent bump for the two lowest dynamical mass bins, which indicates that a significant number of lenses in these bins are satellites.

well with the mean dynamical mass. In particular, the best fit halo masses of the D5 and D6 late-type bins are low. These low values may be explained if rotation constitutes a major part of the observed velocity dispersions of late-type galaxies, leading to an overestimation of the dynamical mass. Additionally, the effective radius for some late-type galaxies at high redshift may be overestimated, since a significant fraction consists of multiple objects with small separations as we observed in Section 3.2.

For early-type galaxies the dynamical mass is a useful tracer of the total mass at small scales, but it appears to be less reliable for late-type galaxies. How the dynamical mass changes for galaxies where rotation is important, or for galaxies that are populated over a large range of redshifts, may be studied with numerical simulations. In any case, it is not clear how to translate a dynamical mass estimate into a total mass estimate of the halo of a galaxy. With weak lensing we measure the total halo masses of galaxies directly, providing estimates that can easily be compared to simulations.

3.6 Luminosity results

The optical luminosity is a readily measured quantity which is related to the stellar mass, and hence the baryonic content of a galaxy. Therefore, we continue by measuring the lensing signal as a function of luminosity. We divide our lens sample into eight luminosity bins, as detailed in Table 3.2. We measure $\Delta\Sigma$ of the stacked lenses and show the results in Figure 3.8, together with the best fit halo model. The amplitude of the lensing signal clearly increases

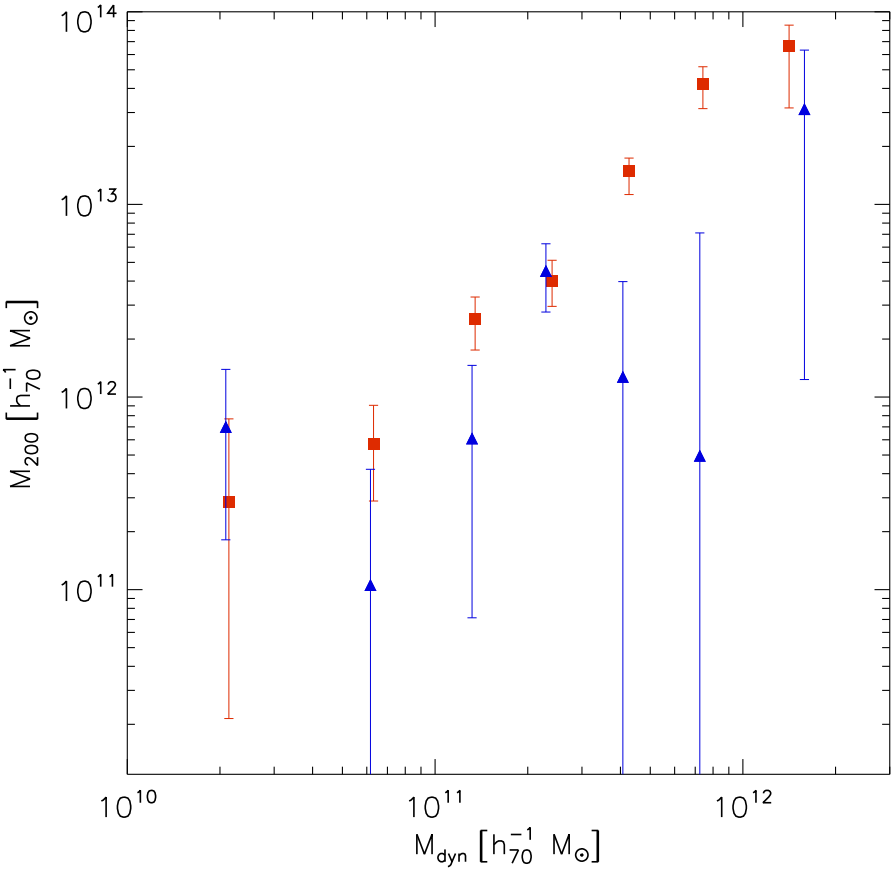

Figure 3.7: Best fit halo mass as a function of the mean dynamical mass. The red squares (blue triangles) denote the halo mass for the early-types (late-types). The early-/late-type division is based on the brightness profiles of the lenses. The dynamical mass correlates well with the lensing mass for the early-type galaxies, but not for the late-type galaxies.

for the brighter galaxies as expected. Furthermore, the shear from the $\gamma_{t,sat}^{1h}$ term causes a prominent bump for the fainter lenses, but not for the brighter ones. This indicates that a considerable fraction of the low luminosity lenses are satellites. We split the lenses into early- and late-types using the $frac\_deV$ parameter as before, and study the signals separately.

There are various issues we have to address before we can interpret the measurements. First of all, lens galaxies scatter between luminosity bins due to luminosity errors. If the luminosity errors are large compared to the width of the bins this could potentially introduce a bias. This bias is greatest at the highest luminosities, where the luminosity function is steep. In this case, on average more low luminosity (and mass) galaxies scatter into the higher luminosity bins, biasing the best fit halo mass low. The average absolute magnitude

Table 3.2: Luminosity results

Sample	M_r	$n_{\rm lens}$	$\langle z \rangle$	$f_{\rm late}$	$\langle L_r^{early} \rangle$	$M_h^{\rm early}$	$\alpha^{\rm early}$	$L_{200}^{\rm early}$	$\langle L_r^{late} \rangle$	$M_h^{\rm late}$	$\alpha^{\rm late}$	$L_{200}^{\rm late}$
	(1)	(2)	(3)	(4)	(5)	(6)	(7)	(8)	(9)	(10)	(11)	(12)
L1	$[-21.0, -20.0]$	3 563	0.08	0.44	1.17	$6.83^{+5.07}_{-3.80}$	$0.37^{+0.08}_{-0.07}$	1.32±0.01	1.23	$2.37^{+3.99}_{-2.36}$	$0.07^{+0.11}_{-0.07}$	1.26±0.01
L2	$[-21.5, -21.0]$	2 772	0.10	0.35	2.14	$5.24^{+4.59}_{-3.23}$	$0.38^{+0.09}_{-0.08}$	2.36±0.01	2.34	$5.14^{+6.44}_{-4.40}$	$0.06^{+0.10}_{-0.06}$	2.52±0.01
L3	$[-22.0, -21.5]$	3 064	0.13	0.29	3.24	$23.6^{+8.94}_{-7.01}$	$0.19^{+0.07}_{-0.07}$	4.01±0.02	3.63	$3.06^{+6.70}_{-3.04}$	$0.35^{+0.28}_{-0.12}$	3.67±0.01
L4	$[-22.5, -22.0]$	2 370	0.16	0.20	5.01	$30.4^{+10.8}_{-10.4}$	$0.34^{+0.09}_{-0.09}$	6.57±0.03	5.62	$23.7^{+15.3}_{-12.2}$	$0.00^{+0.05}_{-0.00}$	6.50±0.04
L5	$[-23.0, -22.5]$	1 658	0.20	0.11	7.59	$150^{+31.3}_{-30.4}$	$0.05^{+0.11}_{-0.05}$	12.3±0.1	8.91	$18.1^{+26.9}_{-18.1}$	$0.20^{+0.00}_{-0.13}$	10.0±0.1
L6	$[-23.5, -23.0]$	1 453	0.32	0.03	11.0	$381^{+87.3}_{-88.3}$	$0.19^{+0.01}_{-0.19}$	21.2±0.2	13.8	201^{+213}_{-197}	$0.20^{+0.00}_{-0.20}$	23.4±1.7
L7	$[-24.0, -23.5]$	607	0.41	0.05	15.8	814^{+109}_{-243}	$0.00^{+0.20}_{-0.00}$	45.2±0.8	21.9	437^{+350}_{-390}	$0.00^{+0.20}_{-0.00}$	-
L8	$[-24.5, -24.0]$	83	0.47	0.04	22.9	1169^{+367}_{-776}	$0.00^{+0.20}_{-0.00}$	68.0±3.6	-	-	-	-

(1) the magnitude range of the bin; (2) the number of lenses; (3) the mean redshift; (4) the fraction of late type galaxies; (5) the mean luminosity for the early types in units of $10^{10}\ h_{70}^{-2} L_\odot$; (6) the best fit halo mass for the early types in units of $10^{11} h_{70}^{-1} M_\odot$; (7) the best fit satellite fraction for the early types; (8) the total luminosity within r_{200} for the early types in units of $10^{10}\ h_{70}^{-2} L_\odot$; (9) the mean luminosity for the late types in units of $10^{10}\ h_{70}^{-2} L_\odot$; (10) the best fit halo mass for the late types in units of $10^{11} h_{70}^{-1} M_\odot$; (11) the best fit satellite fraction for the late types; (12) the total luminosity within r_{200} for the late types in units of $10^{10}\ h_{70}^{-2} L_\odot$.

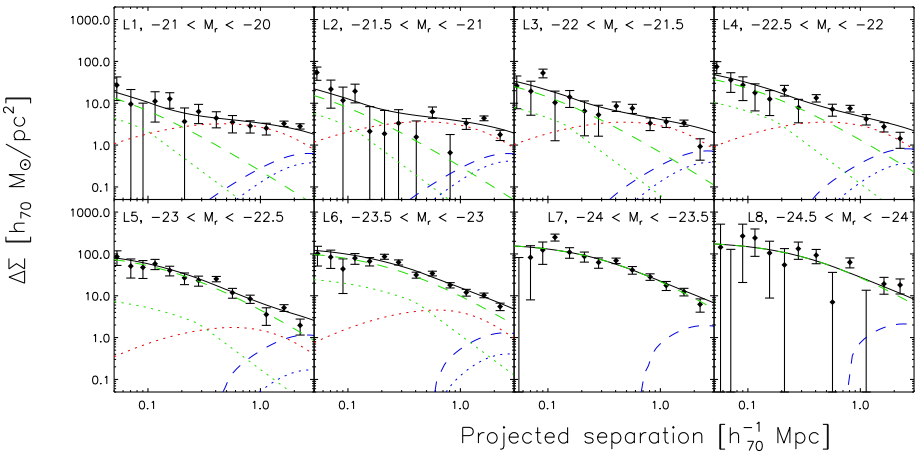

Figure 3.8: Lensing signal $\Delta\Sigma$ for each luminosity bin as a function of physical distance from the lens. The green dashed line shows the $\gamma_{t,\mathrm{cent}}^{1h}$ term, the blue dashed line the $\gamma_{t,\mathrm{cent}}^{2h}$ term, the green dotted line the $\gamma_{t,\mathrm{sat}}^{\mathrm{trunc}}$ term, the red dotted line the $\gamma_{t,\mathrm{sat}}^{\mathrm{1h}}$ term, the blue dotted line the $\gamma_{t,\mathrm{sat}}^{\mathrm{2h}}$ term, and the black line shows the sum of the terms. A significant fraction of the low luminosity lenses are satellites in larger haloes, as the $\gamma_{t,sat}^{1h}$ term causes a prominent bump at $\sim$ 1Mpc in the lensing signal.

error is $\sim$0.03 for $z < 0.33$, and $\sim$0.07 for $z > 0.33$, small compared to the minimal bin-width of 0.5. We find that the induced bias is relevant for the L7 and L8 bins of the early-types only, with corrections of 4% and 7% respectively. The corrections are smaller than the measurement errors on the halo mass for these bins. We detail the calculation of the correction factor in Appendix 3.A.

When we fit a halo mass to the stacked shear signal of galaxies within a luminosity bin, the resulting mass is not equal to the mean halo mass, nor to the central mass of the original distribution (Tasitsiomi et al. 2004; Mandelbaum et al. 2005b; Cacciato et al. 2009; Leauthaud et al. 2010) because the distribution in halo mass is not uniform (in addition, the NFW profile itself depends on mass). It is useful to convert the measured lensing mass to the mean halo mass to allow comparison with simulations. The correction we have to apply depends not only on the distribution of halo masses for a given luminosity, but also on the halo mass function. Since the halo mass function is a declining function — steeply at the high mass end — we will preferentially select lower mass haloes. Hence, the underlying function from which we draw our galaxies is the halo mass function convolved with the halo mass distribution. In Appendix 3.B we discuss how we calculate the correction factor that we apply to obtain the mean of the halo mass in each luminosity bin. The values are given in Table 3.4, and range between 5-30%.

The best fit halo mass for each luminosity bin, corrected for the scatter and the width of the halo mass distribution, is given in Table 3.2, and is shown as a function of luminosity in Figure 3.9a. The error bars on the halo masses are the 1σ deviations determined by marginalizing over the satellite fraction. We fit a powerlaw of the form $M_{200} = M_{0,L}(L/L_0)^{\beta_L}$, with a pivot $L_0 = 10^{11}$

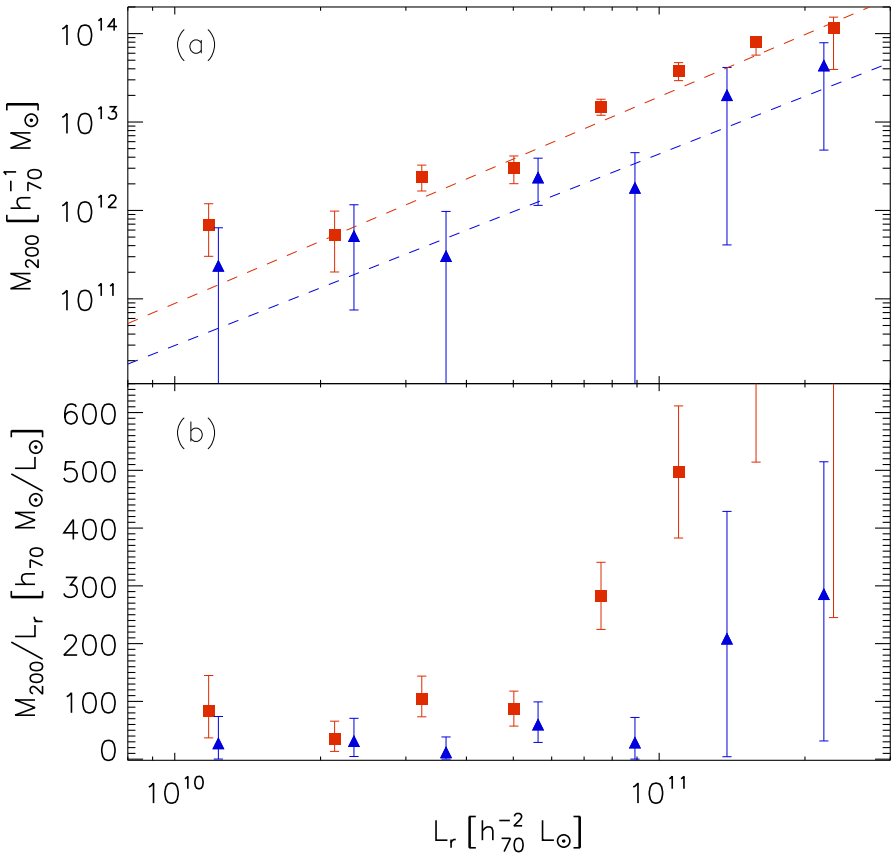

Figure 3.9: Best fit halo mass (*top*), and the mass-to-light ratio (*bottom*) as a function of mean luminosity. The red squares (blue triangles) denote the early-type (late-type) results. The division in early-/late-types is based on the brightness profiles of the lenses. The dashed lines are the powerlaw fits, with values as indicated in the text.

$h_{70}^{-2}L_{r,\odot}$. As the errors of the best fit halo masses are asymmetric due to the constraints we impose on the halo model fits, we fit the powerlaw directly to the shear measurements (with symmetric error bars). Hence we do not fit for the halo mass for each bin, but determine the best fit $M_{0,L}$ and β_L for all bins simultaneously, whilst fitting the satellite fraction for each bin separately. Note that the best fit satellite fractions from this approach are close to the values given in Table 3.2. For the early-types, we find $M_{0,L} = 2.76^{+0.19}_{-0.20} \times 10^{13} h_{70}^{-1} M_\odot$ and $\beta_L = 2.34^{+0.09}_{-0.16}$, and for the late-types $M_{0,L} = 0.61^{+0.29}_{-0.24} \times 10^{13} h_{70}^{-1} M_\odot$ and $\beta_L = 2.2^{+0.7}_{-0.6}$, as shown in Figure 3.9a. The error on $M_{0,L}$ (β_L) is determined by marginalizing over β_L ($M_{0,L}$). We show the 67.8%, 95.4% and 99.7% confidence limits of the two powerlaw fits in Figure 3.10. The results for the early-types are better constrained because we have more early-type galaxies in our lensing sample. These are also more massive than the late-type galaxies and hence

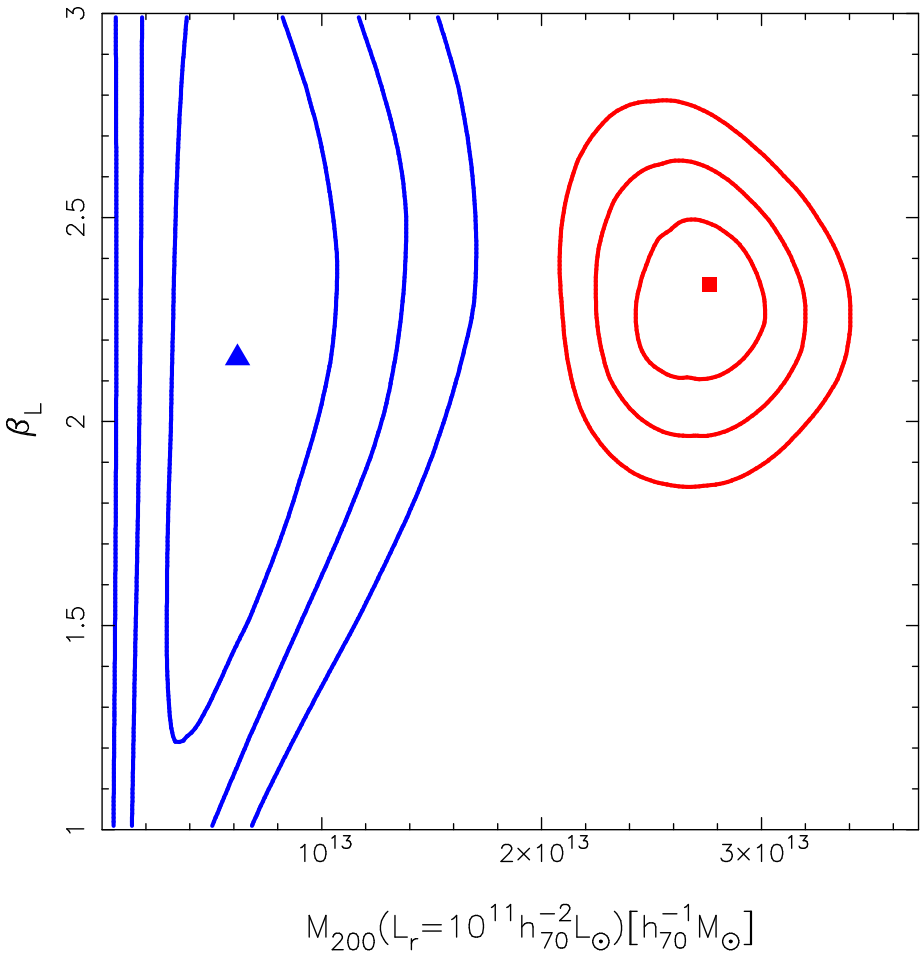

Figure 3.10: 67.8%, 95.4% and 99.7% confidence limits of the powerlaw fits between luminosity and halo mass, in red (blue) for the early-type (late-type) galaxies. The red square (blue triangle) indicates the best fit of the early-types (late-types). The powerlaw fit for the early-types is better constrained than for the late-types, because the majority of galaxies in our lens sample are early-types. The early-types also reside in more massive haloes, and consequently produce a stronger lensing signal.

produce a stronger lensing signal.

We compare our analysis to two previous weak lensing studies. Hoekstra et al. (2005) measured the lensing signal of $\sim 1.4 \times 10^5$ isolated galaxies with photometric redshift $0.2 < z < 0.4$ in the RCS. In the R-band, they found a virial mass of $M_R^{\rm H05} = 7.5^{+1.2}_{-1.1} \times 10^{11} h^{-1} M_\odot$ for a galaxy of luminosity $L_R = 10^{10} h^{-2} L_\odot$, and a powerlaw index of $\beta_R^{\rm H05} = 1.6 \pm 0.2$. We use the transformations from Lupton (2005)[8], and find that $r \approx R + 0.24$ for the early-type galaxies in our sample, which make up the majority of the lenses. We convert

[8] http://www.sdss.org/dr7/algorithms/sdssUBVRITransform.html#Lupton2005

L_R to L_r, use our powerlaw fit to predict M_{200}, and convert that to the virial mass by increasing it by 30%. We find that $M_{\rm vir} = (7.2 \pm 1.5) \times 10^{11} h^{-1} M_\odot$ for a $L_R = 10^{10} h^{-2} L_\odot$ galaxy, in good agreement with Hoekstra et al. (2005). The powerlaw index of Hoekstra et al. (2005) is shallower than the $\beta_L = 2.34^{+0.09}_{-0.16}$ that we find. A possible explanation is that a fraction of the low luminosity galaxies in Hoekstra et al. (2005) are satellites, whose masses are biased high due to the added lensing signal of nearby galaxies, flattening the powerlaw index. We note two caveats: the lens sample of Hoekstra et al. (2005) does not exclusively consist of early-types, and the lens samples we compare reside in different environments.

Mandelbaum et al. (2006) present results for 3.5×10^5 galaxies using SDSS data. Galaxies are divided into early-types and late-types based on their brightness profile (using the same selection criterium that we have applied to our lenses), and are studied in bins of absolute r-band magnitude. To compare the results, we convert our luminosities according to the definitions used in Mandelbaum et al. (2006): the absolute magnitude is calculated using a k-correction to z=0.1, the distance modulus is calculated using $h = 1.0$ and a passive evolution term is included which is given by $1.6(z - 0.1)$. As a result, we decrease the absolute magnitudes of our lenses by roughly one magnitude. Additionally, we increase our masses by 30% since Mandelbaum et al. (2006) define the halo mass using $180\bar{\rho}$ instead of $200\rho_c$. There are various other differences between the analyses, such as the use of a different correction factor for the width of the halo mass distribution, a different cosmology, a different mass-concentration relation for the NFW profiles, and differences in the modelling of the lensing signal. These differences are expected to have a minor impact on the best fit halo mass, but they limit the accuracy of a detailed comparison.

Matching our luminosity bins to those of Mandelbaum et al. (2006) closest in mean luminosity, we find that the best fit halo masses for the early- and late-type galaxies are generally in agreement. To quantify whether the results are consistent, we fit a powerlaw of the form $M_{180} = \tilde{M}_{0,L}(\tilde{L}/\tilde{L}_0)^{\beta_{\tilde{L}}}$, where $\tilde{L}_0 = 1.2 \times 10^{10} h^{-2} L_\odot$. The tilde indicates that the luminosity is calculated following Mandelbaum et al. (2006). The powerlaw is fitted to the best fit halo mass directly, and the weights of the measurements are calculated from the error bars through which the model passes, i.e., if the model is larger (smaller) than the data point, we use the positive (negative) error bar. For the early-types we find $\tilde{M}_{0,L} = 7.3^{+2.1}_{-1.7} \times 10^{11} h^{-1} M_\odot$ and $\beta_{\tilde{L}} = 2.7 \pm 0.2$ for our data, while using Mandelbaum et al. (2006) results we find $\tilde{M}_{0,L} = 11.2^{+1.9}_{-1.8} \times 10^{11} h^{-1} M_\odot$ and $\beta_{\tilde{L}} = 2.3 \pm 0.2$, in fair agreement with our findings. For the late-types we find $\tilde{M}_{0,L} = 2.7^{+3.9}_{-1.8} \times 10^{11} h^{-1} M_\odot$ and $\beta_{\tilde{L}} = 3.0^{+1.0}_{-1.6}$, while using the results of Mandelbaum et al. (2006) we find $\tilde{M}_{0,L} = 7.8 \pm 1.1 \times 10^{11} h^{-1} M_\odot$ and $\beta_{\tilde{L}} = 1.1^{+0.3}_{-0.4}$. The results from Mandelbaum et al. (2006) prefer a shallower slope and a higher offset, but the fits are consistent.

3.6.1 Mass-to-light ratio

A large number of the galaxies in our brightest luminosity bins reside in groups or small clusters. To identify those lenses, we cross-correlate our lens sample with the preliminary RCS2 cluster catalogue, to be presented in a future publi-

cation. We take galaxies with a separation $<360h_{70}^{-1}$kpc from the cluster centre, and within 0.05 from the cluster redshift, to be cluster members. Using these criteria, we find that from L5 to L7, 3%, 26%, 43% of the late-type galaxies, and from L5 to L8, 12%, 31%, 48% and 66% of the early-type galaxies can be associated with clusters. The best fit halo mass of these galaxies is the mass of the group or cluster within r_{200}, while the luminosity is only measured for the lens galaxy. The resulting mass-to-light ratio, shown in Figure 3.9b, is therefore higher than what we would measure for the individual galaxies, or for the clusters.

To obtain the mass-to-light ratios of the groups and clusters, we estimate the amount of additional luminosity coming from other cluster members within r_{200}. We assume that the spectral energy distributions (SEDs) of the galaxies physically associated with the lens are similar to the SED of the lens, and convert their apparent magnitudes to absolute magnitudes using the same conversion that has been used for the lenses. The apparent magnitudes we use are those from the photometric catalogues from Gilbank et al. (2011). As these catalogues do not cover all fields (e.g. the fields in the uncompleted patch 1303), only ∼90% of the lenses are used for the calculation of L_{200}. We measure the source galaxy overdensity as in Section 3.3.3 using all the galaxies with $m_{\rm low} < m_r < 24$, where $m_{\rm low}$ is the magnitude of the brightest galaxy that resides at the lens redshift, and calculate the mean luminosity overdensity as a function of lens-source separation. $m_{\rm low}$ is determined by selecting the brightest galaxy in the photometric redshift catalogues from Ilbert et al. (2006) that resides at the redshift of the lens or higher. We sum the luminosity overdensity to r_{200} and add it to the lens luminosity to obtain the total luminosity within r_{200}, L_{200}. To make sure that we do not miss a signicant fraction of L_{200} from galaxies with $m_r > 24$, we also calculate L_{200} using an upper limit of 23.5, and find that the results do not change significantly. The values of L_{200} are given in Table 3.2. We show the mass-to-light ratio M_{200}/L_{200} as a function of L_{200} in Figure 3.11. For $L_{200} < 10^{11}\ h_{70}^{-2}L_{\odot}$ we calculate the weighted mean, and find a value of $M_{200}/L_{200} = 42 \pm 10\ h_{70}M_{\odot}/L_{\odot}$ for early-type galaxies, whilst $M_{200}/L_{200} = 17 \pm 9\ h_{70}M_{\odot}/L_{\odot}$ for late-type galaxies. The total mass-to-light ratio increases with L_{200} for the early-types to $\sim$180 $h_{70}M_{\odot}/L_{\odot}$ at $L_{200} = 5 \times 10^{11}h_{70}^{-2}L_{\odot}$. The total mass-to-light ratio is roughly a factor of two larger for early-types than for late-types. This suggests that the difference in the best fit halo mass between early- and late-types for a given luminosity is not solely due to the fact that early-types reside in denser environments, but is at least partly intrinsic. The value of L_{200} for the L7 late-type bin could not be robustly determined, and is excluded from the results.

We compare our results to the M_{200}/L_{200} from Sheldon et al. (2009a,b) which have been determined for the clusters in the maxBCG catalogue (Koester et al. 2007). The quoted values of L_{200} in their work have been measured in the i-band, and are calculated using a k-correction to $z = 0.25$. We convert them to the r-band luminosities we use by accounting for the mean difference between i-band and r-band absolute magnitudes of early-type galaxies at $z = 0.25$, the mean difference between the k-corrections to $z = 0.25$ and $z = 0.0$, and the difference between the i-band and r-band solar magnitudes. The final conversion factor is small as the corrections partly cancel each other, and we convert their luminosities to our definition by multiplying them by 1.06. Note that we do not account for differences in the redshift evolution of the luminosities, as it is not

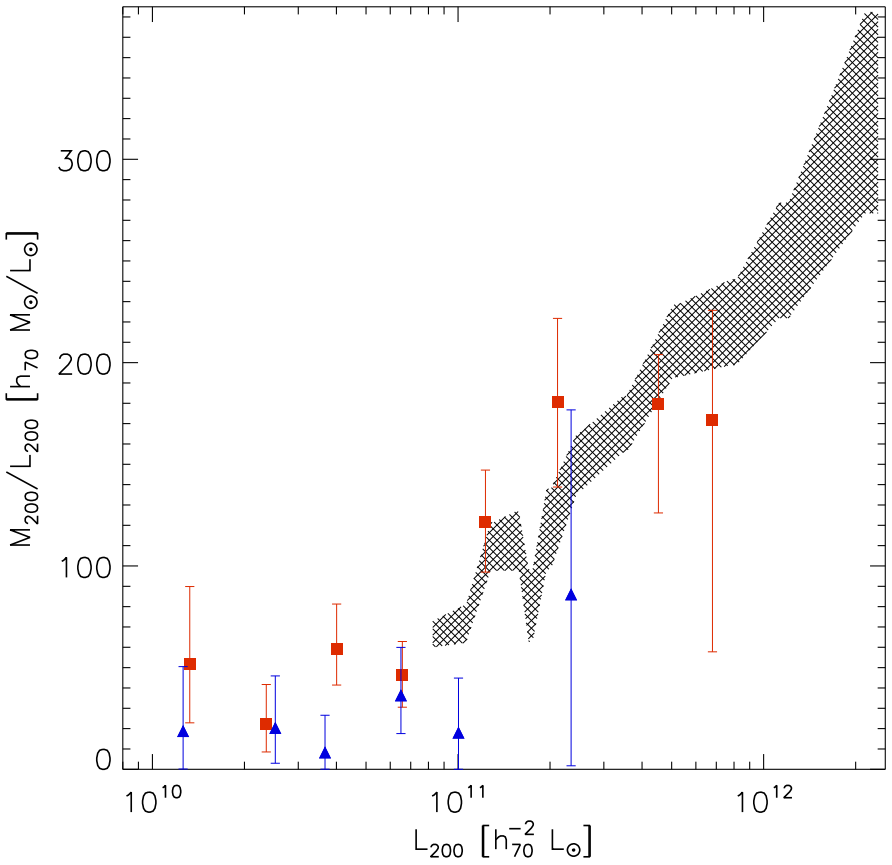

Figure 3.11: Mass-to-light ratio using the total halo mass and luminosity within r_{200}, as a function of L_{200}. The red squares (blue triangles) denote the early-type (late-type) results. The hatched area indicates the converted M_{200}/L_{200} of the maxBCG clusters from Sheldon et al. (2009a). The M_{200}/L_{200} for individual galaxies at low luminosities are naturally extended to the ratios for the maxBCG clusters.

mentioned in Sheldon et al. (2009a) which correction, if any, they have used. The converted M_{200}/L_{200} from Sheldon et al. (2009a) are indicated with the hatched area in Figure 3.11. The mass-to-light ratios overlap, and the ratios we have determined, for individual galaxies at low luminosities, and for galaxy groups and small clusters at high luminosities, are naturally extended to the M_{200}/L_{200} of clusters from the maxBCG cluster sample.

3.6.2 Satellite fraction

Figure 3.12 shows the best fit satellite fraction as a function of luminosity. The satellite fraction is decreasing with increasing luminosity for the early-type galaxies, from $\sim 40\%$ at $L_r = 10^{10} h_{70}^{-2} L_\odot$ to $< 10\%$ at $L_r = 10^{11} h_{70}^{-2} L_\odot$. For the

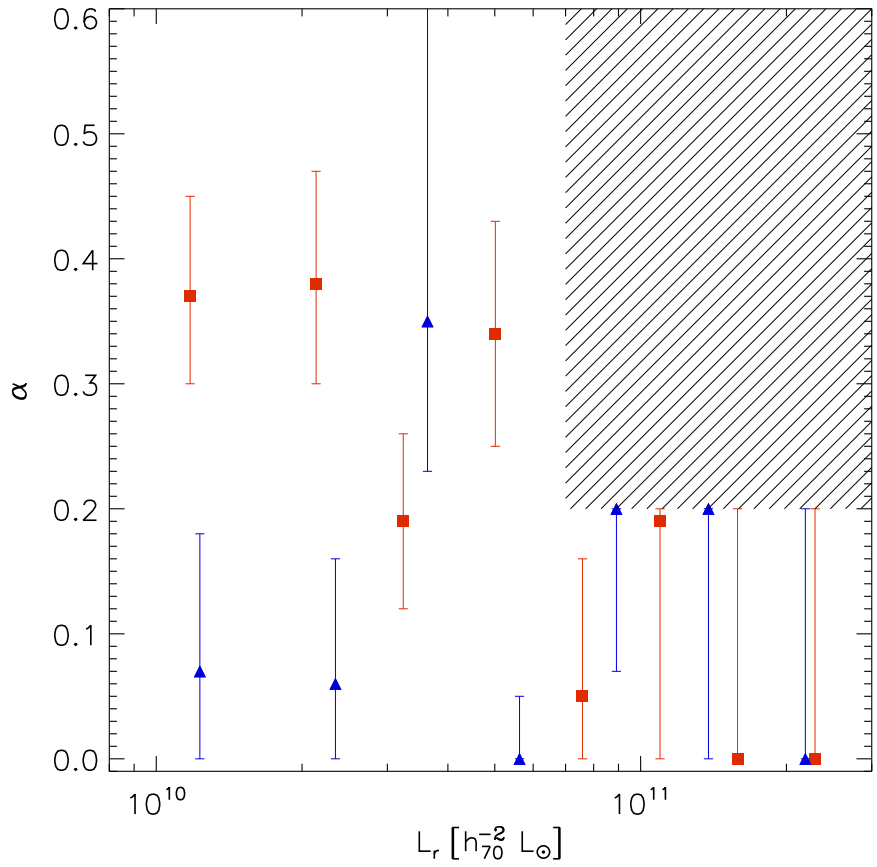

Figure 3.12: Best fit satellite fraction as a function of mean luminosity. The red squares (blue triangles) denote the satellite fraction for the early-type (late-type) galaxies. The satellite fraction decreases with luminosity for the early-types, and no trend is observed for the late-types. The dashed area indicates the area excluded by the prior on the satellite fraction.

late-type galaxies, no clear trend with luminosity is observed, and the satellite fraction has a value of 0-20%. The satellite fractions are not well constrained for the highest luminosity bins. As demonstrated in Appendix 3.C, the sum of the halo model satellite terms has the same shape as the central term at the high halo mass end. As a result, the halo model fit cannot discriminate between the two profiles. The implementation of a more sophisticated description of the truncation of the subhaloes is necessary to improve the constraints on the satellite fraction at the high luminosity/stellar mass end. For instance, recent work by Limousin et al. (2009) suggests that massive early-type satellite galaxies are stripped of a far larger fraction of their dark matter than the 50% we have assumed so far, and we discuss the implications in Appendix 3.C.

Mandelbaum et al. (2006) find a satellite fraction of 10-15% for late-type galaxies, independent of stellar mass or luminosity. The satellite fraction for

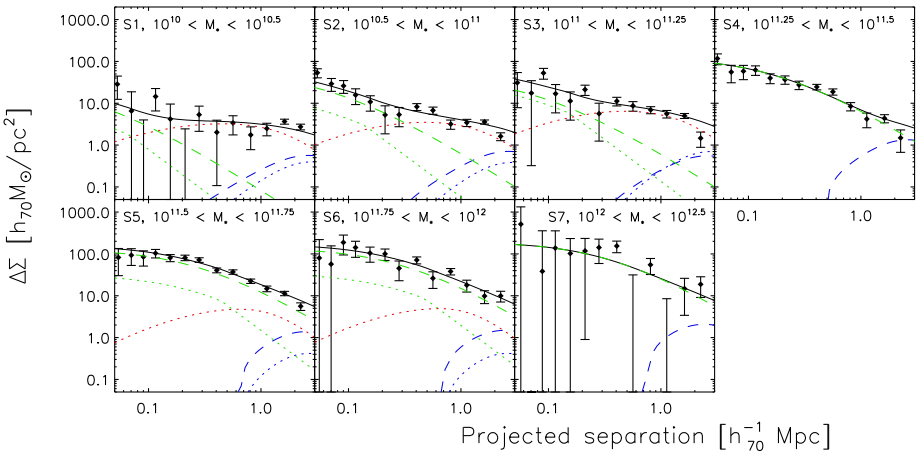

Figure 3.13: Lensing signal $\Delta\Sigma$ for each stellar mass bin as a function of physical distance from the lens. The green dashed line shows the $\gamma_{t,\mathrm{cent}}^{1h}$ term, the blue dashed line the $\gamma_{t,\mathrm{cent}}^{2h}$ term, the green dotted line the $\gamma_{t,\mathrm{sat}}^{\mathrm{trunc}}$ term, the red dotted line the $\gamma_{t,\mathrm{sat}}^{\mathrm{1h}}$ term, the blue dotted line the $\gamma_{t,\mathrm{sat}}^{\mathrm{2h}}$ term, and the black line shows the sum of the terms. Similar to the lensing signal of the luminosity bins, we find that the $\gamma_{t,sat}^{1h}$ term causes a clearly noticeable bump at $\sim 1 h_{70}^{-1}$Mpc in the lensing signal for the low stellar mass bins, which indicates that a significant fraction of these galaxies are satellites.

early-types decreases with luminosity from 27% at $\langle \tilde{L}/\tilde{L}_0 \rangle = 1.1$ to 15% at $\langle \tilde{L}/\tilde{L}_0 \rangle = 4.9$, and both trends are consistent with our findings.

3.7 Stellar mass results

The stellar mass of a galaxy is believed to be a better tracer of the baryonic content of a galaxy than the luminosity, as it is less sensitive to recent star formation. Therefore, we divide our lens sample into seven stellar mass bins and study the lensing signal. The details of the samples are listed in Table 3.3. Figure 3.13 shows the lensing signal of the stacked lenses in each bin, together with the best fit halo model. Similar to the luminosity results, we find that the lensing signal increases with stellar mass, and observe the presence of the $\gamma_{t,sat}^{1h}$ bump for the lower stellar mass bins. We split the lens sample into early- and late-types using the $frac\_deV$ parameter as before, and study the signals separately.

To interpret the results, we have to account for a number of issues. The random stellar mass errors are about 0.1 dex, independent of stellar mass, and do not include the systematic error. The random error determines the scattering of lenses amongst bins, and its value is large compared to the bin width. We calculate the bias resulting from this scatter in Appendix 3.A, and find that the best fit halo masses have to be corrected with a factor ranging between $0.9 - 1.4$. Once corrected for the scatter, we convert the lensing mass to the mean halo mass. This correction has already been introduced in Section 3.6,

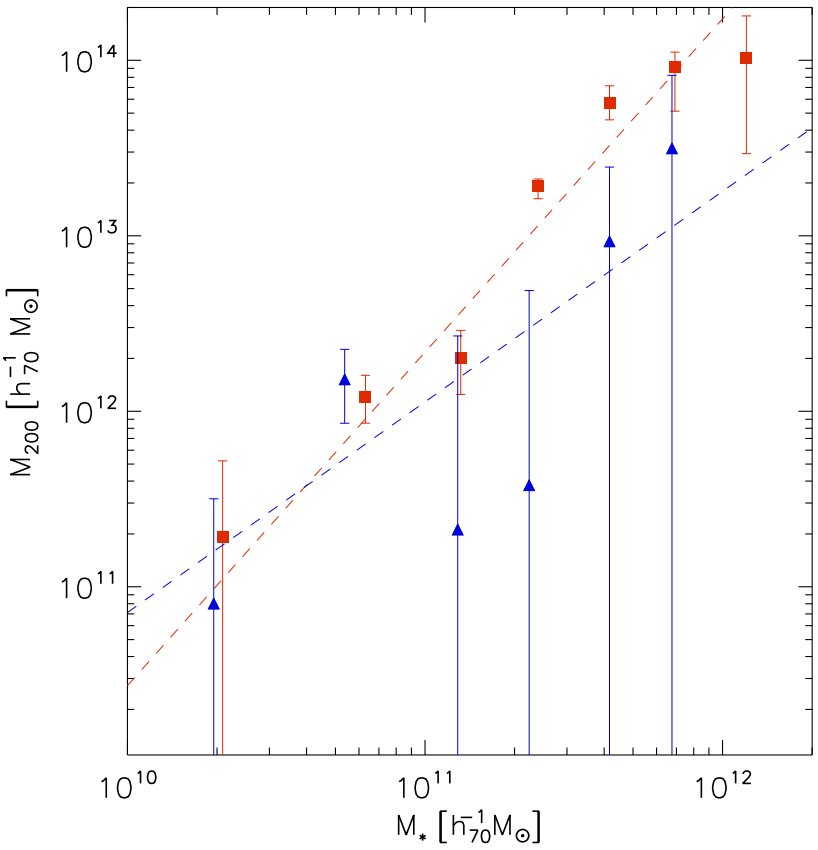

Figure 3.14: Best fit halo mass as a function of mean stellar mass. The red squares (blue triangles) denote the early-type (late-type) galaxies. The separation of the lenses into early/late-types is based on their brightness profiles. The dashed lines are the powerlaw fits, with values as indicated in the text. For stellar masses lower than 10^{11} $h_{70}^{-1}M_\odot$ the best fit halo masses of early- and late-type galaxies are similar, but for $M_* > 10^{11}$ $h_{70}^{-1}M_\odot$ we find that the best fit halo masses of early-types are larger.

and we discuss in Appendix 3.B how we calculate it. We increase the corrected halo mass accordingly to obtain the mean halo mass (see Table 3.4 for details).

The resulting halo masses are given in Table 3.3, and shown in Figure 3.14. This figure shows that the relation is different for early-types and late-types. Below a stellar mass of $10^{11}h_{70}^{-1}M_\odot$, the halo mass is similar for both galaxy types, but for stellar masses larger than $10^{11}h_{70}^{-1}M_\odot$ the halo masses of early-type galaxies are more massive for a given stellar mass than the halo masses of late-type galaxies, and increase more steeply with stellar mass. These trends in the stellar mass to halo mass relation are in agreement with those found by Mandelbaum et al. (2006).

We fit a powerlaw of the form $M_{200} = M_{0,M}(M_*/M_0)^{\beta_M}$, with $M_0 =$

Table 3.3: Stellar mass results

Sample	$\log(M_*)$	$n_{\rm lens}$	$\langle z\rangle$	$\langle M_*\rangle$	$f_{\rm late}$	$M_h^{\rm early}$	$\alpha^{\rm early}$	$M_{*,200}^{\rm early}$	$M_h^{\rm late}$	$\alpha^{\rm late}$	$M_{*,200}^{\rm late}$
	(1)	(2)	(3)	(4)	(5)	(6)	(7)	(8)	(9)	(10)	(11)
S1	$[10.00, 10.50]$	3 359	0.08	2.04	0.51	$1.93^{+3.29}_{-1.91}$	$0.44^{+0.21}_{-0.09}$	2.15±0.004	$0.80^{+2.37}_{-0.79}$	$0.10^{+0.11}_{-0.07}$	2.04±0.001
S2	$[10.50, 11.00]$	5 870	0.11	6.03	0.28	$12.0^{+4.04}_{-3.44}$	$0.19^{+0.04}_{-0.04}$	7.66±0.02	$15.3^{+7.30}_{-6.69}$	$0.12^{+0.08}_{-0.08}$	6.75±0.01
S3	$[11.00, 11.25]$	2 428	0.15	13.2	0.10	$20.0^{+8.87}_{-5.57}$	$0.44^{+0.09}_{-0.08}$	16.8±0.1	$2.13^{+24.7}_{-2.11}$	$0.40^{+0.46}_{-0.31}$	14.4±0.1
S4	$[11.25, 11.50]$	1 631	0.20	24.0	0.05	$193^{+17.9}_{-30.1}$	$0.00^{+0.07}_{-0.00}$	40.3±0.3	$3.80^{+45.0}_{-3.79}$	$0.70^{+0.30}_{-0.51}$	27.3±0.4
S5	$[11.50, 11.75]$	1 505	0.34	41.7	0.03	571^{+144}_{-114}	$0.20^{+0.00}_{-0.20}$	88.9±1.1	$93.1^{+153}_{-93.1}$	$0.20^{+0.00}_{-0.20}$	71.0±4.6
S6	$[11.75, 12.00]$	396	0.41	69.2	0.05	914^{+199}_{-401}	$0.06^{+0.14}_{-0.06}$	230±6	316^{+504}_{-316}	$0.20^{+0.00}_{-0.20}$	-
S7	$[12.00, 12.50]$	48	0.48	123	0.02	1031^{+759}_{-739}	$0.20^{+0.00}_{-0.00}$	385±28	-	-	-

(1) the stellar mass range of the bin in units of $h_{70}^{-1}\ M_\odot$; (2) the number of lenses; (3) the mean redshift; (4) the mean stellar mass in units of $10^{10}\ h_{70}^{-1} M_\odot$; (5) the fraction of late type galaxies; (6) the best fit halo mass for the early types in units of $10^{11}\ h_{70}^{-1} M_\odot$; (7) the best fit satellite fraction for the early types; (8) the total stellar mass within r_{200} for the early types in units of $10^{10}\ h_{70}^{-1} M_\odot$; (9) the best fit halo mass for the late types in units of $10^{11}\ h_{70}^{-1} M_\odot$; (10) the best fit satellite fraction for the late types; (11) the total stellar mass within r_{200} for the late types in units of $10^{10}\ h_{70}^{-1} M_\odot$.

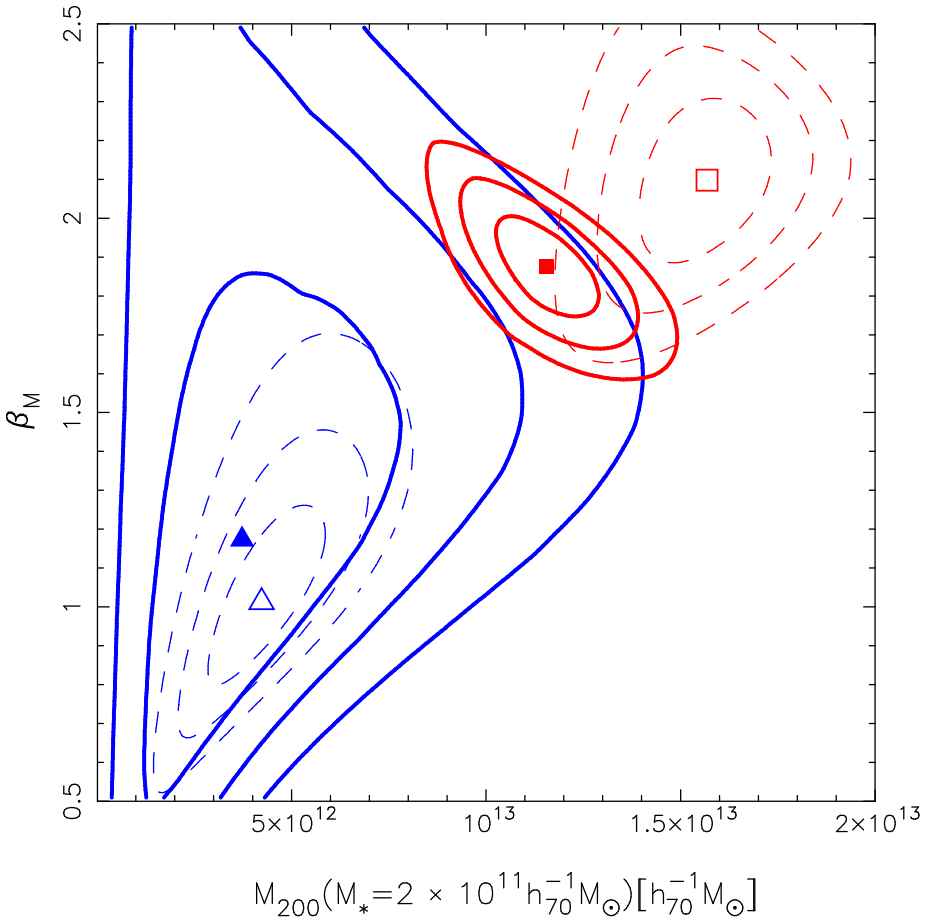

Figure 3.15: 67.8%, 95.4% and 99.7% confidence limits of the powerlaw fits between stellar mass and halo mass, in red (blue) for the early-type (late-type) galaxies. The red square (blue triangle) indicates the best fit of the early-types (late-types). The solid contour lines result from fitting the powerlaw to all the lensing data as described in the text. The dashed contours are the results from fitting the powerlaw between stellar mass and halo mass to the measurements in Mandelbaum et al. (2006).

$2 \times 10^{11} h_{70}^{-1} M_\odot$, fitting the lensing measurements simultaneously as we did for the luminosities. For the early-types, we find $M_{0,M} = 11.6 \pm 0.9 \times 10^{12} h_{70}^{-1} M_\odot$ and $\beta_M = 1.9 \pm 0.1$, and for the late-types $M_{0,M} = 3.7^{+2.6}_{-1.9} \times 10^{12} h_{70}^{-1} M_\odot$ and $\beta_M = 1.2 \pm 0.4$. These fits are shown in Figure 3.14 as the dashed red and blue lines for the early- and late-type galaxies respectively. We show the 67.8%, 95.4% and 99.7% confidence limits of the two powerlaw fits in Figure 3.15.

In order to compare with the results of Mandelbaum et al. (2006), we lower their halo masses by 30% to account for the difference between $M_{\rm vir}$ and M_{200}. We compare the halo masses of the bins with comparable mean stellar mass, and find that the best fit halo masses generally agree well. We fit a powerlaw between stellar mass and halo mass to their results, and the dashed contours in

Figure 3.15 show the resulting best fit normalisation and slope. The results of the late-types agree, although the errors are large. For the early-types, Mandelbaum et al. (2006) find a somewhat steeper slope and a higher offset. Note that this difference is mostly driven by their highest stellar mass bin, for which they fit a halo mass that is 50% larger than what we find for our corresponding bin. If we exclude that point from the fit, the 1σ contours overlap.

Moster et al. (2010) used numerical simulations to predict the relation between stellar mass and halo mass. We find that for $M_* < 4 \times 10^{11}\ h_{70}^{-1} M_\odot$, the halo masses we have determined are about 1-2 σ lower than their models. At higher stellar masses, the discrepancy is significantly larger. Not only their model, but also the models of various other groups (e.g. Wang et al. 2006; Croton et al. 2006; Somerville et al. 2008; Behroozi et al. 2010; Neistein et al. 2011) predict that the halo masses of galaxies with a stellar mass $>10^{11}\ h_{70}^{-1} M_\odot$ increases rapidly as a function of stellar mass, a trend we do not observe in our measurements. This would imply that the predicted relation between stellar mass and halo mass for galaxies with $M_* > 4 \times 10^{11}\ h_{70}^{-1} M_\odot$ is too steep, possibly because the relation has not yet been well constrained by observations in this mass range. Although contamination of the high stellar mass bins by unresolved mergers may bias the best fit halo masses low, we estimate that this is not sufficient to explain the discrepancy.

3.7.1 Baryon conversion efficiency

To study the efficiency of star formation as a function of stellar mass, we measure the baryon conversion efficiency $\eta = M_*/(M_h \times f_b)$, where $f_b = \Omega_b/\Omega_M$ is the cosmological baryon fraction. We cannot simply use the mean stellar and halo mass, because we measure the halo mass of the environment where the galaxy resides. The mean stellar mass, however, is determined using the individual lenses only, which leads to an underestimation of η. To account for this, we estimate the additional amount of stellar mass within r_{200} assuming that the SEDs of the cluster members are similar to that of the lens galaxy. Under that assumption we determine $M_{*,200} = \langle M_* \rangle \times (L_{200}/L_r)$, where L_{200} is the total luminosity within r_{200} as discussed in Section 3.6.1. The error bars assume that the number of source galaxies in each radial bin follows a Poisson distribution. We give the values of $M_{*,200}$ in Table 3.3, and plot η as a function of $M_{*,200}$ in Figure 3.16.

The stars that make up the diffuse intracluster light (ICL) also contribute to the total stellar mass. The ICL typically makes up 10–20% of the stellar light in galaxy groups and clusters (see Giodini et al. 2009, and references therein). We do not account for the additional stellar mass from the ICL, because our lens sample consists of a mixture of isolated galaxies and galaxies in groups and clusters. The average contribution from the ICL is hard to determine, particularly because the contribution for low mass structures is very uncertain. The ICL is expected to be of importance for the S6 and S7 bins only, as they contain the largest fraction of cluster associated galaxies, and the derived values of η might at most increase with 10–20%.

We find that η decreases from $\sim$40% at $M_* \sim 5 \times 10^{10}\ h_{70}^{-1} M_\odot$ to a minimum of $\sim$10% for a stellar mass $M_{*,200} = 10^{12}\ h_{70}^{-1} M_\odot$, and seems to increase again at higher stellar masses. The baryon conversion efficiency for the late-types is higher, and no clear trend is observable because of the large errors. For

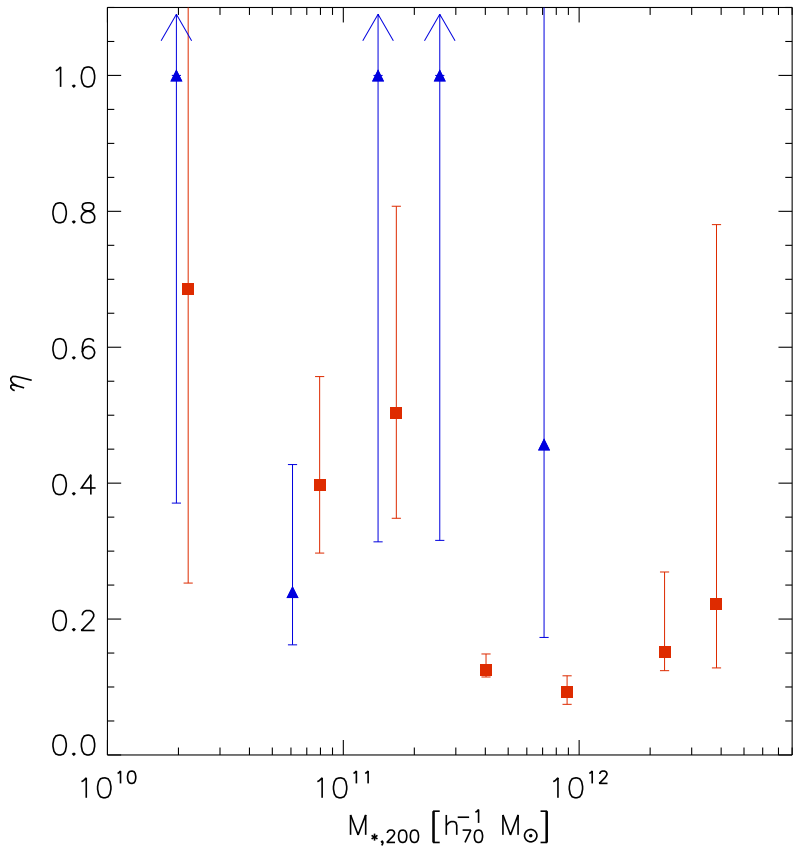

Figure 3.16: Baryon conversion efficiency η as a function of $M_{*,200}$, the stellar mass enclosed within r_{200}. The red squares (blue triangles) denote the early-type (late-type) galaxies. η is smaller for the early-types than for the late-types for $M_{*,200} > 10^{11}\ h_{70}^{-1} M_{\odot}$.

some bins η is larger than unity, but the error bars cover the reasonable range of $\eta < 1$. The value of $M_{*,200}$ for the S6 late-type bin could not be robustly determined, and is excluded from the results.

Hoekstra et al. (2005) divide the lens sample in red and blue galaxies based on their $B - V$ colour, and find that the baryon conversion efficiency for isolated blue galaxies in the magnitude range $18 < R_C < 24$ is about twice the value found for isolated red galaxies. Although we cannot compare the results in detail due to differences in the type selection and differences in the adopted IMF, our results also suggest a larger value for η for late-type galaxies in the range $M_{*,200} > 10^{11}\ h_{70}^{-1} M_{\odot}$. A similar trend has also been observed in Mandelbaum et al. (2006) for stellar masses $M_* > 10^{11}\ h_{70}^{-1} M_{\odot}$, but note that the baryon conversion efficiencies were determined using M_* instead of $M_{*,200}$, and the values are therefore lower limits.

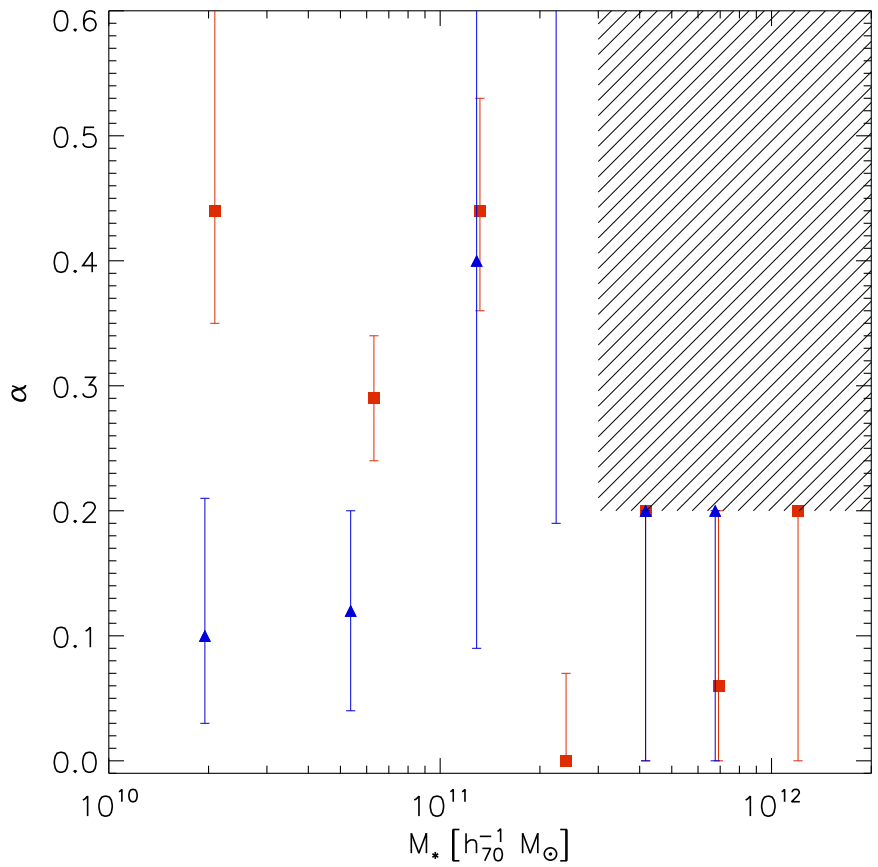

Figure 3.17: Best fit satellite fraction as a function of the mean stellar mass. The red squares (blue triangles) denote the early-type (late-type) results. The satellite fraction decreases with stellar mass for the early-types, and no trend is observed for the late-types. The dashed area indicates the area excluded by the prior on the satellite fraction.

3.7.2 Satellite fraction

In Figure 3.17 we show the satellite fraction for the early- and late-type galaxies as a function of stellar mass. The satellite fraction of the late-types is only well determined for the S1 and S2 bins, and appears to be constant as a function of stellar mass, with a value of ∼10%. The satellite fraction of the early-types is 45% for the lowest stellar mass bin, but decreases to $< 10\%$ for $M_* \geq 2 \times 10^{11}$ $h_{70}^{-1} M_\odot$. Mandelbaum et al. (2006) find a satellite fraction of about 10-15% for late-type galaxies, independent of stellar mass or luminosity. For the early-types, Mandelbaum et al. (2006) find that the satellite fraction decreases with stellar mass from 50% at 10^{10} $h_{70}^{-1} M_\odot$ to roughly 10% at 3×10^{11} $h_{70}^{-1} M_\odot$, consistent with our findings.

3.7.3 Dependence on redshift

The stellar mass of a galaxy and the dark matter content of its halo evolve with time. The stellar mass increases as galaxies form stars and merge with satellites and other galaxies. Satellite galaxies residing in subhaloes are tidally stripped of their dark matter, whilst the dark matter content of central haloes increases due to mergers. The evolution of the relation between stellar mass and dark matter content of galaxies has been studied with numerical simulations (e.g. Moster et al. 2010; Conroy & Wechsler 2009). These simulations predict that the dark matter content of haloes that host galaxies of $M_* > 10^{11}\ h_{70}^{-1} M_\odot$ increases faster than the stellar mass, while the stellar mass grows faster for haloes hosting galaxies of $M_* < 10^{11}\ h_{70}^{-1} M_\odot$.

To study this, we bin the early-type galaxies in stellar mass and redshift, and measure their halo mass. To avoid the degeneracy between halo mass and satellite fraction affecting the results, we fix the satellite fraction to the value we find by fitting the halo model to all lenses in each stellar mass bin. We apply the various corrections (e.g. scattering of lenses between bins), and show the results in Figure 3.18.

The errors on the best fit halo masses are large, and we therefore do not obtain tight constraints on the evolution of the halo masses for the low stellar mass bins. For the highest stellar mass bin, however, it appears that the halo mass is smaller by roughly a factor of two for the two highest redshift slices. The redshift dependent stellar-to-halo mass relation of Moster et al. (2010) predicts that at $M_* = 6 \times 10^{11}\ h_{70}^{-1} M_\odot$, the halo mass increases by $\sim 35\%$ between $z = 0.5$ and $z = 0.0$. In Leauthaud et al. (2012), the evolution of the stellar-to-halo mass relation from $z = 1$ to $z = 0.2$ is studied using a combined galaxy-galaxy weak lensing, galaxy spatial clustering, and galaxy number densities analysis in the COSMOS survey (Scoville et al. 2007). At stellar masses $M_* > h_{70}^{-1} 10^{11}$, the halo mass appears to decrease with redshift for a given stellar mass, but the small volume probed by COSMOS prevents a clear detection. Brown et al. (2008) study the growth of the dark matter content of massive early-type galaxies between a redshift of 0.0 and 1.0 by measuring the space density and spatial clustering of the galaxies. They find that between redshift $z = 1.0$ and $z = 0.0$, the dark matter haloes grow with $\sim$100%, while the stellar masses of these galaxies only grow with $\sim$30%. Conroy et al. (2007) utilizes the motions of satellite galaxies around isolated galaxies to constrain the evolution of the virial-to-stellar mass ratio, and they find that between $z \sim 1$ and $z \sim 0$ this ratio remains constant for host galaxies with a stellar mass below 1.5×10^{11} $h_{70}^{-1} M_\odot$, but increases by a factor 3.3 ± 2.2 for hosts with $M_* > 1.5 \times 10^{11}$ $h_{70}^{-1} M_\odot$. These findings are in qualitative agreement with our results.

3.8 Conclusions

We measured the halo masses for early- and late-type galaxies and compared these to their luminosity and stellar mass. For this purpose, we measured the weak lensing signal induced by the galaxies with SDSS spectroscopy that overlap with the RCS2, and modelled the data with a halo model. This enabled us to improve the constraints on the lensing measurements for the most massive galaxies, which typically reside at redshifts where the SDSS is not very sensitive.

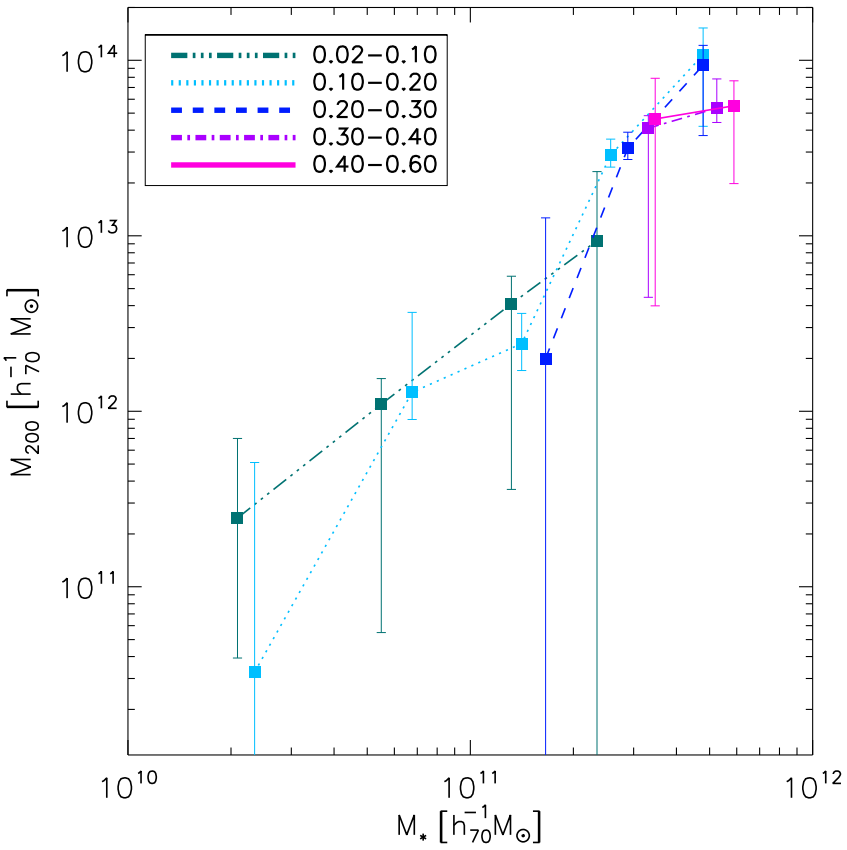

Figure 3.18: Halo mass as a function of the mean stellar mass for early-type galaxies in different redshift slices. Although we lack the statistical precision to draw definite conclusions, the measurements support the view that at the high stellar mass end, galaxies at a higher redshift have lower halo masses.

The halo mass and the dynamical mass correlate well for early-type galaxies, but not for late-type galaxies. A likely explanation is that late-type galaxies are rotating, resulting in an overestimation of the velocity dispersion, and hence of the dynamical mass. Furthermore, in contrast to the dynamical mass, the weak lensing mass can easily be related to numerical simulations, and provides constraints for the models that describe the relationship between baryons and dark matter.

The halo masses of galaxies increase with luminosity and stellar mass. For a given luminosity, the halo mass of the early-types is on average about five times larger than the late-types. We fitted a powerlaw relation between the luminosity and halo mass, and find that in the range $10^{10} < L_r < 10^{11.5}\ h_{70}^{-2} L_\odot$, the halo mass scales with luminosity as $M_h \propto L^{2.34^{+0.09}_{-0.16}}$ and $M_h \propto L^{2.2^{+0.7}_{-0.6}}$ for the early- and late-type galaxies respectively. For an early-type galaxy with a fiducal luminosity $L_0 = 10^{11}\ h_{70}^{-2} L_{r,\odot}$, we obtain a mass $M_{200} = (2.76^{+0.19}_{-0.20}) \times 10^{13} h_{70}^{-1} M_\odot$.

We computed L_{200}, the additional luminosity around the lenses within r_{200}, and find that the M_{200}/L_{200} ratio of the early-types is larger than for the late-types: for $L_{200} < 10^{11}\ h_{70}^{-2} L_\odot$ we find $M_{200}/L_{200} = 42 \pm 10\ h_{70} M_\odot/L_\odot$ for early-types, whilst $M_{200}/L_{200} = 17 \pm 9\ h_{70} M_\odot/L_\odot$ for late-types. This suggests that the difference in halo mass is not solely due to the fact that early-types reside in denser environments, but is at least partly intrinsic.

Below a stellar mass of $10^{11}\ h_{70}^{-1} M_\odot$ the halo mass of early- and late-types are comparable. For larger stellar masses, the best fit halo masses of the early-types are larger than the late-types. We computed $M_{*,200}$, the total stellar mass within r_{200}, in order to calculate the baryon conversion efficiency η. Our results for early-type galaxies suggest a variation in efficiency with a minimum of $\sim$10% for a stellar mass $M_{*,200} = 10^{12}\ h_{70}^{-1} M_\odot$. The results for the late-type galaxies are not well constrained, but do suggest a larger value.

The satellite fraction is $\sim$40% for the low luminosity (stellar mass) early-type galaxies, and decreases rapidly to $< 10\%$ with increasing luminosity (stellar mass). The satellite fraction of the late-types has a value in the range 0-15%, independent of luminosity or stellar mass. The satellite fraction is difficult to constrain at the high stellar mass/luminosity end, as the shape of the combined shear signal from the satellites mimics an NFW profile. Decreasing the truncation parameter leads to tighter constraints, and appears to be justified for the most massive early-type satellites based on the N-body simulation results of Limousin et al. (2009). Additional support comes from studying the shear signal of massive early-type galaxies that were selected to be satellites shown in Appendix 3.C, but the errors are currently too large to constrain the fraction of dark matter that is stripped. A more realistic description of the stripping of the haloes of massive satellite galaxies may result in an improvement of the constraints on the satellite fraction from weak lensing studies alone.

The halo mass appears to decrease with redshift for the highest stellar mass bins, a trend that is qualitatively in agreement with predictions from numerical simulations. The signal-to-noise on the measurements is currently too low to provide a detailed view on the growth of dark matter haloes, but it shows that with future surveys weak lensing can be used to study in great detail the evolution of the relation between baryons and dark matter.

Acknowledgements

We would like to thank Jarle Brinchman for his extensive help with the MPA/JHU catalogues, Alexie Leauthaud for useful discussions and suggestions concerning the halo model, and Thomas Erben and Hendrik Hildebrandt for their help with the THELI pipeline. Additionally, we would like to thank our colleagues at Leiden Observatory, in particular Konrad Kuijken and Elisabetta Semboloni, and Tim Schrabback, for useful suggestions and comments. Finally, we would like the anonymous referee for useful comments.

HH and EvU acknowledge support from a Marie Curie International Reintegration Grant, and from a VIDI grant from the Nederlandse Organisatie voor Wetenschappelijk Onderzoek (NWO). The RCS2 project is supported in part by grants to HKCY from the Canada Research Chairs program and the Natural Science and Engineering Research Council of Canada.

This work is based on observations obtained with MegaPrime/MegaCam, a

joint project of CFHT and CEA/DAPNIA, at the Canada-France-Hawaii Telescope (CFHT) which is operated by the National Research Council (NRC) of Canada, the Institute National des Sciences de l'Univers of the Centre National de la Recherche Scientifique of France, and the University of Hawaii. We used the facilities of the Canadian Astronomy Data Centre operated by the NRC with the support of the Canadian Space Agency.

Bibliography

Abazajian, K. N., Adelman-McCarthy, J. K., Agüeros, M. A., et al. 2009, ApJS, 182, 543

Adelman-McCarthy, J. K., Agüeros, M. A., Allam, S. S., et al. 2008, ApJS, 175, 297

Adelman-McCarthy, J. K., Agüeros, M. A., Allam, S. S., et al. 2006, ApJS, 162, 38

Agustsson, I. & Brainerd, T. G. 2006, ApJ, 644, L25

Ann, H. B., Park, C., & Choi, Y. 2008, MNRAS, 389, 86

Bartelmann, M. 1996, A&A, 313, 697

Behroozi, P. S., Conroy, C., & Wechsler, R. H. 2010, ApJ, 717, 379

Bell, E. F. & de Jong, R. S. 2001, ApJ, 550, 212

Bertin, E. 2006, in Astronomical Society of the Pacific Conference Series, Vol. 351, Astronomical Data Analysis Software and Systems XV, ed. C. Gabriel, C. Arviset, D. Ponz, & S. Enrique, 112

Bertin, E. & Arnouts, S. 1996, A&AS, 117, 393

Bertin, G., Ciotti, L., & Del Principe, M. 2002, A&A, 386, 149

Blanton, M. R., Brinkmann, J., Csabai, I., et al. 2003, AJ, 125, 2348

Blanton, M. R., Dalcanton, J., Eisenstein, D., et al. 2001, AJ, 121, 2358

Blanton, M. R. & Roweis, S. 2007, AJ, 133, 734

Blanton, M. R., Schlegel, D. J., Strauss, M. A., et al. 2005, AJ, 129, 2562

Bolton, A. S., Treu, T., Koopmans, L. V. E., et al. 2008, ApJ, 684, 248

Bower, R. G., Vernon, I., Goldstein, M., et al. 2010, MNRAS, 407, 2017

Brainerd, T. G., Blandford, R. D., & Smail, I. 1996, ApJ, 466, 623

Brown, M. J. I., Zheng, Z., White, M., et al. 2008, ApJ, 682, 937

Bruzual, G. & Charlot, S. 2003, MNRAS, 344, 1000

Cacciato, M., van den Bosch, F. C., More, S., et al. 2009, MNRAS, 394, 929

Conroy, C., Prada, F., Newman, J. A., et al. 2007, ApJ, 654, 153

Conroy, C. & Wechsler, R. H. 2009, ApJ, 696, 620

Cooray, A. & Sheth, R. 2002, Phys. Rep., 372, 1

Coupon, J., Kilbinger, M., McCracken, H. J., et al. 2011, A&A, submitted [arXiv:1107.0616]

Cresswell, J. G. & Percival, W. J. 2009, MNRAS, 392, 682

Croton, D. J., Springel, V., White, S. D. M., et al. 2006, MNRAS, 365, 11

Duffy, A. R., Schaye, J., Kay, S. T., & Dalla Vecchia, C. 2008, MNRAS, 390, L64

Eisenstein, D. J., Annis, J., Gunn, J. E., et al. 2001, AJ, 122, 2267

Emsellem, E., Cappellari, M., Krajnović, D., et al. 2007, MNRAS, 379, 401

Erben, T., Hildebrandt, H., Lerchster, M., et al. 2009, A&A, 493, 1197

Erben, T., Schirmer, M., Dietrich, J. P., et al. 2005, Astronomische Nachrichten, 326, 432

Faltenbacher, A., Li, C., Mao, S., et al. 2007, ApJ, 662, L71
Fischer, P., McKay, T. A., Sheldon, E., et al. 2000, AJ, 120, 1198
Gallazzi, A., Charlot, S., Brinchmann, J., White, S. D. M., & Tremonti, C. A. 2005, MNRAS, 362, 41
Gilbank, D. G., Gladders, M. D., Yee, H. K. C., & Hsieh, B. C. 2011, AJ, 141, 94
Giodini, S., Pierini, D., Finoguenov, A., et al. 2009, ApJ, 703, 982
Gladders, M. D. & Yee, H. K. C. 2005, ApJS, 157, 1
Grützbauch, R., Conselice, C. J., Varela, J., et al. 2011, MNRAS, 411, 929
Guo, Y., McIntosh, D. H., Mo, H. J., et al. 2009, MNRAS, 398, 1129
Guzik, J. & Seljak, U. 2001, MNRAS, 321, 439
Guzik, J. & Seljak, U. 2002, MNRAS, 335, 311
Hao, J., Kubo, J. M., Feldmann, R., et al. 2011, ApJ, 740, 39
Heymans, C., Van Waerbeke, L., Bacon, D., et al. 2006, MNRAS, 368, 1323
Hirata, C. M., Mandelbaum, R., Seljak, U., et al. 2004, MNRAS, 353, 529
Hoekstra, H., Franx, M., & Kuijken, K. 2000, ApJ, 532, 88
Hoekstra, H., Franx, M., Kuijken, K., & Squires, G. 1998, ApJ, 504, 636
Hoekstra, H., Hsieh, B. C., Yee, H. K. C., Lin, H., & Gladders, M. D. 2005, ApJ, 635, 73
Hoekstra, H., Yee, H. K. C., & Gladders, M. D. 2004, ApJ, 606, 67
Hsieh, B. C., Yee, H. K. C., Lin, H., & Gladders, M. D. 2005, ApJS, 158, 161
Ilbert, O., Arnouts, S., McCracken, H. J., et al. 2006, A&A, 457, 841
Kaiser, N., Aussel, H., Burke, B. E., et al. 2002, in Presented at the Society of Photo-Optical Instrumentation Engineers (SPIE) Conference, Vol. 4836, Society of Photo-Optical Instrumentation Engineers (SPIE) Conference Series, ed. J. A. Tyson & S. Wolff, 154–164
Kaiser, N., Squires, G., & Broadhurst, T. 1995, ApJ, 449, 460
Kauffmann, G., Heckman, T. M., White, S. D. M., et al. 2003, MNRAS, 341, 33
Kim, H., Baugh, C. M., Cole, S., Frenk, C. S., & Benson, A. J. 2009, MNRAS, 400, 1527
Koester, B. P., McKay, T. A., Annis, J., et al. 2007, ApJ, 660, 239
Komatsu, E., Dunkley, J., Nolta, M. R., et al. 2009, ApJS, 180, 330
Kovač, K., Porciani, C., Lilly, S. J., et al. 2011, ApJ, 731, 102
Kravtsov, A. V., Berlind, A. A., Wechsler, R. H., et al. 2004, ApJ, 609, 35
Kroupa, P. 2001, MNRAS, 322, 231
Leauthaud, A., Finoguenov, A., Kneib, J., et al. 2010, ApJ, 709, 97
Leauthaud, A., Tinker, J., Bundy, K., et al. 2012, ApJ, 744, 159
Limousin, M., Sommer-Larsen, J., Natarajan, P., & Milvang-Jensen, B. 2009, ApJ, 696, 1771
Luppino, G. A. & Kaiser, N. 1997, ApJ, 475, 20
Mandelbaum, R., Hirata, C. M., Seljak, U., et al. 2005a, MNRAS, 361, 1287
Mandelbaum, R., Seljak, U., Kauffmann, G., Hirata, C. M., & Brinkmann, J. 2006, MNRAS, 368, 715
Mandelbaum, R., Tasitsiomi, A., Seljak, U., Kravtsov, A. V., & Wechsler, R. H. 2005b, MNRAS, 362, 1451
Massey, R., Heymans, C., Bergé, J., et al. 2007, MNRAS, 376, 13
More, S., van den Bosch, F. C., Cacciato, M., et al. 2011, MNRAS, 410, 210
Moster, B. P., Somerville, R. S., Maulbetsch, C., et al. 2010, ApJ, 710, 903
Napolitano, N. R., Romanowsky, A. J., Coccato, L., et al. 2009, MNRAS, 393,

329
Navarro, J. F., Frenk, C. S., & White, S. D. M. 1996, ApJ, 462, 563
Neistein, E., Li, C., Khochfar, S., et al. 2011, MNRAS, 416, 1486
Padmanabhan, N., Schlegel, D. J., Finkbeiner, D. P., et al. 2008, ApJ, 674, 1217
Peacock, J. A. & Dodds, S. J. 1996, MNRAS, 280, L19
Pielorz, J., Rödiger, J., Tereno, I., & Schneider, P. 2010, A&A, 514, A79
Pozzetti, L., Bolzonella, M., Zucca, E., et al. 2010, A&A, 523, A13
Press, W. H. & Schechter, P. 1974, ApJ, 187, 425
Salim, S., Rich, R. M., Charlot, S., et al. 2007, ApJS, 173, 267
Schlegel, D. J., Finkbeiner, D. P., & Davis, M. 1998, ApJ, 500, 525
Scoville, N., Abraham, R. G., Aussel, H., et al. 2007, ApJS, 172, 38
Seljak, U. 2000, MNRAS, 318, 203
Sérsic, J. L. 1968, Atlas de galaxias australes, ed. Sérsic, J. L., Cordoba, Argentina: Observatorio Astronomico
Sheldon, E. S., Johnston, D. E., Masjedi, M., et al. 2009a, ApJ, 703, 2232
Sheldon, E. S., Johnston, D. E., Scranton, R., et al. 2009b, ApJ, 703, 2217
Sheth, R. K., Mo, H. J., & Tormen, G. 2001, MNRAS, 323, 1
Siverd, R. J., Ryden, B. S., & Gaudi, B. S. 2009, ApJ, submitted [arXiv:0903.2264]
Smith, R. E., Peacock, J. A., Jenkins, A., et al. 2003, MNRAS, 341, 1311
Somerville, R. S., Hopkins, P. F., Cox, T. J., Robertson, B. E., & Hernquist, L. 2008, MNRAS, 391, 481
Springel, V., White, S. D. M., Jenkins, A., et al. 2005, Nature, 435, 629
Strateva, I., Ivezić, Ž., Knapp, G. R., et al. 2001, AJ, 122, 1861
Strauss, M. A., Weinberg, D. H., Lupton, R. H., et al. 2002, AJ, 124, 1810
Tasitsiomi, A., Kravtsov, A. V., Wechsler, R. H., & Primack, J. R. 2004, ApJ, 614, 533
Tinker, J. L., Weinberg, D. H., Zheng, Z., & Zehavi, I. 2005, ApJ, 631, 41
Vulcani, B., Poggianti, B. M., Aragón-Salamanca, A., et al. 2011, MNRAS, 412, 246
Wang, L., Li, C., Kauffmann, G., & De Lucia, G. 2006, MNRAS, 371, 537
Wright, C. O. & Brainerd, T. G. 2000, ApJ, 534, 34
York, D. G., Adelman, J., Anderson, Jr., J. E., et al. 2000, AJ, 120, 1579
Zheng, Z., Berlind, A. A., Weinberg, D. H., et al. 2005, ApJ, 633, 791

Appendices

3.A Scatter of lenses between bins

In this Appendix we describe how we calculate the bias that results from the scatter of galaxies between lensing bins due to the stellar mass errors. The bias that results from the scatter due to the luminosity errors has been calculated in a similar fashion. To begin, we create a large set of simulated lens catalogues. We construct the stellar mass function from the MPA/JHU catalogue, randomly draw stellar masses from this distribution and assign these to our lenses. We fit a powerlaw of the form $M_{200} = \alpha_* M_*^{\beta_*}$ to our initial observations, and calculate the halo mass of each galaxy. Assuming that the density profile of each lens follows an NFW profile, we calculate the ellipticities of the source galaxies under the assumption that they are intrinsically round. Next we create 20 new lens catalogues by applying a log-normal scatter with a width of 0.1 to the stellar masses. We use the stellar mass bins from Table 3.3 to stack the lensing signal of the scattered lenses, and measure the tangential shear using the original source catalogue. We fit the lensing signal between 30 and 200 h_{70}^{-1} kpc with the halo model, imposing a satellite fraction of 0% as the lenses were randomly inserted in the images. The ratio of the best fit halo masses for the original lenses and the lenses with scattered stellar masses gives the bias.

As the stellar mass function and the best fit powerlaw are different for the two galaxy types, we make two sets of simulations to study the bias for early- and late-type galaxies separately. We do not account for evolution with redshift, although the stellar mass function evolves between $z = 0.0$ and $z = 1.0$, most strongly for $M_* < 10^{11}\ h_{70}^{-1} M_\odot$ (e.g. Vulcani et al. 2011; Pozzetti et al. 2010). We are only sensitive to the change of the shape of the stellar mass function, which is most noticeable for $10^{10.5} < M_* < 10^{11}\ h_{70}^{-1} M_\odot$. However, the bias in this regime is small, and we do not expect the change in shape to strongly affect our results. The relation between stellar mass and halo mass may also evolve between $z = 0.0$ and $z = 0.5$ (e.g. Moster et al. 2010; Leauthaud et al. 2012). We currently lack sufficient signal-to-noise to study this in detail. As we will demonstrate, the bias is not very sensitive to changes in the powerlaw slope, and a mild evolution does not significantly alter the results.

The ratio of the input halo masses to the best fit halo mass measured for the lenses that have been scattered is shown in Figure 3.19. The error bars indicate the standard deviation of the simulations. We find that the bias is highest for the early-types at the high mass end. This is due to the steepness of the stellar mass function, which leads to the net effect that low stellar mass objects scatter into and contaminate the high stellar mass bins. The bias for early-types at the low mass end is slightly smaller than 1, as the stellar mass function turns over at $\sim 5 \times 10^{10}\ h_{70}^{-1} M_*$ and becomes smaller with decreasing stellar mass. The stellar mass function of the late-types is monotonically decreasing, and consequently the bias does not become smaller than unity. At the high mass end, the stellar mass function of the late-types is poorly determined due to the lack of objects. We cannot reliably determine the bias for the S6 late-type bin, and therefore apply the correction factor of the S5 bin to this bin as well.

The observed stellar masses have already been scattered, and the best fit powerlaw is therefore too shallow. To investigate how this affects the bias, we

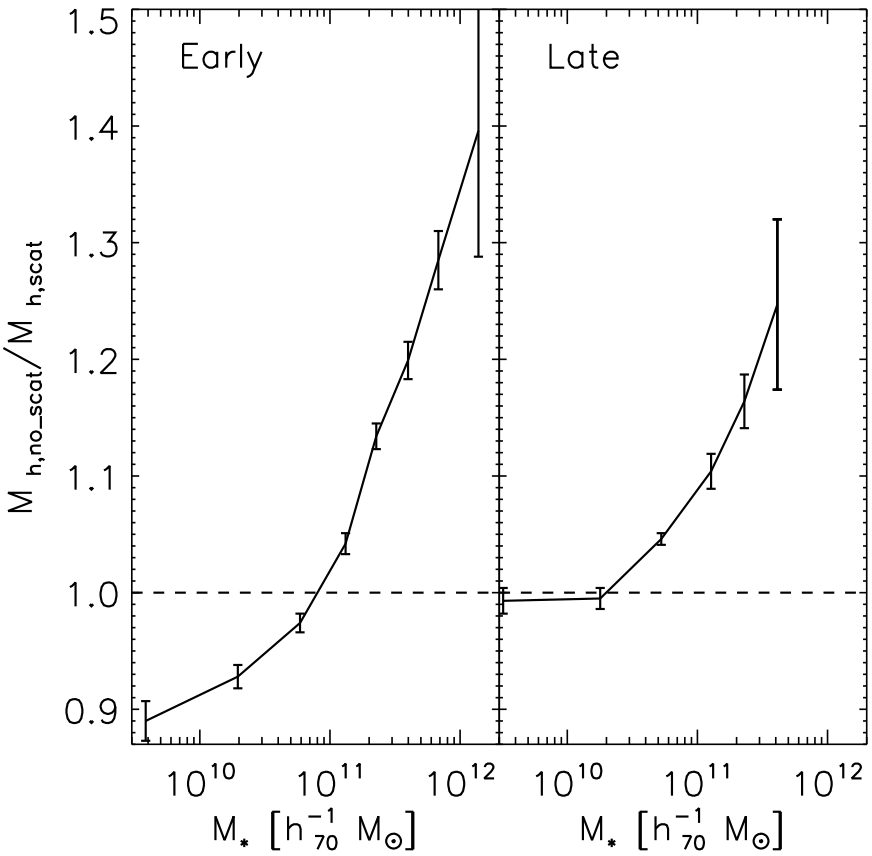

Figure 3.19: Ratio of the best fit halo mass for the unscattered lens catalogue to the best fit halo mass for the lenses to which a log-normal scatter of 0.1 in stellar mass has been applied, for the early-type galaxies (*left*) and the late-type galaxies (*right*). The halo masses are underestimated at the high stellar mass end due to low mass objects scattering into the high mass bins.

correct our initial halo masses for the scattering, and again fit a powerlaw between stellar mass and halo mass. We repeat our simulations with these new powerlaw slopes, and find that the correction factors change by at most 4%. The correction we apply is obtained using the corrected powerlaw slopes.

The intrinsic stellar mass function is steeper than the observed one as on average more low stellar mass objects have scattered upward. Although we cannot retrieve the intrinsic stellar mass function, we can obtain an estimate of the level of contamination. For this purpose, we draw 1×10^8 objects from the observed stellar mass function, apply the log-normal scatter, and compare the number of objects in the stellar mass bins before and after the scatter. The number of lenses in the three lowest stellar mass bins does not change much after the scatter, but it increases with stellar mass for the more massive bins, reaching a maximum of 36% more lenses in the S7 early-type bin. The increase

in the number of objects may be even larger, as the observed stellar masses have already been scattered, and therefore the observed stellar mass function is smoother than the intrinsic one. As the stellar mass function at the high mass end is already very uncertain, we do not attempt to retrieve the intrinsic stellar mass function. However, the bias correction is sensitive to the slope at the high mass end, and the correction factors may actually be larger.

3.B Mean versus fitted halo mass

The distribution of halo masses for a certain luminosity (or stellar mass) is given by the conditional probability function, which is usually described by a log-normal function of the form

$$P(m_h|l) \propto \exp\Big(-\frac{(m_h - m_{h,cent})^2}{2\sigma^2_{m_h}}\Big) \tag{3.22}$$

where $l = \log(L)$, $m_h = \log(M_h)$ and σ_{m_h} is the scatter in m_h. In this Appendix we study how the best fit lensing mass is related to either the mean halo mass or to the centre of the halo mass distribution, $m_{h,cent}$. To mimic the selection of real galaxies, we assign a value to $m_{h,cent}$ and σ_{m_h}, and randomly draw 1000 galaxies from the conditional probability function which has been convolved with the halo mass function (Equation 3.10). We calculate the NFW shear profiles of these galaxies, average their signals to simulate the usual lensing procedure, and fit an NFW profile to the stacked shear. Figure 3.20 shows the ratio of $M_{h,cent}$ to the best fit NFW mass in the top panel, and the ratio of the mean halo mass to the best fit NFW mass in the lower panel. The lines correspond to different values of σ_{m_h}, ranging from 0.10 to 0.40 from bottom to top. Note that the scale of the vertical axes in the two panels is different.

In Figure 3.20a we see that the best fit NFW mass is considerably lower than the central mass of the distribution. This is mainly the result of the declining halo mass function, which leads us to preferentially pick lower mass haloes. The shape of an NFW profile changes with halo mass because the NFW concentration parameter depends on halo mass. The shape and amplitude of the stacked shear signal is therefore not equal to the profile of an NFW with a corresponding mean halo mass. Therefore, the best fit NFW mass underestimates the mean halo mass, as demonstrated in Figure 3.20b.

The ratios in Figure 3.20a and 3.20b are sensitive to the value of σ_{m_h}. We use the results from More et al. (2011), who studied the distribution of halo masses as a function of luminosity and stellar mass using the kinematics of satellite galaxies orbiting central galaxies. As only central galaxies are considered in their work, the actual scatter for a sample of galaxies consisting of both centrals and satellites may be larger. On the other hand, part of the scatter may be introduced through uncertainties in the determination of the halo masses, which would imply a lower intrinsic scatter.

We use Figures 4 and 9 from More et al. (2011) to read off the values we assign to σ_{m_h} for the luminosity and stellar mass bins. We list these values, and the corresponding correction factor to the mean halo mass, in Table 3.4. The luminosities and stellar masses in our sample extend to higher values than More et al. (2011) use, but their figures suggest that σ_{m_h} does not change rapidly at

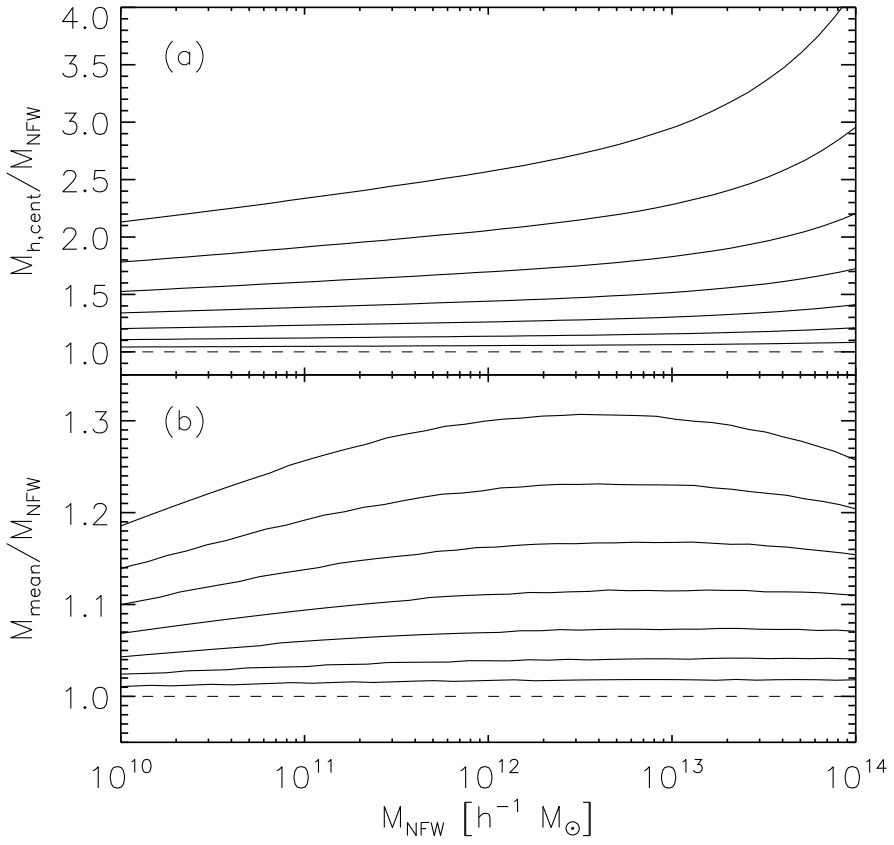

Figure 3.20: Ratio of the central mass of the halo mass distribution, $m_{h,cent}$, and the best fit NFW mass (*top*) and the ratio of the mean halo mass and the best fit NFW mass (*bottom*) as a function of best fit NFW mass. Different lines correspond to values of σ_{m_h} 0.10 (bottom line), 0.15, 0.20, 0.25, 0.30, 0.35 and 0.40 (top line). The lensing mass is converted to the mean halo mass using the corrections from the bottom panel.

the high mass/luminosity end, and we therefore assume that the values remain constant. For the stellar masses we use the NFW masses that have been corrected for the scattering of objects between the bins.

There are further sources of uncertainty to consider in future studies, and we list a few of them: luminosity bins have a certain width, the luminosity function is not constant inside a luminosity bin, and lens galaxies are located at a range of redshifts. We expect that these complications further broaden the conditional probability function, which means that the correction factors we use may be too low. These complications should be taken into account to enable a detailed comparison between observations and simulations.

Table 3.4: Values of σ_{m_h} assigned to the luminosity and stellar mass bins, and the correction factors f_{corr} we apply to convert the measured lensing mass into the mean halo mass.

Sample	σ_{m_h}(early)	f_{corr}(early)	σ_{m_h}(late)	f_{corr}(late)
L1	0.20	1.07	0.25	1.10
L2	0.25	1.11	0.29	1.14
L3	0.30	1.17	0.30	1.15
L4	0.33	1.20	0.33	1.20
L5	0.37	1.26	0.34	1.21
L6	0.39	1.28	0.35	1.23
L7	0.40	1.28	0.35	1.22
L8	0.40	1.27	0.35	1.23
S1	0.15	1.03	0.10	1.01
S2	0.18	1.06	0.10	1.02
S3	0.26	1.12	0.10	1.02
S4	0.32	1.19	0.10	1.02
S5	0.36	1.24	0.10	1.02
S6	0.40	1.28	0.10	1.02
S7	0.40	1.27	-	-

3.C Constraints on the satellite fraction at high halo masses

The satellite fraction is not well constrained at the high luminosity/stellar mass end. The reason for this is illustrated in Figure 3.21. In Figure 3.21a we show the lensing signal of the L6 luminosity bin, together with the five terms of the halo model, using the standard truncation radius of $0.4r_{200}$ for the satellite galaxies. The satellite shear signal on scales $< 1.5\ h_{70}^{-1}$Mpc in the halo model is the sum of stripped satellite term and the $\gamma_{t,sat}^{1h}$ term. It is clear that the shape of the combined signal is very similar to the shape of the shear signal coming from the central halo. As a result the error on the satellite fraction is large. The satellite fraction and the halo mass are anti-correlated, as we can see from Figure 3.22. The model either prefers a large mass and small satellite fraction, or a small mass and large satellite fraction. To reduce any bias in the best fit halo mass, we decrease the allowed range for the satellite fractions to a uniform prior between 0% and 20% for the highest stellar mass and luminosity bins, as almost all of the galaxies in these bins are expected to be centrals.

Recent work by Limousin et al. (2009) shows that the half mass radius of a subhalo is a strongly decreasing function of projected cluster-centric distance. Furthermore, the radial distribution of early-type satellites is more peaked around the cluster centre than the radial distribution of late-type satellites (e.g. Ann et al. 2008). Hence we expect that the massive elliptical satellite galaxies, which practically always reside close to the centre of a cluster, are stripped of a

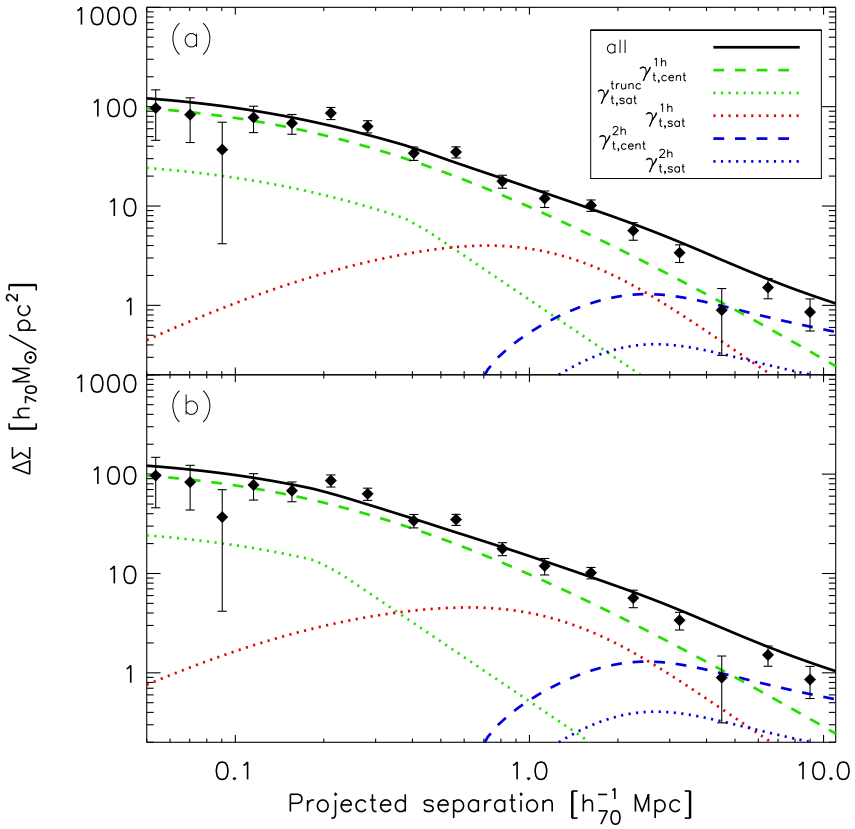

Figure 3.21: Lensing signal of the L6 early-type bin, shown together with the five components of the best fit halo model. In the upper panel the truncation radius of the stripped satellites is $0.4r_{200}$, and the shape of the combined satellite 1-halo terms mimicks the shape of the central NFW term. In the lower panel the truncation radius is $0.2r_{200}$, changing the shape of the combined satellite 1-halo terms. Note that the halo model in the lower panel is not a fit, but serves to illustrate the effect of choosing a different truncation radius.

far larger fraction of their dark matter.

To determine whether we can observe a change in the truncation radius of massive early-type satellite galaxies, we make a selection of galaxies that are likely to be satellites and study their shear profile. We consider early-types in the mass range $10^{10.5} < M_* < 10^{11.75}\ h_{70}^{-1}M_\odot$, and divide them in three mass bins; galaxies more massive than $10^{11.75}\ h_{70}^{-1}M_\odot$ will almost exclusively be central galaxies and hence not significantly stripped. To determine whether the galaxies are satellites or centrals, we use the SDSS DR7 photometric redshift catalogue *Photoz*, which contains the photometric redshifts of 260 million galaxies, and match them to our source galaxy catalogue. The lenses that have a neighbouring galaxy of the same luminosity or brighter within 750 h_{70}^{-1}kpc, and

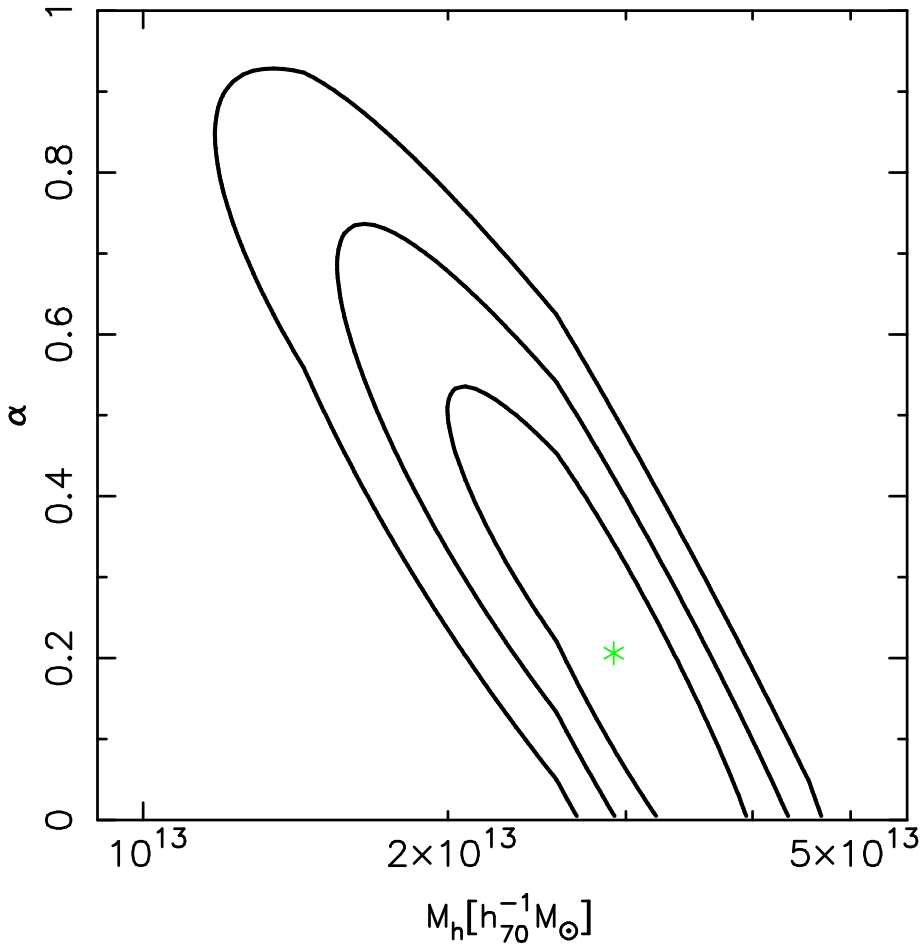

Figure 3.22: χ^2 values of the halo model fits to the L6 early-type bin. The green star indicates the best fit. The three contours show the 67.8%, 95.4% and 99.7% confidence intervals ($\Delta\chi^2$ of 2.3, 6.2 and 11.8 respectively). The best fit halo mass is anti-correlated with the best fit satellite fraction.

lie within the 1σ errors of the photometric redshift of the source, are selected for the satellite sample. The galaxies that do not have brighter neighbours within 1 h_{70}^{-1}Mpc and within the 1σ errors of the photometric redshift are selected for the central sample. Note that we do not aim to obtain samples that are complete, but we strive to make a selection that enables us to quantitatively study the differences in the lensing signal.

In Figure 3.23 we show the stacked shear signal of the galaxies, for the central sample and for the satellite sample, together with their halo model components. The shear signals of the central sample are indeed described well by an NFW profile. The galaxies preferentially live in isolated environments, and consequently the $\gamma_{t,\mathrm{cent}}^{2h}$ term is overestimated. The halo model fits of the satellite sample are dominated by the satellite terms, as can be observed from the best fit satellite fractions indicated in the plot. The shear signal around 100 h_{70}^{-1}kpc is different from the signal of the central sample at the same scale, and is lower

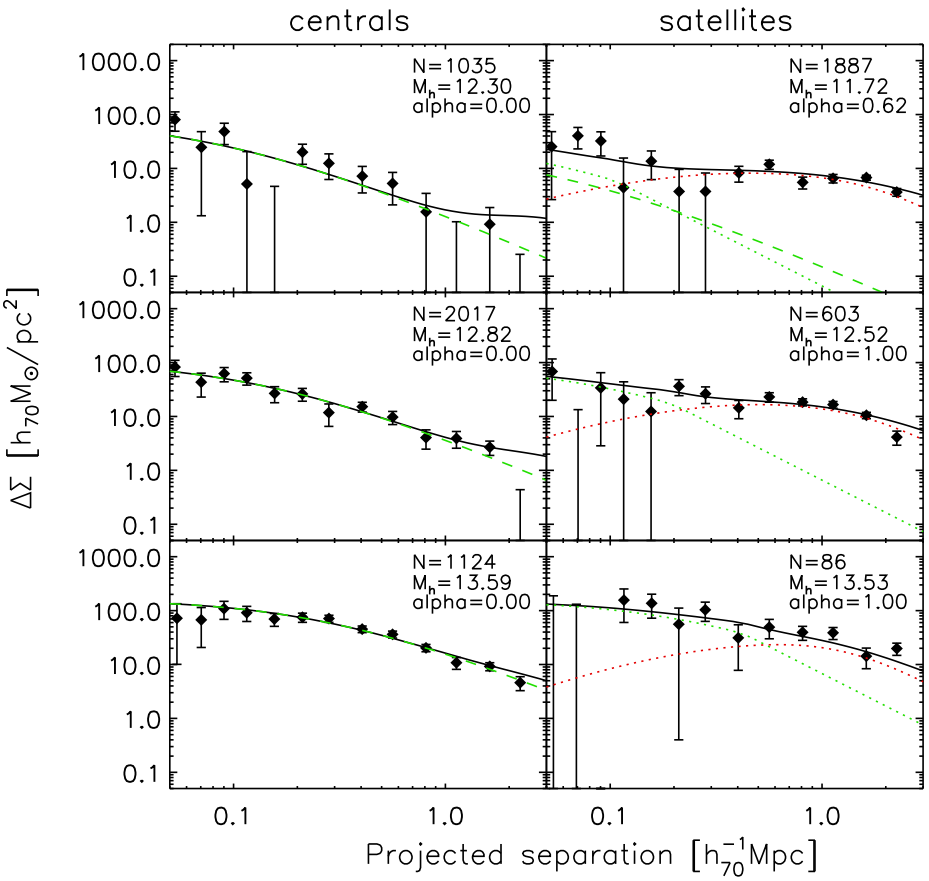

Figure 3.23: Lensing signal $\Delta\Sigma$ as a function of physical distance from the lens. The lensing signal is measured for central galaxies (*left*) and for the satellite galaxies (*right*), for the $10^{10.5} < M_* < 10^{11.0}$ $h_{70}^{-1}M_\odot$ bin (*top*), $10^{11.0} < M_* < 10^{11.5}$ $h_{70}^{-1}M_\odot$ bin (*middle*) and $10^{11.5} < M_* < 10^{11.75}$ $h_{70}^{-1}M_\odot$ bin (*bottom*). Indicated in each plot is the number of lenses, the logarithm of the best fit halo mass in units of $h_{70}^{-1}M_\odot$ and the best fit satellite fraction. The shear signal is reduced at large lens-source separations for the central galaxies, indicating that they are isolated. At small lens-source separations the shear signal of the satellite sample appears to be reduced compared to the central sample. Note that the 2-halo terms are not shown for clarity.

than the halo model fit. This suggests that additional stripping of dark matter occurs at small scales. The measurements are too noisy, however, to constrain which fraction of the dark matter haloes is stripped.

To illustrate the impact the choice of truncation radius has on the best fit satellite fractions, we also consider stripped satellite profiles with a truncation radius of $0.2r_{200}$. In Figure 3.21b we show the shear signal of the same bin, but with this smaller truncation radius. Note that the halo model parameters are identical in both panels for illustrative purposes, and that the model in the

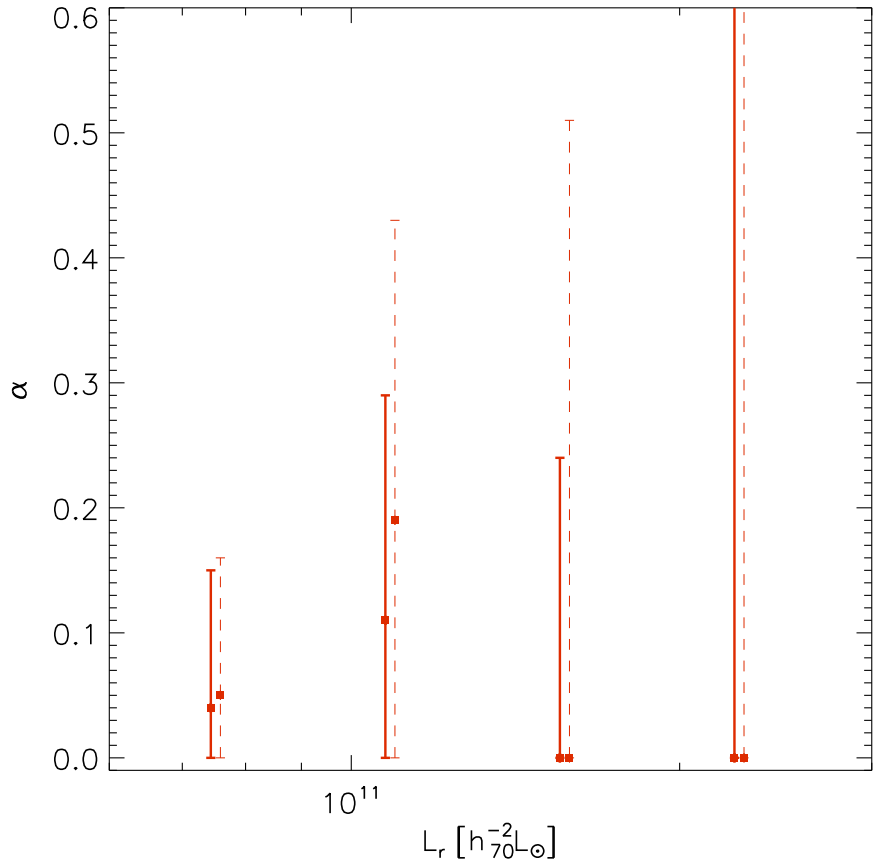

Figure 3.24: Best fit satellite fraction for the four highest luminosity bins of early-types. The thick solid (thin dashed) lines indicate the results determined using a truncation radius of $0.2r_{200}$ ($0.4r_{200}$). Decreasing the truncation radius tightens the constraints on the satellite fraction.

lower panel is not a fit. The shear signal of the satellites at small scales is now clearly different from the central halo term, and the satellite fraction can be better constrained. We have also fit halo models with a truncation radius of $0.2r_{200}$ to the four most luminous early-type bins. The constraints on the satellite fraction for both models are shown in Figure 3.24. The satellite fraction is better constrained for the models with a truncation radius of $0.2r_{200}$. Setting the truncation radius to $0.2r_{200}$ is a rather arbitrary choice, however, and in future studies it is necessary to include a more realistic prescription for the stripping of the satellites.

Mandelbaum et al. (2006) study the environmental dependence of the shear profile as a function of luminosity. They distinguish galaxies residing in a high-density environment and in a low-density environment. The brightest galaxies of their low-density sample are almost exclusively centrals, whilst in the high-density sample they are a mixture of centrals and satellites. As the lensing

signal is then an average of the shear profiles from satellites and centrals, this may explain why they do not observe a reduction of the signal at small scales. Note that the satellite galaxies we study are more massive, and hence are expected to reside in denser environments where the haloes are stripped of a larger fraction of their dark matter content.

4

Stellar mass versus velocity dispersion as tracer of the lensing signal around galaxies

We present the results of a weak gravitational lensing analysis to determine whether the stellar mass or the velocity dispersion is more closely related to the amplitude of the lensing signal around galaxies - and hence to the projected distribution of dark matter. The lensing signal on small scales corresponds most closely to the lensing velocity dispersion in the case of a singular isothermal profile, but is on larger scales also sensitive to the clustering of the haloes. We select over 4000 lens galaxies at a redshift $z < 0.2$ with de Vaucouleur surface brightness profiles that reside in the $\sim$300 square degree overlap between the Red Sequence Cluster Survey 2 (RCS2) and the data release 7 (DR7) of the Sloan Digital Sky Survey (SDSS). We consider both the spectroscopic velocity dispersion and the model velocity dispersion (a combination of the stellar mass, the size and the Sérsic index of a galaxy). The latter is thought to be a more reliable velocity dispersion estimator because it is calculated using quantities that are more robustly determined in the SDSS than the spectroscopic velocity dispersion. Comparing the model and spectroscopic velocity dispersion we find that they correlate well for de Vaucouleur-type galaxies. We find that the stellar mass and the spectroscopic velocity dispersion trace the amplitude of the lensing signal on small scales equally well. The model velocity dispersion, however, does significantly worse. A possible explanation is that the halo properties that determine the small-scale lensing signal - mainly the total mass - also depend on the structural parameters of galaxies, such as the effective radius and Sérsic index. We need, however, a larger lens sample to explore which combination of galaxy properties fully determine the distribution of dark matter around galaxies, which will provide valuable insights into galaxy formation processes.

E. van Uitert, H. Hoekstra, M. Franx, D.G. Gilbank, M.D. Gladders, H.K.C. Yee, to be submitted;

4.1 Introduction

Galaxies form and evolve in the gravitational potentials of large dark matter haloes. The physical processes that drive galaxy formation cause correlations between the properties of the galaxies and their dark matter haloes. Hence to gain insight into these processes, various properties of galaxies (e.g. colour, metallicity, stellar mass, luminosity, velocity dispersion) can be observed and compared (e.g. Smith et al. 2009; Graves et al. 2009). This has lead to the discovery of a large number of empirical scaling laws, such as the Faber-Jackson relation (Faber & Jackson 1976). These scaling laws help us to disentangle the processes that govern galaxy formation, and serve as important constraints for the theoretical and numerical efforts in this field. Although much progress has been made over the last few decades, many details are still unclear and warrant further investigation.

One key parameter in galaxy formation is thought to be the total mass of a galaxy. Galaxies that have more massive dark matter haloes than others attract more baryons as well, consequently form more stars which results in larger stellar masses. The relation between the stellar mass and the total mass of galaxies has been the subject of various studies based on observations (e.g. Mandelbaum et al. 2006; van Uitert et al. 2011; Leauthaud et al. 2012; More et al. 2011; Wake et al. 2011) and simulations (e.g. Guo et al. 2010; Moster et al. 2010), and the two components are indeed found to be correlated. Another property of galaxies that is related to the total mass is the velocity dispersion, the luminosity weighted dispersion of the motions of stars along the line-of-sight within a spectroscopic aperture. The velocity dispersion provides a dynamical estimate of the central mass, and correlates with the stellar mass (Taylor et al. 2010) and the total mass of galaxies (van Uitert et al. 2011).

A fundamental question that is of interest in this context is which property of galaxies is most tightly correlated to the total mass. This is interesting, because it shows which property in the centre of dark matter haloes is most intimately linked to the large-scale potential, and is therefore least sensitive to galaxy formation processes such as galaxy mergers and supernova activity that introduce scatter in these relations. The properties of galaxies we compare in this work are the stellar mass and the velocity dispersion. Note that there are various other observables that trace the total mass, and could have been used instead, but most of them are either expected to exhibit a large amount of scatter (e.g. metallicity), or they are directly related to the stellar mass (e.g. luminosity).

The total mass of galaxies is not directly observable, and can only be determined by indirect means. An excellent tool to do this is via weak gravitational lensing. In weak lensing the distortion of the images of faint background galaxies (sources) due to the gravitational potentials of intervening structures (lenses) is measured. From this distortion, the differential surface mass density of the lenses can be deduced, which can be modelled to obtain the total mass. A major advantage of gravitational lensing over other methods that aim to determine the total mass is that it does not rely on optical tracers. Dark matter haloes of galaxies generally extend over hundreds of kpcs, but at large distances no optical tracers can be used. This complicates studies that rely on optical tracers to determine the total mass. This does not affect weak lensing, as the distortion can be measured for any galaxy, out to very large radii (several Mpcs).

The major disadvantage of weak lensing is that the lensing signal of individual galaxies is too weak to detect as the induced distortions are typically 10-100 times smaller than the intrinsic ellipticities of galaxies. Therefore, the signal has to be averaged over hundreds or thousands of lenses to yield a useful signal. However, the average total mass for a certain selection of galaxies is still a very useful measurement, which can be compared to simulations.

It is important to note that the lensing signal on small and large scales measures different properties of the dark matter haloes. On small scales, within the virial radius, the lensing signal traces the dark matter distribution of the halo that hosts the galaxy and is therefore directly related to the halo mass. On projected separations larger than a few times the virial radius, however, the lensing signal is mainly determined by neighbouring structures, and therefore depends on the clustering properties of the lens sample under investigation. In this work, we ignore the lensing signal at large scales and focus at the signal at small scales, which mainly depends on the halo mass of galaxies.

The outline of this work is as follows. In Section 4.2, we discuss the various steps of the lensing analysis: we start with a description of the lens selection, then provide a brief outline of the creation of the shape measurement catalogues, and finally discuss the lensing analysis. The measurements are shown in Section 4.3, and we conclude in Section 4.4. Throughout the paper we assume a WMAP7 cosmology (Komatsu et al. 2011) with $\sigma_8 = 0.8$, $\Omega_\Lambda = 0.73$, $\Omega_M = 0.27$, $\Omega_b = 0.046$ and $h = 0.7$ the dimensionless Hubble parameter. All distances quoted are in physical (rather than comoving) units unless explicitly stated otherwise.

4.2 Lensing analysis

In this study we use the ∼300 square degrees of overlapping area between the Sloan Digital Sky Survey (SDSS; York et al. 2000) and the Red Sequence Cluster Survey 2 (RCS2; Gilbank et al. 2011). We use the SDSS to obtain the properties of the lenses (e.g. stellar mass, velocity dispersion), information that is not available in the RCS2. The lensing analysis is performed on the RCS2, because it is ∼2 magnitudes deeper than the SDSS in r'. The increase in depth combined with a median seeing of $0.7''$, which is a factor of two smaller than the seeing in the SDSS, results in a source galaxy number density that is about five times higher, and a source redshift distribution that peaks at z∼0.7. Therefore, the RCS2 enables a high-quality detection of the lensing signal, even for a moderate number of lens galaxies.

4.2.1 Lenses

The SDSS has imaged roughly a quarter of the entire sky, and has measured the spectra for about one million galaxies (Eisenstein et al. 2001; Strauss et al. 2002). The combination of spectroscopic coverage and photometry in five optical bands (u, g, r, i, z) in the SDSS provides a wealth of galaxy information that is not available from the RCS2. To use this information, but also benefit from the improved lensing quality of the RCS2, we use the 300 square degrees overlap between the surveys for our analysis. We match the RCS2 catalogues to the DR7 (Abazajian et al. 2009) spectroscopic catalogue, to the MPA-JHU

DR7[1] stellar mass catalogue and to the NYU Value Added Galaxy Catalogue (NYU-VAGC)[2] (Blanton et al. 2005; Adelman-McCarthy et al. 2008; Padmanabhan et al. 2008) which yields the spectroscopic redshifts, velocity dispersions, and the stellar masses of 1.7×10^4 galaxies. From these galaxies we select our lenses using criteria that are detailed below.

The spectroscopic fibre within which the velocity dispersion is measured has a fixed size. The physical region where the velocity dispersion is averaged is therefore different for a sample of galaxies with different sizes and redshifts. To account for this, we follow Bezanson et al. (2011) and scale the observed spectroscopic velocity dispersion to a fixed size of $R_e/8$ using $\sigma_{\rm spec} = \sigma^{\rm ap}_{\rm spec}(8.0 r_{\rm ap}/R_e)^{0.066}$, with $r_{\rm ap}$=1.5″ the radius of the SDSS spectroscopic fiber, R_e the effective radius in the r-band, and $\sigma^{\rm ap}_{\rm spec}$ the observed velocity dispersion. This correction is based on the best-fit relation determined using 40 galaxies in the SAURON sample (Cappellari et al. 2006). However, the spectroscopic velocity dispersions provided in the DR7 spectroscopic catalogues are generally noisy for exponential galaxies. To obtain more reliable velocity dispersion estimates for these galaxies, we also predict the velocity dispersion based on quantities that are more robustly determined following Bezanson et al. (2011):

$$\sigma_{\rm mod} = \sqrt{\frac{GM_*}{0.557 K_V(n) R_e}} \tag{4.1}$$

with M_* the stellar mass, n the Sérsic index and $K_V(n)$ a term that includes the effects of structure on stellar dynamics, and can be approximated by (Bertin et al. 2002)

$$K_V(n) \cong \frac{73.32}{10.465 + (n - 0.94)^2} + 0.954. \tag{4.2}$$

The equation for $\sigma_{\rm mod}$ is based on the results of Taylor et al. (2010), who demonstrated that the structure-corrected dynamical mass is linearly related to the stellar mass for a selection of low-redshift galaxies in the SDSS.

The stellar mass estimates in the MPA-JHU DR7 catalogues are based on the model magnitudes. The Sérsic index and the effective radius in Equation (4.1), however, correspond to a different flux, i.e. the Sérsic model flux, which is the total flux of the best fit Sérsic model. This flux is also provided in the NYU-VAGC catalogue, and differs slightly from the model flux. To calculate $\sigma_{\rm mod}$ consistently, we therefore scale the stellar mass with the ratio of the model flux to the Sérsic model flux.

Bezanson et al. (2011) find that the model and the observed velocity dispersion correlate very well in the range 60 km s^{-1} $< \sigma <$ 300 km s^{-1}, for galaxies in the redshift range $0.05 < z < 0.07$, and for a few galaxies with redshifts $1 < z < 2.5$. The SDSS spectroscopic sample extends to $z \sim 0.5$, and therefore contains many more massive galaxies. To determine whether the velocity dispersions correlate well in this range too, we compare the dispersions for the complete SDSS spectroscopic sample in Figure 4.1. We find that the velocity dispersions agree well, though at $z > 0.2$ the range in velocity dispersion becomes too small to assess whether the velocity dispersions are still correlated.

To study whether the spectroscopic velocity dispersion and the model

[1] http://www.mpa-garching.mpg.de/SDSS/DR7/
[2] http://sdss.physics.nyu.edu/vagc/

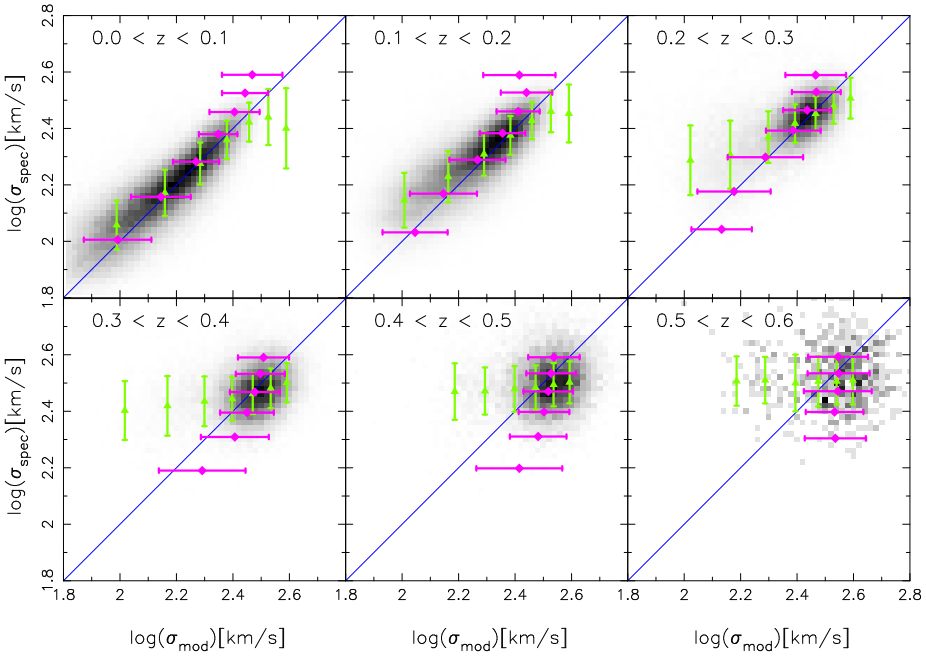

Figure 4.1: Comparison of the spectroscopic velocity dispersions to the model velocity dispersions for all galaxies with SDSS spectroscopy. The green triangles show the average spectroscopic velocity dispersion for bins of model velocity dispersion, the purple diamonds show the average model velocity dispersion for bins of spectroscopic velocity dispersion. The error bars indicate the scatter. The blue line shows the one-to-one correspondence. Only galaxies with a spectroscopic velocity dispersion error smaller than 15% have been used in the comparison. The velocity dispersions correlate well at $z < 0.2$, but at $z > 0.2$ the range in velocity dispersion becomes too small to assess whether this is still the case .

velocity dispersion agree equally well for de Vaucouleur and exponential galaxies, we split the galaxies based on their *frac_dev* parameter from the SDSS photometric catalogues. This parameter is determined by simultaneously fitting $frac\_deV$ times the best-fitting De Vaucouleur profile plus (1-$frac\_deV$) times the best-fitting exponential profile to an object's brightness profile. The *frac_dev* parameter is therefore a measure of the slope of the brightness profile of a galaxy; galaxies with *frac_dev* > 0.5 predominantly have a de Vaucouleurs profile, and *frac_dev* < 0.5 an exponential profile. We select all galaxies with redshifts $z < 0.2$, and show the comparison in Figure 4.2. We find that for the de Vaucouleur galaxies, the spectroscopic and model velocity dispersion agree very well. For the exponentials, however, we find that the spectroscopic velocity dispersion is $\sim$0.1 dex higher than the model velocity dispersion. This is not surprising: Taylor et al. (2010) found that the relation between the stellar mass and the structure-corrected dynamical mass has a weak dependence on the Sérsic index, i.e. the ratio of the stellar mass and the dynamical mass increases with increasing Sérsic index (see Figure 14 in Taylor et al. 2010). The offset in the relation between spectroscopic and model velocity dispersion for exponen-

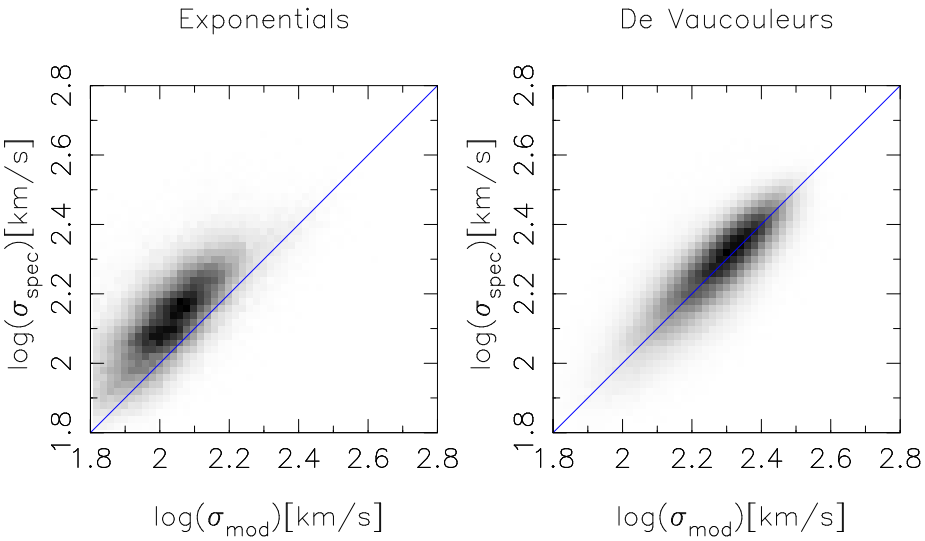

Figure 4.2: Comparison of the spectroscopic velocity dispersions to the model velocity dispersions for exponential galaxies (*left*) and de Vaucouleur galaxies (*right*) in the redshift range $0 < z < 0.2$. For de Vaucouleurs, the dispersions agree very well, but for exponential galaxies, we find that the spectroscopic velocity dispersion is roughly 0.1 dex higher than the model velocity dispersion.

tial galaxies is a direct consequence. It might be caused by the contribution of the disk velocity of spiral galaxies to the spectroscopic velocity dispersion. One could in principle apply a Sérsic index dependent correction, but we choose to use only de Vaucouleur galaxies, because there are very few exponentials in the velocity dispersion range we are interested in.

In Figure 4.3, we plot the spectroscopic and model velocity dispersion as a function of stellar mass. We only select galaxies with redshifts $z < 0.2$; at higher redshifts, the range in velocity dispersions is too small to establish whether the correlation works well. The three lens samples we use are indicated by the dashed lines. We select all de Vaucouleur galaxies with a stellar mass $10.8 < \log(M_*) < 11.5$ in units of $h_{70}^{-1} M_\odot$; all de Vaucouleur galaxies with a model velocity dispersion 180 km s^{-1} $< \sigma_{\rm mod} <$ 300 km s^{-1}; and all de Vaucouleurs with a spectroscopic velocity dispersion 200 km s^{-1} $< \sigma_{\rm spec} <$ 300 km s^{-1} and $\delta\sigma_{\rm spec}/\sigma_{\rm spec} < 0.15$. With these criteria we select 4735, 4218 and 4317 lenses respectively, and they form the lens samples of this study.

4.2.2 Data reduction

The RCS2 is a nearly 900 square degree imaging survey in three bands (g', r' and z') carried out with the Canada-France-Hawaii Telescope (CFHT) using the 1 square degree camera MegaCam. The photometric calibration of the RCS2 is described in detail in Gilbank et al. (2011). The magnitudes are calibrated using the colours of the stellar locus and the overlapping Two-Micron All-Sky Survey (2MASS), and are accurate to < 0.03 mag in each band compared to the SDSS. The creation of the galaxy shape catalogues is described in detail in van Uitert et al. (2011). We refer readers to that paper for more detail, and present

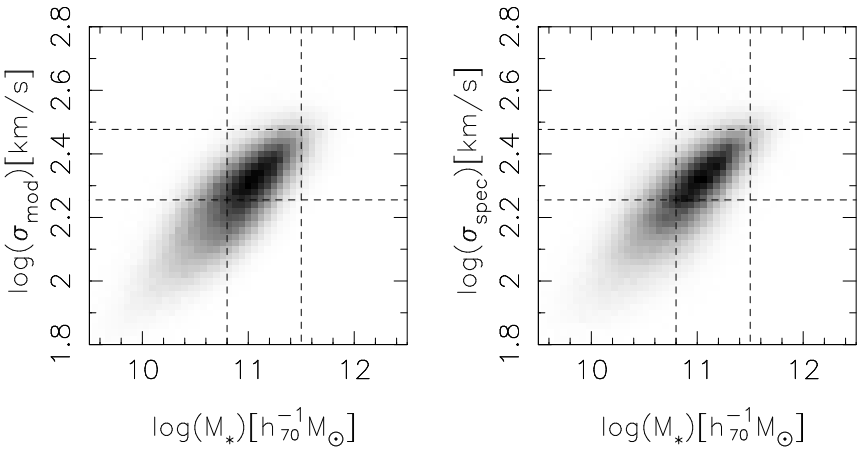

Figure 4.3: Model velocity dispersion (*left*) and spectroscopic velocity dispersion (*right*) as a function of stellar mass. The dashed lines indicate the selection cuts for the lenses.

here a short summary of the most important steps.

We retrieve the Elixir[3] processed images from the Canadian Astronomy Data Centre (CADC) archive[4]. We use the THELI pipeline (Erben et al. 2005, 2009) to subtract the image backgrounds, create weight maps that we use in the object detection phase, and to identify satellite and asteroid trails. To detect the objects in the images, we use `SExtractor` (Bertin & Arnouts 1996). The stars that are used to model the PSF variation across the image are selected using size-magnitude diagrams. All objects larger than 1.2 times the local size of the PSF are identified as galaxies. We measure the shapes of the galaxies with the KSB method (Kaiser et al. 1995; Luppino & Kaiser 1997; Hoekstra et al. 1998), using the implementation described by Hoekstra et al. (1998, 2000). This implementation has been tested on simulated images as part of the Shear Testing Programme (STEP) 1 and 2 (the 'HH' method in Heymans et al. 2006 and Massey et al. 2007 respectively), and these tests have shown that it reliably measures the unconvolved shapes of galaxies for a variety of PSFs. Finally, we correct the source ellipticities for camera shear, a false shear signal which originates from slight non-linearities in the camera optics. The resulting shape catalogue of the RCS2 contains the ellipticities of 2.2×10^7 galaxies, from which we select the subset of approximately 1×10^7 galaxies that coincides with the SDSS.

4.2.3 Lensing measurement

In weak lensing, the ellipticities of the source galaxies are used to measure the azimuthally averaged tangential shear around the lenses as a function of projected separation:

$$\langle\gamma_t\rangle(r) = \frac{\Delta\Sigma(r)}{\Sigma_{\rm crit}}, \tag{4.3}$$

[3]http://www.cfht.hawaii.edu/Instruments/Elixir/
[4]http://www1.cadc-ccda.hia-iha.nrc-cnrc.gc.ca/cadc/

where $\Delta\Sigma(r) = \bar{\Sigma}(< r) - \bar{\Sigma}(r)$ is the difference between the mean projected surface density enclosed by r and the mean projected surface density at a radius r, and $\Sigma_{\rm crit}$ is the critical surface density:

$$\Sigma_{\rm crit} = \frac{c^2}{4\pi G}\frac{D_s}{D_l D_{ls}}, \tag{4.4}$$

with D_l, D_s and D_{ls} the angular diameter distance to the lens, the source, and between the lens and the source, respectively. Since we lack redshifts for the background galaxies, we select galaxies with $22 < m_{r'} < 24$ that have a reliable shape estimate (ellipticities smaller than one, no SExtractor flag raised) as sources. We obtain the approximate source redshift distribution by applying identical magnitude cuts to the photometric redshift catalogues of the Canada-France-Hawaii-Telescope Legacy Survey (CFHTLS) "Deep Survey" fields (Ilbert et al. 2006).

To correct the signal for systematic contributions, we subtract the random shear signal from the measured source ellipticities. Details on the calculation of this correction can be found in van Uitert et al. (2011). Note that this correction mostly affects large scales (>20 arcmin), as on small scales the lensing signal is generally averaged over many lens-source orientations causing the systematic contributions to average out. As the lenses and sources barely overlap in redshift, we do not have to correct the lensing signal for the contamination of physically associated galaxies in the source sample. The source galaxy overdensity near the lenses is found to be a few percent at most, confirming that this correction is unimportant.

Although neither the dark matter nor the baryonic component are well described by a singular isothermal sphere (SIS), the sum of the two components is remarkably close (e.g. Treu & Koopmans 2004; Koopmans et al. 2009). The SIS signal is given by

$$\gamma_{t,\rm SIS}(r) = \frac{r_E}{2r} = \frac{4\pi\sigma^2_{\rm lens}}{c^2}\frac{D_l D_{ls}}{D_s}\frac{1}{2r}, \tag{4.5}$$

where r_E is the Einstein radius and $\sigma_{\rm lens}$ the lensing velocity dispersion. Based on the range of stellar masses and velocity dispersions of our lenses, we expect the majority of lenses to be central galaxies (see, e.g. van Uitert et al. 2011 or Mandelbaum et al. 2006 for estimates of the satellite fraction for galaxies in these ranges). Therefore, the lensing signal of our galaxies should be reasonably well described by an SIS profile over a relatively large range of projected separations.

To determine whether the stellar mass or the velocity dispersion is a better tracer of the amplitude of the lensing signal, we would ideally select lenses in a very narrow range in stellar mass, split those in a high and low velocity dispersion bin, and compare their lensing signals. A difference between the lensing signal of the low and high velocity dispersion would indicate a residual dependence on velocity dispersion. Similarly, we would like to select lenses in a very narrow range of velocity dispersion, split them in stellar mass and compare their signals. Comparing the lensing signals of these four bins would allow us to determine whether the stellar mass or the velocity dispersion is more closely related to the lensing signal on small scales - and hence to the projected

distribution of dark matter. Unfortunately, we do not have a sufficient number of lenses for this approach.

Instead, we have to select lenses that cover a larger range in stellar mass (and velocity dispersion). We cannot simply split the lenses in velocity dispersion and compare their lensing signals, because the stellar mass and velocity dispersion are correlated, and the high velocity dispersion bin also has a larger mean stellar mass. To account for this, we determine how the lensing signal scales with stellar mass, and subtract this trend from the high and low velocity dispersion bins. We also determine how the lensing signal scales with velocity dispersion, and remove this trend from the high and low stellar mass bin. If the lensing signal of galaxies strongly depends on the velocity dispersion, but only weakly on stellar mass, we expect a clear positive difference between the high and low velocity dispersion bins after we removed the trend with stellar mass. At the same time, we should see only a very small difference between the high and low stellar mass bin after removing the trend with velocity dispersion. Hence by studying the differences in the residual lensing signals, we can tell which observable is more closely related to the lensing signal of galaxies.

4.3 Results

To study whether the lensing signal mainly depends on stellar mass or velocity dispersion, we first have to determine how the lensing signal scales with these observables. We discuss how this is done for the model velocity dispersion; for the spectroscopic velocity and the stellar mass, we follow a similar approach. The general procedure is summarized below.

- We sort the lenses in model velocity dispersion, and divide them in five quintiles;
- We measure the lensing signal of each quintile, to which we fit an SIS profile on scales between 50 h_{70}^{-1}kpc and 1 h_{70}^{-1}Mpc. This is roughly the range where the galaxy dark matter halo dominates the lensing signal. This results in five best-fit lensing velocity dispersions, $\sigma_{\rm lens}$;
- We use the five values of $\sigma_{\rm lens}$ to fit the linear relation $\sigma_{\rm lens} = a_{\rm mod} \times (\sigma_{\rm mod}/200\,{\rm km\ s^{-1}}) + b_{\rm mod}$. We show the measurements and the fit in Figure 4.4, and give the best-fit parameters in Table 4.1;
- We determine the median stellar mass of these lenses, and divide them into a low and high stellar mass sample. We measure the lensing signal of both samples, and show them in the top-left panel of Figure 4.5;
- For each lens in the low and high stellar mass sample, we use the model velocity dispersion to calculate $\sigma_{\rm lens}$ using the linear relation, and subtract their SIS profiles from the lensing signal. The residuals are shown in the middle-left panel of the same figure;
- Finally, we determine the difference between the residual lensing signal of the high and low stellar mass bin, $\delta(\Delta\Sigma - \Delta\Sigma_{\rm trend})$, which is shown in the bottom-left panel.

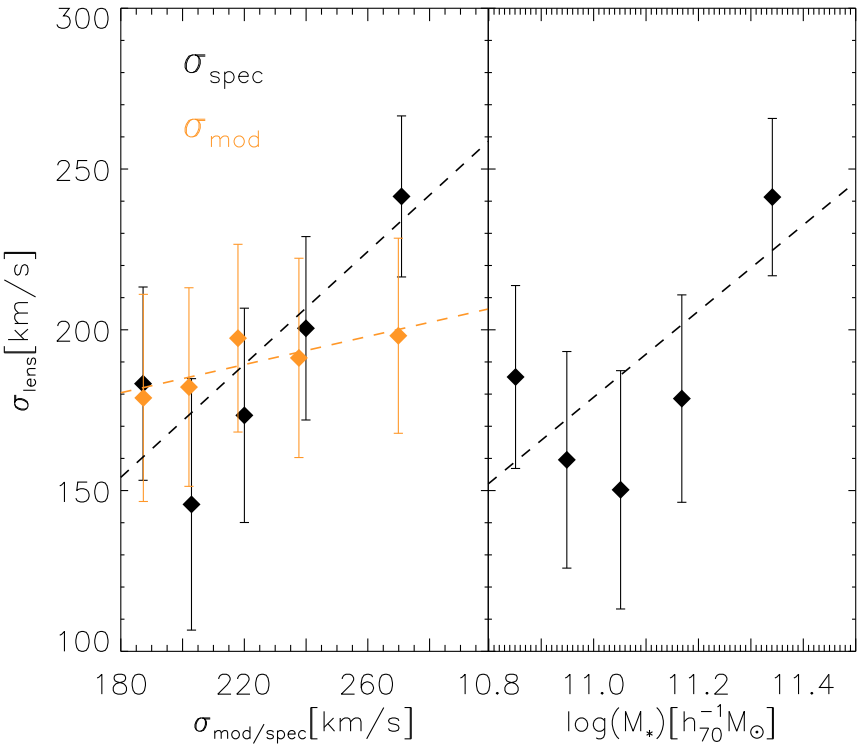

Figure 4.4: Best-fit lensing velocity dispersion as a function of spectroscopic velocity dispersion (*left panel, black*), model velocity dispersion (*left panel, orange*) and stellar mass (*right panel*). Dashed lines indicate the best-fit linear relation between the observable and $\sigma_{\rm lens}$. The linear relations are used to remove the dependence of the lensing signal on these observables.

When we subtract two SIS profiles with different amplitudes from each other, the result is also an SIS profile. Therefore, to quantify the residuals, we fit an SIS to $\delta(\Delta\Sigma - \Delta\Sigma_{\rm trend})$ on the same scales, and determine the residual Einstein radius, $r_E^{\rm res}$. These values can be found in Table 4.2.

Similarly, we determine the dependence of the lensing signal on spectroscopic velocity dispersion and stellar mass. For the spectroscopic velocity dispersion, we fit $\sigma_{\rm lens} = a_{\rm spec} \times (\sigma_{\rm spec}/200\,{\rm km\ s^{-1}}) + b_{\rm spec}$ and for the stellar mass, we fit $\sigma_{\rm lens} = a_{\rm stel} \times \log(M_*/10^{11}\,h_{70}^{-1} M_\odot) + b_{\rm stel}$. The best-fit parameters are shown in Table 4.1. These trends are removed from the lensing signals, and the residuals are shown in Figure 4.5 (middle panel).

From the bottom panels of the first and second columns of Figure 4.5, we observe that if we remove the dependence on model velocity dispersion, the lensing signal still depends on stellar mass. When we remove the dependence on

Table 4.1: Best-fit powerlaw parameters that describe the relation between the galaxy property and the lensing velocity dispersion in the indicated range. Details of the fitting are described in the text.

$\sigma_{\rm mod}$ [km/s]	$a_{\rm mod}$ [km/s]	$b_{\rm mod}$ [km/s]
$180 < \sigma_{\rm mod} < 300$	44 ± 96	141 ± 108
$100 < \sigma_{\rm mod} < 400$	93 ± 49	80 ± 50
$\sigma_{\rm spec}$ [km/s]	$a_{\rm spec}$ [km/s]	$b_{\rm spec}$ [km/s]
$180 < \sigma_{\rm spec} < 300$	176 ± 86	-5 ± 100
$100 < \sigma_{\rm spec} < 400$	129 ± 42	45 ± 45
$\log(M_*)$ $[h_{70}^{-1} M_\odot]$	$a_{\rm stel}$ [km/s]	$b_{\rm stel}$ [km/s]
$10.8 < \log(M_*) < 11.5$	134 ± 71	179 ± 15
$10.5 < \log(M_*) < 12.0$	118 ± 44	178 ± 12

Table 4.2: The residual Einstein radius, obtained by fitting an SIS profile to $\delta(\Delta\Sigma - \Delta\Sigma_{\rm trend})$ between 50 h_{70}^{-1}kpc and 1 h_{70}^{-1}Mpc for a mean lens redshift of $z = 0.13$. The bracketed values show the results for a different linear relation between the observable and $\sigma_{\rm lens}$, as detailed in the text.

removed trend	residual dependence	$r_E^{\rm res}$ [h_{70}^{-1}kpc]	
$\sigma_{\rm mod}$	M_*	0.88 ± 0.25	(0.78 ± 0.25)
M_*	$\sigma_{\rm mod}$	-0.18 ± 0.24	(-0.12 ± 0.24)
$\sigma_{\rm spec}$	M_*	0.30 ± 0.25	(0.42 ± 0.25)
M_*	$\sigma_{\rm spec}$	0.37 ± 0.24	(0.42 ± 0.24)

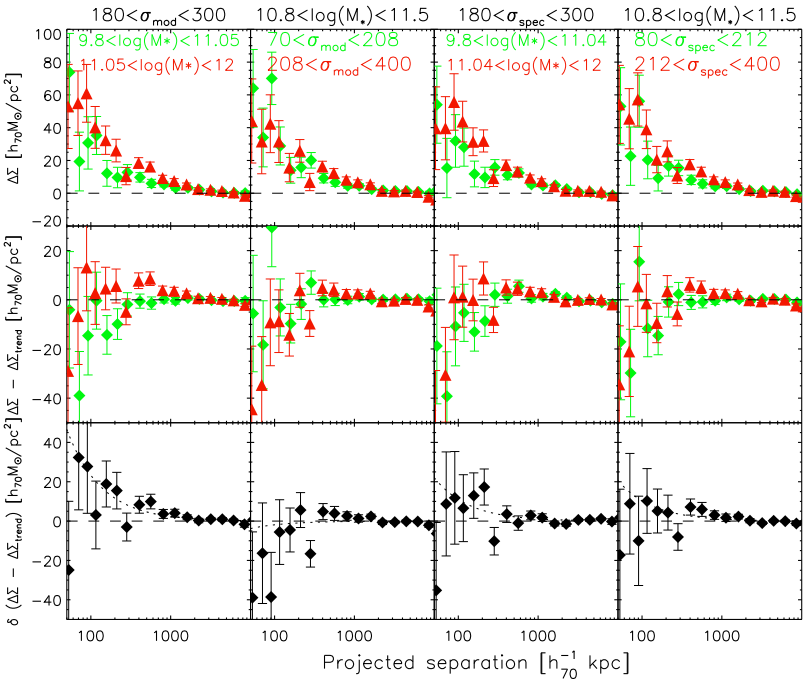

Figure 4.5: In the top row, we show the lensing signal $\Delta\Sigma$ as a function of physical distance from the lens, for the lens samples that have been split by the median value of one of the observables, as indicated in the plots. Red triangles (green diamonds) indicate the signal of the lenses with larger (smaller) stellar masses/velocity dispersions. In the middle row, we show the lensing signal of the same samples after we subtracted the trend with the observable that is indicated on top of each column. The difference between the residual trends for the two lens samples are shown in the bottom row. The dotted lines show the best-fit SIS profiles to the difference between the residuals.

stellar mass, the difference between the residuals of the model velocity samples is consistent with zero. These trends are reflected by the values for $r_E^{\rm res}$ in Table 4.2. The third and fourth columns of Figure 4.5 show that if we remove the dependence on spectroscopic velocity dispersion, the difference of the residual signal of the high and low stellar mass sample is consistent with the difference between the residual signal of the high and low spectroscopic velocity dispersion samples after we removed the dependence on stellar mass.

These results suggest that the stellar mass is a better tracer of the lensing signal of galaxies than the model velocity dispersion. Furthermore, the stellar mass and the spectroscopic velocity dispersion trace the lensing signal equally well, as the residual Einstein radii are consistent. As a consistency test, we have also looked at the residual dependence on model velocity dispersion after removing the trend with spectroscopic velocity dispersion, and vice versa. These trends confirm our previous findings: the spectroscopic velocity dispersion is more sensitive to the lensing signal of galaxies than the model velocity dispersion.

There is a weak indication that the lensing signal has a residual dependence on stellar mass after we remove the trend with spectroscopic velocity dispersion, and vice versa. This would imply that both the stellar mass and the velocity dispersion contain independent information on the projected distribution of dark matter around galaxies. Unfortunately, we do not have sufficient signal-to-noise to obtain a clear detection.

The results depend on the linear relations we have fit to remove the dependence on the observables. To study how sensitive the residual trends are on these relations, we have also fit them using all de Vaucouleur galaxies in the range 100 km s^{-1} $< \sigma_{\rm spec} <$ 400 km s^{-1}, 100 km s^{-1} $< \sigma_{\rm mod} <$ 400 km s^{-1} and 10.5 $h_{70}^{-1} M_\odot < \log(M_*) <$ 12 $h_{70}^{-1} M_\odot$, respectively. The best-fit parameters of these fits are shown in Table 4.1. We repeated the analysis using these values, and show the residual Einstein radii between brackets in Table 4.2. We find that this does not significantly change the results, i.e. the model velocity dispersion traces the lensing signal of galaxies worse than either the stellar mass or the spectroscopic velocity dispersion.

It is somewhat surprising that $\sigma_{\rm mod}$ is a poorer tracer of the total mass than $\sigma_{\rm spec}$, particularly because we observe in Figure 4.1 that they correlate well. To study where the samples differ, we plot the average effective radii and Sérsic indices as a function $\sigma_{\rm mod}$ and $\sigma_{\rm spec}$ in Figure 4.6. We find that at low velocity dispersions, the values of r_e and n are similar, but at high velocity dispersions, the lenses in the $\sigma_{\rm spec}$ samples have larger effective radii, whilst the lenses in the $\sigma_{\rm mod}$ have larger Sérsic indices. Hence the difference between the performance of $\sigma_{\rm mod}$ and $\sigma_{\rm spec}$ could be due to an additional dependence of the lensing signal on the structural parameters of the lenses.

To test whether the lensing signal depends on the size of galaxies, we select the lenses from the model velocity dispersion sample, and remove the lensing signal dependence on $\sigma_{\rm mod}$. Then we determine the median effective radius, split the lenses into a low and high effective radius sample and measure their residual lensing signal. As before, we measure the difference between the residual lensing signals of the high and low effective radius sample, to which we fit an SIS profile. We find $r_E^{\rm res} = 0.53 \pm 0.25\ h_{70}^{-1}$ kpc, which suggests that the lensing signal depends on the size of a galaxy. However, in Figure 4.7 we find that the effective radius is correlated with stellar mass, so part of this residual may be caused by the dependence on stellar mass. Therefore, we repeat the test using the lenses from the stellar mass sample, and remove the lensing signal dependence on stellar mass. Then we determine the median effective radius, split the lenses into a low and high effective radius sample and measure the difference between their residual lensing signals. We find $r_E^{\rm res} = 0.14 \pm 0.24\ h_{70}^{-1}$ kpc. Studying the residual dependence on Sérsic index, we find $r_E^{\rm res} = 0.04 \pm 0.25\ h_{70}^{-1}$ kpc for the model velocity dispersion sample, and $r_E^{\rm res} = 0.11 \pm 0.24\ h_{70}^{-1}$ kpc for the stellar mass sample. These results do not provide conclusive evidence that the small-scale lensing signal depends on these structural parameters.

Although the three lens samples overlap, they are not identical. Hence part of the trends we observe might actually be due to differences in the lens samples. To test this, we could define a fourth sample by selecting galaxies that pass all selection criteria, i.e. 180 km s^{-1} $< \sigma_{\rm mod} <$ 300 km s^{-1}, 180 km s^{-1} $< \sigma_{\rm spec} <$ 300 km s^{-1}, $\delta\sigma_{\rm spec}/\sigma_{\rm spec} < 0.15$ and 10.8 $h_{70}^{-1} M_\odot < \log(M_*) <$ 11.5 $h_{70}^{-1} M_\odot$. However, if we simultaneously select on stellar mass and model velocity dispersion, we implicitly also select on effective radius and Sérsic index. This is demon-

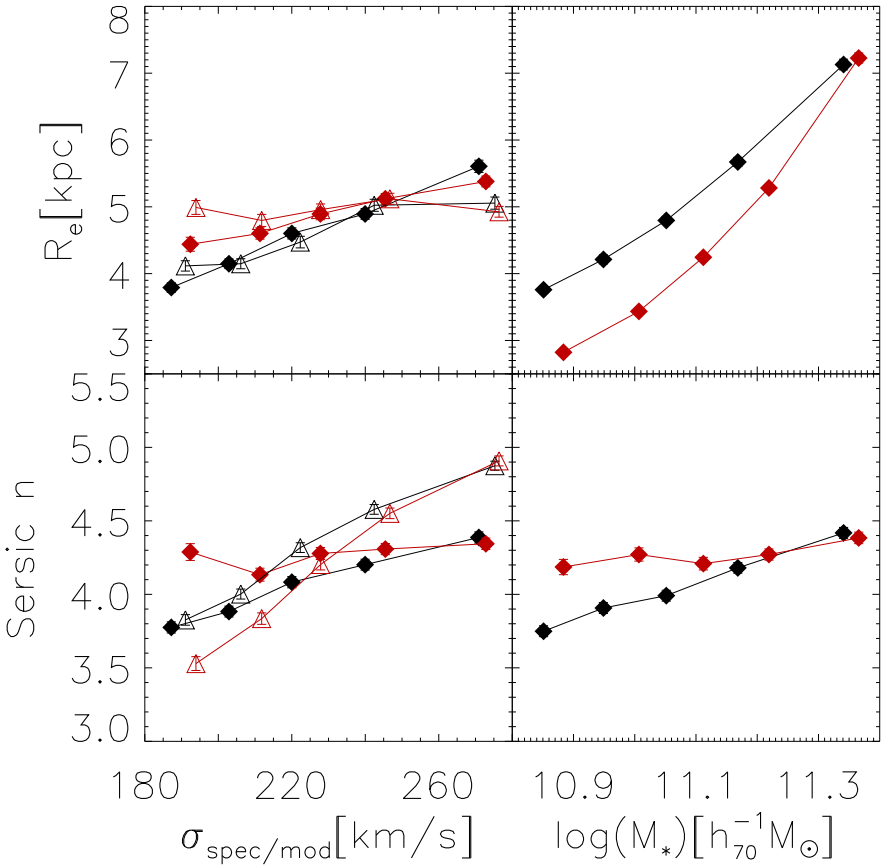

Figure 4.6: Mean effective radius and Sérsic index as a function of spectroscopic velocity dispersion (*left, black filled diamonds*), model velocity dispersion (*left, black open triangles*) and stellar mass (*right, black diamonds*). In red, we show the averages for the lens samples that simultaneously satisfy 180 km s^{-1} $<$ $\sigma_{\rm mod}$ $<$ 300 km s^{-1}, 180 km s^{-1} $<$ $\sigma_{\rm spec}$ $<$ 300 km s^{-1}, $\delta\sigma_{\rm spec}/\sigma_{\rm spec} < 0.15$ and $10.8\,h_{70}^{-1}M_{\odot} < \log(M_*) < 11.5\,h_{70}^{-1}M_{\odot}$. By simultaneously applying all selection criteria the average sizes and Sérsic indices of the samples change, which shows that we implicitly exclude galaxies from a certain area of structural parameter space.

strated in Figure 4.6 and Figure 4.7, where we show the mean effective radius and Sérsic index for the lens samples. When we select lenses that pass all selection criteria, we exclude lenses with large effective radii and small Sérsic indices at low stellar mass, lenses with small effective radii and small Sérsic indices at low spectroscopic velocity dispersions, and lenses with small effective radii and large Sérsic indices at low model velocity dispersions. If the lensing signal of a galaxy also depends on its structural parameters, the lensing measurements of this fourth sample could be biased, making the results harder to interpret.

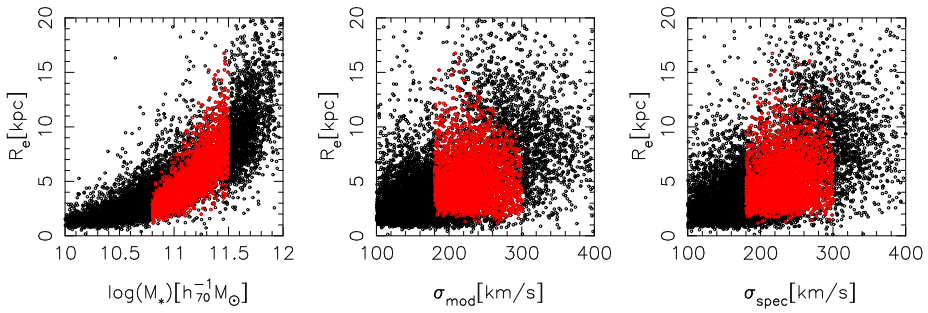

Figure 4.7: The effective radius as a function of stellar mass (*left*), model velocity dispersion (*middle*) and spectroscopic velocity dispersion (*middle*). The black dots show all de Vaucouleur galaxies with $z < 0.2$, the red dots are the lenses that satisfy 180 km s^{-1} $< \sigma_{\rm mod} <$ 300 km s^{-1}, 180 km s^{-1} $< \sigma_{\rm spec} <$ 300 km s^{-1}, $\delta\sigma_{\rm spec}/\sigma_{\rm spec} < 0.15$ and 10.8 $h_{70}^{-1} M_\odot < \log(M_*) <$ 11.5 $h_{70}^{-1} M_\odot$. By using all selection criteria simultaneously, we exclude large galaxies at low stellar masses and high model velocity dispersions, and small galaxies in the velocity dispersion samples. These selection biases could bias the lensing analysis if the lensing signal of a galaxy also depends on the effective radius.

4.4 Conclusion

In this work, we study which property of galaxies is most tightly correlated to the weak gravitational lensing signal on small scales. The properties we compare are the stellar mass, the spectroscopic velocity dispersion and the model velocity dispersion. We find that the lensing signal of galaxies is equally well traced by the stellar mass and the spectroscopic velocity dispersion. There is a weak indication for a residual dependence on stellar mass after removing the trend with spectroscopic velocity dispersion, and vice versa. This suggests that both tracers contain independent information on the projected distribution of dark matter around galaxies. Unfortunately, the signal-to-noise of our lensing measurements is not sufficient to make a definite statement.

The model velocity dispersion traces the lensing signal significantly worse, which is surprising as the spectroscopic velocity dispersion and model velocity dispersion correlate well for our lenses. At high velocity dispersions, however, the lenses in the $\sigma_{\rm mod}$-sample have smaller effective radii and larger Sérsic indices than those in the $\sigma_{\rm spec}$-sample. This suggests that these structural parameters contain additional information on the projected distribution of dark matter around galaxies. To test this, we measure how the lensing signal depends on the size and Sérsic index of the lenses. We do not find conclusive evidence for a residual dependence on these structural parameters, which could be due to insufficient signal-to-noise caused by the relatively small lens sample of this study.

The lensing signal on small projected separations from the lenses mainly depends on the halo mass. Our results therefore suggest that the stellar mass and spectroscopic velocity dispersion trace the halo mass equally well, but the model velocity dispersion does worse. However, at larger separations, neighbouring structures contribute to the lensing signal as well, and we cannot exclude the possibility that differences between the clustering properties of the lens samples

also has some effect. To account for the clustering properties of the galaxies, and remove their contribution from the lensing signal, we could model the lensing signal using the halo model formalism (Seljak 2000; Cooray & Sheth 2002). An additional advantage of this approach would be that it enables a simultaneous study of the halo mass and the clustering properties of galaxies. We postpone this analysis to a future work.

Ideally, one should also remove the potential lensing signal dependence on the structural parameters of galaxies, i.e. split the lens sample both in velocity dispersion and structural parameters, and study the residual dependence on stellar mass. With the current data, we do not have sufficient signal-to-noise to perform such an analysis. Ultimately, one could simultaneously fit all these parameters, i.e. $M_h = f(\sigma, M_*, r_e, n, ...)$, which could also contain products of the parameters such as σM_*, and determine the covariance matrix between the coefficients. The relative magnitude of the coefficients would give new insights into which observables are important, and hence would provide valuable insights into galaxy formation processes.

Acknowledgements

We would like to thank Pieter van Dokkum and David Wake for useful discussions. HH and EvU acknowledge support from a Marie Curie International Reintegration Grant. HH is also supported by a VIDI grant from the Nederlandse Organisatie voor Wetenschappelijk Onderzoek (NWO). MDG thanks the Research Corporation for support via a Cottrell Scholars Award. The RCS2 project is supported in part by grants to HKCY from the Canada Research Chairs program and the Natural Science and Engineering Research Council of Canada.

This work is based on observations obtained with MegaPrime/MegaCam, a joint project of CFHT and CEA/DAPNIA, at the Canada-France-Hawaii Telescope (CFHT) which is operated by the National Research Council (NRC) of Canada, the Institute National des Sciences de l'Univers of the Centre National de la Recherche Scientifique of France, and the University of Hawaii. We used the facilities of the Canadian Astronomy Data Centre operated by the NRC with the support of the Canadian Space Agency.

Bibliography

Abazajian, K. N., Adelman-McCarthy, J. K., Agüeros, M. A., et al. 2009, ApJS, 182, 543

Adelman-McCarthy, J. K., Agüeros, M. A., Allam, S. S., et al. 2008, ApJS, 175, 297

Bertin, E. & Arnouts, S. 1996, A&AS, 117, 393

Bertin, G., Ciotti, L., & Del Principe, M. 2002, A&A, 386, 149

Bezanson, R., van Dokkum, P. G., Franx, M., et al. 2011, ApJ, 737, L31

Blanton, M. R., Schlegel, D. J., Strauss, M. A., et al. 2005, AJ, 129, 2562

Cappellari, M., Bacon, R., Bureau, M., et al. 2006, MNRAS, 366, 1126

Cooray, A. & Sheth, R. 2002, Phys. Rep., 372, 1

Eisenstein, D. J., Annis, J., Gunn, J. E., et al. 2001, AJ, 122, 2267

Erben, T., Hildebrandt, H., Lerchster, M., et al. 2009, A&A, 493, 1197
Erben, T., Schirmer, M., Dietrich, J. P., et al. 2005, Astronomische Nachrichten, 326, 432
Faber, S. M. & Jackson, R. E. 1976, ApJ, 204, 668
Gilbank, D. G., Gladders, M. D., Yee, H. K. C., & Hsieh, B. C. 2011, AJ, 141, 94
Graves, G. J., Faber, S. M., & Schiavon, R. P. 2009, ApJ, 693, 486
Guo, Q., White, S., Li, C., & Boylan-Kolchin, M. 2010, MNRAS, 404, 1111
Hoekstra, H., Franx, M., & Kuijken, K. 2000, ApJ, 532, 88
Hoekstra, H., Franx, M., Kuijken, K., & Squires, G. 1998, ApJ, 504, 636
Ilbert, O., Arnouts, S., McCracken, H. J., et al. 2006, A&A, 457, 841
Kaiser, N., Squires, G., & Broadhurst, T. 1995, ApJ, 449, 460
Komatsu, E., Smith, K. M., Dunkley, J., et al. 2011, ApJS, 192, 18
Koopmans, L. V. E., Bolton, A., Treu, T., et al. 2009, ApJ, 703, L51
Leauthaud, A., Tinker, J., Bundy, K., et al. 2012, ApJ, 744, 159
Luppino, G. A. & Kaiser, N. 1997, ApJ, 475, 20
Mandelbaum, R., Seljak, U., Kauffmann, G., Hirata, C. M., & Brinkmann, J. 2006, MNRAS, 368, 715
More, S., van den Bosch, F. C., Cacciato, M., et al. 2011, MNRAS, 410, 210
Moster, B. P., Somerville, R. S., Maulbetsch, C., et al. 2010, ApJ, 710, 903
Padmanabhan, N., Schlegel, D. J., Finkbeiner, D. P., et al. 2008, ApJ, 674, 1217
Seljak, U. 2000, MNRAS, 318, 203
Smith, R. J., Lucey, J. R., & Hudson, M. J. 2009, MNRAS, 400, 1690
Strauss, M. A., Weinberg, D. H., Lupton, R. H., et al. 2002, AJ, 124, 1810
Taylor, E. N., Franx, M., Brinchmann, J., van der Wel, A., & van Dokkum, P. G. 2010, ApJ, 722, 1
Treu, T. & Koopmans, L. V. E. 2004, ApJ, 611, 739
van Uitert, E., Hoekstra, H., Velander, M., et al. 2011, A&A, 534, A14
Wake, D. A., Whitaker, K. E., Labbé, I., et al. 2011, ApJ, 728, 46
York, D. G., Adelman, J., Anderson, Jr., J. E., et al. 2000, AJ, 120, 1579

5

Constraints on the shapes of dark matter haloes from weak gravitational lensing

We study the shapes of galaxy dark matter haloes by measuring the anisotropy of the weak gravitational lensing signal around galaxies in the second Red-sequence Cluster Survey (RCS2). We determine the average shear anisotropy within the virial radius for three lens samples: the 'all' sample, which contains all galaxies with $19 < m_{r'} < 21.5$, and the 'red' and 'blue' samples, whose lensing signals are dominated by massive low-redshift early-type and late-type galaxies, respectively. To study the environmental dependence of the lensing signal, we separate each lens sample into an isolated and clustered part and analyse them separately. We address the impact of several complications on the halo ellipticity measurement, including PSF residual systematics in the shape catalogues, multiple deflections, and the clustering of lenses. We estimate that the impact of these is small for our lens selections. Furthermore, we measure the azimuthal dependence of the distribution of physically associated galaxies around the lens samples. We find that these satellites preferentially reside near the major axis of the lenses, and constrain the angle between the major axis of the lens and the average location of the satellites to $\langle\theta\rangle = 43.7^\circ \pm 0.3^\circ$ for the 'all' lenses, $\langle\theta\rangle = 41.7^\circ \pm 0.5^\circ$ for the 'red' lenses and $\langle\theta\rangle = 42.0^\circ \pm 1.4^\circ$ for the 'blue' lenses. For the 'red' galaxies, the shear anisotropy is on average marginally positive, although close to the lens the signal turns negative. For the 'blue' galaxies, the signal is marginally negative. For the 'all' sample, we find that the anisotropy of the galaxy-mass cross-correlation function $\langle f - f_{45}\rangle = 0.23 \pm 0.12$, providing weak support for the view that the average galaxy is embedded in, and preferentially aligned with, a triaxial dark matter halo. Assuming an elliptical Navarro-Frenk-White (NFW) profile, we find that the ratio of the dark matter halo ellipticity and the galaxy ellipticity $f_h = e_h/e_g = 1.50^{+1.03}_{-1.01}$, which for a mean lens ellipticity of 0.25 corresponds to a projected halo ellipticity of $e_h = 0.38^{+0.26}_{-0.25}$ if the halo and the lens are perfectly aligned. For isolated galaxies of the 'all' sample, the average shear anisotropy increases to $\langle f - f_{45}\rangle = 0.51^{+0.26}_{-0.25}$ and $f_h = 4.73^{+2.17}_{-2.05}$, whilst for clustered galaxies the signal is consistent with zero. These constraints provide lower limits on the average dark matter halo ellipticity, as scatter in the relative position angle between the galaxies and the dark matter haloes is expected to reduce the shear anisotropy by a factor $\sim$2.

E. van Uitert, H. Hoekstra, T. Schrabback, D.G. Gilbank, M.D. Gladders,

H.K.C. Yee, submitted to A&A;

5.1 Introduction

Over the last few decades a coherent cosmological paradigm has developed, ΛCDM, which provides a framework for the study of the formation and evolution of structure in the Universe. N-body simulations that are based on ΛCDM predict that (dark) matter haloes collapse such that their density profiles closely follow a Navarro-Frenk-White profile (NFW; Navarro et al. 1996), which is in excellent agreement with observations. Another fundamental prediction from simulations is that the haloes are triaxial (e.g. Dubinski & Carlberg 1991; Allgood et al. 2006), which appear elliptical in projection. This prediction of dark matter haloes, as well as many others concerning the evolution of their shapes (e.g Vera-Ciro et al. 2011), the effect of the central galaxy on the dark matter halo shape (e.g. Kazantzidis et al. 2010; Abadi et al. 2010; Machado & Athanassoula 2010) and their dependence on environment (e.g Wang et al. 2011), remain largely untested observationally.

Direct observational constraints on the halo ellipticities have proven to be difficult, mainly due to the lack of useful tracers of the gravitational potential. On small scales (∼few kpc), halo ellipticity estimates have been obtained through the combination of strong lensing and stellar dynamics (e.g. van de Ven et al. 2010; Dutton et al. 2011; Suyu et al. 2011), planetary nebulae (e.g. Napolitano et al. 2011) and HI observations in late-type galaxies (e.g. Banerjee & Jog 2008; O'Brien et al. 2010). On larger scales, the distribution of satellite galaxies around centrals has been used (e.g. Bailin et al. 2008), but such studies have only provided constraints for rich systems that may not be representative for the typical galaxy in the universe.

Weak gravitational lensing does not depend on the presence of optical tracers and is capable of providing ellipticity estimates on a large range of scales (between a few kpc to a few Mpc). Therefore it is a powerful observational technique to study the ellipticity of dark matter haloes. In weak lensing the distortion of the images of faint background galaxies due to the dark matter potentials of intervening structures, the lenses, is measured. This has been used to determine halo masses (e.g. van Uitert et al. 2011) as well as the extent of haloes. If galaxies preferentially align (or anti-align) with respect to the dark matter haloes in which they are embedded, the lensing signal becomes anisotropic. This signature can be used to constrain the ellipticity of dark matter haloes of galaxies (Brainerd & Wright 2000; Natarajan & Refregier 2000).

The core assumption in the weak-lensing-based halo ellipticity studies is that the orientation of galaxies and dark matter haloes are correlated; if they are not, the shear signal is isotropic and cannot be used to constrain the ellipticity of the haloes. The relative alignment between the baryons and the dark matter has been addressed in a large number of studies based on numerical simulations (e.g. van den Bosch et al. 2002, 2003; Bailin et al. 2005; Kang et al. 2007; Bett et al. 2010; Hahn et al. 2010; Deason et al. 2011), in studies based on the distribution of satellite galaxies around centrals (Wang et al. 2008; Agustsson & Brainerd 2010) and in studies based on the ellipticity correlation function (Faltenbacher et al. 2009; Okumura et al. 2009). The general consensus is that although the galaxy and dark matter are aligned on average, the scatter in the differential position angle distribution is large. Bett (2011) examined a broad range of galaxy-halo alignment models by combining N-body simulations with

semi-analytic galaxy formation models, and found that for most of the models under consideration, the stacked projected axis ratio becomes close to unity. Consequently, the ellipticity of dark matter haloes may be difficult to measure with weak lensing in practice.

Knowledge of the relative alignment distribution is not only crucial for halo ellipticity studies, but also for studies of the intrinsic alignments of galaxies. Numerical simulations predict that the shapes of neighbouring dark matter haloes are correlated (e.g. Splinter et al. 1997; Croft & Metzler 2000; Heavens et al. 2000; Lee et al. 2008). The shapes of galaxies that form inside these haloes may therefore be intrinsically aligned as well. Measuring this effect is interesting as it provides constraints on structure formation. Also, the lensing properties of the large-scale structure in the universe, known as cosmic shear, are affected by intrinsic alignments, and benefit from a careful characterization of the effect. Intrinsic alignments are studied observationally by correlating the ellipticities of galaxies as a function of separation; misalignments can significantly reduce these ellipticity correlation functions (e.g. Heymans et al. 2004).

To date, only three observational weak lensing studies have detected the anisotropy of the lensing signal (Hoekstra et al. 2004; Mandelbaum et al. 2006a; Parker et al. 2007). These studies have provided only tentative support for the existence of elliptical dark matter haloes, as they were limited by either their survey size and lack of colour information (Hoekstra et al. 2004; Parker et al. 2007) or their depth (Mandelbaum et al. 2006a). To improve on these constraints, we use the Red-sequence Cluster Survey 2 (RCS2, Gilbank et al. 2011). Covering 900 square degree in the $g'r'z'$-bands, a limiting magnitude of $r'_{\rm lim} \sim 24.3$ and a median seeing of $0.7''$, this survey is very well suited for lensing studies (see van Uitert et al. 2011). Using the colours we select massive luminous foreground galaxies at low redshifts. To investigate whether the formation histories and environment affect the average halo ellipticity of galaxies, the lenses are separated by galaxy type and environment, and the signals are studied separately.

The structure of this paper is as follows. We describe the lensing analysis, including the data reduction of the RCS2 survey, the lens selection and the definition of the shear anisotropy estimators, in Section 5.2. We present measurements using a simple shear anisotropy estimator in Section 5.3, and use it to study the potential impact of PSF residual systematics in the shape catalogues. Various complications exist that might have altered the observed shear anisotropy, and in Section 5.4 we study the impact of two of them: multiple deflection and the clustering of the lenses. The shear anisotropy measurements are shown and interpreted in Section 5.5. We conclude in Section 5.6. Throughout the paper we assume a WMAP7 cosmology (Komatsu et al. 2011) with $\sigma_8 = 0.8$, $\Omega_\Lambda = 0.73$, $\Omega_M = 0.27$, $\Omega_b = 0.046$ and the dimensionless Hubble parameter $h = 0.7$. The errors on the measured and derived quantities in this work generally show the 68% confidence interval, unless explicitly stated otherwise.

5.2 Lensing analysis

For our lensing analysis we use the imaging data from the second Red-sequence Cluster Survey (RCS2; Gilbank et al. 2011). The RCS2 is a nearly 900 square degree imaging survey in three bands (g', r' and z') carried out with

the Canada-France-Hawaii Telescope (CFHT) using the 1 square degree camera MegaCam. In this work, we use the ∼700 square degrees of the primary survey area. The remainder constitutes the 'Wide' component of the CFHT Legacy Survey (CFHTLS) which we do not consider here. We perform the lensing analysis on the 8 minute exposures of the r'-band (r'_{lim} ∼24.3), which is best suited for lensing with a median seeing of $0.71''$.

5.2.1 Data reduction

The photometric calibration of the RCS2 is described in detail in Gilbank et al. (2011). The magnitudes are calibrated using the colours of the stellar locus and the overlapping Two-Micron All-Sky Survey (2MASS), and have an accuracy better than 0.03 mag in each band compared to the SDSS. The creation of the galaxy shape catalogues is described in detail in van Uitert et al. (2011). We refer readers to that paper for more detail, and present here a short summary of the most important steps.

We retrieve the Elixir[1] processed images from the Canadian Astronomy Data Centre (CADC) archive[2]. We use the THELI pipeline (Erben et al. 2005, 2009) to subtract the image backgrounds, create weight maps that we use in the object detection phase, and to identify satellite and asteroid trails. To detect the objects in the images, we use `SExtractor` (Bertin & Arnouts 1996). The stars that are used to model the PSF variation across the image are selected using size-magnitude diagrams. All objects larger than 1.2 times the local size of the PSF are identified as galaxies. We measure the shapes of the galaxies with the KSB method (Kaiser et al. 1995; Luppino & Kaiser 1997; Hoekstra et al. 1998), using the implementation described by Hoekstra et al. (1998, 2000). This implementation has been tested on simulated images as part of the Shear Testing Programmes (STEP) (the 'HH' method in Heymans et al. 2006 and Massey et al. 2007), and these tests have shown that it reliably measures the unconvolved shapes of galaxies for a variety of PSFs. Finally, the source ellipticities are corrected for camera shear, which originates from slight non-linearities in the camera optics. The resulting shape catalogue of the RCS2 contains the ellipticities of 2.2×10^7 galaxies. A more detailed discussion of the analysis can be found in van Uitert et al. (2011).

5.2.2 Lenses

To study the halo ellipticity of galaxies, we measure the shear anisotropy of three lens samples. The first sample contains all galaxies with $19 < m_{r'} < 21.5$, and is referred to as the 'all' sample. This sample consists of different types of galaxies that cover a broad range in luminosity and redshift. The shear anisotropy measurement of this sample enables us to determine whether galaxies are on average aligned with their dark matter haloes.

The formation history of galaxies differs between galaxy types, and consequently the relation between baryons and dark matter may differ too. Therefore, the average dark matter halo shapes, and the orientation of galaxies within these haloes, might depend on galaxy type. To examine this, we separate the lenses

[1] http://www.cfht.hawaii.edu/Instruments/Elixir/
[2] http://www1.cadc-ccda.hia-iha.nrc-cnrc.gc.ca/cadc/

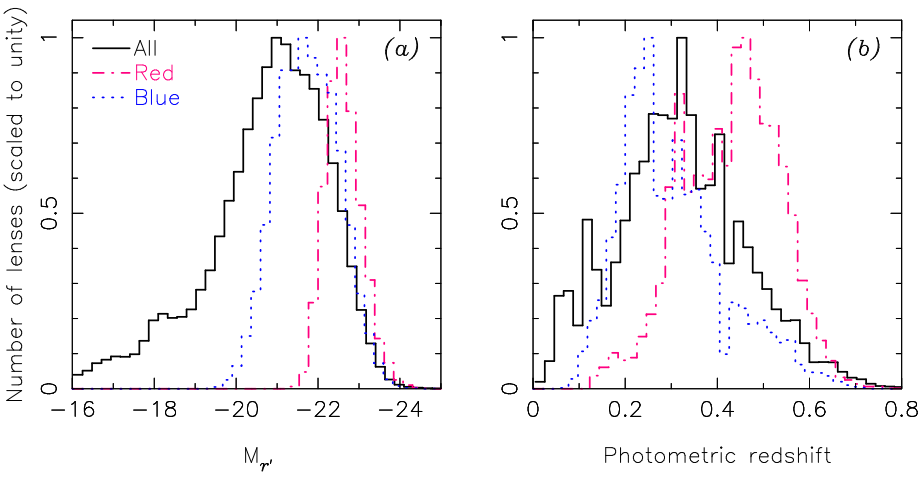

Figure 5.1: Number of lenses as a function of absolute magnitude (a) and redshift (b) for the three lens samples, obtained by applying identical cuts to the CFHTLS W1 photometric redshift catalogue from the CFHTLenS collaboration (Hildebrandt et al. 2011). The 'all' sample (black solid lines) has the broadest distributions, and covers absolute r'-band magnitudes between -18 and -24, and redshifts between 0 and 0.6. The luminosities of the 'blue' sample (blue dotted lines) are in the range $-24 < M_r < -20$, with redshifts $0.15 < z < 0.6$. The 'red' sample (purple dot-dashed lines) has the narrowest distributions, with luminosities $-24 < M_r < -22$ and redshifts $0.3 < z < 0.6$.

as a function of their type.

Various selection criteria have been employed to separate early-type from late-type galaxies. In most cases, galaxies are either selected based on the slope of their brightness profiles (Mandelbaum et al. 2006b; van Uitert et al. 2011), or on their colours (Mandelbaum et al. 2006a; Hoekstra et al. 2005). To study how these selection criteria relate, Mandelbaum et al. (2006a) compare the selection based on their SDSS $u-r$ model colour to the selection based on the $frac\_dev$ parameter[3], and find that the assigned galaxy types agree for 90% of the galaxies.

We choose to separate the galaxy types based on their colours, as the g'-, r'- and z'- band colours are readily available for all galaxies in the RCS2. The aim of the separation is two-fold: to make a clean separation between the red quiescent galaxies which typically exhibit early-type morphologies and blue star-forming galaxies that typically have late-type morphologies, and to select massive lenses at low redshifts to optimize the lensing signal-to-noise, and minimize potential contributions from multiple deflections (see Section 5.4.1). To determine where these massive low-redshift galaxies reside in the colour-magnitude plane, we use the photometric redshift catalogues of the CFHTLS Wide from the CFHTLenS collaboration (Hildebrandt et al. 2011), and define our boxes accordingly; details of the selection of the 'red' and 'blue' lens sample are described in Appendix 5.A. Note that these lens samples overlap with the 'all' sample, but not with

[3]The $frac\_dev$ parameter is determined by simultaneously fitting $frac\_deV$ times the best-fitting de Vaucouleur profile plus (1-$frac\_deV$) times the best-fitting exponential profile to an object's brightness profile

Table 5.1: Properties of the lens samples: the number of lenses, the mean redshift, the mean luminosity, the mean ellipticity, the fraction of lenses that are isolated, the virial mass, the virial radius and the scale radius.

Sample	$N_{\rm lens}$	$\langle z \rangle$	$\langle L_{r'} \rangle$ $[10^{10}\ h_{70}^{-2} L_\odot]$	$\langle \lvert e_g \rvert \rangle$	$f_{\rm iso}$	M_{200} $[10^{10}\ h_{70}^{-1} M_\odot]$	r_{200} $[h_{70}^{-1}{\rm kpc}]$	r_s $[h_{70}^{-1}{\rm kpc}]$
All	1 681 826	0.31	2.86	0.25	0.20	$21.1^{+0.5}_{-1.4}$	150^{+1}_{-3}	$23.9^{+0.2}_{-0.5}$
Red	136 196	0.43	8.91	0.20	0.41	138 ± 8	280 ± 5	$54.6^{+1.1}_{-1.0}$
Blue	147 079	0.31	4.68	0.26	0.55	$44.4^{+3.3}_{-3.8}$	192 ± 5	$32.7^{+0.8}_{-0.9}$

each other. Details of the samples are given in Table 5.1.

To study how well we can separate early-types from late-types, we compare our selection to previously employed separation criteria. Details of the comparison can be found in Appendix 5.A. We find that the 'red' sample is very similar to the selection based on the $u' - r'$ colour, whilst ∼58% of the 'blue' sample are actually red according to their $u' - r'$ colour. Most of these contaminants of the 'blue' sample are not massive, and actually dilute the lensing signal. The purity of the 'blue' sample could be improved by shifting the selection boxes to bluer colours, but this at the expense of removing the majority of massive late-type lenses. Finally, we note that ∼70% of the 'all' sample are considered blue based on their $u' - r'$ colours.

To study the second objective of the lens selection, i.e. to select massive and bright low-redshift lenses, we apply the colour cuts to the CFHTLS W1 photometric catalogue, and show the distribution of absolute magnitudes and photometric redshifts of the lens samples in Figure 5.1. We find that the 'red' lens sample consists of galaxies with absolute magnitudes in the range $-24 < M_r < -22$, and most with redshifts between 0.3 and 0.6. The galaxies from the 'blue' sample have absolute magnitudes in the range $-24 < M_r < -20$, and are located at redshifts between 0.1 and 0.6. For the blue galaxies, we cannot define a criterion that exclusively selects luminous lenses in a narrow redshift range, based on the $g'r'z'$ magnitudes alone. Finally, the 'all' sample has the broadest luminosity and redshift distribution. It is possible to narrow down the redshift range by discarding the lenses with the largest apparent magnitudes from each sample. We choose not to, however, because this lowers the signal-to-noise of the lensing measurement, which consequently broadens the constraints on the average halo ellipticity.

Note that due to the lack of a very blue observing band in the CFHTLS, the photometric redshifts below 0.2 are biased high (Hildebrandt et al. 2011). As a consequence, a fraction of the galaxies of the 'blue' lens sample may have been shifted to higher redshifts, and thus larger luminosities. The mean redshift and luminosity of the sample may therefore be somewhat smaller than the values quoted in Table 5.1, and the distributions shown in Figure 5.1 are only indicative.

Since the dark matter halo ellipticity is measured relative to the ellipticity of the galaxy, it is interesting to examine the distribution of the latter. In Figure 5.2, we show the ellipticity distribution of the lens samples; the mean galaxy ellipticity of each sample is given in Table 5.1. The ellipticity distribu-

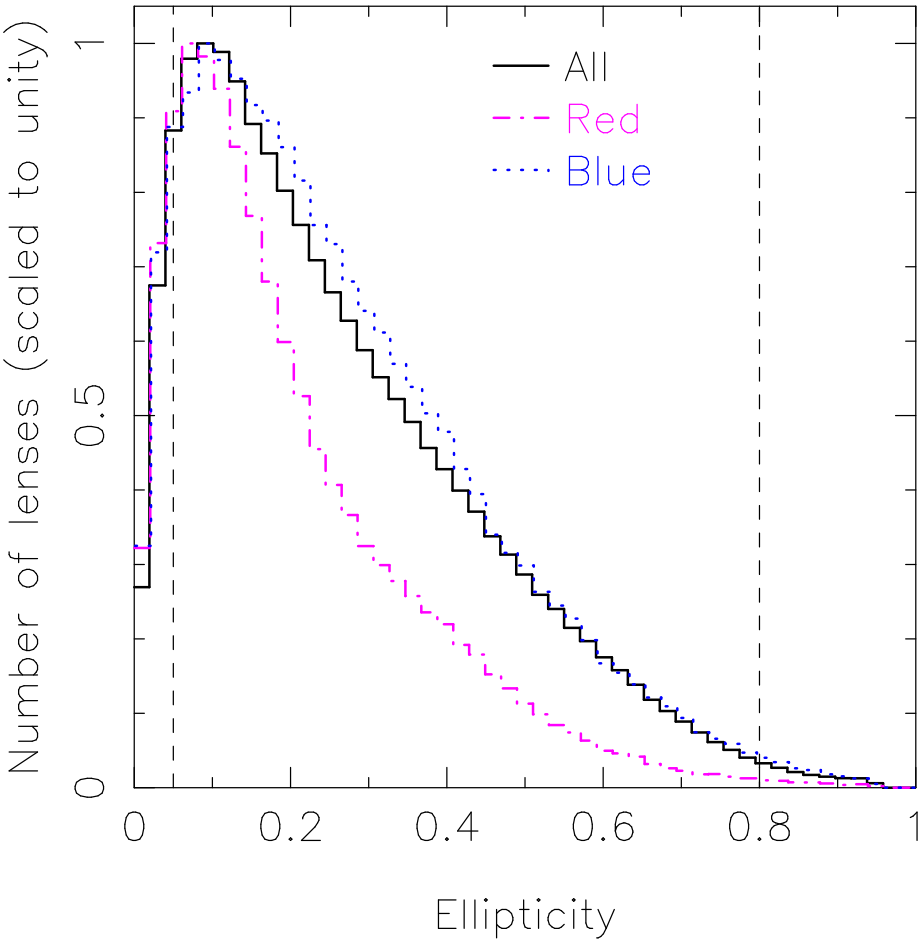

Figure 5.2: Ellipticity distribution of the $g'r'z'$-colour selected lens samples. The dashed lines indicate the ellipticity cuts we apply to exclude the roundest and most elliptical lenses. The ellipticity distributions of the 'all' and the 'blue' sample are similar, but the 'red' sample contains relatively more round galaxies.

tions of the 'all' and 'blue' sample are comparable, and are broader than the 'red' sample one, because the 'all' and 'blue' sample have a considerable fraction of disk galaxies. The differences between the ellipticity distributions have consequences for the weighting scheme of the lensing anisotropy measurements, as we will discuss in Section 5.2.3. In the analysis, we only use galaxies with $0.05 < e_g < 0.8$, which excludes round lenses that do not have a well-defined position angle, and very elliptical galaxies whose shapes are potentially affected by neighbours and/or cosmic rays.

The ellipticity of dark matter haloes may depend on the environment of a galaxy. We therefore divide the lens samples further into isolated and clustered ones, and study the lensing signal separately. As we lack redshifts for all the galaxies, we have to use an isolation criterion based on projected angular separations: if the lens has a neighbouring galaxy within a fixed projected separation that is brighter (in apparent magnitude) than the lens, it is selected for the clus-

tered sample. If the lens is the brightest object, it is selected for the isolated sample. We test various values for the fixed minimum separation, and compare the tangential shear at large scales in Appendix 5.B. Based on these results, we use a minimum separation of 1 arcmin. Note that an environment selection based on apparent magnitudes cannot be very pure; a fraction of the lenses from the isolated sample may still be the brightest galaxy in a cluster. Some of the lenses of the clustered sample may in reality be isolated, but have been selected for the clustered sample due to the presence of bright foreground galaxies. However, the difference between the large-scale lensing signal of the isolated and the clustered sample indicates that our selection criterion works reasonably well. The fraction of the lens sample that is isolated, $f_{\rm iso}$, is indicated in Table 5.1.

5.2.3 Shear anisotropy

The lensing signal is quantified by the tangential shear, γ_t, around the lenses as a function of projected separation. As the distortions are small compared to the shape noise, the tangential shear needs to be azimuthally averaged over a large number of lens-source pairs:

$$\langle\gamma_t\rangle(r) = \frac{\Delta\Sigma(r)}{\Sigma_{\rm crit}}, \tag{5.1}$$

where $\Delta\Sigma(r) = \bar{\Sigma}(< r) - \bar{\Sigma}(r)$ is the difference between the mean projected surface density enclosed by r and the mean projected surface density at a radius r, and $\Sigma_{\rm crit}$ is the critical surface density:

$$\Sigma_{\rm crit} = \frac{c^2}{4\pi G}\frac{D_s}{D_l D_{ls}}, \tag{5.2}$$

with D_l, D_s and D_{ls} the angular diameter distance to the lens, the source, and between the lens and the source respectively. Since we lack redshifts, we select galaxies with $22 < m_{r'} < 24$ and a reliable shape estimate as sources. We obtain the approximate source redshift distribution by applying identical magnitude cuts to the photometric redshift catalogues of the Canada-France-Hawaii-Telescope Legacy Survey (CFHTLS) "Deep Survey" fields (Ilbert et al. 2006), and find a median source redshift of $z_s = 0.74$. To convert the tangential shear to $\Delta\Sigma$, we use the average critical surface density that is determined by integrating over the source redshift distribution:

$$\begin{aligned}\langle\Sigma_{\rm crit}\rangle = \frac{c^2}{4\pi G}\frac{1}{A_{\rm norm}}\int_{z_l}^{\infty} dz_s\, p(z_s)\frac{D_s}{D_l D_{ls}};\\ A_{\rm norm} = \int_0^{\infty} dz_s\, p(z_s),\end{aligned} \tag{5.3}$$

with $p(z_s)$ the redshift distribution of the sources, and z_l the mean redshift of the lens sample used to determine D_l and D_{ls}. We also measure the cross shear, $\gamma_\times$, the component of the shear in the direction of 45° from the lens-source separation vector. The azimuthally averaged cross shear signal should vanish since gravitational lensing does not produce it. If this signal is non-zero, however, it indicates the presence of systematics in the shape catalogues. As the lenses are large and their light may contaminate the lensing signal near the lenses, we only

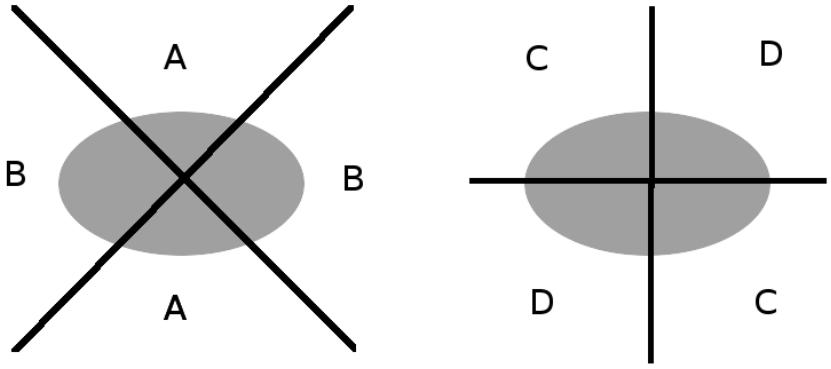

Figure 5.3: Schematic of a lens galaxy. The tangential shear is measured in regions `A` and `B`, the cross shear is measured in regions `C` and `D`. The cross shear is subtracted from the tangential shear to correct for systematic contributions to the shear.

consider the signal on scales larger than 0.1 arcmin for lenses with $m_{r'} > 19$, and scales larger than 0.2 arcmin for lenses with $m_{r'} < 19$. These criteria are based on the reduction of the source number density near the lenses, as discussed in Appendix 5.D. Hence the smallest scales we probe is 28 kpc for the 'all' and 'blue' sample, and 34 kpc for the 'red' sample at the mean lens redshift. To remove contributions of systematic shear (from, e.g., the image masks), we subtract the signal computed around random points from the signal computed around the real lenses (see van Uitert et al. 2011).

The lensing signal around triaxial dark matter haloes has an azimuthal dependence. If galaxies are preferentially aligned or oriented at a 90° angle (anti-aligned) with respect to the dark matter distribution, the lensing signal along the galaxies' major axis is respectively larger or smaller than along the minor axis, and this dependence can be determined.

To measure the anisotropy in the signal, we first follow the approach used by Parker et al. (2007). For each lens, the tangential shear is measured separately using the sources that lie within 45° of the semi-major axis ($\gamma_{t,\mathrm{B}}$), and using those that lie within 45° of the semi-minor axis ($\gamma_{t,\mathrm{A}}$) (indicated by `B` and `A` in Figure 5.3, respectively). The ratio of the shears captures the anisotropy of the signal:

$$f_{\mathrm{mm}}(r) = \frac{\gamma_{t,\mathrm{B}}(r)}{\gamma_{t,\mathrm{A}}(r)}. \tag{5.4}$$

A value of f_{mm} that is significantly larger (smaller) than unity at small scales indicates that the dark matter haloes are (anti-)aligned with the galaxies. Systematic contributions to the shear, however, may bias the anisotropy of the lensing signal. If the systematic shear is fairly constant on the scales where we measure the signal, it can be removed following Mandelbaum et al. (2006a). In this approach, the cross shear component computed in the regions that are

rotated by 45° with respect to the major/minor axes (region C and D in Figure 5.3), $\gamma_{\times,\mathrm{C-D}} \equiv (\gamma_{\times,\mathrm{C}} - \gamma_{\times,\mathrm{D}})/2$, is subtracted from the tangential shear. Spurious shear signals contribute equally to $\gamma_{t,\mathrm{A}}$, $\gamma_{t,\mathrm{B}}$ and $\gamma_{\times,\mathrm{C-D}}$, and are therefore removed. The corrected ratio then becomes:

$$f_{\mathrm{mm}}^{\mathrm{corr}}(r) = \frac{\gamma_{t,\mathrm{B}}(r) + \gamma_{\times,\mathrm{C-D}}(r)}{\gamma_{t,\mathrm{A}}(r) - \gamma_{\times,\mathrm{C-D}}(r)}. \tag{5.5}$$

If $\gamma_{\times,\mathrm{C-D}}$ is zero, the errors on $f_{\mathrm{mm}}^{\mathrm{corr}}$ approximately increase by a factor $\sqrt{1+1/\sqrt{2}}$; if $\gamma_{\times,\mathrm{C-D}}$ is non-zero, however, the errors of $f_{\mathrm{mm}}^{\mathrm{corr}}$ can either become larger or smaller than those of f_{mm}.

Alternatively, we can assume that the differential surface density distribution can be described by an isotropic part plus an azimuthally varying part (Mandelbaum et al. 2006a):

$$\Delta\Sigma_{\mathrm{model}}(r) = \Delta\Sigma_{\mathrm{iso}}(r)[1 + 2fe_g\cos(2\Delta\theta)], \tag{5.6}$$

where e_g is the observed ellipticity of the lens, $\Delta\theta$ is the angle from the major axis, and f is the ratio of the amplitude of the anisotropy of the lensing signal and the ellipticity of the galaxy, which is the parameter we want to determine. Mandelbaum et al. (2006a) show that the azimuthally varying part is given by:

$$f\Delta\Sigma_{\mathrm{iso}}(r) = \frac{\sum_i w_i \Delta\Sigma_i e_{g,i}\cos(2\Delta\theta_i)}{2\sum_i w_i e_{g,i}^2\cos^2(2\Delta\theta_i)}, \tag{5.7}$$

with i the index of the lens-source pairs, w_i the weight applied to the ellipticity estimate of each source galaxy, which is calculated from the shape noise, and $e_{g,i}$ the ellipticity of the lens. This ellipticity is also determined using the KSB method, and it is a measure of $(1-R^2)/(1+R^2)$ with R the axis ratio ($R \leq 1$) if the lens has elliptical isophotes. To remove contributions from systematic shear, we also measure

$$f_{45}\Delta\Sigma_{\mathrm{iso}}(r) = \frac{\sum_i w_i \Delta\Sigma_{i,45} e_{g,i}\cos(2\Delta\theta_i + \pi/2)}{2\sum_i w_i e_{g,i}^2\cos^2(2\Delta\theta_i + \pi/2)}, \tag{5.8}$$

where $\Sigma_{i,45}$ is the projected surface density measured by rotating the source galaxies by 45°. The systematic shear corrected halo ellipticity estimator is then given by $(f - f_{45})\Delta\Sigma_{\mathrm{iso}}(r)$. The average values of f_{mm}, $f_{\mathrm{mm}}^{\mathrm{corr}}$ and $(f - f_{45})$ within a certain range of projected separations are determined by calculating the ratio of two measurements for each radial bin, and subsequently averaging that ratio within the range of interest. We assume that the errors of each measurement are Gaussian. Consequently, the probability distribution of the ratio is asymmetric, which we have to account for. We describe how to calculate the mean and the errors of the ratio for a radial bin, and how to average that ratio within a certain range of projected separations, in Appendix 5.C. Note that to convert f, the anisotropy in the shear field, to $f_h = e_h/e_g$, the ratio of the ellipticity of the dark matter halo and the ellipticity of the galaxy, we have to adopt a density profile (e.g. f/f_h=0.25 for a singular isothermal ellipsoid, see Mandelbaum et al. 2006a).

It is clear from Figure 5.2 that the ellipticity distributions of the red and blue lens samples are different. It is unclear, however, whether the underlying

ellipticity distribution of the dark matter haloes differs as well. If the underlying distribution is similar for both samples, the projected dark matter halo ellipticity cannot depend linearly on the galaxy ellipticity. Hence Equation (5.6) might not be optimal, and could depend differently on e_g. We therefore generalise Equation (5.7) to

$$f\Delta\Sigma_{\rm iso}(r) = A\frac{\sum_i w_i \Delta\Sigma_i e_{g,i}^{\alpha}\cos(2\Delta\theta_i)}{2\sum_i w_i e_{g,i}^{2\alpha}\cos^2(2\Delta\theta_i)}, \tag{5.9}$$

$$A = \frac{\Sigma_i e_{g,i}^{2\alpha}}{\Sigma_i e_{g,i}^{\alpha}}\frac{\Sigma_i e_{g,i}}{\Sigma_i e_{g,i}^2} \tag{5.10}$$

and calculate it for different values of α. Equation (5.8) changes similarly. The factor A in Equation (5.9) scales each measurement of f to the 'standard' of $\alpha = 1$ as used in Mandelbaum et al. (2006a), which eases a comparison of f for different values of α. The optimal weight results in the best signal-to-noise of the measurement.

The different halo ellipticity estimators can in principle be used to study the relation between the ellipticity of the galaxy and the ellipticity of their dark matter hosts. In particular, Equation (5.5) is defined such that it depends on the average dark matter halo ellipticity, whilst Equation (5.9) is sensitive to the relation between the galaxy ellipticity and the dark matter ellipticity. Hence by comparing the $f\Delta\Sigma_{\rm iso}(r)$ for different values of α, we gain insight in the relation between the ellipticity of the galaxies and their dark matter haloes. Note that as an alternative, we could weight Equation (5.5) with the lens ellipticity.

It is useful to assess the signal-to-noise we expect to obtain for the shear anisotropy measurement compared to the signal-to-noise of the tangential shear itself. For this purpose, we write Equation (5.6) in its most basic form:

$$\Delta\Sigma_{\rm model}(r) = \Delta\Sigma_{\rm iso}(r)[1 + \bar{f}\cos(2\Delta\theta)], \tag{5.11}$$

which has the following solution for the anisotropic part:

$$\bar{f}\Delta\Sigma_{\rm iso} = \frac{\sum_i w_i \Delta\Sigma_i \cos(2\Delta\theta_i)}{\sum_i w_i \cos^2(2\Delta\theta_i)}. \tag{5.12}$$

If the dark matter halo is described by a singular isothermal ellipsoid (SIE; see Mandelbaum et al. 2006a), and if the galaxy is perfectly aligned with the halo, we find $\bar{f} = e_h/2$. Hence the anisotropic signal is a factor $e_h/2$ lower than the isotropic signal. To assess the relative size of the error of $\bar{f}\Delta\Sigma_{\rm iso}$ compared to $\Sigma_{\rm iso}$, we insert Equation (5.11) into Equation (5.12), define a new weight $\widetilde{w_i} \equiv w_i\cos^2(2\Delta\theta_i)$, and determine the error using $\sigma_{\bar{f}\Delta\Sigma_{\rm iso}} = 1/\sqrt{\sum_i \widetilde{w_i}}$. Since w_i and $\cos^2(2\Delta\theta_i)$ are uncorrelated, it follows that $\sigma_{\bar{f}\Delta\Sigma_{\rm iso}} = 1/\sqrt{\sum_i w_i\langle\cos^2(2\Delta\theta)\rangle} = \sqrt{2}\sigma_{\Delta\Sigma_{\rm iso}}$, with $\sigma_{\Delta\Sigma_{\rm iso}} = 1/\sqrt{\sum_i w_i}$ the error on $\Delta\Sigma_{\rm iso}$. Hence the error of $\bar{f}\Delta\Sigma_{\rm iso}$ is a factor $\sqrt{2}$ larger than the error of $\Delta\Sigma_{\rm iso}$. Consequently, the signal-to-noise of the anisotropic part of the lensing signal, $({\rm S/N})_{\rm ani}$, is related to the signal-to-noise of the isotropic part, $({\rm S/N})_{\rm iso}$, as:

$$({\rm S/N})_{\rm ani} = \frac{0.15}{\sqrt{2}}\left(\frac{e_h}{0.3}\right)({\rm S/N})_{\rm iso}. \tag{5.13}$$

In the best-case scenario, the expected signal-to-noise of the shear anisotropy is an order of magnitude lower than the signal-to-noise of the azimuthally averaged

shear. Applying the correction to remove systematic contributions increases the errors of the shear anisotropy by another factor of $\sqrt{2}$. If the dark matter is described by an elliptical NFW, the signal decreases rapidly with increasing separation (see Figure 2 of Mandelbaum et al. 2006a), and is only larger than the SIE signal on very small scales. If no redshift information is available for the lenses, the rapid decline of the shear anisotropy is particularly disadvantageous as the signal can only be averaged as a function of angular separation. Consequently, the anisotropy signal is smeared out, making it harder to detect. Finally, if the galaxy and the halo are misaligned, the signal decreases even further. These considerations show that we need very large lens samples to achieve sufficient signal-to-noise to enable a detection, and it motivates our choice to select broad lens samples.

5.2.4 Contamination correction

A fraction of our source galaxies are physically associated with the lenses. They cannot be removed from the source sample because we lack redshifts. Since these galaxies are not lensed, but are included in calculating the average lensing signal, they dilute the signal. To correct for this dilution, we boost the lensing signal with a boost factor, i.e. the excess source galaxy density ratio around the lenses, $1+f_{cg}(r)$. This is the ratio of the local total (satellites + source galaxies) number density and the average source galaxy number density. This correction assumes that the satellite galaxies are randomly oriented. If the satellites are preferentially radially aligned to the lens, the contamination correction for the azimuthally averaged tangential shear will be too low. If the radial alignment of the physically associated galaxies has an azimuthal dependence, the shear anisotropy can either be biased high or low.

This type of intrinsic alignment has been studied with seemingly different results; some authors (e.g. Agustsson & Brainerd 2006; Faltenbacher et al. 2007) who determined the galaxy orientation using the isophotal position angles, have observed a stronger alignment than others (e.g. Hirata et al. 2004; Mandelbaum et al. 2005a) who used galaxy moments. This discrepancy was attributed by Siverd et al. (2009) and Hao et al. (2011) to the different definitions of the position angle of a galaxy; the favoured explanation is that light from the central galaxy contaminates the light from the satellites, which affects the isophotal position angle more than the galaxy moments one. As we measure the shapes of source galaxies using galaxy moments, we expect that intrinsic alignment has a minor impact at most and can be ignored.

To study whether the distribution of source galaxies has an azimuthal dependence, we perform the analysis separately using the galaxies residing within 45 degrees of the major axis, and within 45 degrees of the minor axis. On small scales, the extended light of bright lenses leads to erroneous sky background estimates, which causes a local deficiency in the source number density. This deficiency is different along the major axis and minor axis, which could bias the correction we make to account for physically associated galaxies in the source sample. To determine which scales are affected, we study the source number density around galaxies as a function of their brightness and ellipticity. The results are shown in Appendix 5.D. For galaxies with $m_{r'} < 19$, we find a larger deficiency along the major axis on projected scales smaller than 0.2 arcmin; for galaxies with $m_{r'} > 19$, the deficiency is larger on projected scales smaller than

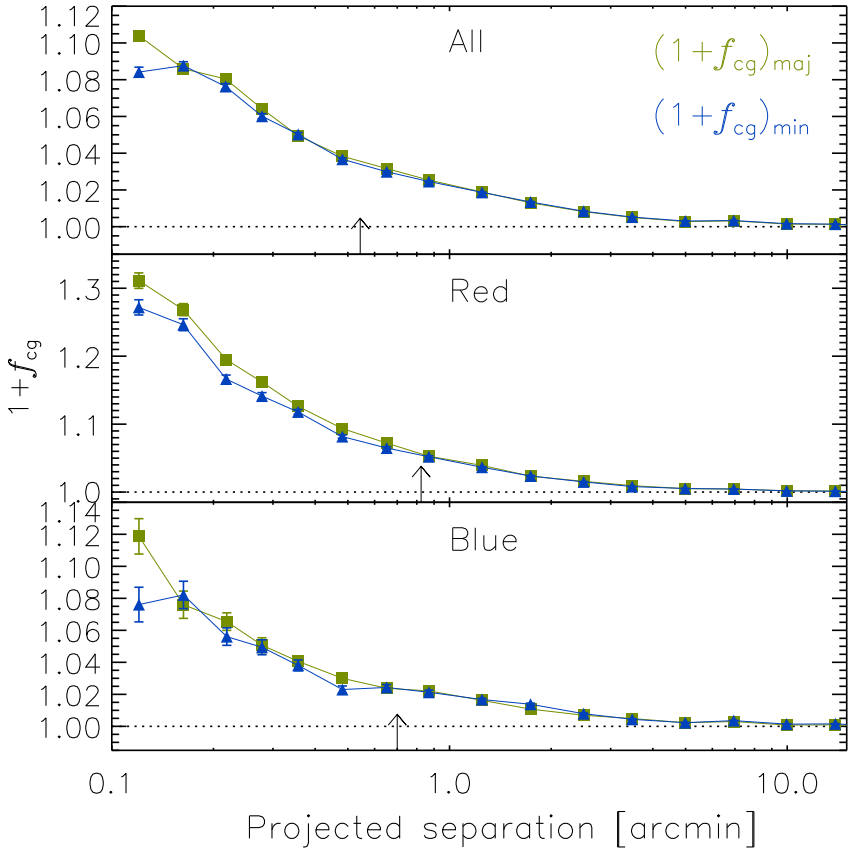

Figure 5.4: Excess source galaxy density ratio as a function of projected distance to the lenses. The green squares (blue triangles) indicate the excess density ratio measured using sources within 45 degrees of the major (minor) axis. The arrows indicate the location of the virial radius at the mean redshift of the lenses. We find that the excess density ratio along the major axis is higher than along the minor axis, most noticeably for the 'red' sample. Please note the different scales of the vertical axes.

0.1 arcmin. Therefore, we only use scales larger than 0.1 arcmin for galaxies with $m_{r'} > 19$, and scales larger than 0.2 arcmin for galaxies with $m_{r'} < 19$. The overdensities around the lens samples are shown in Figure 5.4. We find that the source sample is only mildly contaminated by physically associated galaxies, as the overdensities reach a maximum excess of only 30% for the 'red' lenses at the smallest projected separations. The excess source galaxy density ratio is a few percent larger along the major axis than along the minor axis within the virial radii of the lens samples, most noticeably for the 'red' lens sample.

The measured anisotropy is caused by two effects[4]: anisotropic magnifica-

[4]Another effect is mentioned in Mandelbaum et al. (2006a) that could cause an anisotropic source density ratio: additional lensing by foreground galaxies. We estimate that this has a

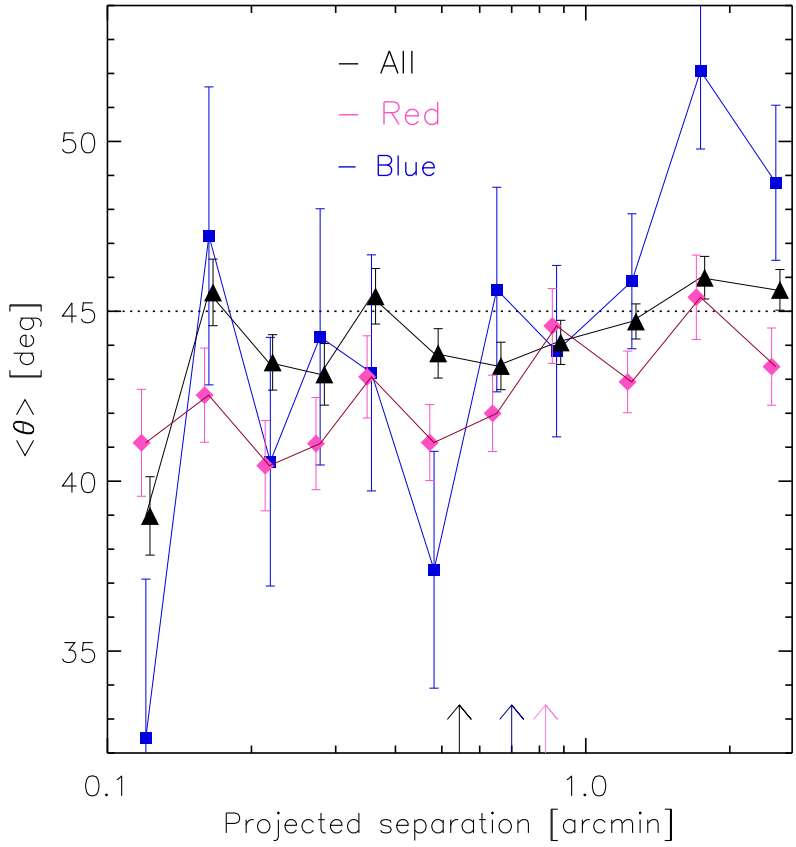

Figure 5.5: Mean angle between the location of the satellites and the major axis of the lens galaxy as a function of projected separation. The orange triangles, purple diamonds and blue squares indicate the results for the 'all', 'red' and 'blue' lens sample. The arrows on the horizontal axis indicate the location of the virial radii at the mean redshift of the lenses, and correspond to 150 kpc, 280 kpc and 192 kpc for the 'all', 'red' and 'blue' lens samples, respectively. The satellite galaxies preferentially reside near the major axis of the lenses.

tion, and the presence of physically associated sources that are anisotropically distributed. As we lack redshifts for our galaxies, we cannot disentangle the two effects. However, we estimate the impact of anisotropic magnification for the lens samples in Appendix 5.E, and find that even in the case where the galaxy and the dark matter halo are perfectly aligned, the effect is small. We conclude therefore that the observed anisotropy is the result of the anisotropy of the distribution of satellite galaxies.

We correct the tangential shear in the major and minor axis quadrant for the contamination by satellites by multiplying with their respective excess galaxy

negligible impact because the number of additional massive foreground galaxies is small due to our lens sample selection.

density ratio, before we measure the shear ratios. To calculate the correction of $(f - f_{45})$, we observe how $f\Delta\Sigma_{\rm iso}(r)$ changes in the presence of physically associated galaxies in the source sample that are anisotropically distributed. Rather than Equation (5.7), the quantity we actually measure is

$$\widetilde{f\Delta\Sigma_{\rm iso}}(r) = \frac{A}{N}\sum_i \frac{w_i \Delta\Sigma_i e_{g,i}^{\alpha}\cos(2\Delta\theta_i)}{1+f_{\rm cg}(r,\Delta\theta)}; \\ N = 2\sum_i w_i e_{g,i}^{2\alpha}\cos^2(2\Delta\theta_i), \tag{5.14}$$

with $1 + f_{\rm cg}(r, \Delta\theta)$ the azimuthally varying excess galaxy density ratio, and $\widetilde{\Delta\Sigma_{\rm iso}}$ the unboosted lensing signal. We assume that $1+f_{\rm cg}(r, \Delta\theta)$ has a similar azimuthal dependence as the shear, and can be described by

$$1 + f_{\rm cg}(r, \Delta\theta) = N_{\rm iso}(r) + 2N_{\Delta\theta}(r)e_g^{\alpha}\cos(2\Delta\theta), \tag{5.15}$$

with α the exponent of the ellipticity used to weigh the shear measurement, $N_{\rm iso}$ the azimuthally averaged boost factor and $N_{\Delta\theta}$ the amplitude of the anisotropy. Using a Taylor expansion, we find that to first order

$$f(r) = \widetilde{f(r)} + f_{\rm eff}(r), \tag{5.16}$$

with $f_{\rm eff}(r) = AN_{\Delta\theta}(r)/N_{\rm iso}(r)$. To determine $f_{\rm eff}(r)$, we measure both the angle-averaged boost factor, $N_{\rm iso}(r) = N_{\rm LS}/N_{\rm LR}$, where $N_{\rm LS}$ denotes the number of lens-source pairs and $N_{\rm LR}$ the number of pairs of lenses with random sources, and the azimuthally varying part, $\xi_{\Delta\theta}(r) = \sum_{\rm LS} e_g^{\alpha}\cos(2\Delta\theta)/N_{\rm LR}$. For the adopted model of the excess galaxy density ratio this gives $N_{\rm iso}(r) = \langle 1 + f_{\rm cg}(r)\rangle_{\Delta\theta}$, which is averaged over the angle, and $\xi_{\Delta\theta} = 2N_{\Delta\theta}(r)e_g^{2\alpha}$. These measurements are combined to give

$$f_{\rm eff}(r) = A\frac{\xi_{\Delta\theta}(r)}{\langle 1 + f_{\rm cg}(r)\rangle_{\Delta\theta}\langle e_g^{2\alpha}\rangle}. \tag{5.17}$$

We determine the average value of $f_{\rm eff}(r)$ within the virial radius, and add it to $\langle f - f_{45}\rangle$. The values are tabulated in Table 5.3. Note that a similar correction is applied in Mandelbaum et al. (2006a).

To compare the anisotropy of the distribution of satellites to the literature, we now assume that at a narrow radial range the excess galaxy density ratio can be described by $1 + f_{\rm cg} = N_{\rm iso} + \widetilde{N_{\Delta\theta}\cos(2\Delta\theta)}$. We fit this to the excess density ratio in the major and minor axis quadrants, separately for each radial bin. We use these fits to compute $\langle\theta\rangle$, the mean angle between the location of the satellites and the major axis of the central galaxy, using

$$\langle\theta\rangle = \frac{\int_0^{\pi/2} d\theta\theta f_{\rm cg}(\theta)}{\int_0^{\pi/2} d\theta f_{\rm cg}(\theta)}. \tag{5.18}$$

In Figure 5.5, we show $\langle\theta\rangle$ as a function of projected separation for the three lens samples.

We find that satellite galaxies preferentially reside near the major axis of the lenses, most strongly for the 'red' lenses. We determine the weighted mean

of $\langle\theta\rangle$ within the virial radius, and find $\langle\theta\rangle = 43.7^\circ \pm 0.3^\circ$ for the 'all' sample, $\langle\theta\rangle = 41.7^\circ \pm 0.5^\circ$ for the 'red' sample and $\langle\theta\rangle = 42.0^\circ \pm 0.4^\circ$ for 'blue' sample. Additionally, for the 'red' lenses we find that $\langle\theta\rangle$ becomes more isotropic at larger projected separations. It is useful to compare our results to previous studies, that are based on simulations (e.g. Sales et al. 2007; Faltenbacher et al. 2008; Agustsson & Brainerd 2010) and observations (e.g. Brainerd 2005; Agustsson & Brainerd 2006, 2010; Faltenbacher et al. 2007; Bailin et al. 2008; Nierenberg et al. 2011). In these works, $\langle\theta\rangle$ is found to be in the range between 41° and 43° for red central galaxies, whilst no anisotropy is observed for blue central galaxies. We can only make a useful comparison for the 'red' lens sample, as this sample is comparable to previously studied red galaxy samples (i.e. predominantly containing red early-type galaxies, the majority of them expected to be centrals based on their luminosity distribution). We find that the constraints agree well. For the 'blue' and 'all' sample, we cannot make a comparison to previous work as these samples contain a mixture of early-type and late-type galaxies, and a fair fraction of them is expected to be a satellite of a larger system. The constraints we obtained are still interesting, however, as similar selection criteria can be applied to simulations, and the results compared.

5.2.5 Virial masses and radii

To determine to which projected separations the dark matter haloes of the galaxies dominate the lensing signal, we estimate the average halo size of each lens sample. For this purpose we model the azimuthally averaged tangential shear (after applying the contamination corrections) with an NFW profile, and fit for the mass. The NFW density profile is given by

$$\rho(r) = \frac{\delta_c \rho_c}{(r/r_s)(1 + r/r_s)^2}, \tag{5.19}$$

with δ_c the characteristic overdensity of the halo, ρ_c the critical density for closure of the universe, and $r_s = r_{200}/c_{\rm NFW}$ the scale radius, with $c_{\rm NFW}$ the concentration parameter. We adopt the mass-concentration relation from Duffy et al. (2008)

$$c_{\rm NFW} = 5.71 \left(\frac{M_{200}}{2 \times 10^{12} h^{-1} M_\odot}\right)^{-0.084} (1+z)^{-0.47}, \tag{5.20}$$

which is based on numerical simulations using the best fit parameters of the WMAP5 cosmology. M_{200} is defined as the mass inside a sphere with radius r_{200}, the radius inside of which the density is 200 times the critical density ρ_c. We calculate the tangential shear profile using the analytical expressions provided by Bartelmann (1996) and Wright & Brainerd (2000). We fit the NFW profile between 50 and 500 kpc at the mean lens redshift; closer to the lens the lensing signal might be contaminated by lens light, and at larger separations neighbouring structures bias the lensing signal high. The best fit M_{200}, r_{200} and r_s are given in Table 5.1. Note that in general, the best fit masses are lower than the mean halo mass because the shear of NFW profiles does not scale linearly with mass, and the distribution of the halo masses is not uniform (Tasitsiomi et al. 2004; Mandelbaum et al. 2005b; Cacciato et al. 2009; Leauthaud et al. 2012; van Uitert et al. 2011). The resulting uncertainty in the actual mass is not

Table 5.2: Shear ratios for the lens samples

Sample	$\langle 1/f_{\rm mm}\rangle$	$\langle 1/f_{\rm mm}^{\rm corr}\rangle$
All	$1.15^{+0.10}_{-0.09}$	0.87 ± 0.09
Red	$0.93^{+0.10}_{-0.09}$	$0.81^{+0.11}_{-0.10}$
Blue	$1.16^{+0.19}_{-0.16}$	$1.04^{+0.21}_{-0.17}$

important here as we are mainly interested in the extent of the haloes, which is affected less (an increase of 30% in mass leads to an increase of only 10% in size).

5.3 Shear ratio

In this section we present the measurements of the ensemble-averaged ratio of the tangential shear along the major and minor axis of the lenses. This is a basic indicator of the presence of anisotropies in the lensing signal. We note that the shear ratio is not an optimal estimator as the weight is simply a step function, and does not depend on the ellipticity of the galaxy. It enables, however, a comparison to Parker et al. (2007). Furthermore, we will use the shear ratio to examine how PSF residual systematics in the shape catalogues affect the anisotropy (Section 5.3.1).

For all elliptical non-power law profiles, the shear ratio varies as a function of distance to the lens. This radial dependence differs for different dark matter density profiles (Mandelbaum et al. 2006a). Hence to obtain constraints on the halo ellipticity of the dark matter, we have to adopt a particular density profile. To compare our results to those from Parker et al. (2007), we first assume that the density profile follows an SIE profile on small scales. In that case, the shear ratio is constant, and we determine the average and the 68% confidence limits as detailed in Appendix 5.C.

In Figure 5.6, we show the average tangential shear along the major and minor axis, the average cross shear in the quadrants that are rotated by 45 degrees, and the inverse of the shear ratios $f_{\rm mm}$ and $f_{\rm mm}^{\rm corr}$. The tangential shear and the cross shear have been multiplied with the projected separation in arcmin, to enhance the visibility of the measurements on large scales where the signal is close to zero and the error bars are small. We show the inverse of the ratios following the definition used in Parker et al. (2007). We do not observe a clear signature for an alignment or anti-alignment between the lenses and their dark matter haloes. Furthermore, we find that on small scales (<1 arcmin), $f_{\rm mm}$ and $f_{\rm mm}^{\rm corr}$ are consistent, which suggests that the systematics present on these scales are smaller than the measurement errors. On larger scales, the difference is larger, which underlines the importance of applying the corrections to remove systematic contributions. The correction is largest for the 'all' lens sample, because its lensing signal is smallest and therefore most susceptible to systematic contributions. We determine the average shear ratio within the virial radius at the mean lens redshift, and show the results in Table 5.2.

Parker et al. (2007) used 22 square degrees of the CFHTLS to measure the

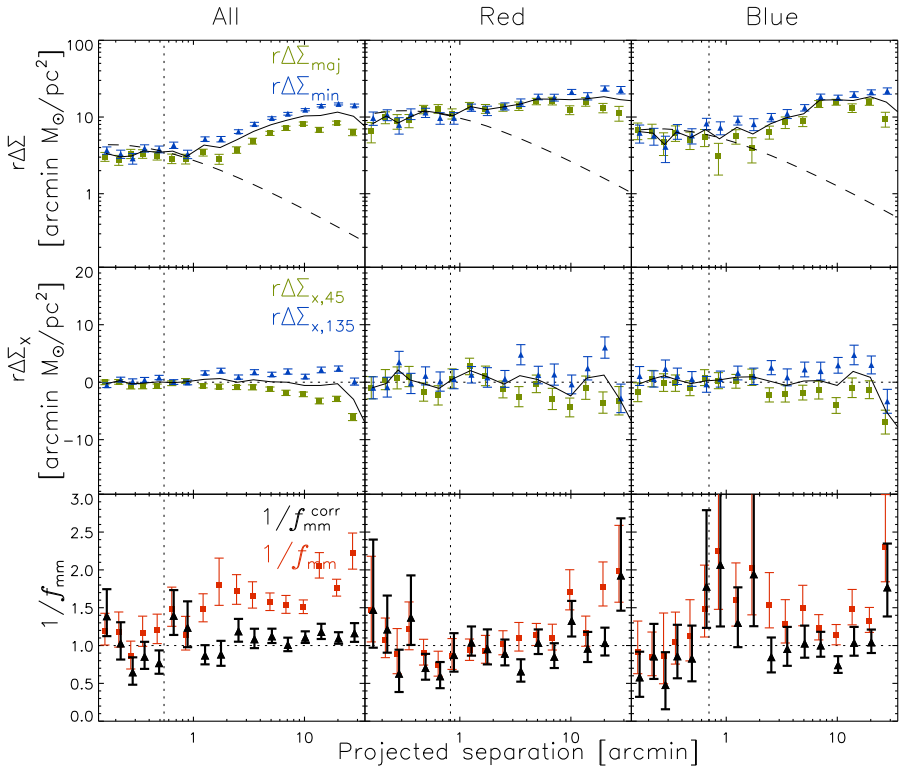

Figure 5.6: Lensing signal multiplied with the projected separation in arcmin as a function of angular distance from the lens, for the 'all' lens sample (left-hand panels), the 'red' lens sample (middle panels) and the 'blue' lens sample (right-hand panels). In the top panels, the green squares (blue triangles) show the average $r\Delta\Sigma$ along the major (minor) axis (quadrants `B` (`A`) in Figure 5.3). The dashed lines indicate the best fit NFW profile times the projected separation, fitted to the azimuthally averaged lensing signal on scales between 50 and 500 kpc using the mean lens redshift. In the middle panel, the green squares (blue triangles) show the cross shear signal averaged in quadrant `D` (`C`) of Figure 5.3. In the bottom panels, $1/f_{\rm mm}$ and $1/f_{\rm mm}^{\rm corr}$ are shown by the red squares and black triangles, respectively. The dotted lines indicate the virial radius from the best-fit NFW profiles. The shear ratio does not provide clear signs for the alignment between galaxies and their dark matter haloes.

shapes of $\sim 2\times10^5$ lenses, selected with a brightness cut of $19 < i' < 22$. Their lens sample consisted of a mixture of early-type and late-type galaxies with a median redshift of 0.4. The shear ratio was determined using measurements out to 70 arcsec (corresponding to 250 h^{-1} kpc at $z = 0.4$), with a best-fit value of $\langle 1/f_{\rm mm}\rangle = 0.76 \pm 0.10$. Excluding the round lenses with $e < 0.15$, the best-fit ratio is $\langle 1/f_{\rm mm}\rangle = 0.56 \pm 0.13$. The lens sample from Parker et al. (2007) can be best compared to our 'all' sample; comparing the relative number of early-/late-types in both samples using the CFHTLS W1 photometric redshift catalogue (Hildebrandt et al. 2011), we find they are similar. Also, the average mass of the lenses are comparable. Fitting the shear ratio on the same physical scale, we find

$\langle 1/f_{\rm mm}^{\rm corr}\rangle = 0.98\pm0.08$ for the 'all' sample, which is $\sim 2\sigma$ larger than Parker et al. (2007). Excluding lenses with $e < 0.15$, we find $\langle 1/f_{\rm mm}^{\rm corr}\rangle = 0.95^{+0.11}_{-0.10}$, which is even almost 3σ apart. Since the lens samples are comparable, this is most likely the result of differences in the analysis. Firstly, Parker et al. (2007) do not apply a correction for systematic contributions. However, systematic shear only tends to increase $1/f_{\rm mm}$; if systematics were present, the discrepancy would be even larger. Secondly, it is not clear whether Parker et al. (2007) accounted for the non-gaussianity of the ratio of two gaussian distributed variables in determining the shear ratio; this is particularly important when the signal-to-noise of the lensing measurements is not very high. Generally, accounting for the non-gaussianity increases the positive error bar of the shear ratio, and decreases the negative one. This could bring their result closer to ours. Finally, it is not described how the average ratio was determined. These differences could explain the discrepancy between the results.

5.3.1 Imperfect PSF correction

To measure the ellipticities of galaxies, we have to correct their observed shapes for smearing by the PSF. The precision of the PSF correction is limited, which is mainly due to the inaccuracy of the PSF model (Hoekstra 2004). Hence, residual PSF patterns may still be present in the shape catalogues. These residuals affect both the ellipticity estimates of the lens and the source galaxies, albeit with a different amount. Lens galaxies are typically large and bright, while source galaxies are small and faint, and hence harder to correct for. Regardless of that, PSF residuals tend to align the lens and source galaxies. If not accounted for, it could add a false anti-alignment signal to the shear anisotropy measurement (see Hoekstra et al. 2004).

We correct for PSF residual systematics in the catalogues by subtracting the cross shear signal in the quadrants that are rotated by 45 degrees with respect to the major and minor axes ($\gamma_{x,\rm C-D}$ and $f_{45}\Delta_{\rm iso}(r)$ in $f_{\rm mm}^{\rm corr}$ and $(f - f_{45})$, respectively). To quantify how much PSF residuals actually contribute to these correction terms, and test whether they are properly removed, we introduce on purpose an additional bias in the PSF correction, and recalculate the shapes of the galaxies. Usually, the ellipticities of galaxies in the KSB method are computed as follows:

$$e_g = \frac{1}{P_\gamma}\Big[\epsilon - (1+b)\times\frac{P^{\rm sm}}{P^{\rm sm\star}}\epsilon^\star\Big], \tag{5.21}$$

with P_γ the shear polarisability, $P^{\rm sm}$ the smear susceptibility tensor, and ϵ the polarizations (Kaiser et al. 1995). The starred quantities are determined using the PSF stars. The bias b is normally equal to zero, but to mimic an imperfect PSF correction we set it to -0.05, and recalculate the shapes of all galaxies. We create new random shear catalogues, and repeat the analysis using these biased shapes. We show the difference between the original and the biased shear ratios of the lens samples in Figure 5.7.

We find that the difference of the shear ratios that are determined using the original and the PSF biased catalogues is consistent with zero on all scales for $1/f_{\rm mm}^{\rm corr}$, the shear ratio estimator that is corrected with the cross shear terms. For the uncorrected shear ratio estimator, $1/f_{\rm mm}$, we find that the difference is consistent with zero on small scales, but turns negative for projected separations

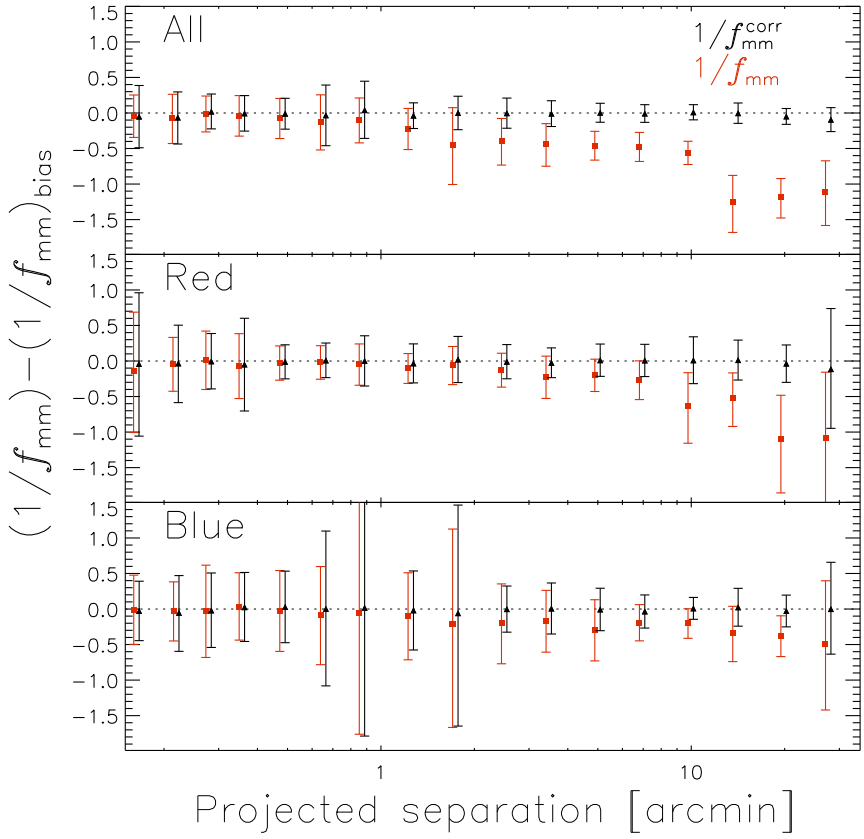

Figure 5.7: Difference between the original and the PSF biased shear ratios $(1/f_{\rm mm}^{\rm corr})-(1/f_{\rm mm}^{\rm corr})_{\rm bias}$ (black triangles) and $(1/f_{\rm mm})-(1/f_{\rm mm})_{\rm bias}$ (red squares) as a function of projected separation from the lens for the three lens samples. We find that the PSF residuals are properly removed from the corrected ratio $1/f_{\rm mm}^{\rm corr}$, as the difference is consistent with zero on all scales. For the uncorrected ratio $1/f_{\rm mm}$, the difference is negative and decreases with projected separation. This result shows that the cross term effectively removes PSF residuals in the shear ratio estimators.

larger than a few arcmins. This shows that if PSF residuals are still present in the shape catalogues, it affects $1/f_{\rm mm}$, but not $1/f_{\rm mm}^{\rm corr}$. Hence we conclude that PSF residuals are properly accounted for using the cross shear signal.

5.4 Impact of multiple lenses

More than one lens may contribute to the shearing of a single source galaxy. Furthermore, some of the lenses are lensed themselves. In this section, we estimate the impact of these multiple lensing events on the halo ellipticity measurements. We also study the impact of the clustering of the lenses, and the

correlation between their shapes, on the shear anisotropy.

5.4.1 Multiple deflections

Some foreground galaxies in our data lens both the lenses from the lens samples and the source galaxies. We denote these foreground galaxies with L2, and our selected lenses with L1. The impact of these 'multiple deflections' on the halo ellipticity measurements were first discussed in Howell & Brainerd (2010), who found that it adds a strong false anti-alignment signal to the shear anisotropy measurements. Multiple deflections affect the halo shape measurement in three ways. Firstly, the orientation of the lens light changes, leading to a misalignment if the light was aligned with the halo. Consequently, the lensing signal is averaged in quadrants that are rotated with respect to the unlensed ones, causing a reduction of the shear anisotropy. This effect is only important if the projected separation between L2 and L1 is small, as only those configurations lead to significant changes in the ellipticity of L1. Secondly, the source galaxies experience shear not only from L1, but also from L2. Especially source galaxies close to L2 are affected. Finally, the lensing of L2 changes the observed positions of L1 and the sources. We ignore this third effect as the impact is negligible.

In the presence of L2, Equation (5.4) changes to

$$\tilde{f}_{\rm mm}(r) = \frac{\int_{-\pi/4+\delta\theta}^{\pi/4+\delta\theta} \tilde{\gamma_t} d\theta + \int_{3\pi/4+\delta\theta}^{5\pi/4+\delta\theta} \tilde{\gamma_t} d\theta}{\int_{\pi/4+\delta\theta}^{3\pi/4+\delta\theta} \tilde{\gamma_t} d\theta + \int_{5\pi/4+\delta\theta}^{7\pi/4+\delta\theta} \tilde{\gamma_t} d\theta}, \tag{5.22}$$

where the integration is performed over quadrants that are rotated by $\delta\theta$, the change of the position angle of L1 caused by the lensing of L2. $\tilde{\gamma_t}$ is the sum of the shear of L1 and L2 at the location of a source galaxy. The $\tilde{\gamma_1}$-component is given by $\tilde{\gamma_1} = \gamma_{t,L1}\cos(2\theta) + \gamma_{t,L2}\cos(2\phi)$, with $\gamma_{t,L1}$ and $\gamma_{t,L2}$ the tangential shear of L1 and L2, θ the angle between the source galaxy and L1 and ϕ the angle between the source galaxy and L2. Hence the signal that is measured is given by

$$\begin{aligned}\tilde{\gamma_t} = &[\gamma_{t,L1}\cos(2\theta) + \gamma_{t,L2}\cos(2\phi)] \times \cos(2\theta) + \\ &[\gamma_{t,L1}\sin(2\theta) + \gamma_{t,L2}\sin(2\phi)] \times \sin(2\theta).\end{aligned} \tag{5.23}$$

The change of the equations for $f_{\rm mm}^{\rm corr}(r)$, $f\Delta\Sigma_{\rm iso}(r)$ and $f_{45}\Delta\Sigma_{\rm iso}(r)$ in the presence of L2 can be derived in a similar way.

To obtain an intuitive understanding of the impact of multiple deflections on the halo ellipticity measurements, we compute the change of the shear anisotropy of a single lens in the presence of an additional foreground galaxy using simple idealised simulations. These simulations, which are discussed in Appendix 5.F, suggest that multiple deflections mainly affect the shear anisotropy of round ($e < 0.15$) lens galaxies, and at large projected separations. To confirm these findings, we create a large set of simulated image catalogues to obtain a rough estimate of the impact.

For the simulated catalogues we adopt an image size of 30×30 arcmins. We randomly assign positions to 10 000 galaxies (approximately the galaxy number density of the RCS2). Redshifts are assigned to each background galaxy by drawing from the redshift distribution of the RCS2 source galaxies. The

background galaxies are intrinsically round, and not convolved with a PSF, to avoid introducing unnecessary sources of noise. We insert 50 lenses at a typical lens redshift of $z = 0.4$, to which we assign an ellipticity e_g with a random value between 0 and 0.4 and a random position angle. The ellipticity of the dark matter halo, e_h, is proportional to the ellipticity of the galaxy via $e_h = f_{\rm h} \times e_g$. We use a fixed value for $f_{\rm h} = 1.0$, but we also test the impact of loosening this assumption. Each lens is modeled with an SIE profile, and the induced shear on each source is computed with (Mandelbaum et al. 2006a)

$$\gamma_t = \frac{4\pi\sigma^2}{c^2}\frac{D_l D_{ls}}{D_s}\frac{1}{2r} \times \left[1 + \frac{e_h}{2}\cos(2\theta)\right], \tag{5.24}$$

with e_h the ellipticity of the dark matter halo, and σ the velocity dispersion of the lens which we have set to 200 km s^{-1}. We create 20 sets of 500 catalogues, and determine the mean lensing signal and the scatter between the simulations sets. This enables us to assess the significance of potential trends.

To study the impact of multiple deflections, we would ideally assign velocity dispersions to all galaxies that reside in front of the lenses following their velocity dispersion distribution, and use them to compute the shear on the lenses and sources. The galaxies that reside behind the lenses only introduce noise, and can be ignored. This is computationally expensive as there are many galaxies at lower redshifts. However, the majority of the foreground galaxies are not massive, and are close in redshift to the lenses (resulting in small lensing efficiencies), so their contribution to multiple deflections is negligible.

For computational speed-up, we therefore define a smaller number of foreground galaxies. We choose their velocity dispersions and redshifts such that the impact of multiple deflections is comparable to what is expected using all the foreground galaxies[5]. On these grounds, we randomly insert a second set of 500 round lenses with a truncated isothermal sphere (TIS) profile with a velocity dispersion of 100 km s^{-1} and truncation radius of 150 arcsecs, located at a redshift of 0.1. Both the source galaxies and the L1 lenses are lensed by the L2 lenses, and we change their ellipticities accordingly. Then we measure the shear anisotropy around the L1 lenses as we would in observations, i.e. using the 'observed' ellipticities. We show the anisotropy of the lensing signal in panel (a) of Figure 5.8, confirming the predicted trends from Appendix 5.F: multiple deflections lead to a reduction of the shear anisotropy, with a magnitude that increases for larger separations to the lens. On small scales, the reduction of the shear anisotropy is larger for the shear estimators that have not been corrected for systematic contributions (f and $f_{\rm mm}$) than for the corrected ones ($(f - f_{45})$ and $f_{\rm mm}^{\rm corr}$) (see Figure 5.18b). As long as the separation between the sources and L1 is small, the additional shear from L2 is relatively constant and hence efficiently removed using the cross terms. The correction does not work on larger scales as the additional shear from L2 varies spatially. Note that the

[5]Using the photometric redshift catalogue of the CFHTLS "Deep Survey" fields from Ilbert et al. (2006), we find that approximately 30% of all galaxies in the RCS2 have a redshift $z < 0.4$, with a mean of $z = 0.35$. The lensing efficiency at $z = 0.1$ is about 6 times larger than at $z = 0.35$ for a source at $z = 0.4$, hence we can reduce the number of L2 lenses by a factor of six when we place them at $z = 0.1$. Note that we ignore the increase of the lensing efficiency by a factor of two for the source galaxies when the L2 lenses are placed at $z = 0.1$, which increases the impact of multiple deflections. Additionally, the use of a smaller number of more efficient lenses also leads to an increase of the impact of multiple deflections.

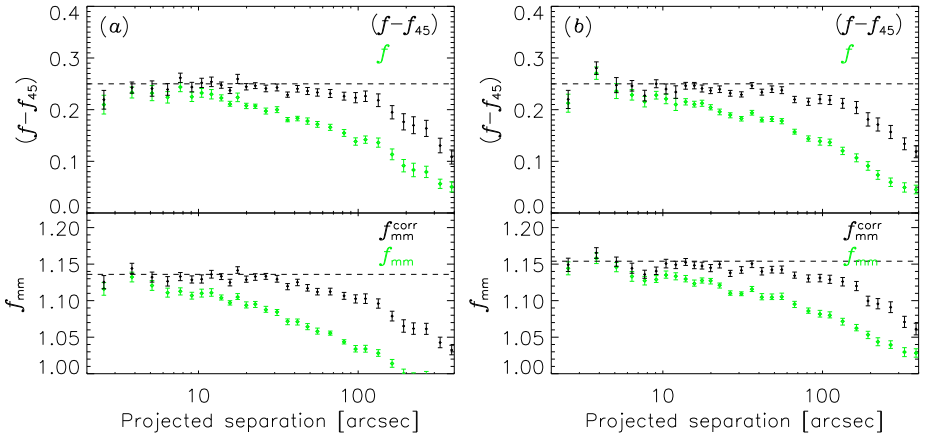

Figure 5.8: (a) Anisotropy of the lensing signal in the simulations in the presence of additional foreground galaxies that lens both the lenses and the sources. In the top panel, we show $(f-f_{45})$ and f with the filled black and open green diamonds, computed with the exponent in the weight $\alpha = 1.0$. In the lower panel, we show $f_{\rm mm}^{\rm corr}$ ($f_{\rm mm}$) with the filled black diamonds (open green diamonds). The dashed lines show the signal in the absence of multiple deflections. The uncorrected shear estimators f and $f_{\rm mm}$ are increasingly reduced for larger distances to the lens. The reduction of the systematic shear corrected estimators is clearly smaller on scales < 100 arcsec, but the difference decreases at larger separations as the systematic shear is not constant anymore and the correction therefore inaccurate. (b) Anisotropy of the lensing signal in the simulations in the presence of additional foreground galaxies, excluding lens galaxies with $e < 0.05$ from the analysis. The exclusion of round lenses is found to reduce the impact of multiple deflections, particularly for $f_{\rm mm}$ and $f_{\rm mm}^{\rm corr}$ as these measurements are not weighed with the lens ellipticity.

reduction of the shear anisotropy is smaller for $(f - f_{45})$ than for $f_{\rm mm}^{\rm corr}$, because the signal of the former is weighted with the ellipticity of the lenses; the most elliptical lenses are less affected by multiple deflections (see Appendix 5.F).

Based on Figure 5.18c in Appendix 5.F, we expect that the impact of multiple deflections is reduced if we exclude the roundest lenses. Therefore, we repeat the simulations, excluding lenses with an observed (rather than intrinsic) ellipticity $e < 0.05$ as is done in the measurements on the real data. We show the results in panel (b) of Figure 5.8. Excluding the roundest lenses significantly reduces the impact of multiple deflections for $f_{\rm mm}$ and $f_{\rm mm}^{\rm corr}$. The improvement for f and $(f - f_{45})$ is minor, as the roundest lenses are already downweighted in this measurement. There is some residual signal left on the largest scales, but to constrain halo shapes in real data we only use measurements on small scales. Therefore, we find it unlikely that multiple deflections strongly biases the lensing anisotropy.

These conclusions do, however, depend on our assumptions. The number and the masses of the L2 lenses is most critical. In our simulations, we have assumed an average velocity dispersion of 100 km s^{-1} for the L2 lenses. However,

more massive L2 lenses contribute more to multiple deflections as their shear patterns affect larger patches of the sky. Most of the massive L2 lenses reside relatively close in redshift to the L1 lenses, and consequently their lensing efficiency is small. Therefore, we do not expect that assuming a constant velocity dispersion for the L2 lenses rather than drawing them from the distribution has a large impact on the results.

A second important assumption is that we have modeled the density distribution of the L1 galaxy with an SIS. This is a reasonably accurate description of a galaxy density profile at small scales, but not on large scales. For NFW profiles, which are more appropriate, the lensing anisotropy declines strongly as a function of radius (Mandelbaum et al. 2006a). A small reduction by multiple deflections of an already small signal has a relatively larger impact. One way to account for this is to give larger weights to the measurements on small scales. Alternatively, the shear anisotropy could be fit using measurements on small scales only.

We also assumed that the relation between the ellipticity of the galaxy and the ellipticity of the dark matter halo is linear. To study the impact this might have on the anisotropy of the lensing signal, we loosen the assumption. We assign a random value to e_h between 0 and 0.4, but we keep the position angles of the dark matter and the galaxy perfectly aligned. Not surprisingly, we find that the shear ratios $f_{\rm mm}$ and $f_{\rm mm}^{\rm corr}$ are unchanged, as the average halo ellipticity does not change. Without multiple deflections, we find that $\langle f - f_{45} \rangle$ is reduced by 25% to 0.1875. In this case, the anisotropy of the lensing signal is no longer proportional to e_g^2, but to $e_h \times e_g$: the factor e_h comes from Equation (5.24), and the factor e_g from the weight in Equation (5.7). When we average over a flat lens ellipticity distribution, the lensing signal in the original case is $\propto \int de_g \, e_g^2$, which becomes $\propto \langle e_h \rangle \int de_g \, e_g$ if e_h is randomly assigned. The second integral is 25% smaller than the original. Hence the decrease of $\langle f - f_{45} \rangle$ results from no longer giving a larger weight to the galaxies with large dark matter halo ellipticities in the measurement. If we include multiple deflections, the relative decrease of $(f - f_{45})$ is similar as in Figure 5.8a.

Our simulations show that on small scales (<1 arcmin), the impact of multiple deflections is a few percent at most. This result is robust to changes in the simulation set-up, which shows that it is very unlikely that multiple deflections affect the shear anisotropy measurements on these scales. On larger scales, the impact of multiple deflection is more uncertain, and could have an important effect on weak lensing studies that investigate the alignment between galaxies and the large-scale structure. Ultimately, realistic numerical simulations should be used to accurately assess and model the impact multiple deflections have as a function of the selection of the lens sample. This is necessary to improve the precision of the gravitational lensing constraints on the shapes of dark matter haloes with data from upcoming surveys.

Howell & Brainerd (2010) report a significant and strong decrease in $f_{\rm mm}$ with projected lens-source separation. However, for computational speed-up, Howell & Brainerd (2010) only use those foreground galaxies that reside within 100 arcsec from the lens to calculate the multiple deflection signal. Figure 5.18a shows that this leads to an overestimation of the reduction of the shear ratios. Furthermore, redshifts are assigned to galaxies whose positions have been observed in real data. This causes an unphysical correlation between the positions of foreground and background galaxies, and amplifies the chance of having a

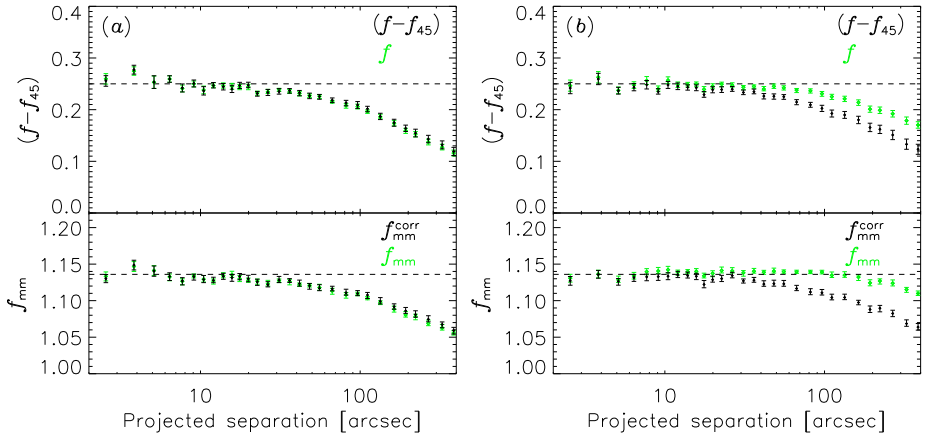

Figure 5.9: (a) Anisotropy of the lensing signal in the simulations using the observed positions of the 'red' lens sample in the RCS2. The filled black diamonds (open green diamonds) show the shear anisotropy estimators (not) corrected for systematic shear. The ellipticities of the lenses have been randomly assigned. The lensing anisotropy declines slightly at scales > 20 arcsec, which is expected as clustering of lenses with random position angles leads to an isotropic signal at large scales. In panel (b), we add an additional ellipticity of 0.03 to the e_1 component of the lenses to mimic intrinsic alignments. This increases the shear anisotropy, but also induces cross shear, so that the systematic shear corrected shear anisotropy estimators are unchanged.

low-redshift foreground galaxy close to a lens, which could result in an overestimate of the effect. Finally, no correction for systematic shear is implemented, which would have reduced the impact as well.

5.4.2 Clustering of lenses

Many galaxies in the Universe reside in groups and clusters. Hence the shear we measure around a lens galaxy is the sum of the shear from the lens and neighbouring galaxies. At small projected separations from the lens, the signal is dominated by the lens galaxy, but at larger separations the shear from the neighbours becomes increasingly important. This may affect the shear anisotropy measurements. To study this, we assign the positions of the lenses from the real lens samples to the simulated lenses. The lens ellipticities are randomly drawn between 0 and 0.3, and are modeled with an SIE profile. The positions of the galaxies with $22 < m_{r'} < 24$ in the RCS2 are assigned to the simulated sources. The lenses are put at a redshift $z = 0.4$, and the source redshifts are randomly drawn from their redshift distribution. We assume that $f_{\rm h} = 1$, and that no foreground lenses are present as that would potentially mix different effects. To obtain the errors, we determine the scatter between 20 random realizations. We show the results in Figure 5.9a for the 'red' lens sample.

We find that clustering of the red lenses slightly reduces the lensing anisotropy on large scales. This can be easily understood: if galaxies with random ellip-

ticities cluster, the resulting lensing signal around the lens ensemble at large scales becomes more isotropic. The impact of clustering on the shear anisotropy around the 'blue' and 'all' lenses is smaller, and is therefore not shown. We note that, additionally, dark matter haloes may be stripped in high-density environments, which could reduce the anisotropy signal as well.

Numerical simulations suggest that dark matter haloes are aligned, and point toward each other (e.g. Splinter et al. 1997; Croft & Metzler 2000; Heavens et al. 2000; Lee et al. 2008). If the galaxies that reside in these haloes are preferentially aligned with the halo - a prerequisite for measuring halo shapes - the observed galaxy ellipticities are expected to show this alignment as well. In particular, the ellipticities of luminous red galaxies are believed to be increasingly correlated with decreasing separations (e.g. Hirata et al. 2007; Okumura et al. 2009; Joachimi et al. 2011), which can be understood in a framework in which galaxies form in a linear tidal field (Blazek et al. 2011). Similar studies for spiral galaxies show the effect is considerably weaker (Mandelbaum et al. 2011). Intrinsic alignments also affect the shear anisotropy signal.

To obtain a conservative estimate of the impact of intrinsic alignments, we add an ellipticity of 0.03 to all the e_1 components of the lenses. The result for the 'red' lenses is shown in Figure 5.9b. We find that correlated lens ellipticities increases the shear anisotropy on large scales; the shear pattern of neighbouring lenses amplifies each other. However, correlated lens ellipticities also induces cross shear of an equal magnitude, hence the corrected shear anisotropy estimator is unchanged. In reality, the intrinsic alignments are scale dependent, and the correlation decreases for larger separations. Furthermore, if the lens galaxies are pointing towards each other, the contributions of the shear along the major axis systematically add up, which could amplify the effect. This is difficult to model, however, but we will assess it with numerical simulations in a future work.

The main conclusion from our simulations is that the impact of multiple deflections, clustering of lenses and the correlations of their ellipticities is small, and can be safely ignored for the lens selection in this work (i.e. particularly for the 'blue' and 'red' lens sample, which were selected to contain massive, elliptical, and low-redshift galaxies). More realistic studies using numerical simulations are required to quantify the effects more precisely. This is a crucial step in correctly interpreting the lensing anisotropy in future lensing data that are of higher precision.

5.5 Halo ellipticity

The simulations from the previous section indicate that multiple deflections and clustering have a small impact on the shear anisotropy, in particular for the 'blue' and 'red' lens samples where we have selected massive, elliptical, low-redshift lenses. Now we proceed with the actual measurements. We show $(f - f_{45})\Delta\Sigma_{\rm iso}$ as a function of projected distance to the lens in Figure 5.10. We multiply the lensing signal with the projected separation in arcmin to enhance the visibility of the signal on large scales. Each row shows the measurements for one of the lens samples, whilst the exponent of the galaxy ellipticities, α in Equation (5.9), differs between the columns. To quantify the shear anisotropy, we first determine the average value of $(f - f_{45})$ non-parametrically, as detailed

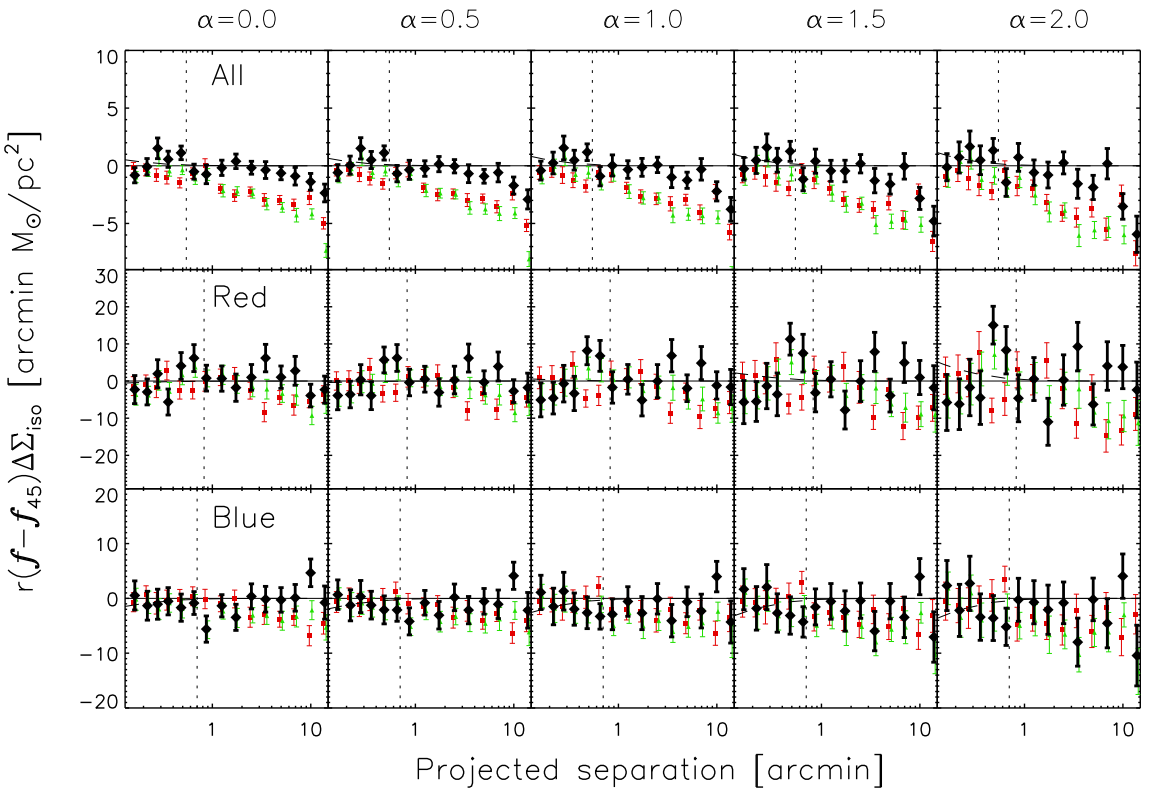

Figure 5.10: Anisotropic shear signal around the 'all' lenses (top panels), the 'red' lenses (middle panels) and the 'blue' lenses (bottom panels). The signal has been multiplied with the projected separation in arcmin to enhance the visibility of the signal on large scales. The green triangles denote $r\, f \Delta\Sigma_{\rm iso}$, the red squares $r\, f_{45} \Delta\Sigma_{\rm iso}$, and the black diamonds $r(f - f_{45})\Delta\Sigma_{\rm iso}$. The vertical dotted lines indicate the virial radius at the mean lens redshift, the dashed lines show the best fit elliptical NFW profiles. Indicated on top of each column is the weight applied to the measurement. The average shear anisotropy of the 'all' and 'red' lenses is weakly positive within the virial radius, supporting the presence of triaxial dark matter haloes that are reasonably aligned with the galaxies. For the 'blue' lenses the signal is marginally negative. Note that the measurements shown here are not corrected for the anisotropic distribution of satellite galaxies.

in Appendix 5.C. The best-fit values are summarized in Table 5.3.

For the 'all' sample of lenses, we find that $\langle f - f_{45} \rangle$ is marginally positive, independent of the applied weight. For the 'red' lenses, we find that $\langle f - f_{45} \rangle$ is consistent with zero if we take $w \propto e^{0.0}$. For larger values of α, however, $\langle f - f_{45} \rangle$ turns marginally positive due to the two data points near the virial radius. Closer to the lens, the signal is slightly negative. For the blue galaxies, the signal is marginally negative.

Next, we fit an SIE and an elliptical NFW profile. For the SIE fit, we first determine the Einstein radius $r_{\rm E}$ by fitting a singular isothermal sphere (SIS) profile to the azimuthally averaged tangential shear measurements within the virial radius at the mean lens redshift. To determine $f_{\rm h}$, we fit (Mandelbaum et al. 2006a)

$$(f - f_{45})\Delta\Sigma(r) = \frac{\Sigma_{\rm crit} r_{\rm E} f_{\rm h}}{8r}; \tag{5.25}$$

the errors of $f_{\rm h}$ are determined from the χ^2-values of the fit. Since $(f - f_{45})/f_{\rm h} = 0.25$ on all scales for an SIE profile (Mandelbaum et al. 2006a), we expect to find best-fit values for $f_{\rm h}$ that are four times larger than the non-parametrically determined $\langle f - f_{45} \rangle$. The best-fit values are shown in Table 5.3. We find that $f_{\rm h}$ is consistent with, but not exactly, four times $\langle f - f_{45} \rangle$. The difference may be due to differences between the fitting methods; if we first fit an SIS profile, we correlate the azimuthally averaged tangential shear measurements, whilst if we determine $\langle f - f_{45} \rangle$ non-parametrically, each data point is treated separately. The general trends, however, are consistent and the conclusions do not depend on how we fit the data.

Currently, no analytical expression exists for the shear anisotropy of an elliptical NFW profile. Therefore, we use the numerically integrated values of f/f_h and f_{45}/f_h as a function of r/r_s from Mandelbaum et al. (2006a) (shown in Figure 2 of that paper), which have been kindly provided by Rachel Mandelbaum. Since our lens galaxies span a broad range in redshifts, we first determine the redshift-averaged lensing model by integrating the elliptical NFW profiles over the redshift distribution of each lens sample (shown in Figure 5.1), and weigh each lens redshift bin with the lensing efficiency $\langle D_{ls}/D_s \rangle$ that is averaged over the source redshift distribution. Note that this is an important correction; for the 'all' sample, the integrated profile results in about 50% larger values for $(f - f_{45})$ compared to the profile computed using the mean lens redshift. For the 'red' and 'blue' sample, the difference is smaller because their redshift distributions are narrower. Also note that the SIE profiles do not have to be corrected, since the azimuthally averaged lensing signal and the anisotropic part are equally changed when we integrate over the lens redshift distribution as both scale $\sim 1/r$, leaving the best-fit value of f_h unaffected.

The best fit values of f_h for the elliptical NFW profiles are less significant than $\langle f - f_{45} \rangle$ for the same lensing measurements. The reason is that the elliptical NFW fit is very sensitive to the signal close to the lens, but not to the signal at larger separations. We find that for the 'all' and 'red' sample, $(f - f_{45})$ actually turns slightly negative close to the lens, rather than increasing strongly as would have been expected for an elliptical NFW profile that is aligned with the lens. Although this might be just caused by noise, it could also indicate that a single elliptical NFW profile does not describe the shear anisotropy signal well.

Finally, we note that for the 'all' sample $\langle f - f_{45} \rangle \Delta\Sigma_{\rm iso}$ turns negative at

Table 5.3: The best-fit values for the anisotropy of the galaxy-mass cross-correlations function, $\langle f - f_{45} \rangle$, and the ratio of the dark matter halo ellipticity and the galaxy ellipticity, $f_{\rm h}$, for an SIE and an elliptical NFW profile.

Sample	α	$\langle f_{\rm eff} \rangle$	$\langle f - f_{45} \rangle$	$f_{\rm h}$(SIE)	$f_{\rm h}$(NFW)
All	0.0	$1.3 \pm 0.6 \times 10^{-3}$	0.19 ± 0.10	0.47 ± 0.37	$0.96^{+0.83}_{-0.80}$
All	0.5	$1.1 \pm 0.7 \times 10^{-3}$	$0.21^{+0.11}_{-0.10}$	0.57 ± 0.40	$1.19^{+0.89}_{-0.85}$
All	1.0	$0.8 \pm 0.8 \times 10^{-3}$	0.23 ± 0.12	0.70 ± 0.46	$1.50^{+1.03}_{-1.01}$
All	1.5	$0.6 \pm 1.0 \times 10^{-3}$	0.26 ± 0.15	0.83 ± 0.55	$1.80^{+1.23}_{-1.19}$
All	2.0	$0.4 \pm 1.2 \times 10^{-3}$	0.29 ± 0.17	0.97 ± 0.65	$2.12^{+1.45}_{-1.42}$
Red	0.0	$11.9 \pm 1.8 \times 10^{-3}$	0.13 ± 0.15	0.00 ± 0.58	$-0.19^{+1.09}_{-1.08}$
Red	0.5	$11.3 \pm 2.1 \times 10^{-3}$	0.19 ± 0.16	0.05 ± 0.60	$-0.14^{+1.12}_{-1.10}$
Red	1.0	$9.3 \pm 2.5 \times 10^{-3}$	0.28 ± 0.18	0.25 ± 0.70	$0.20^{+1.34}_{-1.31}$
Red	1.5	$7.2 \pm 3.1 \times 10^{-3}$	0.40 ± 0.22	0.61 ± 0.86	$0.87^{+1.67}_{-1.63}$
Red	2.0	$5.2 \pm 4.0 \times 10^{-3}$	0.54 ± 0.27	1.09 ± 1.07	$1.82^{+2.12}_{-2.08}$
Blue	0.0	$1.5 \pm 1.4 \times 10^{-3}$	$-0.16^{+0.18}_{-0.19}$	-0.56 ± 0.68	$-1.24^{+1.62}_{-1.65}$
Blue	0.5	$2.0 \pm 1.6 \times 10^{-3}$	-0.25 ± 0.19	-0.75 ± 0.70	$-1.62^{+1.69}_{-1.72}$
Blue	1.0	$2.3 \pm 1.9 \times 10^{-3}$	$-0.35^{+0.21}_{-0.22}$	-1.01 ± 0.81	$-2.17^{+1.97}_{-2.03}$
Blue	1.5	$2.5 \pm 2.3 \times 10^{-3}$	-0.45 ± 0.26	-1.24 ± 0.96	$-2.67^{+2.36}_{-2.44}$
Blue	2.0	$2.5 \pm 2.7 \times 10^{-3}$	$-0.53^{+0.31}_{-0.32}$	-1.44 ± 1.17	$-3.06^{+2.85}_{-2.95}$

projected separations >5 arcmin. A similar trend can be observed in Figure 5.6, where the inverse of the corrected shear ratio of the 'all' sample is slightly larger than unity. We cannot directly interpret this as the result of an anti-alignment of galaxies with the large-scale structure, as we found in the previous section that multiple deflections and the clustering of galaxies produce a similar trend at these scales, and we cannot disentangle the effects. To constrain the average halo ellipticities of galaxies we only use the lensing signal on scales <1 arcmin, however, where the effect of multiple deflections and clustering of galaxies can be safely ignored, and a non-zero signal reflects an anisotropy of the projected gravitational potential.

5.5.1 Environmental dependence

To study whether the lensing anisotropy depends on the lens environment we measure the signal for the isolated and clustered lens sample. In Figure 5.11 we show $(f - f_{45})\Delta\Sigma_{\rm iso}$ for the $w \propto e^{1.0}$ bin, which is the same weight as used in Mandelbaum et al. (2006a) and hence enables a direct comparison. We determine $\langle f - f_{45} \rangle$ and fit $f_{\rm h}$ for the elliptical density profiles, and show the results in Table 5.4.

The lensing anisotropy for the isolated 'all' lenses is positive, and the values of $(f - f_{45})\Delta\Sigma_{\rm iso}$ and f_h are larger than those of the clustered sample by almost $\sim 2\sigma$. For the 'red' and the 'blue' lenses, we find that on small scales, the lensing anisotropy is more negative for the clustered sample. When we average

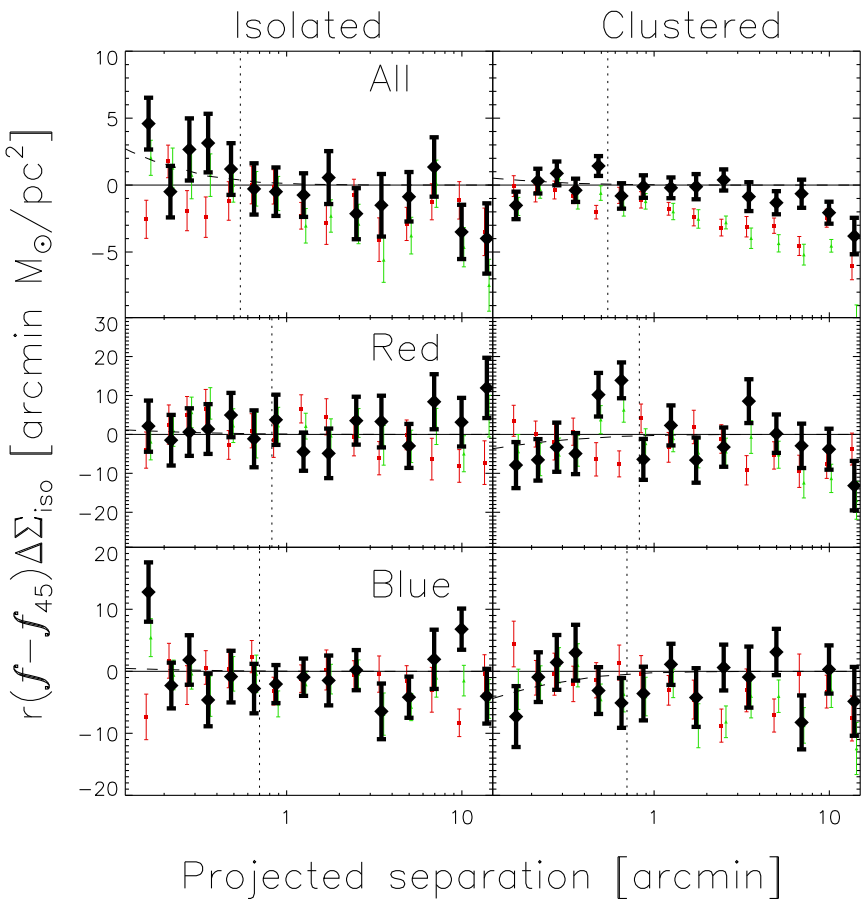

Figure 5.11: Anisotropic shear signal multiplied with the projected separation in arcmin around the 'all' sample (top panels), the 'red' sample (middle panels) and the 'blue' sample (bottom panels), for the isolated lenses on the left-hand side, and the clustered lenses on the right-hand side (using $w \propto e^{1.0}$). The green triangles denote $f\Delta\Sigma_{\rm iso}$, the red squares $f_{45}\Delta\Sigma_{\rm iso}$, and the black diamonds $(f - f_{45})\Delta\Sigma_{\rm iso}$. The vertical dotted lines indicate the virial radius at the mean lens redshift, the dashed lines indicate the best fit elliptical NFW profiles. Please note the different scalings of the vertical axes. For the 'all' sample, the shear anisotropy is larger for the isolated sample; for the 'red' and 'blue' sample, the shear anisotropy is more negative on small scales for the clustered samples, but the differences are not significant when averaged within the virial radius.

the signals within the virial radius, or fit the elliptical density profiles, we find that this difference is not statistically significant.

Table 5.4: Similar to Table 5.3 for the isolated and clustered lenses.

Sample	α	Environment	$\langle f - f_{45} \rangle$	$f_{\rm h}$(SIE)	$f_{\rm h}$(NFW)
All	1.0	isolated	$0.51^{+0.26}_{-0.25}$	2.35 ± 1.00	$4.73^{+2.17}_{-2.05}$
All	1.0	clustered	0.18 ± 0.13	0.40 ± 0.51	$0.90^{+1.17}_{-1.15}$
Red	1.0	isolated	0.11 ± 0.25	0.49 ± 0.97	$0.40^{+1.96}_{-1.90}$
Red	1.0	clustered	0.47 ± 0.26	0.46 ± 1.05	$-1.23^{+1.90}_{-1.83}$
Blue	1.0	isolated	-0.18 ± 0.30	0.05 ± 1.06	$0.38^{+2.32}_{-2.45}$
Blue	1.0	clustered	$-0.43^{+0.34}_{-0.35}$	-1.54 ± 1.33	$-3.46^{+3.26}_{-3.45}$

5.5.2 Interpretation

The shear anisotropy measurements provide weak support that the average galaxy is preferentially aligned with its triaxial dark matter host. The significance of the detection for the 'all' sample does not depend on how we weigh the measurement with the observed galaxy ellipticity, which indicates that more elliptical galaxies do not reside in, or are better aligned with, more elliptical dark matter haloes. We find that the errors on $\langle f - f_{45} \rangle$ increase for larger values of the exponents of the weights, because the effective number of lenses decreases: round lenses barely contribute to the signal for the largest exponents. Furthermore, we find that the shear anisotropy signal of isolated galaxies is stronger than that of clustered galaxies: the difference is almost 2σ. One possible explanation is that the dark matter haloes of isolated galaxies are less subject to stripping, and may preserve their original shapes. Clustered galaxies, on the other hand, may lose more of their dark matter, particularly in the outer regions. An alternative explanation is that the fraction of lenses in the clustered sample that are satellites is larger. Since the host halo in which satellite galaxies are embedded dominates the lensing signal, and since the orientation of the major axis of the satellites and the major axis of the central galaxy are expected to not be strongly aligned, this would also lead to a reduction of the anisotropy of the lensing signal.

The average shear anisotropy of both the 'red' and 'blue' lenses is consistent with zero. We find no significant differences between the clustered and isolated sample, because we lack precision. For the 'red' lenses, the anisotropy signal on small scales appears negative, whilst near the virial radius it turns positive. We find a weak indication that the shear anisotropy and the detection significance increases for larger exponents of the lens ellipticity in the weights, which could indicate that the red galaxies with larger ellipticities preferentially reside in, and align with, more elliptical dark matter haloes. For the 'blue' lenses, we find that for the largest exponents the anisotropy is marginally negative, which is suggestive of an anti-alignment between the galaxy and the dark matter halo.

The negative shear anisotropy at small projected separations for the 'red' lens sample occurs at the same scale where the contamination is highest. Since we observed in Section 5.2.4 that the distribution of satellites is anisotropic,

the observed signal could also be caused by a radial alignment of physically associated galaxies in the source sample. We estimate the value of the average tangential intrinsic alignment that would produce the signal we observe in Appendix 5.G. We find that we require a value that is roughly ten times larger then the results from Hirata et al. (2004). Conversely, the expected impact of intrinsic alignments is about a factor ten smaller than the signal we observe, hence it is unlikely that our measurements are significantly affected. Hence the negative shear anisotropy on small scales is unlikely caused by intrinsic alignments.

Currently, weak lensing constraints on the ellipticity of dark matter haloes have been presented in Hoekstra et al. (2004), Mandelbaum et al. (2006a) and Parker et al. (2007). We already compared our results with those from Parker et al. (2007) in Section 5.3. Mandelbaum et al. (2006a) measured the weak lensing anisotropy around 2×10^6 lenses with photometric redshifts in the SDSS. On average, they find $f_h = -0.06\pm0.19$ for the red galaxies, and $f_h = -1.1\pm0.6$ for the blue galaxies on scales 20-300 h^{-1}kpc for an SIE profile. Fitting an elliptical NFW profile yields $f_h = 0.60 \pm 0.38$ and $f_h = -1.4^{+1.7}_{-2.0}$ for the red and blue lenses, respectively. Separating the lenses in luminosity bins, they find that the lensing signal is consistent with zero for most of their bins. Only for the brightest red lenses a detection is reported, also at the $\sim$2 sigma level. A detailed comparison between the results is complicated due to differences in the lens selections. Our 'red' lens samples can be best compared with the L5 and L6 red sample from Mandelbaum et al. (2006a), as these are most similar in absolute magnitudes; Mandelbaum et al. (2006a) find $\langle f-f_{45}\rangle = 0.08\pm0.08$ and $\langle f-f_{45}\rangle = 0.29\pm0.12$ for L5 and L6, which agrees well with the $\langle f-f_{45}\rangle = 0.28\pm0.18$ that we found. For the elliptical NFW profile, Mandelbaum et al. (2006a) found $f_h = 0.4\pm0.57$ and $f_h = 1.7 \pm 0.7$ for the red L5 and L6 sample, and the average of those values is roughly within 1σ of our best fit value $0.20^{+1.34}_{-1.31}$. Our 'blue' lens sample covers a broad range in luminosity, and roughly corresponds to the blue lens bins L3 to L5 of Mandelbaum et al. (2006a). For these bins, Mandelbaum et al. (2006a) finds $\langle f - f_{45}\rangle = -0.29^{+0.26}_{-0.27}$, $-0.36^{+0.25}_{-0.26}$ and -0.27 ± 0.28 respectively, which agrees well with $-0.35^{+0.21}_{-0.22}$. In conclusion, we find that our results and the results from Mandelbaum et al. (2006a) are consistent.

In an earlier work, Hoekstra et al. (2004) used 45.5 deg^2 of the RCS (Gladders & Yee 2005) to measure the lensing anisotropy around 1.2×10^5 lenses selected with $19.5 < R_C < 21$. A $\sim2\sigma$ detection of $f_h = 0.77^{+0.18}_{-0.21}$ was obtained by fitting a TIS using a maximum likelihood method. This result appears to be significantly different from ours, and from Mandelbaum et al. (2006a). In the latter, various reasons are given why the results could differ, which also apply to us: most importantly, the lens samples are very different, and the method of analysis differs. Possibly, the maximum likelihood method is a better estimator of the shear anisotropy, as it takes into account the positions and relative orientations of the lens galaxies. The result from a maximum likelihood fit, however, is difficult to interpret as it is not clear how multiple deflections affect the measurement, and because the radial dependence of the signal cannot be visualized, which makes it difficult to identify residual systematics.

Converting the average shear anisotropy into the average projected ellipticity of dark matter haloes is complicated. The simulations in this work have shown

that multiple deflections and clustering can have some impact on the lensing anisotropy. If we select the lens sample carefully as we did (in particular the 'blue' and 'red' lens sample that consist of isolated, elliptical, low-redshift, massive lenses), the impact of these complications is small. However, misalignments between the position angles of the galaxies and their dark matter haloes cause a reduction of the lensing anisotropy. Therefore, the observational constraints on the shear anisotropy from previous weak lensing analyses, as well as from this work, only provide lower limits on the average halo ellipticity. To constrain the halo ellipticity from the lensing anisotropy, we need to know how galaxies are orientated in their triaxial dark matter haloes.

The orientation of galaxies in their dark matter haloes has received considerable attention in recent years. Studies of the distribution of satellite galaxies around centrals in the SDSS (Wang et al. 2008; Agustsson & Brainerd 2010) and in numerical simulations (Kang et al. 2007; Deason et al. 2011), studies based on the ellipticity correlation functions of galaxies (Faltenbacher et al. 2009; Okumura et al. 2009), and studies based on angular momentum considerations in numerical simulations (Bett et al. 2010; Hahn et al. 2010) all point in a similar direction: on average, red galaxies are aligned with their dark matter hosts, but with a considerable scatter between the position angles with a value in the range ∼20-40 degrees. The dispersion for blue galaxies is even larger.

Scatter between the position angles irrevocably leads to a reduction in the anisotropy of the lensing signal; with lensing, we only measure the component of the dark matter halo ellipticity that is aligned with the lens light. To study the magnitude of the reduction, we use the simulations from the previous section, where the position angle of the dark matter halo is given by the position angle of the light, plus a Gaussian with zero mean and a certain width. In Figure 5.12, we show the average $f_{\rm mm}^{\rm corr}$ and $\langle f - f_{45} \rangle$ as a function of σ_θ, the dispersion of the position angle distribution. We find that a σ_θ in the range between 20 to 40 degrees leads to a reduction in the anisotropy of ∼25-65%. This result indicates that the scatter in the relative position angle significantly dilutes the shear anisotropy measurements.

Qualitatively similar results have been obtained by Bett (2011), who used the Millennium simulation (Springel et al. 2005) in combination with semi-analytic galaxy formation models to predict the stacked projected axis ratio, q, of large numbers of haloes. Various alignment models were tested, and different methods used to measure the halo shapes. For most scenarios, q turned very close to unity, implying an nearly isotropic shear signal.

In reality, the alignment between the position angle of the galaxy and the dark matter may be scale dependent. Besides that, the dark matter haloes are not rigid once formed; their shapes continue to evolve in a way that depends on, amongst others, their formation history and environment; the galaxies in the centre of the haloes may evolve differently. Furthermore, the central galaxy is expected to sphericalise the dark matter haloes (e.g. Kazantzidis et al. 2010; Abadi et al. 2010; Machado & Athanassoula 2010). Indications already exist that the alignment depends on lens luminosity (Faltenbacher et al. 2009; Mandelbaum et al. 2006a) and environment (Hahn et al. 2010); it could depend on other lens characteristics (e.g. lens ellipticity, redshift) as well. Finally, once more, multiple deflections and clustering are expected to have some impact on the anisotropy of the lensing signal. All these effects have to be accurately modeled and well understood before we can interpret any measured anisotropy in

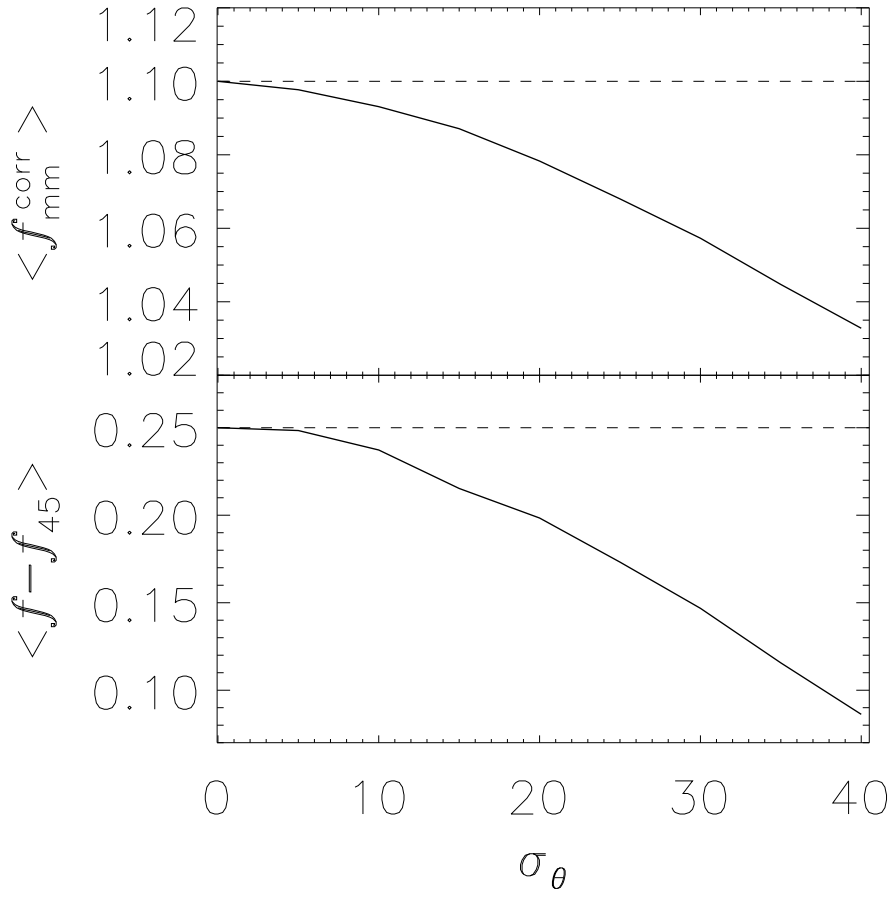

Figure 5.12: Anisotropy of the lensing signal averaged between 1 and 200 arcsec, for a Gaussian distributed position angle difference between the dark matter and the light distribution with zero mean and width σ_θ. Large values for σ_θ as have been reported in the literature lead to significant reductions in the shear anisotropy.

terms of the average property of dark matter haloes. Note that the study of intrinsic alignments of galaxies are similarly affected, and require this knowledge as well for a correct interpretation.

Our results underline the need for photometric redshifts - and consequently luminosities - for the lenses. Without photometric redshifts, we can only select lenses based on their colours and magnitudes. To achieve sufficient signal-to-noise in order to obtain competitive constraints on the average halo ellipticity, we have to select large numbers of galaxies that cover a broad range of luminosities and redshifts. If the average halo ellipticity depends on the luminosity of a galaxy (as the results from Mandelbaum et al. 2006a suggest), the signal-to-noise of the shear anisotropy measurements decrease, and may even average out in the worst case scenario. If luminosities are available, we can not only se-

lect lenses in narrow luminosity ranges, but also weigh the lensing measurement with luminosity, which improves the signal-to-noise of the lensing measurement. The lack of photometric redshifts also forces us to stack the lensing signal as a function of angular separation, rather than physical, which decreases the signal-to-noise as well. This is particular disadvantageous as the shear anisotropy signal of an elliptical NFW profile drops very rapidly with increasing radius, and the signal may be smeared out and become undetectable. We note that a preliminary photometric redshift catalogue exists for the RCS2 for the area that has also been observed in the i'-band, but it only covers the redshift range $z > 0.4$ due to the absence of observations in the u-band, which limits its usefulness for this study.

A new technique has recently been proposed to improve halo ellipticity measurements: the use of a higher order distortion of lensing known as flexion (Hawken & Bridle 2009; Er & Schneider 2011; Er et al. 2011a,b). Although the measurement of the flexion signal is difficult for galaxy-scale potentials, the first positive detections have already been reported (Velander et al. 2011). Using mock simulations of clusters with SIE and elliptical NFW profiles, Er et al. (2011b) find that flexion is more sensitive to the halo ellipticity than the shear; this may be true as well for stacked galaxy potentials. Furthermore, the systematic errors in flexion measurements differ from those in shear. Hence we anticipate that additional useful constraints can be obtained with flexion.

5.6 Conclusion

We present measurements of the anisotropy of the weak lensing signal around galaxies using data from the Red-sequence Cluster Survey 2 (RCS2). We define three lens samples: the 'all' sample contains all galaxies in the range $19 < m_{r'} < 21.5$, whereas the 'red' and 'blue' samples are dominated by massive low-redshift early-type and late-type galaxies, respectively. To study the environmental dependence of the lensing signal, we also subdivide each lens sample into an isolated and clustered part, and analyse them separately.

We address the impact of several complications on the shear anisotropy measurements, including residual PSF systematics in the shape catalogues, multiple deflections, the clustering of lenses, and correlations between their intrinsic shapes. We run a set of idealised simulations to estimate the impact these might have on real data, and find them to be small, but not entirely negligible. We demonstrate that the impact of these complications can be reduced by a careful selection of the lens sample, i.e. low-redshift, massive and elliptical galaxies, as has been done in this work.

We also measure the distribution of physically associated galaxies around the lens samples. We find that these satellites predominantly reside near the major axis of the lenses. The results of the 'red' sample are in good agreement with previously reported values, whilst the constraints of the 'all' and 'blue' sample cannot be easily compared as they consist of a mixture of early-type and late-type galaxies.

The shear anisotropy is quantified by the anisotropy of the galaxy-mass cross-correlation function, $\langle f - f_{45} \rangle$, and by the ratio of the projected dark matter halo ellipticity and the observed galaxy ellipticity, f_h. For the 'all' sample we find

that $\langle f - f_{45} \rangle = 0.23 \pm 0.12$, and $f_h = 1.50^{+1.03}_{-1.01}$ for an elliptical NFW profile, which for a mean lens ellipticity of 0.25 corresponds to a projected halo ellipticity of $e_h = 0.38^{+0.26}_{-0.25}$ if the halo and the lens are perfectly aligned. Note that various studies indicate that this may not be the case. These constraints provide weak support that galaxies are embedded in, and preferentially aligned with, triaxial dark matter haloes. For isolated galaxies, the average shear anisotropy is larger than for clustered galaxies; for elliptical NFW profiles, we find $f_h = 4.73^{+2.17}_{-2.05}$ and $f_h = 0.90^{+1.17}_{-1.15}$, respectively. The decrease of the lensing anisotropy signal around clustered galaxies may be due to the stripping of dark matter haloes in dense environments.

For the 'red' galaxies, the shear anisotropy is on average marginally positive, although close to the lens the signal turns negative. As a result, the elliptical NFW constraints for the 'red' sample are consistent with zero. For the 'blue' lenses, we find that the shear is marginally negative, suggesting an anti-alignment between the galaxy and the dark matter. Our measurements highlight the need for (photometric) redshifts in lensing studies. In order to reach sufficient signal-to-noise that enable competitive constraints on the shear anisotropy, we have to stack large numbers of galaxies that span a broad range in luminosities and redshifts. This smears out the shear anisotropy, and in the worst case the anisotropy might even average out.

Acknowledgements

We would like to thank Elisabetta Semboloni for useful discussions and suggestions on the error estimation of the shear anisotropy measurements, Peter Schneider for valuable comments on the manuscript, and Rachel Mandelbaum for providing the table of the shear anisotropy of an elliptical NFW profile as well as for valuable comments on this work. HH and EvU acknowledge support from a Marie Curie International Reintegration Grant. HH is also supported by a VIDI grant from the Nederlandse Organisatie voor Wetenschappelijk Onderzoek (NWO). TS acknowledges support from NSF through grant AST-0444059-001, and the Smithsonian Astrophysics Observatory through grant GO0-11147A. MDG thanks the Research Corporation for support via a Cottrell Scholars Award. The RCS2 project is supported in part by grants to HKCY from the Canada Research Chairs program and the Natural Science and Engineering Research Council of Canada.

This work is based on observations obtained with MegaPrime/MegaCam, a joint project of CFHT and CEA/DAPNIA, at the Canada-France-Hawaii Telescope (CFHT) which is operated by the National Research Council (NRC) of Canada, the Institute National des Sciences de l'Univers of the Centre National de la Recherche Scientifique of France, and the University of Hawaii. We used the facilities of the Canadian Astronomy Data Centre operated by the NRC with the support of the Canadian Space Agency.

Bibliography

Abadi, M. G., Navarro, J. F., Fardal, M., Babul, A., & Steinmetz, M. 2010, MNRAS, 407, 435

Agustsson, I. & Brainerd, T. G. 2006, ApJ, 644, L25
Agustsson, I. & Brainerd, T. G. 2010, ApJ, 709, 1321
Allgood, B., Flores, R. A., Primack, J. R., et al. 2006, MNRAS, 367, 1781
Bailin, J., Kawata, D., Gibson, B. K., et al. 2005, ApJ, 627, L17
Bailin, J., Power, C., Norberg, P., Zaritsky, D., & Gibson, B. K. 2008, MNRAS, 390, 1133
Banerjee, A. & Jog, C. J. 2008, ApJ, 685, 254
Bartelmann, M. 1996, A&A, 313, 697
Bertin, E. & Arnouts, S. 1996, A&AS, 117, 393
Bett, P., Eke, V., Frenk, C. S., Jenkins, A., & Okamoto, T. 2010, MNRAS, 404, 1137
Bett, P. E. 2011, MNRAS, accepted [arXiv:1108.3717]
Blazek, J., McQuinn, M., & Seljak, U. 2011, J. Cosmology Astropart. Phys., 5, 10
Brainerd, T. G. 2005, ApJ, 628, L101
Brainerd, T. G. & Wright, C. O. 2000, PASP, submitted [arXiv:astro-ph/0006281]
Cacciato, M., van den Bosch, F. C., More, S., et al. 2009, MNRAS, 394, 929
Croft, R. A. C. & Metzler, C. A. 2000, ApJ, 545, 561
Deason, A. J., McCarthy, I. G., Font, A. S., et al. 2011, MNRAS, 415, 2607
Dubinski, J. & Carlberg, R. G. 1991, ApJ, 378, 496
Duffy, A. R., Schaye, J., Kay, S. T., & Dalla Vecchia, C. 2008, MNRAS, 390, L64
Dutton, A. A., Brewer, B. J., Marshall, P. J., et al. 2011, MNRAS, 1542
Er, X., Mao, S., Xu, D., & Cao, Y. 2011a, MNRAS, 417, 2197
Er, X. & Schneider, P. 2011, A&A, 528, A52
Er, X., Tereno, I., & Mao, S. 2011b, MNRAS, accepted [arXiv:1112.4670]
Erben, T., Hildebrandt, H., Lerchster, M., et al. 2009, A&A, 493, 1197
Erben, T., Schirmer, M., Dietrich, J. P., et al. 2005, Astronomische Nachrichten, 326, 432
Faltenbacher, A., Jing, Y. P., Li, C., et al. 2008, ApJ, 675, 146
Faltenbacher, A., Li, C., Mao, S., et al. 2007, ApJ, 662, L71
Faltenbacher, A., Li, C., White, S. D. M., et al. 2009, Research in Astronomy and Astrophysics, 9, 41
Gilbank, D. G., Gladders, M. D., Yee, H. K. C., & Hsieh, B. C. 2011, AJ, 141, 94
Gladders, M. D. & Yee, H. K. C. 2005, ApJS, 157, 1
Hahn, O., Teyssier, R., & Carollo, C. M. 2010, MNRAS, 405, 274
Hao, J., Kubo, J. M., Feldmann, R., et al. 2011, in American Astronomical Society Meeting Abstracts #218, #408.24
Hawken, A. J. & Bridle, S. L. 2009, MNRAS, 400, 1132
Heavens, A., Refregier, A., & Heymans, C. 2000, MNRAS, 319, 649
Heymans, C., Brown, M., Heavens, A., et al. 2004, MNRAS, 347, 895
Hildebrandt, H., Erben, T., Kuijken, K., et al. 2011, MNRAS, accepted [arXiv:1111.4434]
Hinkley, D. V. 1969, Biometrika, 56, 635
Hirata, C. M., Mandelbaum, R., Ishak, M., et al. 2007, MNRAS, 381, 1197
Hirata, C. M., Mandelbaum, R., Seljak, U., et al. 2004, MNRAS, 353, 529
Hoekstra, H. 2004, MNRAS, 347, 1337
Hoekstra, H., Franx, M., & Kuijken, K. 2000, ApJ, 532, 88

Hoekstra, H., Franx, M., Kuijken, K., & Squires, G. 1998, ApJ, 504, 636
Hoekstra, H., Hsieh, B. C., Yee, H. K. C., Lin, H., & Gladders, M. D. 2005, ApJ, 635, 73
Hoekstra, H., Yee, H. K. C., & Gladders, M. D. 2004, ApJ, 606, 67
Howell, P. J. & Brainerd, T. G. 2010, MNRAS, 407, 891
Ilbert, O., Arnouts, S., McCracken, H. J., et al. 2006, A&A, 457, 841
Joachimi, B., Mandelbaum, R., Abdalla, F. B., & Bridle, S. L. 2011, A&A, 527, A26
Kaiser, N., Squires, G., & Broadhurst, T. 1995, ApJ, 449, 460
Kang, X., van den Bosch, F. C., Yang, X., et al. 2007, MNRAS, 378, 1531
Kazantzidis, S., Abadi, M. G., & Navarro, J. F. 2010, ApJ, 720, L62
Komatsu, E., Smith, K. M., Dunkley, J., et al. 2011, ApJS, 192, 18
Leauthaud, A., Tinker, J., Bundy, K., et al. 2012, ApJ, 744, 159
Lee, J., Springel, V., Pen, U.-L., & Lemson, G. 2008, MNRAS, 389, 1266
Luppino, G. A. & Kaiser, N. 1997, ApJ, 475, 20
Machado, R. E. G. & Athanassoula, E. 2010, MNRAS, 406, 2386
Mandelbaum, R., Blake, C., Bridle, S., et al. 2011, MNRAS, 410, 844
Mandelbaum, R., Hirata, C. M., Broderick, T., Seljak, U., & Brinkmann, J. 2006a, MNRAS, 370, 1008
Mandelbaum, R., Hirata, C. M., Seljak, U., et al. 2005a, MNRAS, 361, 1287
Mandelbaum, R., Seljak, U., Kauffmann, G., Hirata, C. M., & Brinkmann, J. 2006b, MNRAS, 368, 715
Mandelbaum, R., Tasitsiomi, A., Seljak, U., Kravtsov, A. V., & Wechsler, R. H. 2005b, MNRAS, 362, 1451
Napolitano, N. R., Romanowsky, A. J., Capaccioli, M., et al. 2011, MNRAS, 411, 2035
Narayan, R. 1989, ApJ, 339, L53
Natarajan, P. & Refregier, A. 2000, ApJ, 538, L113
Navarro, J. F., Frenk, C. S., & White, S. D. M. 1996, ApJ, 462, 563
Nierenberg, A. M., Auger, M. W., Treu, T., Marshall, P. J., & Fassnacht, C. D. 2011, ApJ, 731, 44
O'Brien, J. C., Freeman, K. C., & van der Kruit, P. C. 2010, A&A, 515, A63
Okumura, T., Jing, Y. P., & Li, C. 2009, ApJ, 694, 214
Parker, L. C., Hoekstra, H., Hudson, M. J., van Waerbeke, L., & Mellier, Y. 2007, ApJ, 669, 21
Sales, L. V., Navarro, J. F., Lambas, D. G., White, S. D. M., & Croton, D. J. 2007, MNRAS, 382, 1901
Siverd, R. J., Ryden, B. S., & Gaudi, B. S. 2009, ApJ, submitted [arXiv:0903.2264]
Splinter, R. J., Melott, A. L., Linn, A. M., Buck, C., & Tinker, J. 1997, ApJ, 479, 632
Springel, V., White, S. D. M., Jenkins, A., et al. 2005, Nature, 435, 629
Suyu, S. H., Hensel, S. W., McKean, J. P., et al. 2011, ApJ, submitted [arXiv:1110.2536]
Tasitsiomi, A., Kravtsov, A. V., Wechsler, R. H., & Primack, J. R. 2004, ApJ, 614, 533
van de Ven, G., Falcón-Barroso, J., McDermid, R. M., et al. 2010, ApJ, 719, 1481
van den Bosch, F. C., Abel, T., Croft, R. A. C., Hernquist, L., & White, S. D. M. 2002, ApJ, 576, 21

van den Bosch, F. C., Abel, T., & Hernquist, L. 2003, MNRAS, 346, 177
van Uitert, E., Hoekstra, H., Velander, M., et al. 2011, A&A, 534, A14
Velander, M., Kuijken, K., & Schrabback, T. 2011, MNRAS, 412, 2665
Vera-Ciro, C. A., Sales, L. V., Helmi, A., et al. 2011, MNRAS, 416, 1377
Wang, H., Mo, H. J., Jing, Y. P., Yang, X., & Wang, Y. 2011, MNRAS, 413, 1973
Wang, Y., Yang, X., Mo, H. J., et al. 2008, MNRAS, 385, 1511
Wright, C. O. & Brainerd, T. G. 2000, ApJ, 534, 34

5.A Lens selection

We define our 'red' and 'blue' lens samples using the W1 photometric redshift catalogue from the CFHTLenS collaboration (Hildebrandt et al. 2011). This catalogue contains the apparent magnitudes of galaxies observed in the same filters as in the RCS2, but also their photometric redshifts and absolute magnitudes. We split the sample in quiescent (typically early-type) and star-forming (typically late-type) galaxies according to their photometric type identifier $T_{\rm BPZ}$. $T_{\rm BPZ}$ corresponds to the galaxy type of the best-fit template (E/S0, Sbc, Scd, Im, SB3, SB2, with $T_{\rm BPZ}$ values from 1.0 to 6.0). We select the early-types and late-types with $T_{\rm BPZ} < 1.5$ and $T_{\rm BPZ} > 1.5$ respectively. These selections are further divided into a bright and faint sample using $M_{r'} < -22.5$ and $M_{r'} > -22.5$. For these four samples, we plot the colours as a function of magnitude in Figure 5.13. We define selection boxes of the 'red' and 'blue' lens sample, which are aimed at selecting the bright early-types and late-types. Figure 5.13 shows that the 'red' lens sample contains almost no late-type galaxies, nor faint early-types. Unfortunately, for the 'blue' sample we cannot exclusively select luminous late-type galaxies, and the sample also contains faint late-type and early-type galaxies. These selection criteria are applied to the catalogues of the RCS2 to select the 'red' and 'blue' lens sample.

To study how well we can separate early-types from late-types, we compare our selection to previously employed separation criteria. We find that 98% of the 'red' lenses, 57% of the 'blue' lenses and 28% of the 'all' lenses have a photometric type $T_{\rm BPZ} < 1.5$, and therefore have a spectral energy distributions similar to red elliptical galaxies. The 'red' sample therefore barely contains late-type galaxies. The majority of the 'blue' sample are actually faint red early-type galaxies, as can be seen from Figure 5.13. The lensing signal is dominated, however, by the massive late-type galaxies. The faint lenses mainly add noise. The purity of the 'blue' sample could be improved by shifting the selection boxes to bluer colours, but this at the expense of removing the majority of massive late-type lenses. Finally, the majority of the 'all' sample are blue and not very massive late-type galaxies. As a check, we also compare to the $u-r$ colour selection criterion, which has been used in Mandelbaum et al. (2006a). In this work, galaxies with an SDSS $u-r > 2.22$ model colour are selected for the red sample, whilst galaxies with $u-r < 2.22$ are selected as blue galaxies. When we select galaxies based on identical $u'-r'$ criteria (hence ignoring small differences between the filters), we find very similar results: 99% of the 'red' lenses, 58% of the 'blue' lenses and 30% of the 'all' lenses have a colour $u'-r' > 2.22$ and are red.

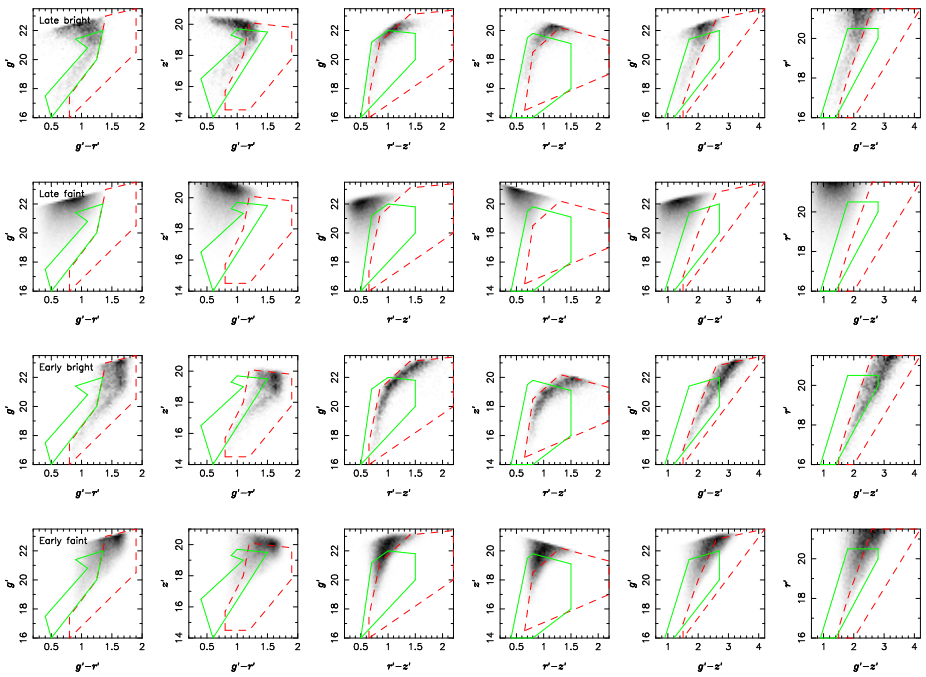

Figure 5.13: Colour-magnitude diagrams that are used to define the lens sample selection. In gray we show the locations of the galaxies with $m_{r'} < 21.5$ from the W1 photometric redshift catalogue from the CFHTLenS collaboration (Hildebrandt et al. 2011). In the top row we show the late-type galaxies with an absolute magnitude $M_{r'} < -22.5$, in the second row we show the late-types with $M_{r'} > -22.5$, and in the third and fourth row we show the early-types with $M_{r'} < -22.5$ and $M_{r'} > -22.5$, respectively. The coloured boxes illustrate the lens sample selection criteria; all galaxies that reside in all the red dashed (green solid) boxes form the 'red' ('blue') lens sample. We find that the 'red' lens sample contains very few late-types, as they are excluded in the $g' - r'$ versus g' diagram (first column). Also, most faint early-type galaxies are excluded from this sample as well (see, e.g., the third and fourth columns). For the 'blue' lens sample, we cannot define selection criteria that exclusively select bright late-type galaxies, and this sample therefore also contains a number of faint late-type and early-type galaxies.

5.B Environment selection

We subdivide the lenses in a clustered and an isolated sample, depending on whether or not the lens has a neighbour within a certain projected radius range that has a lower apparent magnitude than the lens. To determine which radius effectively separates the lenses into a low-density and a high-density sample, we compare the lensing signals for four lens selections: those that have a brighter neighbour within 30 arcsecs, those with a brighter neighbour between 30 arcsecs and 1 arcmin, those with a brighter neighbour between 1 arcmin and 2 arcmins, and those that are the brightest object within 2 arcmins. We show the lensing signal of the four selections in Figure 5.14. We find that the lens-

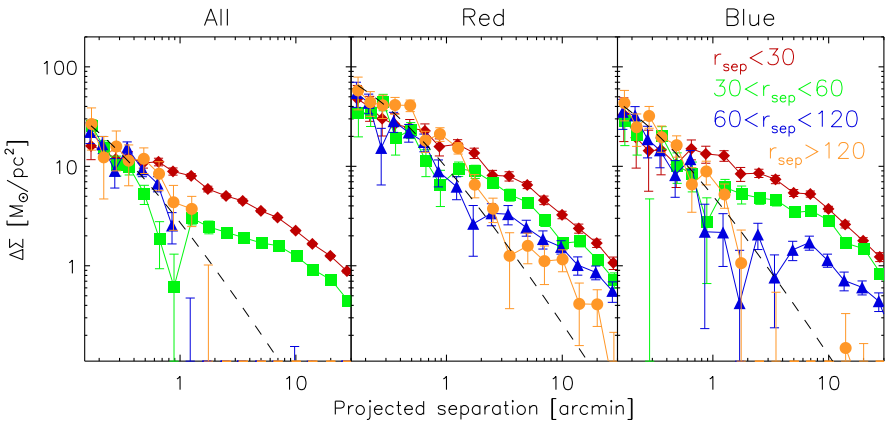

Figure 5.14: The lensing signal as a function of projected separation for the three lens samples that have been divided according to the minimum distance to a brighter galaxy, as indicated in the top right panel. The red diamonds indicate the lensing signal of those lenses that have a brighter neighbour within 30 arcsecs, the green squares the signal of the lenses that have a brighter neighbour between 30 and 60 arcsecs, the blue triangles the signal of the lenses that have a brighter neighbour between 60 and 120 arcsecs, and the orange circles the signal of the lenses that have no brighter neighbour within 2 arcmins. The dashed lines show the best fit NFW profiles fitted to the lensing signal of the total sample between 50 and 500 kpc using the mean lens redshift. The lensing signal on scales <0.5 arcmin is roughly similar for all lens samples, but the lensing signal on larger scales clearly decreases for increasingly isolated galaxies.

ing signal at scales smaller than ∼0.5 arcmin does not change much using the different isolation criteria, which demonstrates that we select haloes of similar mass. However, the large-scale signal decreases significantly for an increasing minimum separation to a brighter neighbour. The galaxies with no brighter object within 1 arcmin are selected for the isolated sample, the other galaxies are selected for the clustered sample. We could in principle select a more clearly distinguished sample of isolated and clustered lenses, e.g. by only selecting those galaxies with no brighter neighbour within 2 arcmins, and those with a brighter neighbour within 30 arcsecs. However, this would reduce the signal-to-noise of the lensing measurements such that no useful constraints could be obtained on the average halo ellipticity, and we therefore choose not to.

Note that the dependence of the large-scale lensing signal on the distance to a brighter neighbour is partly caused by differences in the lens environment, and partly by differences of the projected densities along the line-of-sight (LOS). For the clustered lenses, the LOS projections do not simply add random noise, but systematically increase the large-scale lensing signal because of the neighbour selection. Similarly, for the isolated galaxies, the underdense LOS leads to a decrease of the lensing signal on large scales. For the purpose of this work this is not important, since our main focus is to measure the anisotropy of the lensing signal. However, it should be kept in mind in the interpretation of the results.

5.C Average ratios and their errors

To calculate $f_{\rm mm}$, $f_{\rm mm}^{\rm corr}$ and $(f - f_{45})$ we have to determine the ratio of two variables. Let us call these variables x and y, and $m = x/y$ the ratio we are interested in. If x and y are independent and have a Gaussian distribution with means μ_x and μ_y and widths σ_x and σ_y we can compute the probability distribution of m using (Hinkley 1969)

$$p(m) = \frac{b(m)c(m)}{\sqrt{2\pi}a^3(m)\sigma_x\sigma_y}\left[2\Phi\left(\frac{b(m)}{a(m)}\right)\right] + \frac{1}{\pi a^2(m)\sigma_x\sigma_y}e^{-\frac{1}{2}\left(\frac{\mu_x^2}{\sigma_x^2}+\frac{\mu_y^2}{\sigma_y^2}\right)}, \tag{5.26}$$

where

$$a(m) = \sqrt{\frac{1}{\sigma_x^2}m^2 + \frac{1}{\sigma_y^2}}, \tag{5.27}$$

$$b(m) = \frac{\mu_x}{\sigma_x^2}m + \frac{\mu_y}{\sigma_y^2}, \tag{5.28}$$

$$c(m) = e^{\frac{1}{2}\frac{b^2(m)}{a^2(m)}-\frac{1}{2}\left(\frac{\mu_x^2}{\sigma_x^2}+\frac{\mu_y^2}{\sigma_y^2}\right)}, \tag{5.29}$$

and

$$\Phi(m) = \int_{-\infty}^{m}\frac{1}{\sqrt{2\pi}}e^{-\frac{1}{2}u^2}du. \tag{5.30}$$

By integrating $p(m)$ we can determine the median, and the 68% confidence intervals.

Next, we want to combine various measures of m_i into one average. We follow the approach described in Mandelbaum et al. (2006a). It relies on the use of a slightly different variable, i.e. $y_i - mx_i$, which is again a random Gaussian variable. If the shear ratio is constant over the range of interest, its value can be determined with

$$\frac{-Z}{\sqrt{\sum w_i}} < \frac{\sum w_i(y_i - mx_i)}{\sum w_i} < \frac{Z}{\sqrt{\sum w_i}}, \tag{5.31}$$

where $w_i = 1/(\sigma_{y_i}^2 + m^2\sigma_{x_i}^2)$ and $\sigma_{y_i}^2$ and $\sigma_{x_i}^2$ the error on y_i and x_i, respectively. $Z = 0$ then gives the average ratio, whilst $Z = 1$ gives the 68% confidence intervals. Note that Equation (5.31) can also be used to determine the ratio of a single measurement, but we prefer the use of Equation (5.26) as it directly provides the full probability distribution.

5.D Lens light contamination

The light from bright and elliptical lenses changes the source number density along the major and minor axis differently on small projected separations close to the lens. This could bias the correction we make to account for physically associated galaxies in the source sample. We investigate the size of the effect by

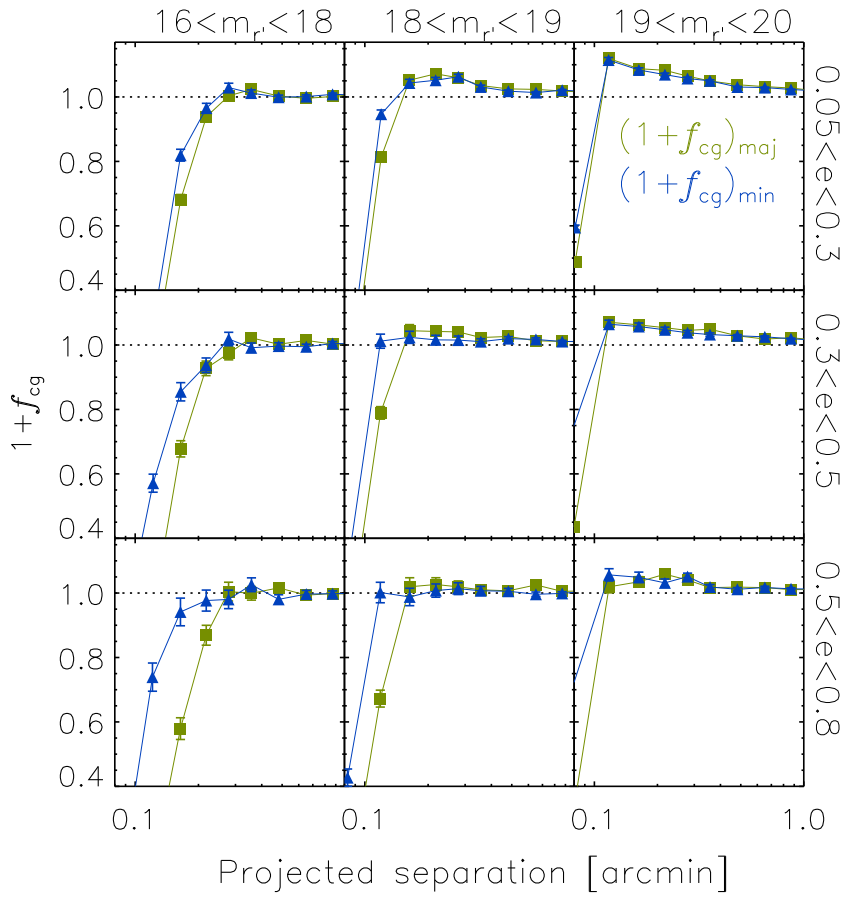

Figure 5.15: The source number density along the major and minor axis close to bright foreground galaxies, indicated by green squares and blue triangles, respectively, selected on their apparent magnitudes (columns) and ellipticity (rows). On small scales, the deficiency of background galaxies along the major axis is larger for brighter and more elliptical galaxies.

selecting all galaxies with $16 < m_{r'} < 18$, $18 < m_{r'} < 19$ and $19 < m_{r'} < 20$, and divide each selection in three ellipticity bins. For each of these samples, we measure the source number density in the major and minor axis quadrants, and show the results in Figure 5.15. On small scales, we find that the deficiency in the major axis quadrants is indeed significantly larger, and the difference increases for brighter and more elliptical galaxies. For projected separations larger than 0.2 arcmin, the difference is negligible, except for the brightest and most elliptical bins. Therefore, for galaxies with $m_{r'} < 19$ we only use scales larger than 0.2 arcmin, whilst for galaxies with $m_{r'} > 19$ we use scales larger than 0.1.

5.E Magnification

Magnification may also affect the shear anisotropy measurements. In this appendix, we address two potential contaminants: anisotropic magnification by the lens, and additional magnification by other foreground galaxies.

5.E.1 Anisotropic magnification

If dark matter haloes are triaxial, the magnification of background sources will have an azimuthal dependence. Hence if the galaxy and dark matter halo are aligned, part of the observed anisotropy in the distribution of source galaxies may be due to anisotropic magnification. The shear anisotropy measurements are corrected, however, assuming that the anisotropic distribution is solely due to physically associated galaxies. If anisotropic magnification has a strong effect on the source density, the correction might therefore be biased. To obtain an estimate of the impact of anisotropic magnification, we assume that the galaxy and the dark matter halo are perfectly aligned. Furthermore, we assume that at small scales the stacked density profile of the lenses is approximately described by an SIE, with a surface density given by (Mandelbaum et al. 2006a)

$$\kappa = \frac{4\pi\sigma^2}{c^2}\frac{D_l D_{ls}}{D_s}\frac{1}{2r} \times \left[1 + \frac{e_h}{2}\cos(2\theta)\right]. \tag{5.32}$$

σ is the average velocity dispersion, which we determine by fitting an SIS to the azimuthally averaged tangential shear within the virial radius, D_{ls}/D_s is determined by integrating over the source redshift distribution, and the halo ellipticity e_h is assumed to be equal to the mean galaxy ellipticity, as tabulated in Table 5.1 (i.e. assuming $f_{\rm h} = 1$). We determine the magnification using $\mu = 1 + 2\kappa$ at a projected separation of 10 arcsecs. The change in number density due to magnification in the major axis quadrant, $f_{\rm B}^{\rm mag}(r)$, is calculated with (Narayan 1989)

$$\begin{aligned} f_{\rm B}^{\rm mag}(r) &= \frac{2}{\pi}\int_{-\pi/4}^{\pi/4} d\theta N_{\rm B}(m,r,\theta)/N_0(m)dm \\ &= \frac{2}{\pi}\int_{-\pi/4}^{\pi/4} d\theta \mu_{\rm B}^{2.5s(m)-1}dm, \end{aligned} \tag{5.33}$$

where $N_0(m)$ is the background galaxy number density, $N_{\rm B}(m,r,\theta)$ is the number density after magnification in the major axis quadrant, and $s(m)$ is the slope of the logarithmic galaxy number counts at magnitude m. The change in number density along the minor axis, $f_{\rm A}^{\rm mag}(r)$, is calculated similarly. We determine $s(m)$ using the photometric redshift catalogue of Ilbert et al. (2006), and find that it decreases from 0.34 at $m_{r'} = 22$ to 0.22 at $m_{r'} = 24$; we use the average value $s(m) = 0.28$. Hence the number density of our source sample is diluted due to magnification, more strongly along the major axis of the lenses than along the minor axis as the magnification along the major axis is larger. For the 'all' lens sample, we find that at 10 arcsecs, $f_{\rm B}^{\rm mag} = 0.9969$ and $f_{\rm A}^{\rm mag} = 0.9974$. For the 'red' lens sample we find $f_{\rm B}^{\rm mag} = 0.9927$ and $f_{\rm A}^{\rm mag} = 0.9935$, and for the 'blue' lens sample we find $f_{\rm B}^{\rm mag} = 0.9946$ and $f_{\rm A}^{\rm mag} = 0.9954$. Hence the effect of anisotropic magnification is expected to be very small, and does not cause

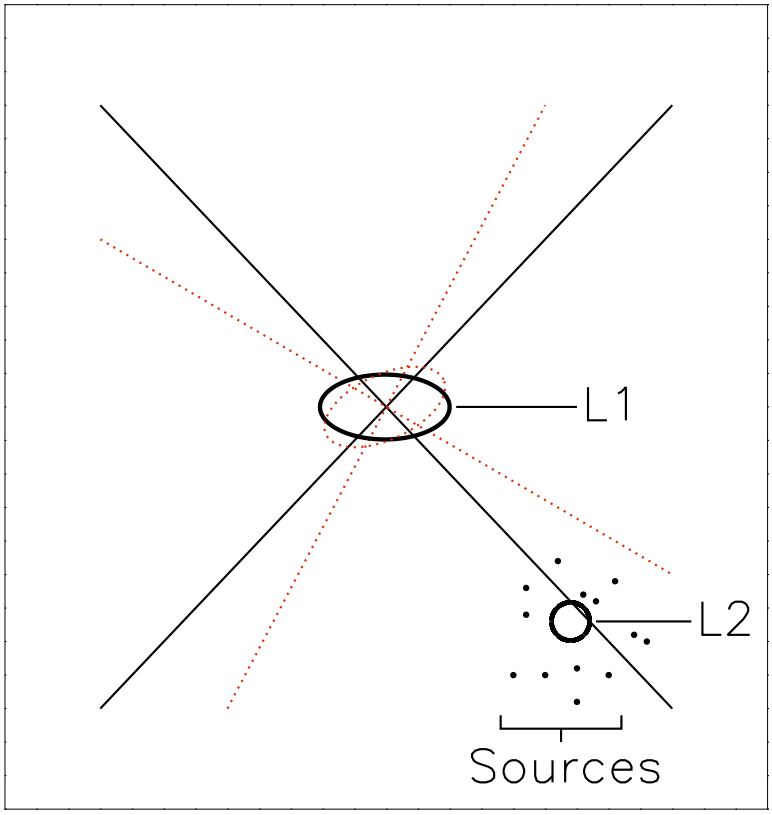

Figure 5.16: Cartoon to illustrate a potential bias in the halo ellipticity measurement due to magnification. In the presence of a foreground galaxy L2, the quadrants where the tangential shear is averaged are rotated. L2 also magnifies the background sky, leading to an relative increase or decrease in number of sources in the minor axis quadrant. This potentially biases the measured shear ratio on small scales.

the observed anisotropy of the excess source galaxy density ratio.

5.E.2 Magnification by L2

Foreground galaxies that lens both the lens galaxy and the sources also magnify the background sky. This causes a change in the source number density around the foreground galaxy. Consequently, the positions of the foreground galaxy and the background sources become related. This could potentially lead to a false shear anisotropy signal. We explain the effect using a cartoon in Figure 5.16.

In this figure, we measure the shear anisotropy around lens L1. The intrin-

sic shape of L1 is shown by the black ellipse, and the regions where we average the tangential shear in the absence of a foreground lens are indicated by the black lines. In the presence of a foreground lens L2 that is located close to one of the original quadrant's axes, the position angle of L1 changes, and the quadrants where we average the shear rotate, as indicated by the red dotted lines. L2 also locally magnifies the background sky, leading to either an increase or decrease in the source number density around L2. When we average the tangential shear in the rotated quadrants as would be done in observations, these magnified sources predominantly move into the minor axis quadrant (region `A` in Figure 5.3). If the source number density increases around L2, we find that we have more sources in the minor axis quadrants than in the major axis quadrants. Furthermore, the average shear changes, biasing the shear ratio high. If the source number density decreases instead, the opposite effect happens.

The presence of this bias could be identified by comparing the number counts of the sources in the two quadrants for the radial bins close to the lens, as the effect is strongest on small scales. The effect is mixed, however, with the anisotropic distribution of satellite galaxies. However, we already found in Appendix 5.E.1 that magnification for our source sample is negligible. Therefore, we expect that this source of bias is small, and can be ignored with the current data. The effect may be measurable by selecting a sample of source galaxies that are clearly in the background, and whose number density slope is steep (e.g. Lyman-break galaxies), as these are the conditions favourable to magnification.

5.F Multiple deflections

To visualize how the shear anisotropy is affected by multiple deflections, we simulate a lens galaxy L1 at a redshift 0.4. We assume the L1 is an SIE, with an ellipticity $e_1 = 0.2$ and $e_2 = 0$. The dark matter halo is perfectly aligned with the light distribution, and has the same ellipticity as the lens. We compute the lensing signal with Equation (5.24) for a velocity dispersion of 200 km s^{-1}. In the absence of multiple deflection, we find that $f_{\rm mm} = (\pi + e_h)/(\pi - e_h) = 1.136$. We insert a second lens L2 in the image, a round SIS at $z = 0.1$ with a velocity dispersion $\sigma = 200$ km s^{-1}. For every position of L2 in the simulated image, we calculate $\tilde{f}_{\rm mm}(r = 100)$, the shear ratio we would observe for a projected lens-source separation of 100 arcsecs, using a source redshift of 0.8. The result is shown in Figure 5.17.

We find that depending on the location of L2, $\tilde{f}_{\rm mm}$ either becomes larger or smaller than 1.136, and even in some configurations turns negative. These trends can easily be understood: e.g. if L2 is located at (50,250), left to the lens and the ring of sources, it increases the tangential shear of the sources along the major axis (region `B` in Figure 5.3), but it decreases the tangential shear of the sources along the minor axis (region `A` in Figure 5.3). The impact on the ellipticity of L1 is very small, and consequently we find that $\tilde{f}_{\rm mm}$ increases. If L2 is located very close to the sources, it can change the source ellipticities by such amounts that the net tangential shear with respect to L1 becomes negative, which results in a negative shear ratio.

Equivalently to Equation (5.23), we compute $\tilde{f}^{\rm corr}_{\rm mm}$ as a function of the position of L2, which is shown in the right-hand panel of Figure 5.17. If L2 is at a

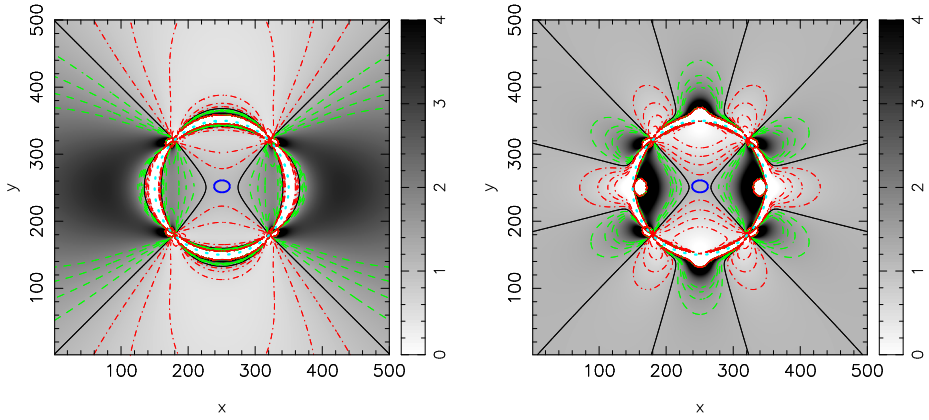

Figure 5.17: Observed shear ratio of an elliptical lens L1 at $z = 0.4$ for sources at a projected separation of 100 arcsecs, in the presence of an additional foreground galaxy L2 at $z = 0.1$ that is located at (x, y). In the left-hand panel we show $\tilde{f}_{\rm mm}$, the ratio of the average shear along the major and minor axis. The location of L1 is indicated by the blue ellipse in the centre of the image, the location of the sources by the cyan dots. We find that depending on the position of L2, the shear ratio either increases or decreases. The black solid lines indicate the position of L2 where $\tilde{f}_{\rm mm}$ remains constant, the red dot-dashed (green dashed) lines indicate a decrease (increase) of $\tilde{f}_{\rm mm}$ of 0.2, 0.4 and 0.6, respectively. In the right-hand panel, we show $\tilde{f}^{\rm corr}_{\rm mm}$, the shear ratio corrected using the cross terms. For large L2-source separations, the induced shear on the lens and the sources is almost constant, and is effectively removed using the cross terms. For small separations, the residual is large as the applied shear from L2 varies strongly along the ring of sources. Note that both L1 and L2 are modeled by an SIS.

large distance from the sources and L1, the induced shear on both L1 and the sources is almost constant, and is effectively removed using the cross terms. For smaller separations, correcting the ratio using the cross terms does not work well as the applied shear from L2 varies strongly along the ring of sources.

To quantify the net effect of multiple deflections on the shear ratio, we determine the total contribution to $\gamma_{t,A}$ and $\gamma_{t,B}$ by integrating over all L2 positions. Then we compute the average value of the ratio:

$$\langle \tilde{f}_{\rm mm}(r) \rangle = \frac{\gamma_{t,B0} + \bar{n_{L2}} \Delta\gamma_{t,B}}{\gamma_{t,A0} + \bar{n_{L2}} \Delta\gamma_{t,A}}, \tag{5.34}$$

where $\gamma_{t,A0}$ and $\gamma_{t,B0}$ are the average tangential shear along the minor and major axis in the absence of L2, $\Delta\gamma_{t,A}$ and $\Delta\gamma_{t,B}$ are the total contributions to the tangential shear along the minor and major axis, and $\bar{n_{L2}}$ is the foreground galaxy number density. The change of the shear ratio depends on the ellipticity of the lens, the density profiles of L1 and L2, the area within which we integrate the contributions of L2, and on the number of second deflectors, $\bar{n_{L2}}$. We study these dependencies below.

In Figure 5.18a, we show $\langle \tilde{f}_{\rm mm} \rangle$ and $\langle \tilde{f}^{\rm corr}_{\rm mm} \rangle$ as a function of $r_{\rm out}$, the radius of the circle centred at L1 within which we integrate the contributions of L2 (hence for a $r_{\rm out}$ of 50 arcsecs, we only account for contributions of L2 that are

Figure 5.18: (*a*) Observed value of $f_{\rm mm}$ (dotted line) and $f_{\rm mm}^{\rm corr}$ (solid line) for a lens L1 with an SIE profile and ellipticity $(e_1, e_2) = (0.2, 0.0)$, measured using sources at 100 arcsec, as a function of $r_{\rm out}$, the projected radius from L1 within which the contributions of L2 are integrated. The black lines show the reduction if L2 is an SIS, the green (red) if L2 is a TIS with a truncation radius of 150 (50) arcsec. The dashed line indicates the shear ratio in the absence of L2. This figure demonstrates that L2 at projected separations > 100 arcsec from L1 have a non-negligible influence on the shear ratio. Multiple deflections reduce the observed shear ratio, but using the cross shear we can correct for most of it. (*b*) Observed value of $f_{\rm mm}^{\rm corr}$ as a function of source radius, for an $r_{\rm out}$ of 4000 arcsec. The reduction of $f_{\rm mm}^{\rm corr}$ increases with increasing L1-source separation. (*c*) Difference between the observed value of $f_{\rm mm}^{\rm corr}$ and the shear ratio in the absence of multiple deflections ($f_{\rm mm,no\ MD}$) as a function of the ellipticity of L1, measured at a L1-source separation of 100 arcsec, for an outer radius of integration of 4000 arcsec. The reduction of the shear ratio increases with decreasing ellipticity.

located within 50 arcsecs from L1), for a L1-source separation of 100 arcsec. We use three different profiles for L2, i.e. an SIS and two truncated SIS (TIS) profiles with a truncation radius of 50 and 150 arcsec. Most real galaxies have a density distribution that falls somewhere in between these extremes. The value for n_{L2}^{-} we have adopted is 100 galaxies per square degree. The velocity dispersions and redshifts of the galaxies are similar to the values used before.

We find that the reduction of the shear ratio is a strong function of $r_{\rm out}$. It reaches a minimum when $r_{\rm out}$ is equal to the L1-source projected separation, which is expected from Figure 5.17; if L2 is located at the ring of sources, the shear ratio becomes large and negative, which leads to a reduction of the average ratio. For larger $r_{\rm out}$, we find that the shear ratio increases again. If L2 is an SIS, we find that the ratio turns over and continues to decrease. If L2 is a TIS, it does not contribute to the shear ratio if it is located at a projected separation much larger than the truncation radius, and the ratio therefore converges to a certain value. We observe that the impact of multiple deflections is mostly removed for $\langle\tilde{f}_{\rm mm}^{\rm corr}\rangle$. Even if L2 is an SIS, the total reduction of the shear ratio is small as long as we integrate the contributions of L2 over a sufficiently large area.

In Figure 5.18b, we show $\langle\tilde{f}_{\rm mm}\rangle$ and $\langle\tilde{f}_{\rm mm}^{\rm corr}\rangle$ as a function of projected source separation for an $r_{\rm out}$ of 4000 arcsec. We find that $\langle\tilde{f}_{\rm mm}\rangle$ decreases with r_s if L2 is an SIS. If L2 is a TIS, $\langle\tilde{f}_{\rm mm}\rangle$ reaches a minimum because L2 cannot shear both L1 and the sources if r_s becomes much larger than the truncation radius, which reduces the impact on $\langle\tilde{f}_{\rm mm}\rangle$. Furthermore, we find that $\langle\tilde{f}_{\rm mm}^{\rm corr}\rangle$ is hardly affected by multiple deflections on small scales. On large scales, however, the contribution from L2 is no longer constant, and the correction scheme fails.

Finally, we show the bias of the shear ratio as a function of ellipticity of L1 in Figure 5.18c. We find that the reduction is largest for the roundest lenses, as their position angles are affected most by the presence of L2. The impact of multiple deflections decreases for lenses with larger ellipticities.

For completeness, we show the impact of an additional foreground lens L2 located at (x, y) on $f\Delta\Sigma_{\rm iso}$ and $(f - f_{45})\Delta\Sigma_{\rm iso}$ in Figure 5.19. Similarly as for the shear ratios shown in Figure 5.17, we find that the cross terms remove most of the systematic contributions as long as L2 is not located very nearby.

5.G Intrinsic alignments

The shear anisotropy $(f - f_{45})\Delta\Sigma_{\rm iso}$ of the 'red' lens sample on small scales is negative (Figure 5.10). Since the source sample contamination of physically associated galaxies is largest at the same scales (see Figure 5.4), and since the distribution of these satellite galaxies is anisotropic (see Figure 5.5), a negative shear signal could also be caused if these satellite galaxies are preferentially radially aligned. To estimate the value of the average tangential intrinsic alignment that would produce such a signal, we rewrite Equation (5.9):

$$\begin{aligned} f\Delta\Sigma_{\rm iso}(r) = \frac{A}{N}\sum_{i=1}^{N_s} w_i\Delta\Sigma_i e_{g,i}^{\alpha}\cos(2\Delta\theta_i) + \\ \frac{A}{N}\sum_{i=1}^{N_I} w_i\Delta\Sigma_{\rm crit}\gamma_I e_{g,i}^{\alpha}\cos(2\Delta\theta_i); \end{aligned} \tag{5.35}$$

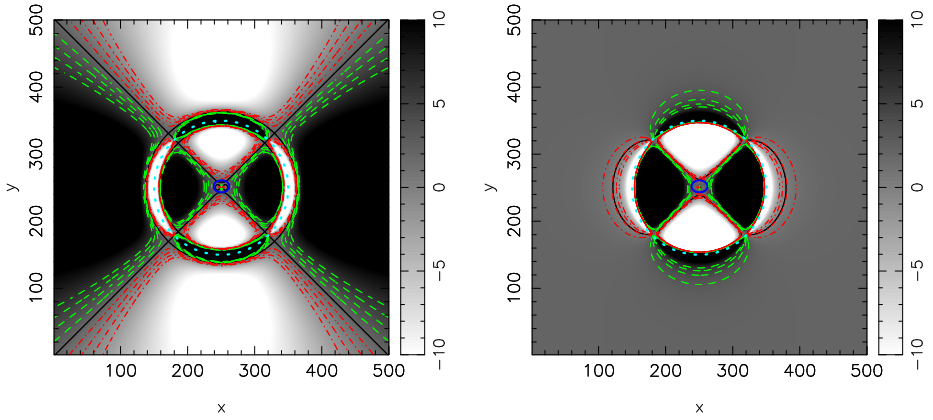

Figure 5.19: Net effect on $f\Delta\Sigma_{\rm iso}$ (left-hand panel) and $(f-f_{45})\Delta\Sigma_{\rm iso}$ (right-hand panel) for a L1 SIS with an ellipticity $(e_1, e_2) = (0.2, 0.0)$, measured using sources at 100 arcsec, in the presence of a second foreground galaxy L2 located at (x, y). The location of L1 is indicated by the blue ellipse in the centre of the image, the location of the sources by the cyan dots. We find that depending on the position of L2, the contribution to the shear is either positive or negative. The black solid lines indicate the position of L2 with no net contributions to $f\Delta\Sigma_{\rm iso}$ and $(f-f_{45})\Delta\Sigma_{\rm iso}$, the red dot-dashed (green dashed) lines indicate a decrease (increase) of $\Delta\Sigma$ of 1, 2 and 3 $[M_\odot/{\rm pc}^2]$ respectively.

$$N = 2\sum_{i=1}^{N_s} w_i e_{g,i}^{2\alpha}\cos^2(2\Delta\theta_i) + 2\sum_{i=1}^{N_I} w_i e_{g,i}^{2\alpha}\cos^2(2\Delta\theta_i),$$

with γ_I the tangential intrinsic alignment, and N_s and N_I the number of sources and physically associated galaxies, respectively. We assume that the shear signal is isotropic, hence the first term on the right-hand side of Equation (5.35) cancels. As the shear anisotropy is expected to be positive for the red early-type galaxies that make up the 'red' lens sample, our estimate of γ_I is a lower limit. To account for the fraction of satellites that is anisotropically distributed, we multiply Equation (5.35) with $f_{\rm cg}(r,\Delta\theta)/\langle f_{\rm cg}(r)\rangle_{\Delta\Theta}$. For $f_{\rm cg}$ we adopt the same form as in Section 5.2.4, i.e. Equation (5.15), which we insert into Equation (5.35). Ignoring the isotropic part, which cancels when averaged over the angle, we obtain:

$$f\Delta\Sigma_{\rm iso}(r) = \frac{A}{N}\sum_{i=1}^{N_I} w_i\Delta\Sigma_{\rm crit}\gamma_I e_{g,i}^{2\alpha}\cos^2(2\Delta\theta_i)\frac{2N_{\Delta\theta}}{N_{\rm iso}-1}, \tag{5.36}$$

and therefore

$$\begin{aligned}\gamma_I &= \frac{f\Delta\Sigma_{\rm iso}(r)}{2A\Sigma_{\rm crit}}\frac{N_s+N_I}{N_I}\frac{N_{\rm iso}-1}{N_{\Delta\theta}} \\ &= \frac{f\Delta\Sigma_{\rm iso}(r)}{2A\Sigma_{\rm crit}}\frac{N_{\rm iso}}{N_{\Delta\theta}},\end{aligned} \tag{5.37}$$

where we used that $(N_s+N_I)/N_I = N_{\rm iso}/(N_{\rm iso}-1)$. Averaging the results of the first two radial bins of the 'red' lenses, we obtain $\gamma_I = -0.062^{+0.042}_{-0.062}$ for $\alpha = 1$ at

an average separation of 0.19 arcmin ($\sim$65 kpc at the mean lens redshift). Our constraints are not particularly competitive (compare, e.g., Hirata et al. 2004), mainly because our methods are not designed for this measurement. For example, had we included brighter galaxies in the source sample, a larger fraction of those would be physically associated to the lenses, improving the constraints on the galaxy overdensity, and hence on γ_I. This, however, is not the purpose of this work. Note that the value and error on γ_I we obtain is roughly a factor 10 larger than the results from Hirata et al. (2004), who aimed their analysis to measure this effect using data from the SDSS (although no division was made between early-type and late-type galaxies, which could average out the effect). Conversely, the expected impact of intrinsic alignments is about a factor ten smaller than the signal we observe, hence it is unlikely that our measurements are significantly affected. Hence the negative shear anisotropy is unlikely caused by intrinsic alignments.

6

Redshift dependence of the mass-richness relation of clusters in the second Red-sequence Cluster Survey

We study the relation between the richness and mass of a sample of 1.4×10^4 clusters of galaxies in the redshift range $0.2 < z < 1.2$ and masses $M_{200} > 2\times10^{13}h_{70}^{-1}M_\odot$, discovered in the second Red-sequence Cluster Survey (RCS2). Cluster masses are determined from the weak gravitational lensing signal of the clusters; the depth and image quality of the RCS2 enable the detection of the cluster-mass cross-correlation signal even at redshifts $z \sim 1$. We fit the mass-richness relation with $M_{200} = A(N_{200}/20)^\alpha$, and find $A = (15.09 \pm 0.66) \times 10^{13}h_{70}^{-1}M_\odot$ and $\alpha = 0.86 \pm 0.05$ for the full sample. To explore any redshift dependence of the scaling relation, we split the cluster sample in four redshift slices. We find that the mass-richness relation depends on redshift. The change with redshift is strongest for galaxy groups and poor clusters; we find that a $N_{200} = 5$ cluster at $z = 0.25$ is $1.6^{+0.6}_{-0.4}$ times more massive than a $N_{200} = 5$ cluster at $z = 0.7$. For the clusters with $N_{200} > 15$, the data are consistent with no change. With this calibration between richness and mass, the RCS2 cluster sample can be exploited to constrain cosmological parameters. We discuss a few potential observational biases and physical processes that may contribute to the observed redshift dependence.

E. van Uitert, H. Hoekstra, E. Semboloni, D.G. Gilbank, M.D. Gladders, H.K.C. Yee, in preparation;

6.1 Introduction

Galaxy clusters correspond to the largest gravitational potentials in the universe. Their abundance as a function of mass sensitively depends on various cosmological parameters, such as the normalization of the matter power spectrum, σ_8, and the cosmological matter density, Ω_M (e.g. Evrard 1989; White et al. 1993). The evolution of the abundance depends on the dark energy equation of state (e.g. Voit 2005; Allen et al. 2011). These cosmological parameters can therefore be constrained by accurately determining the cluster mass function, and its dependence on redshift.

The first step of determining the cluster mass function is the detection of the clusters. Clusters can be found in various ways, such as by detecting X-ray peaks in the sky background (e.g. Böhringer et al. 2000; Lloyd-Davies et al. 2011), by measuring the spectral distortions of the cosmic microwave background radiation from inverse Compton scattering, known as the Sunyaev-Zeldovich effect (SZE; Sunyaev & Zeldovich 1972) which has recently been applied to various dedicated surveys (e.g. Williamson et al. 2011; Marriage et al. 2011), or by detecting galaxy density enhancements in optical surveys (e.g. Gladders & Yee 2005; Koester et al. 2007). These observations provide various cluster properties which can be related to the mass, including the X-ray flux and temperature, SZE properties of the clusters such as the detection significance, the number of cluster members within a certain aperture (the richness), but not the mass itself.

The total mass of a cluster can only be determined indirectly. Various methods have been employed for this purpose. The kinematics of satellite galaxies in clusters have been used (e.g. van der Marel et al. 2000; Łokas et al. 2006), but these observations are generally expensive as they require spectroscopic observations of many cluster members. Additionally, assumptions on the satellite orbits are needed to convert the velocity dispersions into a mass estimate. X-ray luminosities emitted by hot gas in clusters can also be used to estimate the mass (e.g. Reiprich & Böhringer 2002), under the assumption that the gas is in hydrostatical equilibruim. The results of Mahdavi et al. (2008) suggest, however, that clusters are generally not in hydrostatical equilibruim, which could bias the X-ray based mass estimates. The Sunyaev-Zeldovich effect has also been used (e.g. Williamson et al. 2011), and appears particularly useful to estimate the masses of massive clusters at high redshifts. Another popular method, the one employed in this work, is weak gravitational lensing.

In weak lensing the distortion of the images of faint background galaxies (sources) due to the gravitational potentials of intervening structures (lenses) is measured. From this distortion, the differential surface mass density of the lenses can be deduced, which can be modeled to obtain the total mass. A major advantage of gravitational lensing over other methods is that it does not rely on optical tracers; the distortion can be measured for any lens, out to large radii where no optical tracers can be used. Additionally, the weak lensing signal does not depend on the physical state of the matter in the clusters, and no assumptions have to be made (e.g. virial equilibrium) to measure the total mass.

Weak gravitational lensing has been used to determine the mass of individual massive low-redshift clusters (e.g. Hoekstra 2007; Okabe et al. 2010). The signal-to-noise of low-mass clusters or galaxy groups is generally not high enough

to obtain a reliable mass estimate. However, by stacking the signal of a certain set of these clusters, the average mass of these systems can be determined (e.g. Mandelbaum et al. 2006; Sheldon et al. 2009b).

A number of complications limit a simple interpretation of the weak lensing mass estimates of clusters. The two complications that are thought to dominate are the triaxiality of dark matter haloes (e.g. Clowe et al. 2004; Corless & King 2007), and the presence of correlated and uncorrelated structure along the line-of-sight (e.g. Metzler et al. 2001; Hoekstra 2001; Hoekstra et al. 2011b). These complications are mainly thought to increase the scatter of the mass estimates, but may even lead to small ($\sim$5-10%) biases if model fitting techniques are used (Becker & Kravtsov 2011; Rasia et al. 2012). The lensing signal can be modeled in various ways, and particular choices can reduce this bias (Mandelbaum et al. 2010). More detailed numerical simulations are required to quantify this bias more precisely, e.g. as a function of mass and redshift, to interpret the results correctly. This is important for the exploitation of clusters as a percent-level precision tool for cosmology.

To accurately determine the cluster mass function and its redshift dependence, we need mass estimates of large numbers of clusters covering a broad range of masses and redshifts. Since the lensing signal of individual clusters that are not massive, or located at high redshifts, is generally too weak to extract a reliable mass estimate, we cannot measure the cluster mass function directly from the data. A common solution is to determine how a cluster property that can be directly estimated from the data is related to the total mass as determined from lensing. A convenient cluster property that can be used for this purpose is the richness, because it is a quantity that can be obtained from readily available multi-colour imaging data, the same data that is used for the lensing analysis. To constrain the cosmological parameters with the cluster richness function rather than the mass function requires a careful calibration of the relation between the mass and richness of clusters.

To determine the richness of a cluster it is necessary to distinguish the cluster galaxies from the fore- and background galaxies. Cluster members can be identified if their redshift or velocity dispersions are available, which either requires spectroscopy or observations in many bands for reliable photometric redshifts. Alternatively, cluster members can be identified using their colours as the majority of early-type galaxies in a cluster populate a narrow range in colour-magnitude space, i.e. the E/S0 ridge-line or the red sequence (Gladders & Yee 2000). The advantage of the latter is that observations in only two bands suffice, which makes it cheap and particularly suited for the automated detection of clusters in large imaging surveys (e.g. Gladders & Yee 2005). This richness does not include the blue star-forming galaxies, but since we are mainly interested in calibrating a cluster observable to the total mass, this is of no importance.

Note that the mass-richness relation is not only interesting for the exploitation of clusters as cosmological probes, but also to improve our understanding of cluster evolution processes. Once formed, clusters continue to evolve through the accretion of galaxies and dark matter, internal processes in the cluster members, tidal interactions and mergers with other clusters. These processes change both the appearance of clusters as well as other intrinsic properties, such as their mass, shape and angular momentum. To learn more about these processes, we can study the evolution of the relation between various cluster properties, such as the relation between mass and richness.

This study is performed using the imaging data from the second Red-sequence Cluster Survey (RCS2; Gilbank et al. 2011). The study of cluster evolution is one of the main science goals of the RCS2. The survey design was chosen such to optimize the detection of a large number of clusters using the red sequence method (Gladders & Yee 2000). A preliminary cluster catalogue has been made available containing 27 793 clusters spread over a large range in optical richness, and redshifts in the range $0.2 < z < 1.2$ (Gladders et al., in prep.). In contrast, the redshift range of the maxBCG cluster sample (Koester et al. 2007), a catalogue of 13 823 clusters that has been detected in the Sloan Digital Sky Survey (SDSS; York et al. 2000), only covers a redshift range $0.1 < z < 0.3$, which limits their use for evolutionary studies. The redshift range of clusters in the RCS2, however, combined with the excellent lensing quality of the data, makes the RCS2 exceptionally suited for this purpose. This is demonstrated in this work, where we analyse the redshift dependence of the mass-richness relation.

The outline is as follows. In Section 6.2, we discuss the various steps of the lensing analysis: we detail the creation of the shape measurement catalogues, provide a short summary on the detection of clusters, and discuss the modeling of the lensing signal. The mass-richness relation for the RCS2 clusters is presented in Section 6.3, and its redshift dependence is discussed in Section 6.4. We conclude in Section 6.5. Throughout the paper we assume a WMAP7 cosmology (Komatsu et al. 2011) with $\sigma_8 = 0.8$, $\Omega_\Lambda = 0.73$, $\Omega_M = 0.27$, $\Omega_b = 0.046$ and $h = 0.7$ the dimensionless Hubble parameter. All distances quoted are in physical (rather than comoving) units unless explicitly stated otherwise.

6.2 Lensing analysis

The Red-sequence Cluster Survey 2 (RCS2) (Gilbank et al. 2011) is a nearly 900 square degree imaging survey in three bands (g', r' and z') carried out with the Canada-France-Hawaii Telescope (CFHT) using the 1 square degree field of view camera MegaCam. In this work, we use the 740 square degree of the primary imaging data. The remainder constitutes the 'Wide' component of the CFHT Legacy Survey (CFHTLS). The lensing analysis is performed on the 8 minute exposures of the r'-band ($r'_{\rm lim}$ ∼24.3), which is best suited for lensing with a median seeing of $0.71''$.

6.2.1 Data reduction

The photometric calibration of the RCS2 is described in detail in Gilbank et al. (2011). The magnitudes are calibrated using the colours of the stellar locus and the overlapping Two-Micron All-Sky Survey (2MASS), and have an accuracy smaller than 0.03 mag in each band compared to the SDSS. For more details, we refer the reader to Gilbank et al. (2011).

The lensing analysis is described in van Uitert et al. (2011). Here, we present a summary of the essential steps. In order to create the shape catalogues, we retrieve the Elixir[1] processed images from the Canadian Astronomy Data Centre (CADC) archive[2]. We use the THELI pipeline (Erben et al. 2005, 2009) to subtract the image backgrounds, create weight maps that we use in the

[1] http://www.cfht.hawaii.edu/Instruments/Elixir/
[2] http://www1.cadc-ccda.hia-iha.nrc-cnrc.gc.ca/cadc/

object detection phase, and to identify satellite and asteroid trails. To detect the objects in the images, we use `SExtractor` (Bertin & Arnouts 1996). The stars that are used to model the PSF variation across the image are selected using size-magnitude diagrams. All objects larger than 1.2 times the local size of the PSF are identified as galaxies. We measure the shapes of the galaxies with the KSB method (Kaiser et al. 1995; Luppino & Kaiser 1997; Hoekstra et al. 1998), using the implementation described by Hoekstra et al. (1998, 2000). This implementation has been tested on simulated images as part of the Shear Testing Programmes (STEP) (the 'HH' method in Heymans et al. (2006) and Massey et al. (2007), respectively), and these tests have shown that it reliably measures the unconvolved shapes of galaxies for a variety of PSFs. Finally, the source ellipticities are corrected for camera shear, which originates from slight non-linearities in the camera optics. The resulting shape catalogue of the RCS2 contains the ellipticities of 2.2×10^7 galaxies. A more detailed discussion of the analysis can be found in van Uitert et al. (2011).

6.2.2 Cluster detection

The clusters are identified with the Cluster-Red-Sequence method (CRS; Gladders & Yee 2000) using the deep optical imaging data of the RCS2. This technique makes use of the property that the majority of early-type galaxies of a cluster at a given redshift populate a narrow volume in colour-magnitude space, i.e. the red sequence, with a small scatter (e.g. Bower et al. 1992). The intrinsic colour scatter does not significantly evolve up to a redshift of 1.5 (for a compilation of low- and high-redshift results, see Jaffé et al. 2011), and has a low variance between clusters (e.g. López-Cruz et al. 2004). In the CRS method, the colours, magnitudes and the locations of the galaxies are used to span a space in which the overdensities correspond to clusters. These overdensities are detected to identify and characterize the clusters following the methodology of Gladders & Yee (2000), the method that has been successfully applied to detect clusters in the first Red-sequence Cluster Survey (Gladders & Yee 2005). The location of the overdensity in colour space provides an accurate estimate of the redshift of the cluster. The significance of the detected overdensity is related to the richness. Details of the implementation of the CRS method for the RCS2 is presented in Gladders et al. (in prep.).

To identify the centre of the cluster, we use the location of the overdensity in the colour-magnitude-position space. The position of the brightest cluster galaxy is another commonly used estimator of the centre (e.g. Koester et al. 2007), and has been measured as well for the RCS2 clusters (Gralla et al., in prep.). By comparing the lensing signals around both estimates of the cluster centre, we can determine which one is closer to the actual centre of the projected total mass distribution. This will be done in a future work.

The richness of a cluster can be characterized in various ways (e.g. Rykoff et al. 2011; Rozo et al. 2009; Hansen et al. 2005; Yee & López-Cruz 1999). In this work we use N_{200}, the richness estimator that was used in the weak lensing analysis of the maxBCG clusters (Johnston et al. 2007; Sheldon et al. 2009b,a), as it eases a comparison of the results. N_{200} is defined as the number of E/S0 (red sequence) galaxies brighter than M*+2 within $r_{200}^{\rm gal}$, the radius where the

density is 200 times the critical density ρ_c. This radius is determined from the empirical relationship between $N_{\rm gal}$, the number of red sequence cluster members within a fixed 1 h^{-1} Mpc aperture, and $r_{200}^{\rm gal}$, the radius where the mean number density of galaxies is 200 times larger than the mean space density of galaxies, as measured for the maxBCG clusters (Hansen et al. 2005). This relation implicitly assumes that galaxies are unbiased with respect to the dark matter. The relation is given by

$$r_{200}^{\rm gal} = 0.156 N_{\rm gal}^{0.6} h^{-1}{\rm Mpc}. \tag{6.1}$$

This radius agrees within 5% to the r_{200} as determined with lensing (Johnston et al. 2007).

The definition of richness slightly differs between the maxBCG and the RCS2: the N_{200} of a maxBCG cluster includes all red galaxies (within $\pm 2\sigma$ of the red sequence) brighter than $0.4L*$ in the i-band. We study how the richness estimates compare by matching the maxBCG cluster catalogue to the RCS2 cluster catalogue, using the ∼300 square degrees overlap between the RCS2 and the SDSS. Approximately 150 clusters are matched. We find that the richness estimates agree well, albeit with large scatter. However, there is no evidence for a large systematic offset, and we conclude that we do not need to account for the different definitions of richness in order to compare the results of the maxBCG and the RCS2.

In this work, we use a preliminary version of the RCS2 cluster catalogue, which contains 14 279 clusters with $N_{200} > 5$. We show the distribution of redshift and richness of the cluster sample in Figure 6.1. The cluster sample covers a redshift range of $0.2 < z < 1.2$, which makes this sample very well suited for evolutionary studies (in particular compared to the maxBCG cluster sample of the SDSS, that only covers redshifts $0.1 < z < 0.3$). The richness estimates are not discrete values, as the average number of background galaxies is subtracted. Note that the abundance of clusters drops below $N_{200} < 4$ ($\log(N_{200}) < 0.6$). The lack of low-richness clusters at low redshift is not physical, and will be corrected in the final cluster catalogue. The richness estimates are therefore potentially biased in this richness range. We cannot assess this bias by comparing to the publicly available maxBCG catalogue, as this catalogue only covers $10 < N_{200} < 190$. Therefore, we only include clusters with $N_{200} > 5$ in our analysis. Since most of the lensing signal is produced by the rich clusters, this cut only causes a small increase of the errors of the best fit parameters of the mass-richness relation.

6.2.3 Lensing measurement

Imprinted on the ellipticities of the source galaxies are small distortions induced by the density profiles of the clusters. These distortions are measured by averaging the ellipticities of the source galaxies in radial bins centered at the lenses. The resulting tangential shear,

$$\langle \gamma_t \rangle (r) = \frac{\Delta\Sigma(r)}{\Sigma_{\rm crit}}, \tag{6.2}$$

is related to the surface density contrast $\Delta\Sigma(r) = \bar{\Sigma}(< r) - \bar{\Sigma}(r)$, the difference between the mean projected surface density enclosed by r and the mean

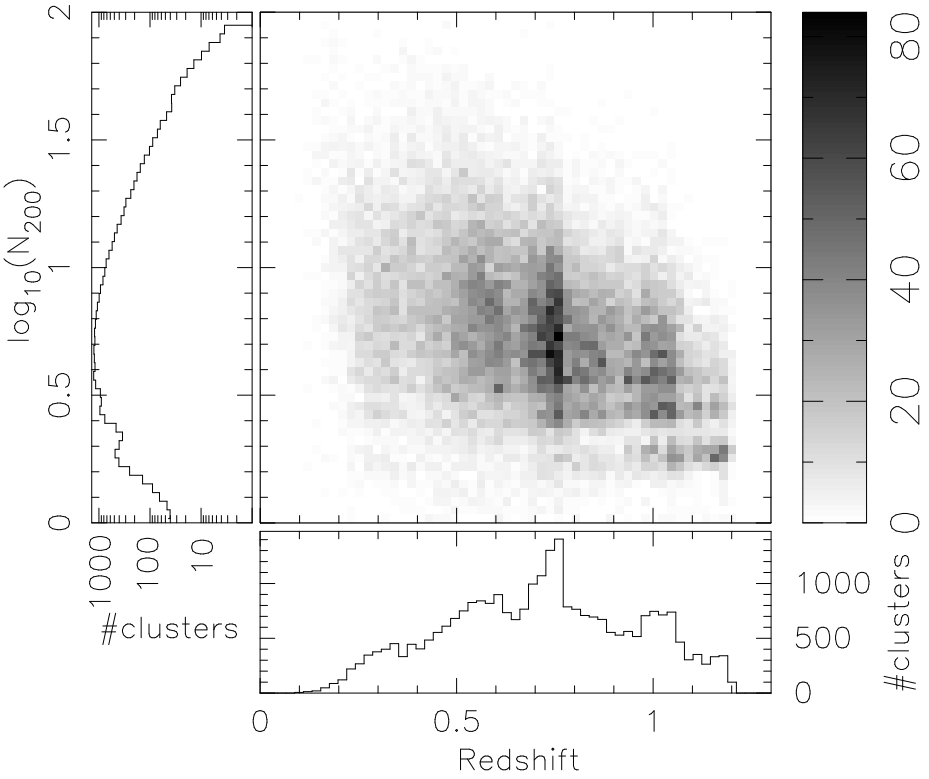

Figure 6.1: Redshift versus $\log(N_{200})$, the logarithm of the number of early-type cluster members brighter than M*+2 inside r_{200}, of the cluster sample. The clusters cover a large range in richness and redshift, and are therefore very well suited to study the redshift dependence of the mass-richness relation.

projected surface density at a radius r. $\Sigma_{\rm crit}$ is the critical surface density:

$$\Sigma_{\rm crit} = \frac{c^2}{4\pi G}\frac{D_s}{D_l D_{ls}}, \tag{6.3}$$

with D_l, D_s and D_{ls} the angular diameter distance to the lens, the source, and between the lens and the source, respectively. Since we lack redshifts, we select galaxies with $22 < m_{r'} < 24$ that have a reliable shape estimate (ellipticities smaller than one, no SExtractor flag raised) as sources. We obtain the approximate source redshift distribution by applying identical magnitude cuts to the photometric redshift catalogues of the Canada-France-Hawaii-Telescope Legacy Survey (CFHTLS) "Deep Survey" fields (Ilbert et al. 2006). To remove contributions of systematic shear (from, e.g., the image masks), we subtract the signal computed around random points from the signal computed around the real lenses (see van Uitert et al. 2011).

The distortions induced by weak lensing are much smaller than the intrinsic ellipticities of the sources. The lensing measurement of a single cluster is therefore generally very noisy. To improve the signal-to-noise, the lensing signal is therefore stacked for a sample of clusters that have similar properties (e.g. within a certain richness range). Stacking the lensing signal has the additional

advantage that the contribution from uncorrelated structures, as well as from potential small-scale residual systematics, averages out.

6.2.4 Contamination

A fraction of our source galaxies is physically associated with the clusters. They are not lensed and therefore dilute the lensing signal. We cannot remove them from the source sample because we lack redshifts. We can remove the bright elliptical cluster members using their colours. The faint cluster members, however, cannot be efficiently removed using their colours, because their red sequence is not well defined, and many of them are blue (Hoekstra 2007). Fortunately, we can account for the dilution of the lensing signal by measuring the excess source galaxy density around the lenses, $f_{cg}(r)$, and boost the lensing signal with $1+f_{cg}(r)$. This correction implicitly assumes that the satellite galaxies are randomly oriented. If the satellites are preferentially radially aligned to the lens, however, the contamination correction may be too low. Attempts have been made to measure this type of intrinsic alignment around galaxies. Some intrinsic alignment was detected in the studies that used the isophotal position angles for the galaxies (e.g. Agustsson & Brainerd 2006; Faltenbacher et al. 2007), whilst studies that used the galaxy moments instead did not measure a significant detection (e.g. Hirata et al. 2004; Mandelbaum et al. 2005). This discrepancy was attributed by Siverd et al. (2009) and Hao et al. (2011) to the different definitions of the position angle of a galaxy; the favoured explanation is that light from the central galaxy contaminates the light from the satellites, which affects the isophotal position angle more than the galaxy moments one. In addition, Sheldon et al. (2009b) detects no intrinsic alignment for a sample of 4119 spectroscopically confirmed clusters from Berlind et al. (2006), using all galaxies from the SDSS main spectroscopic sample (Strauss et al. 2002) in the range ± 2000 km s^{-1}. Since we measure the shapes of source galaxies using galaxy moments, and considering the results from Sheldon et al. (2009b), we expect that intrinsic alignments have a minor impact at most and can be ignored.

6.2.5 Lensing analysis

Numerical simulations suggest that the density distribution of collapsed dark matter haloes over a wide range of masses are well described by a Navarro-Frenk-White profile (NFW; Navarro et al. 1996). Therefore, we use this profile to model the lensing signal. The NFW density profile is given by

$$\rho(r) = \frac{\delta_c \rho_c}{(r/r_s)(1 + r/r_s)^2}, \tag{6.4}$$

with δ_c the characteristic overdensity of the halo, ρ_c the critical density for closure of the universe, and $r_s = r_{200}/c_{200}$ the scale radius, with c_{200} the concentration parameter. The NFW profile is fully specified for a given set of (M_{200}, c_{200}), with M_{200} the mass inside a sphere of radius r_{200}, the radius inside of which the density is 200 times the critical density ρ_c. Since numerical simulations have shown that the concentration depends on the mass and redshift of the halo, we can reduce the number of free parameters in the fit by

adopting a mass-concentration relation. Although the concentration at a fixed cluster mass exhibits a large scatter (e.g. Bahé et al. 2012), this does not affect our analysis since we stack the lensing signals of a large number of clusters. We use the mass-concentration relation from Duffy et al. (2008), which is based on numerical simulations using the best fit parameters of the WMAP5 cosmology. It is given by

$$c_{\rm NFW} = 5.71 \left(\frac{M_{200}}{2 \times 10^{12} h^{-1} M_{\odot}}\right)^{-0.084} (1+z)^{-0.47}. \tag{6.5}$$

Hence the only parameter we fit is M_{200}. We calculate the tangential shear profile using the analytical expressions provided by Bartelmann (1996) and Wright & Brainerd (2000).

To determine in which range the lensing signals of the clusters are accurately described by an NFW profile, we show the tangential shear of the full cluster sample in Figure 6.2. Since the assigned cluster centre used in the lensing measurements does not always correspond to the actual centre of the dark matter distribution, the lensing signal on small scales is biased low (e.g. Johnston et al. 2007; Hoekstra et al. 2011a). On large scales, the lensing signal is increased by the contribution of neighbouring structures. To prevent the effect of miscentering of clusters and the neighbouring structures from biasing the results, we fit the NFW profiles between 0.2 and 2 h_{70}^{-1} Mpc. We find that in this range, the NFW profile describes the lensing signal well, as is shown in Figure 6.2. Note that for this figure, we fit both M_{200} and c_{200} since the clusters cover a broad range of masses and concentrations.

In future work the measurements will be analysed using cluster halo models similar to those described in Johnston et al. (2007), and account for the miscentering of the clusters, for the additional lensing signal on large scales from neighbouring structures and for the scatter between halo mass and richness. This will enable us to include a broader range of scales in the fit, which improves the errors on the best fit parameters. Also, it will enable us to study the relation between the total mass and various other cluster properties, such as the concentration and the bias.

The results from Johnston et al. (2007) show that the distribution of projected radial offsets between the actual and the observed cluster centres is not well constrained by the lensing measurements. The lensing results are therefore sensitive to the assumed shape of this distribution that is used as a prior in the lensing models. To improve the prior from the data, we plan to use the galaxy overdensity measured around the cluster centres. Galaxies trace the dark matter potential, and the number density is therefore also affected by miscentering of clusters. We show the average galaxy overdensity around all clusters in Figure 6.2, and as a function of richness in Appendix 6.A. In short, the results we present here are preliminary, although we do not expect that the best fit values of M_{200} will change significantly.

6.3 Mass-richness relation

To determine the relation between richness and mass, we divide the clusters in bins of richness. Details for the cluster samples are given in Table 6.1. The

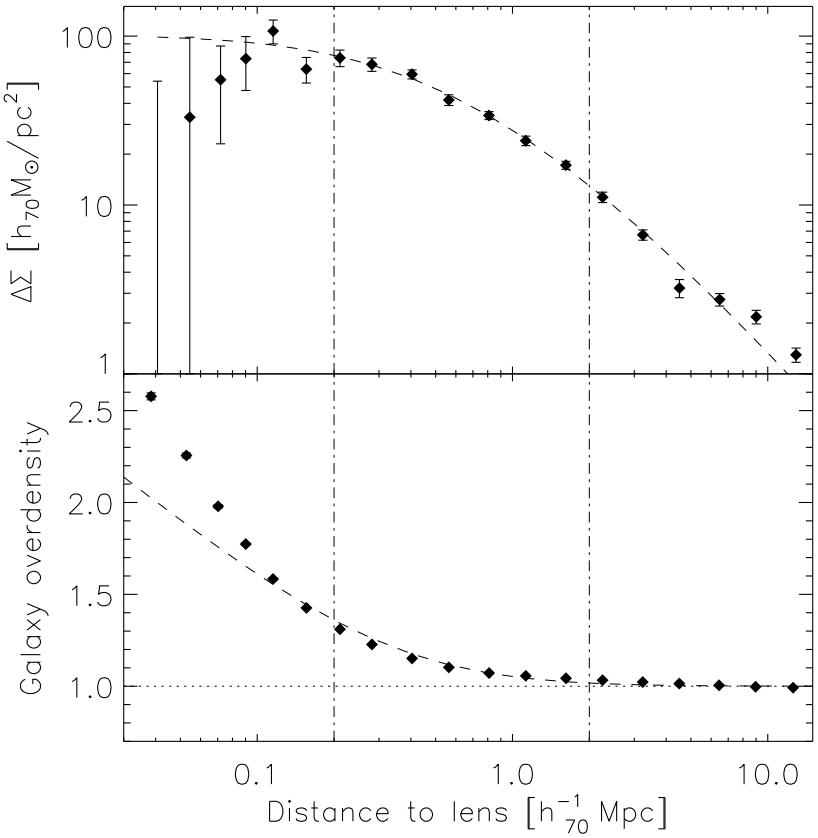

Figure 6.2: Stacked lensing signal and galaxy overdensity measured for all clusters with $N_{200} > 5$ in the RCS2. The dashed line in the top panel indicates the best fit NFW profile fitted to shear; the vertical dot-dashed lines indicate the fitting range. The surface density Σ that corresponds to the best fit lensing profile has been scaled to match the observed galaxy overdensity in the range $0.2 < r < 2$ h_{70}^{-1}Mpc in the bottom panel. Both profiles are shown for illustration only.

richness ranges are chosen such to enable a straightforward comparison to Johnston et al. (2007). The lensing signals of all clusters in each bin are stacked, and boosted with the excess source galaxy density to correct for the contamination of physically associated galaxies in the source sample. The resulting lensing signals are shown in Figure 6.3, together with their best fit NFW profiles. We find that in the range between 200 h_{70}^{-1} kpc and 2 h_{70}^{-1} Mpc, the lensing signal is described reasonably well by a single NFW profile, which is reflected by the χ^2-values of the fit. The average χ^2 is 8.4, whilst the expected value is 6. The largest χ^2 is for the $18< N_{200} <25$ bin, and has a value of 15.0.

Before we can compare the mass-richness relation we need to correct N_{200} for Eddington bias: clusters scatter preferentially from richness ranges where

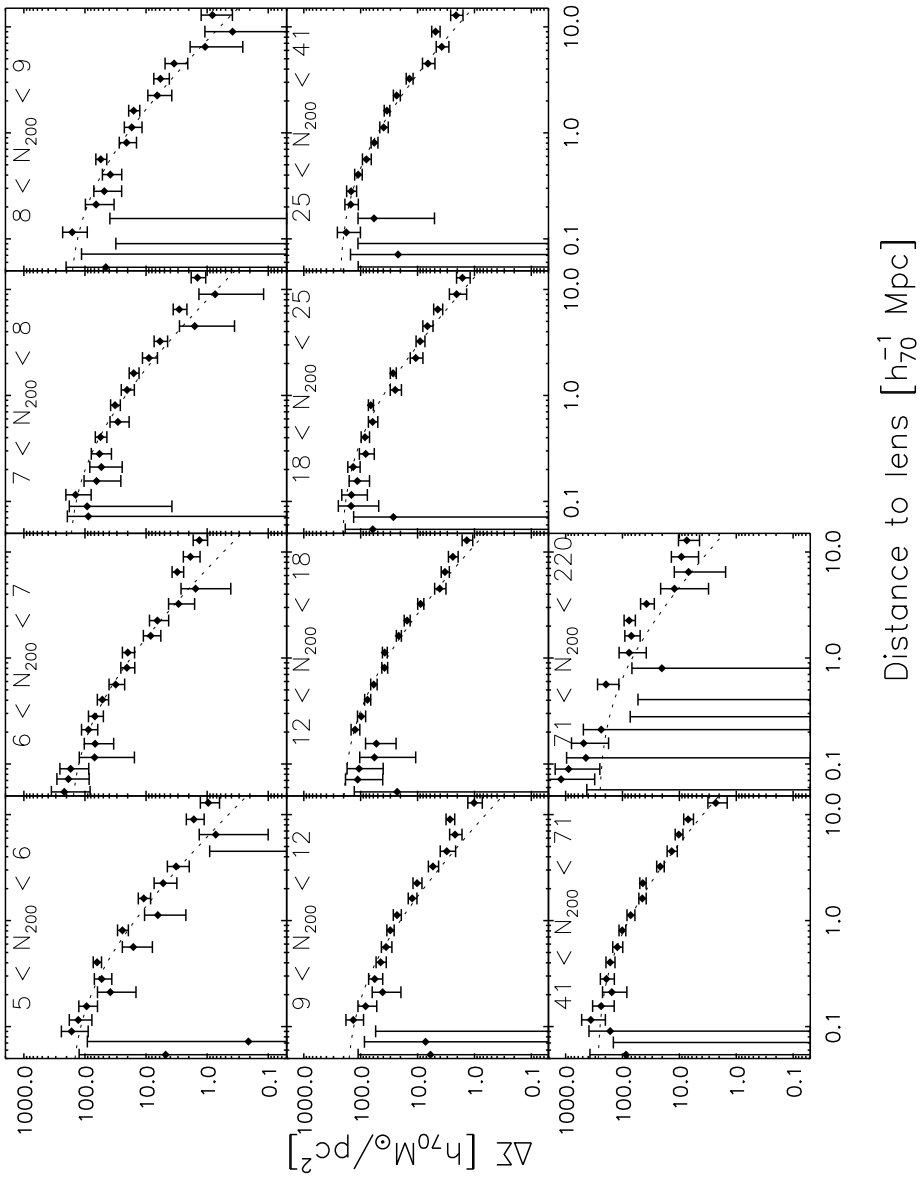

Figure 6.3: Lensing signal $\Delta\Sigma$ for each richness bin as a function of physical distance to the lens. The dashed lines indicate the best fit NFW profile, fitted to scales between 0.2 and 2 h_{70}^{-1} Mpc.

Table 6.1: Cluster sample details

bin	N_{200} (1)	n_{clus} (2)	z_{med} (3)	$\langle N_{200} \rangle$ (4)	N_{200}^{corr} (5)	$M_{200}[10^{13} h_{70}^{-1} M_\odot]$ (6)
N1	5-6	2815	0.72	5.48	2.91	$3.40^{+0.51}_{-0.51}$
N2	6-7	2218	0.69	6.49	3.92	$4.22^{+0.63}_{-0.58}$
N3	7-8	1723	0.68	7.50	4.93	$5.46^{+0.79}_{-0.72}$
N4	8-9	1323	0.66	8.48	5.91	$4.90^{+0.84}_{-0.79}$
N5	9-12	2545	0.63	10.3	7.78	$5.06^{+0.56}_{-0.56}$
N6	12-18	2117	0.58	14.4	11.85	$10.86^{+0.80}_{-0.74}$
N7	18-25	851	0.55	20.9	18.22	$13.59^{+1.35}_{-1.23}$
N8	25-41	513	0.51	30.7	27.40	$19.10^{+1.84}_{-1.80}$
N9	41-71	160	0.47	50.4	47.37	$38.35^{+4.58}_{-4.21}$
N10	71-220	14	0.45	82.0	75.87	$30.65^{+15.21}_{-12.49}$

(1) richness range of the bin; (2) number of clusters; (3) median redshift; (4) mean richness; (5) mean richness corrected for Eddington bias; (6) best fit NFW mass.

the number of clusters is high to those where the abundance is low. Since there are generally more poor clusters than rich clusters, the average richness of clusters within a certain richness range is biased high. For broad richness bins the bias is small, but for small richness ranges as used in our analysis the bias is non-negligible.

To correct the values of N_{200} for Eddington bias, we follow Bayes theorem. The probability distribution of N_{200} given an observed value N_{200}^{obs} (the posterior) is proportional to the product of the chance of having a value of N_{200}^{obs} given a distribution of N_{200} (likelihood) and the probability distribution of N_{200} (prior):

$$p(N_{200}|N_{200}^{obs}) \propto p(N_{200}^{obs}|N_{200}) p(N_{200}). \tag{6.6}$$

The adopted likelihood distribution is a Poisson distribution. In principle, the observed richness distribution can be used as an estimate of the prior. However, as shown in Figure 6.1, the cluster sample is incomplete at the low richness end by an uncertain amount, and using it as a prior would lead to an erroneous correction. Since we expect that the cluster sample is complete for approximately $N_{200} > 15$, we fit a powerlaw to the richness distribution at $N_{200} = 15$. For the prior, we replace the observed richness distribution with this powerlaw at $N_{200} < 15$, whilst at larger richnesses we use the observed richness distribution. The posterior is normalized and integrated up to the mean, N_{200}^{corr}. These values are tabulated in Table 6.1, as well as the uncorrected values.

We show both the original and the Eddington-corrected mass-richness relation in Figure 6.4. The Eddington correction mainly affects the low-richness bins. We fit the corrected mass-richness relation with $M_{200} = A(N_{200}^{corr}/20)^\alpha$, and find $A = (15.09 \pm 0.66) \times 10^{13} h_{70}^{-1} M_\odot$ and $\alpha = 0.86 \pm 0.05$. The errors on the amplitude are determined by marginalizing over the slope, and vice versa.

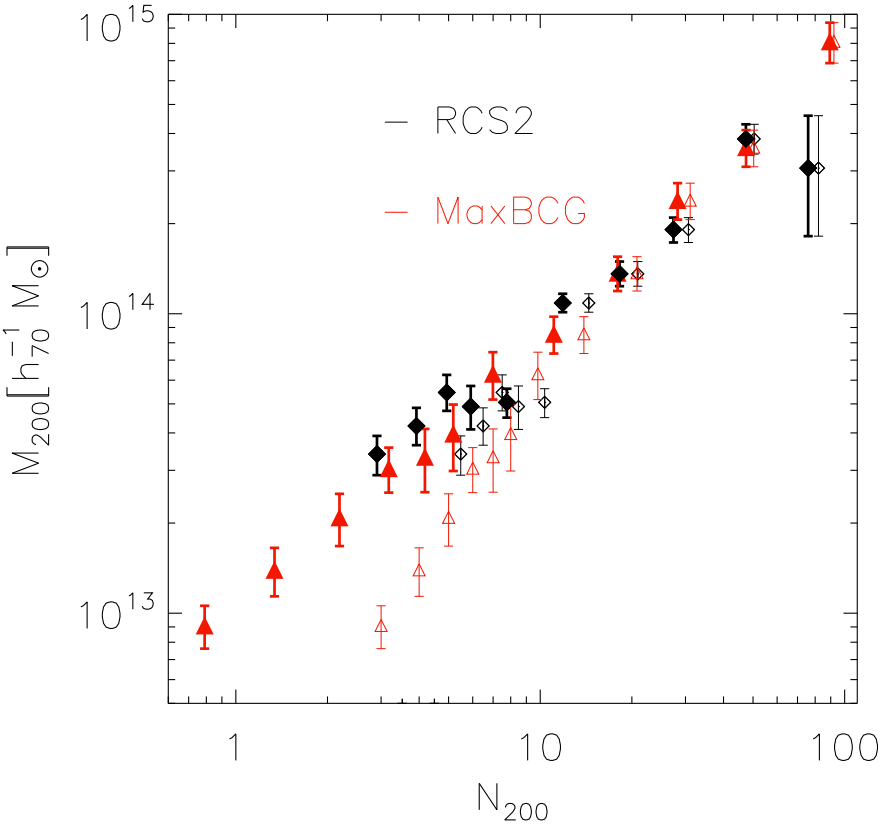

Figure 6.4: Best fit cluster mass versus the richness. The black diamonds denote the results from this work, the red triangles denote the results from the lensing analysis of the maxBCG clusters in Johnston et al. (2007). Open symbols indicate the original measurements, the filled symbols indicate the measurements corrected for Eddington bias.

The likelihood contour of this fit is shown in panel (a) of Figure 6.5. Without the correction for Eddington bias, we obtain $A = (12.84 \pm 0.50) \times 10^{13} h_{70}^{-1} M_\odot$ and $\alpha = 1.03 \pm 0.05$, which demonstrates that the correction is important.

Not all detections in the cluster catalogue are real clusters: a fraction of the clusters may actually correspond to a chance projection of galaxies rather than to a real cluster. These false detections have presumably a different lensing mass than the real clusters of that richness, and therefore potentially bias the average lensing signal. The fraction of real clusters is called the purity, which is generally a function of richness and redshift, but its particular shape depends on the cluster detection algorithm. Therefore, to determine the actual value of the purity for our cluster sample, we need to apply the detection algorithm to simulations that mimic the RCS2, which has currently not been done. The false positives do not add random noise, but a coherent (but likely lower) lensing

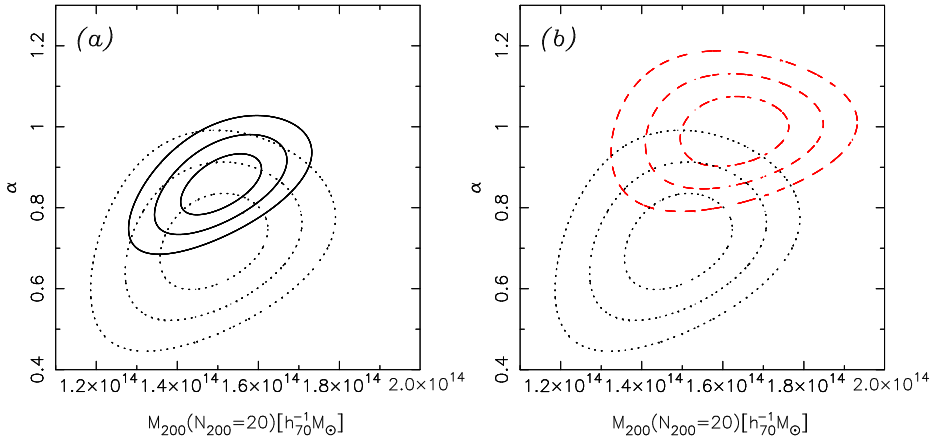

Figure 6.5: 67.8%, 95.4% and 99.7% confidence limits of the fits to the mass-richness relation. In panel (a), the solid black lines indicate the results for the full RCS2 sample, and the dotted black lines indicate the results for the RCS2 clusters in the redshift range $0.1 < z < 0.3$. The contours do not overlap, which suggests that the mass-richness relation depends on redshift. In panel (b) we compare the results for the RCS2 clusters in the redshift range $0.1 < z < 0.3$ to the results of the maxBCG sample covering the same richness range as the RCS2, i.e. $N_{200}^{\rm corr} > 4$, which is indicated by the dashed red lines. The agreement between the results is fair.

signal. How large the impact is on the lensing mass needs to be addressed with simulations. Note, however, that the purity is only expected to be less than 100% for the low-richness bins. The high-richness bins should be very pure, and the bias on the masses negligible. The effect on the best-fit parameters of the mass-richness relation is therefore expected to be small.

6.3.1 Comparison to the maxBCG cluster sample

We compare our results to the weak lensing analysis of the maxBCG cluster sample (Koester et al. 2007), a catalogue of 13 823 clusters that has been detected in the SDSS. The cluster detection algorithm employed in Koester et al. (2007) identifies the cluster red-sequence galaxies, and selects the brightest, the BCG, as centre of the cluster. The resulting cluster sample covers the richness range $10 < N_{200} < 190$ and a redshift range of $0.1 < z < 0.3$. In Sheldon et al. (2009b), the cluster sample is extended to $N_{200} = 3$, which leads to a sample of ∼130 000 galaxy groups and clusters. The lensing analysis of the sample is presented in Sheldon et al. (2009b); the mass-richness relation is derived in Johnston et al. (2007).

The richnesses of Johnston et al. (2007) have not been corrected for Eddington bias. We perform the correction, using a probability distribution for the maxBCG sample of $p(N_{200}) \propto (N_{200})^{-3}$ over the entire richness range, following Andreon & Hurn (2010). We show both the original and the Eddington bias corrected results in Figure 6.4. We fit the same powerlaw to the corrected results in the overlapping richness range, $N_{200}^{\rm corr} > 3$, and find

$A = (16.29 \pm 0.88) \times 10^{13} h_{70}^{-1} M_\odot$ and $\alpha = 0.99 \pm 0.06$, which does not agree well with our results. However, the average redshift of the clusters in the RCS2 sample is considerably higher than those in the maxBCG sample. To account for possible changes with redshift, and to enable a fairer comparison between the results, we only select RCS2 clusters that cover the same redshift range. Hence we select all clusters with $0.1 < z < 0.3$ from the RCS2 cluster sample, measure their lensing signals and fit the mass-richness relation. We find that $A = (14.91 \pm 0.88) \times 10^{13} h_{70}^{-1} M_\odot$ and $\alpha = 0.72 \pm 0.08$, and show the confidence limits in Figure 6.5*b*. The amplitude of the fit is about 2σ lower than the amplitude of the maxBCG results in the range $N_{200}^{\rm corr} > 3$. Using the marginalized errors on the powerlaw slopes, we find that best fit slopes for the maxBCG and the RCS2 are more than $\sim 3\sigma$ apart. Figure 6.5 shows that this discrepancy is partly the result of the particular shapes of the contours, and that the actual tension is somewhat smaller.

There are several differences between the analyses that may contribute to the difference between the results. For example, the lensing models used in this work and in Johnston et al. (2007) are different. To estimate how much this impacts the results, we create a mock lensing signal that mimics a typical lensing model used in Johnston et al. (2007), and fit a single NFW profile to it. The difference between the input mass and the best fit NFW mass then provides an estimate of the sensitivity of the results on the adopted lensing model.

In the lensing models of Johnston et al. (2007), it is assumed that a fraction p_c of the clusters is correctly centered, and their lensing signal follows an NFW profile, $\Delta\Sigma_{\rm NFW}^{\rm cent}$. The other $(1-p_c)$ is miscentered with a Gaussian radial offset distribution that has a width $\sigma_s = 0.42$ [h^{-1} Mpc]. We refer readers to Johnston et al. (2007) for details on the calculation of the average shear of these miscentered clusters, $\Delta\Sigma_{\rm NFW}^{\rm miscent}$. Neighbouring clusters add to the lensing signal at large projected separations. To calculate their contribution to the shear, $\Delta\Sigma^{2h}$, we use the 2-halo term from the halo model described in van Uitert et al. (2011), and use the best fit mass-bias relation from Johnston et al. (2007) to calculate the bias for a given halo mass, $b(M_{200})$. Hence the lensing signal is modeled with

$$\Delta\Sigma_{\rm mod} = p_c \Delta\Sigma_{\rm NFW}^{\rm cent} + (1-p_c)\Delta\Sigma_{\rm NFW}^{\rm miscent} + b(M_{200})\Delta\Sigma^{2h}. \qquad (6.7)$$

To account for the scatter between mass and richness, we integrate this model over a halo mass probability distribution $P(M_{200})$ that is log-normal and has a variance that depends on richness following Equation (25) in Johnston et al. (2007). We fit a single NFW profile to the resulting signal on scales between 200 h_{70}^{-1} kpc and 2 h_{70}^{-1} Mpc, and use a weight that is proportional to the projected separation squared to account for the increase of background galaxies at larger projected separations. The redshift we adopt for the model clusters is $z = 0.3$. We find that the best fit NFW mass overestimates the input mass with 9% for an input cluster of mass $M_{200} = 3 \times 10^{13} h_{70}^{-1} M_\odot$ and richness $N_{200} = 5$, which reduces to 5% for a $M_{200} = 3 \times 10^{14} h_{70}^{-1} M_\odot$ cluster with richness $N_{200} = 50$. Note that we use different values for the fraction of correctly centered clusters for the low and high mass model, i.e. $p_c = 0.6$ and $p_c = 0.75$, respectively, based on Figure 5 from Johnston et al. (2007). Also note that we adopt a concentration of $c = 3.5$ for both clusters, but the results do not sensitively depend on this choice. Therefore, if the RCS2 clusters have a similar miscentering distribution as the maxBCG clusters, we find that the differences between the modeling of

the lensing signal only has a minor effect on the best fit masses. The reason is that various effects cancel each other: the miscentering lowers the model lensing signal on small scales, whilst the 2-halo term increases the model signal on large scales. Additionally, by integrating the models over a log-normal halo mass probability distribution, we increase the model signal on all scales. Note, however, that the actual miscentering distribution for the RCS2 clusters might be different from what we assumed, as the cluster centres have been found with a different algorithm. The actual bias could therefore differ somewhat from the values presented here.

A second potential source of difference between the results from the RCS2 and the maxBCG is that we used the observed richness distribution as the prior in the calculation of the Eddington bias correction. The real richness distribution, which should have been used, is different from the observed one as clusters have already scattered. Therefore, the Eddington bias correction is potentially biased, and this bias could differ between the RCS2 and the maxBCG results. To estimate the size of the bias for the SDSS, we create a mock catalogue of 10^6 clusters by random drawing clusters from a richness distribution that scales as $\mathrm{N}^{\mathrm{clus}}(N_{200}) \propto N_{200}^{\beta}$. These richnesses are assumed to be the real values. Next, we assume that the probability distribution of the richness of each mock cluster is Poisson, and we reassign the richness of each cluster by random drawing from their Poisson distribution, mimicking the scatter that affects the richness estimates in real data. The resulting values are assumed to be the observed richnesses. We try different values of β, and find that the value that, after applying the scatter, results in an observed richness distribution with slope -3 in the range $3 < N_{200} < 200$ is given by $\beta = -2.55$. Hence the real richness distribution of the maxBCG sample is shallower than the observed one. The reason is that the scatter is dominated by the $N_{200} = 1$ and $N_{200} = 2$ clusters, as their abundance is largest. These clusters mainly scatter to other low richnesses, and less and less to increasing richnesses, causing a steepening of the slope.

To obtain the correct Eddingtion bias correction, we use as a prior $p(N_{200}) \propto N_{200}^{-2.55}$, and recalculate the average values of the richness. We find that at low richnesses, the values we obtain are $\sim$25% larger than the values tabulated in Table 6.1, but the difference decreases to less than a percent for the highest richness bins. We use these new values to fit the mass-richness distribution for the maxBCG clusters in the range $N_{200}^{\mathrm{corr}} > 4$, and find $A = (15.74 \pm 0.85) \times 10^{13} h_{70}^{-1} M_{\odot}$ and $\alpha = 1.03 \pm 0.06$, which is consistent with the previous best fit values. Hence the bias from assuming an incorrect prior is small, and does not significantly affect the results. For the RCS2, we cannot perform a similar test due to the fact that the current catalogue cannot be parameterized by a single powerlaw. Nevertheless, for the final RCS2 cluster sample a similar approach might work.

A third potential difference between the results could arise if the purity of the two cluster samples differ, and the lensing signals are not corrected for it. The purity is likely to differ somewhat between the catalogues as different cluster detection algorithms have been used. Koester et al. (2007) show how the purity of the sample depends on particular settings of the maxBCG algorithm using mock catalogues. The purity is typically of the order 90% or higher at richnesses $N_{200} > 10$; how the purity varies at lower richnesses is not shown. In the lensing analysis of the maxBCG clusters, no correction for the purity of the sample is mentioned. Since we do not correct for it either, the impact on

the two lensing analyses may actually be comparable. This can be tested by applying both cluster finding algorithms to simulated data. To compare the results with simulations, it is important to account for the false positives in the cluster sample.

6.4 Redshift dependence of the mass-richness relation

The clusters in the RCS2 survey cover a large redshift range, which makes them particularly suited for evolutionary studies of cluster properties. Here, we study the redshift dependence of the mass-richness relation. We split each richness bin in four redshift slices, and stack the lensing signal of all clusters in each slice. We fit NFW profiles to the shear, and show the best fit NFW masses as a function of richness in Figure 6.6.

We find that the mass-richness relation evolves with redshift. At a fixed richness below $N_{200}^{\rm corr} < 15$, the mass increases with decreasing redshift, whilst at $N_{200}^{\rm corr} \geq 15$ the best fit masses do not increase by much. We fit the mass-richness relation in each redshift slice, and show the best fit models in Figure 6.6. The best fit powerlaw parameters are given in Table 6.2, and shown as a function of redshift in Figure 6.7. To quantify the redshift dependence, we fit a linear relation to the powerlaw parameters of the form $A = a_{A,z} \times (z - 0.4) + b_{A,z}$, and similarly for α. We show the best fit parameters in Table 6.3, and the confidence contours of the fits in Figure 6.8. We find a clear indication that the slope of the mass-richness relation increases with increasing redshift.

We quantify the redshift dependence of the rich and poor clusters separately by performing the fit to the clusters with a richness that is respectively larger and smaller than $N_{200}^{\rm corr} = 15$. The best fit powerlaw parameters are shown in Figure 6.7, and the redshift dependence of these parameters is shown in Table 6.3. We find that the redshift dependence of the amplitude and slope for the poor and rich clusters are similar, although the errors are rather large and potential differences may be buried in the noise.

The redshift dependence of the mass-richness relation is also measured in Sheldon et al. (2009b) for the maxBCG clusters, but due to the limited redshift range of that sample no change with redshift was found. However, in a study of the relation between X-ray luminosity and richness for the maxBCG clusters, Rykoff et al. (2008) find that the X-ray luminosity at $z = 0.28$ is twice as high as the X-ray luminosity at $z = 0.14$. Becker et al. (2007) study the relation between velocity dispersion and richness for the same clusters, and find that the clusters at high redshifts systematically have higher velocity dispersions. Both Becker et al. (2007) and Rykoff et al. (2008) expect the main cause to be the evolution of the N_{200} richness measure, implying a fractional decrease in N_{200} of 30%-40% from $z = 0.14$ to $z = 0.28$ (i.e. N_{200} is underestimated at higher redshifts). No evidence is presented that supports such a strong decrease of N_{200}, and it does not explain why no redshift dependence of the mass-richness relation was detected in Johnston et al. (2007). Note that no correction for the Eddington bias was applied in each of these works, and a redshift dependent bias could contribute to the apparent evolution. To test this assumption, we compare

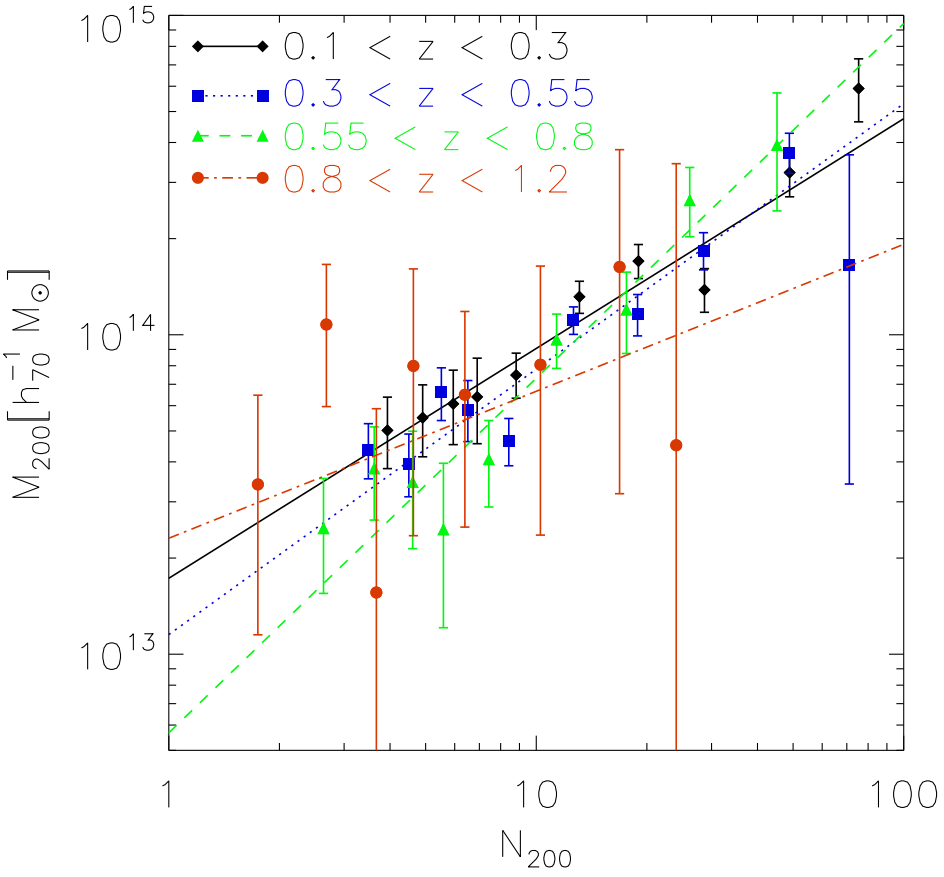

Figure 6.6: Redshift dependence of the mass-richness relation. Different colours correspond to different redshift bins, as indicated in the figure. The dashed lines indicate the powerlaw fits to the mass-richness relation in each redshift slice.

the slope of the cluster number counts for the maxBCG clusters with $z \geq 0.25$ and $z \leq 0.20$, respectively. We find that the slope of the high redshift-sample is ~ -3.5, only slightly steeper than the slope of ~ -3 for the low-redshift sample. The Eddington bias correction for the high-redshift sample is therefore slightly larger, which actually increases the difference between the high- and low-redshift results. The discrepancy remains therefore unexplained.

Our results suggest that the mass-richness relation is steeper at higher redshifts. The strongest change occurs at the lowest richness range: we find that a $N_{200}^{\rm corr} = 5$ cluster at $z = 0.25$ is $1.6^{+0.6}_{-0.4}$ times more massive than a $N_{200}^{\rm corr} = 5$ cluster at $z = 0.7$. This ratio and its errors are determined using the best fit parameters of the fit to the mass-richness relation in the redshift range $0.1 < z < 0.3$ and $0.55 < z < 0.80$, respectively. Clusters with $N_{200}^{\rm corr} > 15$ do not appear to change much in mass over the same redshift interval. In the following sections, we discuss various observational biases and physical processes that may contribute to the observed redshift dependence.

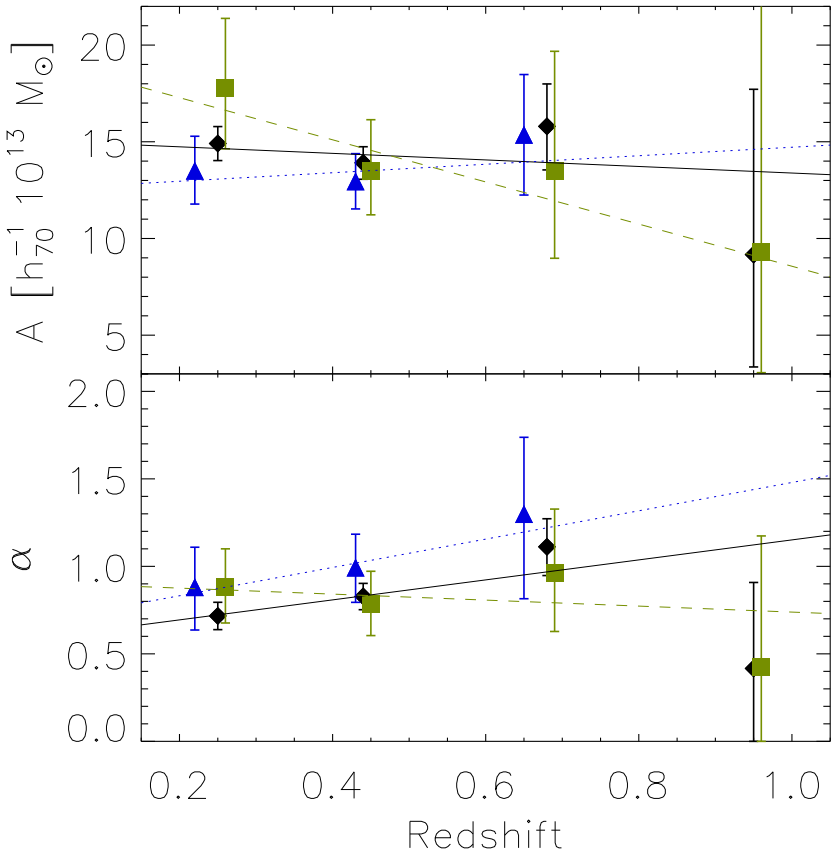

Figure 6.7: Redshift dependence of the powerlaw parameters of the mass-richness relation. The black diamonds indicate the results for all clusters, the green triangles (blue squares) for the clusters in the range $N_{200}^{\rm corr} > 15$ ($N_{200}^{\rm corr} < 15$). The black solid lines indicate the best fit linear relation between these parameters and redshift, and the green dashed (blue dotted) lines are for the clusters in the range $N_{200}^{\rm corr} > 15$ ($N_{200}^{\rm corr} < 15$).

6.4.1 Non-evolutionary causes of redshift dependence $M_{200}-N_{200}$

The observed change in the mass-richness relation with redshift may be caused by cluster evolution processes, but potentially also partly by the way the richness is defined. Additionally, there may be observational effects that cause a change in the mass-richness relation with redshift. Hence to study the cluster evolution processes, we first need to address if the redshift evolution of the mass-richness relation has different causes. We mention various effects below, and discuss how to estimate their impact.

Table 6.2: best fit parameters of the powerlaw fits to the mass-richness relation at different redshifts

z	A $[10^{13} h_{70}^{-1} M_\odot]$	α
0.10-1.20	15.09 ± 0.66	0.86 ± 0.05
0.10-0.30	14.91 ± 0.88	0.72 ± 0.08
0.30-0.55	$13.91^{+0.83}_{-0.85}$	0.83 ± 0.07
0.55-0.80	$15.80^{+2.19}_{-2.25}$	1.11 ± 0.16
0.80-1.20	$9.17^{+8.55}_{-5.81}$	$0.46^{+0.49}_{-0.46}$

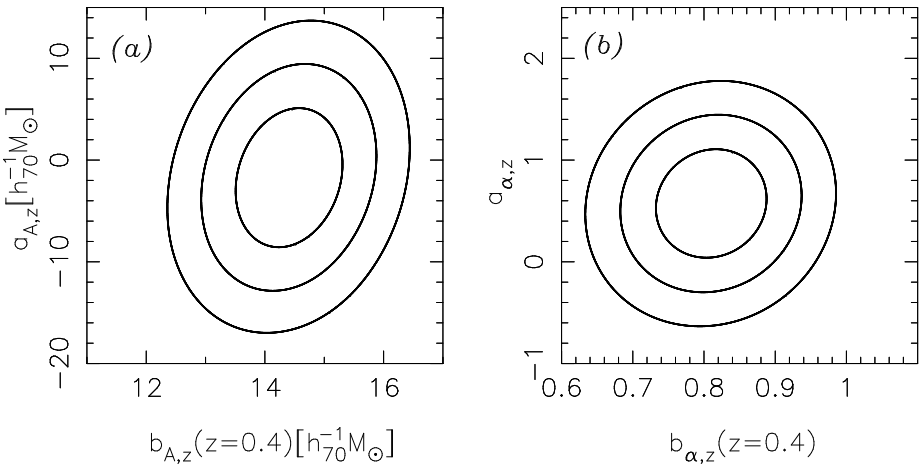

Figure 6.8: 67.8%, 95.4% and 99.7% confidence limits of the fits that describe the linear redshift dependence of the best fit parameters of the mass-richness relation, as detailed in the text. In panel (a) we show the results for the redshift dependence of the amplitude of the mass-richness relation, and in panel (b) for the slope.

The richness measure N_{200} is by definition a redshift dependent quantity: it includes all galaxies brighter than M*+2, which is a lower magnitude limit that evolves with redshift. Also, as the critical density changes with redshift, so does r_{200}, the radius within which we count the number of cluster members. Furthermore, at the high redshift end, the richness estimates are somewhat incomplete, which has not been corrected for. Hence, two identical clusters located at different redshifts are potentially assigned with different values of N_{200}. Note that already for the maxBCG cluster sample, which extends to $z = 0.3$, it has been suggested that N_{200} evolves (Becker et al. 2007; Rykoff et al. 2008). Our cluster sample extends to $z \sim 1$, making an evolution of N_{200} even more relevant. To understand how the richness of a given cluster changes with redshift, we can apply the detection method on simulations that mimic the RCS2 survey.

The purity of the cluster sample may depend not only on richness, but also on redshift. If the fraction of false detections increases with redshift for a fixed richness, this would lower the lensing mass and could cause the trend we ob-

Table 6.3: best fit parameters that describe the linear redshift dependence of the normalization and slope of the mass-richness relation, as detailed in the text.

$N_{200}^{\rm corr}$	$a_{A,z}$ $[10^{13}h_{70}^{-1}M_\odot]$	$b_{A,z}$ $[10^{13}h_{70}^{-1}M_\odot]$	$a_{\alpha,z}$	$b_{\alpha,z}$
all	-1.7 ± 4.5	14.4 ± 0.6	0.57 ± 0.35	0.81 ± 0.05
$N_{200}^{\rm corr} < 15$	$-10.9^{+11.7}_{-8.8}$	15.1 ± 1.8	-0.17 ± 0.75	0.84 ± 0.13
$N_{200}^{\rm corr} > 15$	2.2 ± 7.6	13.4 ± 1.0	0.81 ± 1.09	0.99 ± 0.14

serve. The purity of the sample, and its dependence on richness and redshift, needs to be estimated using simulations as well.

The miscentering distribution of clusters may also depend on redshift. Miscentering causes a drop in the lensing signal on small scales, which biases the lensing mass low if not accounted for (see Figure 4 in Hoekstra et al. (2011a) for estimates of the amplitude of this bias). In our final analysis, we include the miscentering distribution in the cluster halo model fits, and the lensing mass should be unaffected. However, the richness estimates of clusters are also affected by miscentering. Hilbert & White (2010) estimated the impact using the Millennium Simulation, and found that the cluster abundances are reduced by $\sim$20%. The miscentering of clusters may be dependent on the richness and the redshift of the clusters, and so is the size of the bias. We can in principle estimate the impact for each lensing bin once we have fitted the cluster halo model to the shear, using the constraints this has provided on the miscentering distribution.

6.4.2 Impact of cluster evolutionary processes

Next to these observational effects, there are several cluster evolution processes that affect the redshift evolution of the mass-richness relation. Below, we describe some of the processes that may be important in shaping this relation. We cannot disentangle these processes using the mass-richness relation alone. The goal of this section is to describe how each of these processes might impact the evolution of the mass-richness relation, and indicate which of them could contribute to the observed redshift dependence. It is important to realize that the richness estimates only include the red-sequence galaxies. The blue, star-forming galaxies, which are an important component of clusters, are not included.

Galaxy clusters evolve through the accretion of matter. Large clusters accrete matter faster than small clusters, because their potential wells are deeper and more extended (e.g. Fakhouri et al. 2010). Clusters accrete galaxies, gas and dark matter; how this affects the mass-richness relation depends on the relative amount of accreted total mass and galaxies. If the amount of accreted galaxies and total mass would not depend on the richness of a cluster nor on its redshift, clusters would only move up on the mass-richness relation, and no redshift dependence would be observed. A possible explanation for the increase of the mass of poor clusters with decreasing redshift is that poor clusters accrete relatively more dark matter than galaxies, compared to the rich clusters. This

could mean that either the accreted galaxies in poor clusters have more massive dark matter haloes, or lower luminosities such that they do not increase the richness of the clusters. Alternatively, poor clusters could accrete a larger additional amount of dark matter compared to rich clusters. This could be assessed using numerical simulations.

The galaxies that reside in a cluster evolve as well. Galaxies are stripped of their gas through tidal interactions and ram pressure stripping, which quenches their star formation (e.g. Boselli & Gavazzi 2006). Consequently, the late-type spiral galaxies that are accreted turn into early-type S0 galaxies, and subsequently appear on the E/S0 ridgeline. Hence even without accreting new galaxies, the richness of early-type galaxies in clusters may increase as more galaxies turn red. The fraction of satellites whose star formation is quenched strongly increases with halo mass (Wetzel et al. 2011), which could indicate that satellites in rich clusters are more efficiently quenched than those in small clusters. Hence, in the absence of accretion events, the richness of rich clusters may grow faster than the richness of poor clusters. The richness of poor clusters may therefore be lagging behind, which could also be partly responsible for the flattening of the mass-richness relation over time.

The richness of a galaxy cluster decreases if early-type cluster members merge, but the mass remains constant. When we determine the masses of clusters at a fixed richness, this leads to an increase of mass with decreasing redshift. The dependence of galaxy mergers on environment has been studied in Perez et al. (2009). In this work, it is found that the majority of merging galaxies are found in intermediate density environments. If such environments mainly correspond to galaxy groups, hence if mainly the galaxies in poor groups merge, it could explain why the mass of low-richness clusters increase more rapidly than those of high-richness clusters.

There are various other processes that may also have an effect on the redshift dependence of the mass-richness relation. For example, the properties of field galaxies that are accreted by clusters may evolve over time as well; the fraction of late-type galaxies that is accreted is likely larger at high redshift than at low redshift. Additionally, the pre-processing of accreted galaxies may be different for rich and poor clusters. The environment of the cluster is also expected to play a role, as it provides the material that accretes onto the cluster. In short, numerous processes are potentially involved in the evolution of the mass-richness relation, which makes any trend particularly hard to interpret. To start unraveling the various physical processes, we can compare our measurements to predictions from numerical simulations such as those described in Hilbert & White (2010). In this work, the mass-richness relation is predicted using semi-analytic galaxy formation models in the Millennium simulation. The predictions from this work are found to agree well with the maxBCG results from Johnston et al. (2007). It would be very interesting to see if a similar study, but now as a function of redshift, correctly predicts the redshift dependence we find.

6.5 Conclusion

We present the first results of the weak lensing analysis of the RCS2 cluster sample. The preliminary RCS2 cluster catalogue contains 1.4×10^4 galaxy clusters with $N_{200} > 5$, with masses $M_{200} > 2 \times 10^{13} h_{70}^{-1} M_{\odot}$ and redshifts in

the range $0.2 < z < 1.2$. The redshift coverage makes this cluster sample particularly suited for cluster evolution studies. In this work, we study the relation between the mass and richness of clusters, and how this relation depends on redshift. The calibration between richness and mass enables the exploitation of the RCS2 cluster sample to constrain cosmological parameters. Furthermore, the redshift dependence of the mass-richness relation can be used to study cluster evolution processes.

We split the cluster sample in richness bins, stack the lensing signal in each bin and fit an NFW profile between 0.2 and 2 h_{70}^{-1} Mpc. We fit the mass-richness relation with $M_{200} = A(N_{200}^{\rm corr}/20)^{\alpha}$, and find $A = (15.09 \pm 0.66) \times 10^{13} h_{70}^{-1} M_{\odot}$ and $\alpha = 0.86 \pm 0.05$. To study the redshift dependence of the mass-richness relation, we split the cluster sample in four redshift slices. We find that the mass-richness relation depends on redshift. The change with redshift is strongest for galaxy groups and poor clusters: we find that a $N_{200}^{\rm corr} = 5$ cluster at $z = 0.25$ is $1.6^{+0.6}_{-0.4}$ times more massive than a $N_{200}^{\rm corr} = 5$ cluster at $z = 0.7$. The high-richness clusters at different redshifts have comparable masses. Fitting a linear relation to the slope of the mass-richness relation of the form $\alpha = a_{\alpha,z} \times (z - 0.4) + b_{\alpha,z}$, we find $a_{\alpha,z} = 0.57 \pm 0.35$ and $b_{\alpha,z} = 0.81 \pm 0.05$.

Finally, we measure the excess galaxy number density around the cluster samples. We find that the number density profiles of the $N_{200}^{\rm corr} < 7$-bins are steeper than the dark matter profiles on small scales, whilst for the $N_{200}^{\rm corr} > 7$-bins the overdensities are generally less steep. The overdensities can be used to improve the modeling of the lensing signal, as they provide additional constraints on the miscentering distribution of the clusters.

Acknowledgements

HH and EvU acknowledge support from a Marie Curie International Reintegration Grant. HH is also supported by a VIDI grant from the Nederlandse Organisatie voor Wetenschappelijk Onderzoek (NWO). The RCS2 project is supported in part by grants to HKCY from the Canada Research Chairs program and the Natural Science and Engineering Research Council of Canada.

This work is based on observations obtained with MegaPrime/MegaCam, a joint project of CFHT and CEA/DAPNIA, at the Canada-France-Hawaii Telescope (CFHT) which is operated by the National Research Council (NRC) of Canada, the Institute National des Sciences de l'Univers of the Centre National de la Recherche Scientifique of France, and the University of Hawaii. We used the facilities of the Canadian Astronomy Data Centre operated by the NRC with the support of the Canadian Space Agency.

Bibliography

Agustsson, I. & Brainerd, T. G. 2006, ApJ, 644, L25
Allen, S. W., Evrard, A. E., & Mantz, A. B. 2011, ARA&A, 49, 409
Andreon, S. & Hurn, M. A. 2010, MNRAS, 404, 1922
Bahé, Y. M., McCarthy, I. G., & King, L. J. 2012, MNRAS, 2249
Bartelmann, M. 1996, A&A, 313, 697
Becker, M. R. & Kravtsov, A. V. 2011, ApJ, 740, 25

Becker, M. R., McKay, T. A., Koester, B., et al. 2007, ApJ, 669, 905
Berlind, A. A., Frieman, J., Weinberg, D. H., et al. 2006, ApJS, 167, 1
Bertin, E. & Arnouts, S. 1996, A&AS, 117, 393
Böhringer, H., Voges, W., Huchra, J. P., et al. 2000, ApJS, 129, 435
Boselli, A. & Gavazzi, G. 2006, PASP, 118, 517
Bower, R. G., Lucey, J. R., & Ellis, R. S. 1992, MNRAS, 254, 589
Budzynski, J. M., Koposov, S., McCarthy, I. G., McGee, S. L., & Belokurov, V. 2012, MNRAS, submitted [arXiv:1201.5491]
Clowe, D., De Lucia, G., & King, L. 2004, MNRAS, 350, 1038
Corless, V. L. & King, L. J. 2007, MNRAS, 380, 149
Duffy, A. R., Schaye, J., Kay, S. T., & Dalla Vecchia, C. 2008, MNRAS, 390, L64
Erben, T., Hildebrandt, H., Lerchster, M., et al. 2009, A&A, 493, 1197
Erben, T., Schirmer, M., Dietrich, J. P., et al. 2005, Astronomische Nachrichten, 326, 432
Evrard, A. E. 1989, ApJ, 341, L71
Fakhouri, O., Ma, C.-P., & Boylan-Kolchin, M. 2010, MNRAS, 406, 2267
Faltenbacher, A., Li, C., Mao, S., et al. 2007, ApJ, 662, L71
Gilbank, D. G., Gladders, M. D., Yee, H. K. C., & Hsieh, B. C. 2011, AJ, 141, 94
Gladders, M. D. & Yee, H. K. C. 2000, AJ, 120, 2148
Gladders, M. D. & Yee, H. K. C. 2005, ApJS, 157, 1
Hansen, S. M., McKay, T. A., Wechsler, R. H., et al. 2005, ApJ, 633, 122
Hao, J., Kubo, J. M., Feldmann, R., et al. 2011, in American Astronomical Society Meeting Abstracts #218, #408.24
Heymans, C., Van Waerbeke, L., Bacon, D., et al. 2006, MNRAS, 368, 1323
Hilbert, S. & White, S. D. M. 2010, MNRAS, 404, 486
Hirata, C. M., Mandelbaum, R., Seljak, U., et al. 2004, MNRAS, 353, 529
Hoekstra, H. 2001, A&A, 370, 743
Hoekstra, H. 2007, MNRAS, 379, 317
Hoekstra, H., Donahue, M., Conselice, C. J., McNamara, B. R., & Voit, G. M. 2011a, ApJ, 726, 48
Hoekstra, H., Franx, M., & Kuijken, K. 2000, ApJ, 532, 88
Hoekstra, H., Franx, M., Kuijken, K., & Squires, G. 1998, ApJ, 504, 636
Hoekstra, H., Hartlap, J., Hilbert, S., & van Uitert, E. 2011b, MNRAS, 412, 2095
Ilbert, O., Arnouts, S., McCracken, H. J., et al. 2006, A&A, 457, 841
Jaffé, Y. L., Aragón-Salamanca, A., De Lucia, G., et al. 2011, MNRAS, 410, 280
Johnston, D. E., Sheldon, E. S., Wechsler, R. H., et al. 2007, [arXiv:0709.1159]
Kaiser, N., Squires, G., & Broadhurst, T. 1995, ApJ, 449, 460
Koester, B. P., McKay, T. A., Annis, J., et al. 2007, ApJ, 660, 221
Komatsu, E., Smith, K. M., Dunkley, J., et al. 2011, ApJS, 192, 18
Lloyd-Davies, E. J., Romer, A. K., Mehrtens, N., et al. 2011, MNRAS, 418, 14
Łokas, E. L., Wojtak, R., Gottlöber, S., Mamon, G. A., & Prada, F. 2006, MNRAS, 367, 1463
López-Cruz, O., Barkhouse, W. A., & Yee, H. K. C. 2004, ApJ, 614, 679
Luppino, G. A. & Kaiser, N. 1997, ApJ, 475, 20
Mahdavi, A., Hoekstra, H., Babul, A., & Henry, J. P. 2008, MNRAS, 384, 1567

Mandelbaum, R., Hirata, C. M., Seljak, U., et al. 2005, MNRAS, 361, 1287
Mandelbaum, R., Seljak, U., Baldauf, T., & Smith, R. E. 2010, MNRAS, 405, 2078
Mandelbaum, R., Seljak, U., Cool, R. J., et al. 2006, MNRAS, 372, 758
Marriage, T. A., Acquaviva, V., Ade, P. A. R., et al. 2011, ApJ, 737, 61
Massey, R., Heymans, C., Bergé, J., et al. 2007, MNRAS, 376, 13
Metzler, C. A., White, M., & Loken, C. 2001, ApJ, 547, 560
Navarro, J. F., Frenk, C. S., & White, S. D. M. 1996, ApJ, 462, 563
Okabe, N., Takada, M., Umetsu, K., Futamase, T., & Smith, G. P. 2010, PASJ, 62, 811
Perez, J., Tissera, P., Padilla, N., Alonso, M. S., & Lambas, D. G. 2009, MNRAS, 399, 1157
Rasia, E., Meneghetti, M., Martino, R., et al. 2012, New Journal of Physics, submitted [arXiv:1201.1569]
Reiprich, T. H. & Böhringer, H. 2002, ApJ, 567, 716
Rozo, E., Rykoff, E. S., Koester, B. P., et al. 2009, ApJ, 703, 601
Rykoff, E. S., Koester, B. P., Rozo, E., et al. 2011, ApJ, submitted [arXiv:1104.2089]
Rykoff, E. S., McKay, T. A., Becker, M. R., et al. 2008, ApJ, 675, 1106
Sheldon, E. S., Johnston, D. E., Masjedi, M., et al. 2009a, ApJ, 703, 2232
Sheldon, E. S., Johnston, D. E., Scranton, R., et al. 2009b, ApJ, 703, 2217
Siverd, R. J., Ryden, B. S., & Gaudi, B. S. 2009, ApJ, submitted [arXiv:0903.2264]
Strauss, M. A., Weinberg, D. H., Lupton, R. H., et al. 2002, AJ, 124, 1810
Sunyaev, R. A. & Zeldovich, Y. B. 1972, Comments on Astrophysics and Space Physics, 4, 173
Tal, T., Wake, D. A., & van Dokkum, P. G. 2012, ApJL, submitted [arXiv:1201.5114]
van der Marel, R. P., Magorrian, J., Carlberg, R. G., Yee, H. K. C., & Ellingson, E. 2000, AJ, 119, 2038
van Uitert, E., Hoekstra, H., Velander, M., et al. 2011, A&A, 534, A14
Voit, G. M. 2005, Reviews of Modern Physics, 77, 207
Watson, D. F., Berlind, A. A., McBride, C. K., Hogg, D. W., & Jiang, T. 2011, ApJ, submitted [arXiv:1108.1195]
Watson, D. F., Berlind, A. A., McBride, C. K., & Masjedi, M. 2010, ApJ, 709, 115
Wetzel, A. R., Tinker, J. L., & Conroy, C. 2011, MNRAS, submitted [arXiv:1107.5311]
White, S. D. M., Efstathiou, G., & Frenk, C. S. 1993, MNRAS, 262, 1023
Williamson, R., Benson, B. A., High, F. W., et al. 2011, ApJ, 738, 139
Wright, C. O. & Brainerd, T. G. 2000, ApJ, 534, 34
Yee, H. K. C. & López-Cruz, O. 1999, AJ, 117, 1985
York, D. G., Adelman, J., Anderson, Jr., J. E., et al. 2000, AJ, 120, 1579

6.A Distribution of satellites

The galaxies in a cluster trace the dark matter distribution, although there are indications that the slope of the radial distribution of satellites galaxies differs from the slope of the projected total mass distribution (e.g. Watson et al.

2010, 2011; Budzynski et al. 2012; Tal et al. 2012). The radial distribution of satellite galaxies can be determined by measuring the galaxy overdensity around clusters. If a fraction of the clusters is not correctly centered, this also affects the observed distribution of satellites. Hence the overdensity measurement provides additional constraints on the miscentering distribution of the clusters. When we implement a more sophisticated lensing model, in which we account for the miscentering of clusters, the galaxy overdensity can serve as a prior for the miscentering distribution. Including this information is beneficial, as it reduces the errors on the best fit parameters from the lensing model.

To illustrate this, we measure the total galaxy overdensity in a similar way as for the sources, as discussed in Section 6.2.4. We use all galaxies in the magnitude range $16 < m_{r'} < 24$, and show the results for all clusters in Figure 6.2, and for the clusters divided in richness bins in Figure 6.9. Overplotted in each panel is the surface mass density, Σ, that corresponds to the best fit NFW model of the lensing measurements in the same richness bin, scaled with an arbitrary amplitude to match the data between 0.2 and 2 h_{70}^{-1} Mpc. This model is shown for illustration only, and no attempts have been made to improve the fit. It shows, however, that simply rescaling Σ does not describe the excess galaxy density well. In particular, for the $N_{200}^{\rm corr} < 7$-bins we find that the overdensities follow steeper profiles on small scales, whilst for the $N_{200}^{\rm corr} > 7$-bins the overdensities are generally flatter.

Closing in to the lens ($r <$100 h_{70}^{-1} kpc), we find that the overdensities do not increase as rapidly, and even decrease for the innermost radial bin. This is partly due to the miscentering of galaxies, which flattens the Σ profile on small scales (Johnston et al. 2007). Note that miscentering has a significantly smaller effect on Σ than on $\Delta\Sigma$, which is clearly illustrated in Figure 4 in Johnston et al. (2007). However, the signal-to-noise of the overdensity measurements is five to ten times larger than the one from shear, and the overdensity may therefore still provide useful constraints.

There are several other effects that cause a reduction of the galaxy number density near clusters. For example, the presence of large cluster galaxies in the centre of a cluster blocks or swamps the light of small satellites that are close to the line of sight. Additionally, the sky background subtraction near bright clusters could be inaccurate due to the high abundance of galaxies, and due to the diffuse intercluster light. This could affect the detection of faint cluster members, which would bias the excess galaxy number density measurements. Next to that, magnification leads to a reduction in number density of background sources close to the clusters, which also reduces the excess galaxy density. If not accounted for, these effects could be misinterpreted as being the result of miscentering. The impact of these complications have to be estimated before we can use the galaxy overdensity to improve the cluster halo model fits of the lensing signal.

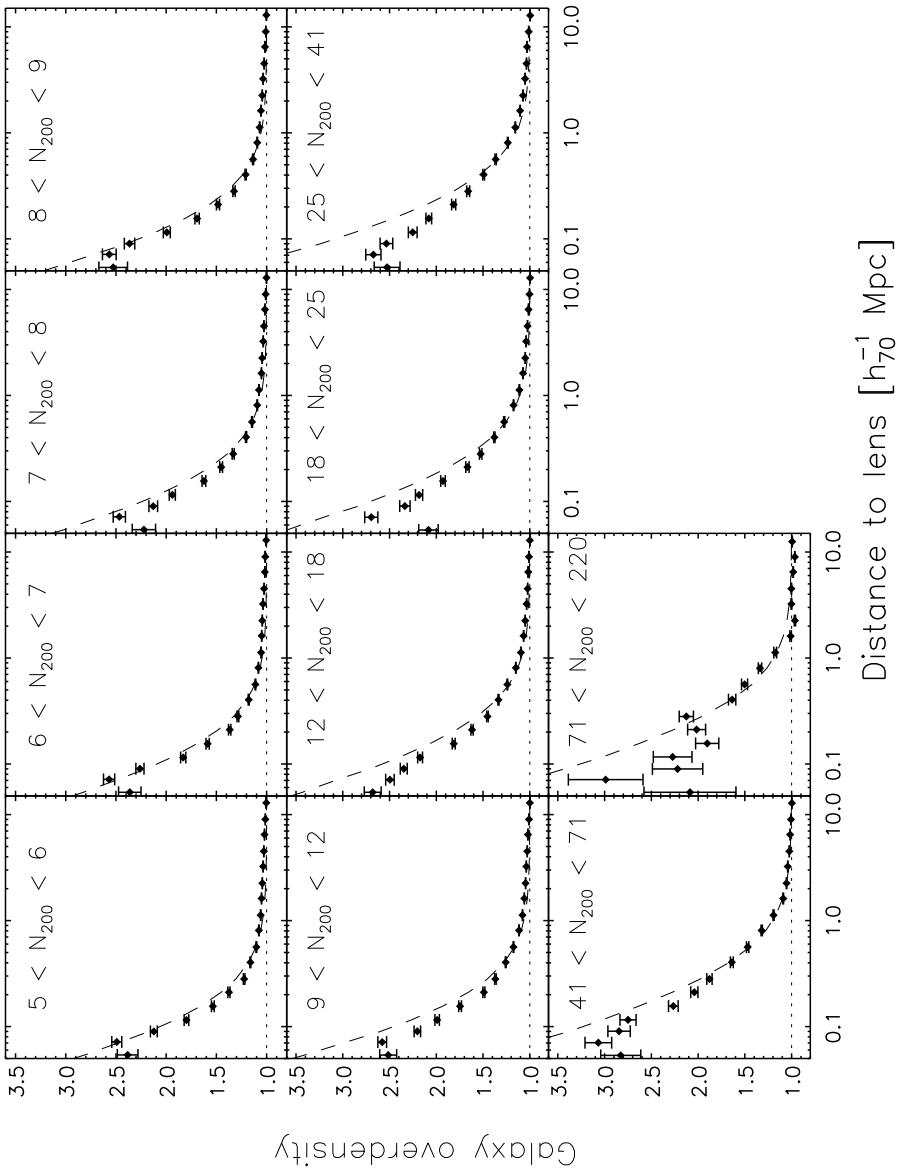

Figure 6.9: The overdensity of galaxies in the magnitude range $16 < m_{r'} < 24$ with shape measurements around the clusters as a function of projected separation. The dashed lines indicate the surface density Σ that correspond to the best fit model to the lensing measurements, scaled with an arbitrary amplitude to match the data between 0.2 and 2 h_{70}^{-1} Mpc.

Nederlandse samenvatting

Een mysterieus heelal

We leven in een mysterieus heelal. Volgens de huidige overtuiging, die gebaseerd is op een groot aantal verschillende waarnemingen, ontstond ons heelal 13.7 miljard jaar geleden uit de oerknal (Big Bang). Het heelal was toen onvoorstelbaar heet, dicht en klein. Er volgde een lange periode waarin het heelal uitzette en afkoelde, een periode die nog steeds gaande is. Na 380 duizend jaar was het heelal voldoende afgekoeld om de vorming van waterstof mogelijk te maken. Daarbij kwam licht met een specifieke frequentie vrij, dat we vandaag de dag nog steeds kunnen waarnemen: de kosmische achtergrond straling. De frequentie van dit licht is in de loop van de tijd steeds lager geworden ten gevolge van de uitdijing van het heelal: we nemen het tegenwoordig waar in het millimeter regime. Dit licht geldt als een van de belangrijkste bewijzen dat de oerknal daadwerkelijk heeft plaatsgevonden, en toont ons als het ware een foto van het heelal op het moment dat waterstof gevormd werd. Dit heeft ontzettend veel belangrijke informatie opgeleverd over het vroege heelal. Het laat bijvoorbeeld zien dat het heelal zeer gelijkmatig was, met slechts miniscule dichtheidsverschillen. Als reden voor deze homogeniteit wordt tegenwoordig aangenomen dat het heelal een fractie van een seconde na de oerknal voor een heel korte periode met een explosieve snelheid expandeerde, een proces dat 'inflatie' genoemd wordt.

Daar waar het heelal ietsje dichter was dan op andere plaatsen, groeiden kleine inhomogeniteiten en klonterden samen ten gevolge van hun onderlinge zwaartekracht, en vormden de basis voor de gigantische structuren waaruit later de sterrenstelsels -zoals onze Melkweg - ontstonden. Bij de vorming van sterrenstelsels speelde een grote variëteit aan processen een rol: door de zwaartekracht werd materie uit de omgeving aangetrokken, sterren vormden en straalden grote hoeveelheden licht uit, massieve sterren ontploften na een kort leven, materie viel in zwarte gaten waarbij ongelooflijke hoeveelheden energie vrijkwam, reusachtige gaswolken botsten met hoge snelheid op elkaar, kleine sterrenstelsels vielen in grotere en werden daarbij door de zwaartekracht uiteen gereten, en ga zo maar door. De wisselwerking van al deze en nog vele andere processes hebben het innerlijk en uiterlijk van de sterrenstelsels in het huidige heelal bepaald.

In de observationele kosmologie, de tak van de sterrenkunde waarin dit proefschrift thuishoort, proberen we het ontstaan en de ontwikkeling van deze grote structuren te begrijpen. We willen te weten komen hoe uit die miniscule inhomogeniteiten in het vroege heelal, de grote variëteit aan structuur in het huidige heelal is ontstaan. Welke processen zijn daarbij betrokken geweest, en wat was hun onderlinge wisselwerking? Waarom zijn er verschillende soorten sterrenstelsels ontstaan, die ruwweg in twee typen onderverdeeld kunnen worden: de zogeheten spiraalstelsels, gekarakteriseerd door de aanwezigheid van spiraalarmen, en elliptische sterrenstelsels, die een zeer gelijkmatige verschijning hebben? Waarom zijn er meer kleine stelsels dan grote? Hoe zijn deze stelsels verdeeld in de ruimte? Kortom, kunnen we een model voor de evolutie van het heelal opstellen, die het huidige heelal zoals deze is waargenomen correct kan voorspellen? Dit zijn het soort vragen die men in de kosmologie probeert te beantwoorden.

NEDERLANDSE SAMENVATTING

Zoals gezegd leven we in een mysterieus heelal. Niet alleen de onstaansgeschiedenis, maar ook de huidige inhoud van ons heelal stelt ons voor grote raadsels. Waarnemingen laten zien dat ons heelal maar voor zo'n 4% uit normale 'baryonische' materie bestaat. Dit is de materie waar we bekend mee zijn in het dagelijkse leven, en waar alles wat we in het heelal rechtstreeks kunnen waarnemen uit is opgebouwd. De overige 96% is onder te verdelen in 23% donkere materie en 73% donkere energie. Het label "donker" refereert naar de eigenschap van deze componenten dat we ze niet direct kunnen waarnemen. Ze stralen geen licht uit, en absorberen dat ook niet. Waar bestaan ze dan uit, zou je je kunnen afvragen? Deze vraag houdt kosmologen al jaren bezig, en is nog steeds niet beantwoord.

Als we de donkere componenten niet kunnen waarnemen, hoe weten we dan dat ze er zijn? En hoe kunnen we er iets over te weten komen? We kunnen het bestaan ervan afleiden uit het effect dat deze componenten hebben op hun omgeving. Donkere materie oefent zwaartekracht uit op zijn omgeving, net als gewone materie. Dat is dan ook de manier waarop donkere materie is ontdekt: in de jaren 30 van de vorige eeuw bestudeerde de Zwitserse sterrenkundige Fritz Zwicky de bewegingen van sterrenstelsels die door de zwaartekracht gebonden zijn in een grote groep van sterrenstelsels, de Coma cluster. De snelheden van deze sterrenstelsels waren dusdanig hoog dat je zou verwachten dat de stelsels uit elkaar zouden vliegen. De massa die de groep van sterrenstelsels zou moeten hebben om door de zwaartekracht gebonden te blijven, was ruwweg 160 keer hoger dan de massa die je op basis van de sterrenstelsels aan de totale cluster zou toewijzen. Er moest dus nog een andere component in het cluster aanwezig zijn, dat zwaartekracht uitoefende op de sterrenstelsels, maar die je niet kon zien: donkere materie.

Het karakter van donkere energie is haast volledig tegengesteld aan dat van donkere materie. Donkere energie wordt verondersteld de veroorzaker te zijn van de versnelde uitdijing van het heelal. Dat het heelal versneld uitdijt is in 1998 voor het eerst waargenomen door twee verschillende onderzoeksgroepen, het *high-z SN search*-team en het *Supernova Cosmology Project*-team, die beiden een vergelijkbaar onderzoek uitvoerden. Men gebruikte hiervoor waarnemingen aan een bepaalde type sterren die, aan het eind van hun leven beland, ontploften, de zogeheten supernova van het type Ia. Een bijzondere eigenschap van deze supernovae is dat ze een karakteristieke lichtcurve hebben: na de explosie verandert hun helderheid met de tijd op een specifieke wijze. De vorm van deze lichtcurve staat in nauw verband met de maximale helderheid van de supernova. Door deze eigenschap kunnen ze gebruikt worden om de afstand te bepalen tot sterrenstelsels: wanneer de helderheidscurve van een supernova is gemeten, en daaruit de maximale helderheid is afgeleid, en deze vergeleken wordt met de waargenomen helderheid, kan de afstand tot die supernova (en dus tot het sterrenstelsel waar deze supernova in verblijft) worden bepaald. Door deze metingen te combineren met de roodverschuiving[1] van dezelfde sterrenstelsels, kon men de uitdijingsgeschiedenis van het heelal achterhalen. Er volgde een onverwachte conclusie: de ver weg gelegen sterrenstelsels lagen verder weg dan men zou verwachten op basis van een aangenomen constante expansie van het heelal, hetgeen betekende dat het heelal versneld uitdijt. De veroorzaker van deze versnelde uitdijing van het heelal heeft de naam 'donkere energie' gekregen.

Gedurende de laatste jaren is het observationele bewijs voor het bestaan van donkere materie en donkere energie flink toegenomen. Mede daardoor is de overgrote meerderheid van de sterrenkundigen ervan overtuigd geraakt dat deze componenten daadwerkelijk bestaan. Over de aard van donkere materie en donkere energie bestaat nog veel onduidelijkheid. Het afgelopen decennium zijn er vrijwel dagelijks nieuwe theorieën ontwikkeld om hun oorsprong te verklaren, maar tot nog toe heeft geen enkele van deze theorieën geleid tot voorspellingen die bevestigd zijn met waarnemingen. Vooralsnog blijven donkere materie en energie veelal benamingen van deze twee verschijnselen - het overschot aan zwaartekracht in- en rondom sterrenstelsels en clusters van sterrenstelsels, en de versnelde uitdijing van het heelal.

Het onderzoek naar donkere materie en energie is een van de meest actieve onderzoeksgebieden binnen de sterrenkunde op dit moment. Dit proefschrift is daar ook een onderdeel van. We beperken ons in dit werk tot het bestuderen van donkere materie. We onderzoeken de distributie van donkere materie rondom sterrenstelsels en clusters van sterrenstelsels. We meten de totale hoeveelheid donkere materie die in sterrenstelsels aanwezig is, en kijken hoe dit afhangt van de eigenschappen van deze stelsels, zoals bijvoorbeeld de totale hoeveelheid licht die wordt uitgestraald, of van het type stelsel. Verder kijken we welke zichtbare eigenschap van een sterrenstelsel de beste indicator is van de totale massa van de donkere materie die in het stelsel aanwezig is. Ook bestuderen we hoe de donkere materie rondom sterrenstelsels is verdeeld, of het de verdeling van sterren volgt, of dat het sferisch symmetrisch is verdeeld, onafhankelijk van de vorm van het sterrenstelsel. Ten slotte meten we de massa van clusters van sterrenstelsels, en bepalen hoe dit afhangt van het aantal sterrenstelsels in het cluster. Al deze metingen geven ons nieuwe informatie over hoe donkere materie in het heelal is verdeeld, wat bijdraagt aan een beter begrip van dit mysterieus component.

De onderzoeken in dit proefschrift zijn uitgevoerd met behulp van een bepaalde techniek, te weten zwaartekrachtlenswerking. Deze techniek heeft de afgelopen tien jaar sterk aan populariteit gewonnen, en is nu een van de meest gebruikte methoden in het onderzoek naar donkere materie en donkere energie. In de volgende sectie beschrijven we hoe zwaartekrachtslenzen werken.

Zwaartekrachtlenswerking

Het licht van een sterrenstelsel legt een lange weg af voordat het wordt opgevangen door onze telescopen. Wanneer het licht onderweg in de buurt van een massief object komt, bijvoorbeeld een cluster van sterrenstelsels, wordt het aangetrokken door de zwaartekracht van dit object. Ten gevolge hiervan wordt het licht afgebogen, vergelijkbaar met de werking van een lens (maar veroorza-

[1] De roodverschuiving geeft aan hoeveel het spectrum van een sterrenstelsel is verschoven ten gevolge van zijn beweging naar ons toe of van ons af. Omdat het heelal uitdijt bewegen sterrenstelsels gemiddeld genomen van ons vandaan en lijken daardoor roder. Hoe verder weg een sterrenstelsel staat, des te sneller beweegt hij van ons vandaan, en des te groter is zijn roodverschuiving. Het licht van verder weg gelegen sterrenstelsels is ook langer onderweg geweest, en het heelal was dus jonger toen het werd uitgezonden. Kortom, hoe verder weg een sterrenstelsel staat, des te groter is zijn roodverschuiving, en des te jonger het heelal toen het licht werd uitgezonden. De roodverschuiving is daarmee ook een maat voor de leeftijd die het heelal had toen de sterrenstelsels hun licht uitzonden.

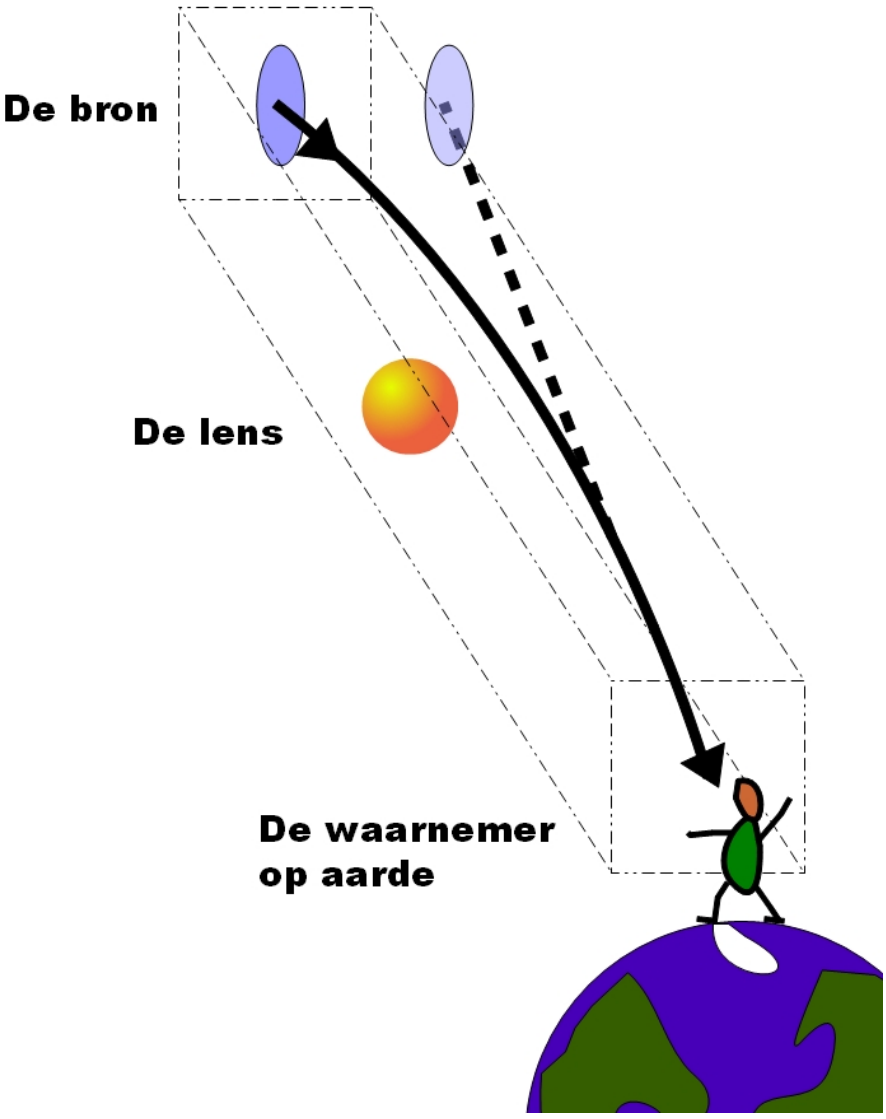

Figuur 6.10: De lichtstralen van een ver weg gelegen sterrenstelsel (de bron) worden onderweg naar de aarde afgebogen door een zwaar object (de lens). De waarnemer op aarde neemt een vervormd sterrenstelsel waar.

akt door een andere reden!). Daarom wordt dit effect zwaartekrachtlenswerking genoemd. In Figuur 6.10 illustreren we dit proces. Het massieve object dat de afbuiging veroorzaakt wordt de lens genoemd, het stelsel wiens lichtstralen worden afgebogen de bron.

Lichtstralen die dichter langs de lens passeren, worden meer afgebogen omdat de zwaartekracht lokaal sterker is. Alle lichtstralen van de bron worden dus

Figuur 6.11: Een voorbeeld van een zwaartekrachtlens, gefotografeerd door de Hubble ruimtetelescoop. De grote ovaalvormige sterrenstelsels in de voorgrond zijn erg zwaar en vervormen daardoor de beelden van de sterrenstelsels die erachter liggen tot dunne slierten.

een beetje anders verbogen. Hierdoor verandert de schijnbare vorm van de bron: de vorm die wij waarnemen, is niet de echte vorm van de bron - de vorm die we zouden waarnemen als er geen zwaartekrachtlens aanwezig was. Wanneer de lichtstralen van de bron vlak langs de lens scheren, en de lens erg zwaar is, kunnen deze vervormingen grote vormen aannemen. In extreme gevallen kan het beeld van de bron tot een lange boog uiteen getrokken worden, zodat het niet meer herkenbaar is als een sterrenstelsel. Een voorbeeld hiervan laten we in Figuur 6.11 zien. Dit effect wordt ook wel 'sterke zwaartekrachtlenswerking' genoemd.

Op grotere afstand van de lens zijn de vervormingen van daarachter gelegen sterrenstelsels minder spectaculair, maar ze zijn nog steeds aanwezig. De zwaartekrachtlenswerking in dit regime wordt 'zwakke zwaartekrachtlenswerking' genoemd. In tegenstelling tot het 'sterke zwaartekrachtlenswerking' signaal, dat alleen in uitzonderelijke gevallen rondom massieve sterrenstelsels is waar te nemen, hebben alle sterrenstelsels een 'zwakke zwaartekrachtlenswerking' op de vormen van erachter gelegen sterrenstelsels. Het effect op een enkele bron is echter te klein om te zien. De reden is dat alle bronnen ook een intrinsieke vorm hebben. Als ze slechts een klein beetje van vorm veranderen, kunnen we dus niet vaststellen of ze door de zwaartekrachtlens van vorm zijn veranderd. We weten echter dat de gemiddelde vorm van een sterrenstelsel rond is. Wanneer we nu de waargenomen vormen van duizenden bronnen middelen rondom een gegeven lens, dan middelen hun intrinsieke vormen weg. Wat we overhouden is de vervorming ten gevolge van de zwaartekrachtlens. De meeste sterrenstelsels hebben echter niet voldoende sterrenstelsels in de achtergrond. Om deze reden wordt het signaal rondom honderden tot duizenden zwaartekrachtslenzen gemiddeld. Gezamenlijk hebben deze sterrenstelsels voldoende bronnen om het

signaal meetbaar te maken. We kunnen dus niet het 'zwakke zwaartekrachtlens' signaal van een individueel sterrenstelsel meten, maar wel het *gemiddelde* signaal van een bepaalde set van sterrenstelsels. Wanneer we nu de lenzen zo selecteren dat ze allemaal dezelfde eigenschap hebben, bijvoorbeeld allemaal een vergelijkbare helderheid, kunnen we het gemiddelde signaal van een bepaald type lens te weten komen. Zelfs van heel kleine en niet massieve sterrenstelsels is de zwakke zwaartekrachtlenswerking te meten, zolang we maar voldoende lenzen hebben om over te middelen.

Het signaal van zwaartekrachtslenzen kan direct vertaald worden naar de verdeling van materie rondom een lens. Niet alleen gewone 'baryonische' materie, maar ook donkere materie oefent zwaartekracht uit op de lichtstralen van bronnen. Met de zwaartekrachtlenswerking kunnen we dus de verdeling van alle materie rondom sterrenstelsels meten. Als we het signaal meten als een functie van de afstand tot de lens, kunnen we bepalen hoe de verdeling van alle materie rondom sterrenstelsels van de straal afhangt. Dit stelt ons in staat om de gemiddelde totale massa van een bepaald type lens te bepalen. Ook kunnen we de verdeling van de totale materie vergelijken met de verdeling van de sterren. Dit stelt ons in staat om te bepalen waar de donkere materie zich ophoudt.

Het gebruik van zwaartekrachtslenzen heeft verscheidene voordelen ten opzichte van andere methoden die de totale massa van sterrenstelsels bepalen. Het signaal dat we meten kan direct worden omgezet in een massa distributie. Andere methoden zijn gebaseerd op verscheidene aannames, die niet in alle gevallen correct zijn en kunnen leiden tot verkeerde conclusies. Een tweede groot voordeel is dat het signaal van zwaartekrachtslenzen tot op grote afstand van de lens te meten is, terwijl andere methoden beperkt zijn tot kleine schaal. De verdeling van materie op zulke grote afstanden tot de lens geeft veel extra inzicht in de formatiegeschiedenis van sterrenstelsels. Ten slotte is het zwaartekrachtlens signaal voor alle type sterrenstelsels te meten, en zijn andere methoden vaak beperkt zijn tot een bepaald type sterrenstelsel.

Om het 'zwakke zwaartekrachtlens' signaal te meten, moeten we de vormen van duizenden sterrenstelsels nauwkeurig meten. Dit vereist waarnemingen van grote delen van de hemel, met een lange integratietijd om ook de vormen van zwakke en ver weg gelegen sterrenstelsels te kunnen bepalen. Er zijn de afgelopen jaren verscheidene waarneemprogramma's uitgevoerd, die een deel van de hemel hebben waargenomen met als doel de vorm van zoveel mogelijk sterrenstelsels te bepalen. In dit werk maken we ook gebruik van zo'n waarneemprogramma, te weten de Red-sequence Cluster Survey 2 (RCS2). De RCS2 bestaat uit waarnemingen van 900 vierkante graden van de hemel (de maan is ongeveer een halve vierkante graad, en de totale hemel beslaat ongeveer 40 000 vierkante graden), die waargenomen zijn in drie verschillende kleurfilters. Met deze filters kunnen we de helderheid van sterrenstelsels in drie golflengte gebieden meten, en daarmee kunnen we hun kleur bepalen. Dit helpt ons om sterrenstelsels van een bepaald type te selecteren. In totaal zijn er meer dan 20 miljoen sterrenstelsels waargenomen, waarvan de vormen zijn bepaald. Deze vormen vormen de basis voor dit proefschrift.

Dit proefschrift

Dit proefschrift gaat over het bepalen van de massaverdeling van alle materie rondom sterrenstelsels en clusters van sterrenstelsels in de RCS2, door middel van het meten van hun zwakke zwaartekrachtlenswerking op de vormen van erachter gelegen sterrenstelsels. In hoofdstuk 2 beschrijven we de RCS2, en de methode die we gebruikt hebben om uit de waarnemingen de vormen van alle waargenomen sterrenstelsels te halen. Verder presenteren we enkele tests om ons ervan te vergewissen dat de catalogi met de vormen van sterrenstelsels die we gebruiken van voldoende kwaliteit is. In hoofdstuk 3 gebruiken we deze vormen om de zwakke zwaartekrachtlenswerking rondom een set van 17 000 sterrenstelsels te meten. Deze sterrenstelsels zijn ook in een ander waarneemprogramma waargenomen (in de Sloan Digital Sky Survey, SDSS). We hebben daardoor veel extra informatie beschikbaar voor deze stelsels, zoals een nauwkeurige schatting van hun roodverschuiving, een bepaling van het type stelsel, hun helderheid en hun stellaire massa (de totale massa aanwezig in sterren), informatie die we anders niet uit de RCS2 hadden kunnen halen. We verdelen deze stelsels in verschillende kleinere sets, onder meer als een functie van helderheid en stellaire massa, en meten het gemiddelde zwaartekrachtlens signaal van elke set om hun gemiddelde massa te bepalen. We vinden onder meer dat spiraalstelsels van een gegeven helderheid minder zwaar zijn dan elliptische stelsels van dezelfde helderheid. Verder vinden we dat de totale massa van spiraalstelsel en elliptische stelsels met een lage stellaire massa vergelijkbaar is, maar voor een hoge stellaire massa vinden we dat de elliptische stelsels zwaarder zijn.

Hoofdstuk 4 is een vervolg op hoofdstuk 3. We gebruiken dezelfde set van lenzen, maar nu om een andere vraag te beantwoorden, te weten: welke waarneembare eigenschap van sterrenstelsels is het nauwst gerelateerd aan hun zwaartekrachtlens signaal? Deze vraag is belangrijk in de context van de formatie van sterrenstelsels; het vertelt ons welke waarneembare eigenschap het nauwst samenhangt met de verdeling van donkere materie, en dus het minste verstoord is door andere processen. We vergelijken drie verschillende eigenschappen van sterrenstelsels: de model snelheidsdispersie, de waargenomen snelheidsdispersie en de stellaire massa. De snelheidsdispersie is een maat voor de snelheid waarmee sterren in het centrum van sterrenstelsels bewegen. De model snelheidsdispersie is een schatting van de snelheidsdispersie, die gebaseerd is op andere eigenschappen van een sterrenstelsel, zoals zijn grootte en stellaire massa. De model snelheidsdispersie komt goed overeen met de waargenomen snelheidsdispersie voor elliptische sterrenstelsels, en daarom kijken we in dit hoofdstuk alleen naar dit type sterrenstelsel. We vinden dat de waargenomen snelheidsdispersie en de stellaire massa evengoed schalen met het signaal van de zwaartekrachtslenzen. De model snelheidsdispersie is echter minder nauw gerelateerd, wat veroorzaakt kan worden door een buiten beschouwing gelaten afhankelijkheid van het signaal van bijvoorbeeld de grootte van een sterrenstelsel.

In hoofdstuk 5 proberen we de vorm van de verdeling van donkere materie rondom sterrenstelsels te meten. Een eventuele meting van dit effect is van groot belang voor verschillende andere onderzoeksgebieden, waaronder de studie hoe sterrenstelsels ten opzichte van elkaar georienteerd zijn. Wanneer een sterrenstelsel in een elliptische donkere materie halo zit, die dezelfe orientatie heeft, dan

wordt het zwaartekrachtlens signaal rondom het sterrenstelsel asymmetrisch. Dit is echter een zeer zwak effect, en om het te meten middelen we het signaal over drie sets met zeer veel lenzen. De eerste set bestaat uit zo'n 100 000 zeer heldere elliptische stelsels, de tweede set uit ongeveer evenveel spiraalstelsels, en de derde set bestaat uit 1.6 miljoen normale sterrenstelsels, en mengsel van allerlei soorten stelsels die het gemiddelde sterrenstelsel in het heelal representeert. We vinden een zwakke aanwijzing dat het gemiddelde sterrenstelsel in een elliptische donkere materie halo zit, die dezelfde orientatie heeft. Voor de spiraalstelsels vinden we een zeer kleine aanwijzing dat hun donkere materie halo ge-anti-alinieerd is, dat wil zeggen dat de vorm van het sterrenstelsel en de donkere materie halo 90 graden ten opzichte van elkaar staan. We bestuderen de invloed van verschillende mogelijk verstorende complicaties op deze metingen, en geven schattingen van de grootte van hun invloed op het signaal.

In het laatste hoofdstuk van dit proefschrift, hoofdstuk 6, maken we gebruik van een catalogus van clusters van sterrenstelsels in de RCS2 die door collega's beschikbaar is gesteld. Deze clusters zijn verdeeld over een grote bereik in afstand (tussen roodverschuiving $0.2 < z < 1.2$), en daarmee leeftijd. Dat maakt deze cluster catalogus zeer geschikt voor het bestuderen van de formatie en evolutie van clusters. Om deze evolutie te kwantificeren, meten we de relatie tussen de 'richness' van een cluster, een schatting van het totale aantal sterrenstelsels dat bij een cluster hoort, en de massa, die we bepalen door de zwaartekrachtlenswerking van de clusters te meten. We vinden dat de relatie tussen de massa en de richness van clusters in het huidige heelal anders is dan die van een paar miljard jaar geleden. Clusters die slechts uit enkele sterrenstelsels bestaan, zijn in de tussentijd tot wel twee keer zwaarder geworden. Clusters die uit tientallen leden bestaan, zijn daarentegen gemiddeld genomen weinig in massa veranderd. We bespreken enkele effecten die deze waargenomen trend kan verklaren, onderverdeeld in mogelijke observationele en fysiche effecten.

Curriculum Vitae

Volgens de overleveringen ben ik op 23 februari 1984 in Groningen geboren. Op 12 jarige leeftijd ging ik naar het Praedinius gymnasium in Groningen, waar ik 6 jaar later met goede herinneringen en een diploma op zak weer vertrok in de richting van Leiden om sterrenkunde te gaan studeren. Eenmaal aangekomen werd ik lid van Minerva, ging op Der Wilde Kaiser wonen, volgde vakken kunstgeschiedenis, klassieke muziek, Spaans en Hebreeuws, haalde mijn motorrijbewijs, nam pianoles bij Arielle Vernède die me aanzette om deel te nemen aan verscheidene piano concoursen en voorspeelavonden, en had daarmee dusdanige afleiding om welhaast te vergeten waarom ik naar Leiden was gekomen. Aan het einde van mijn BSc realiseerde ik mij echter dat ik door wilde gaan in de sterrenkunde, en ik besloot hierop met hernieuwde focus te gaan studeren om dit mogelijk te maken. In mijn MSc zette ik mijn eerste wetenschappelijke stapjes tijdens mijn klein onderzoek bij Walter Jaffe aan PRIMA (Phase-Referenced Imaging and Micro-arcsecond Astrometry), het instrument van de VLTI telescoop voor interferometrie. Ik sloeg echter de huidige weg in toen ik mijn groot onderzoek begon bij Koen Kuijken, om daar met veel plezier aan technieken te werken om de vormen van sterrenstelsels zo nauwkeurig mogelijk te meten, een essentieel onderdeel van het bestuderen van de zwakke zwaartekrachtlenswerking. Dat smaakte naar meer, en tot mijn vreugde kreeg ik eind 2007 de gelegenheid om aan mijn promotie te beginnen. Het eerste jaar werkte ik met Koen Kuijken aan een nieuwe vorm-meting techniek, en ontwikkelde een nieuwe methode. Een jaar later kwam Henk Hoekstra naar Leiden, en begon ik aan de Red-sequence Cluster Survey 2 te werken, wat heeft geleid tot dit proefschrift. Tijdens mijn promotie heb ik de gelegenheid gehad menig conferentie te bezoeken, en heb ik resultaten van mijn proefschrift gepresenteerd door middel van posters en presentaties op internationale conferenties in Canada, Duitsland, Italië, Groot Brittannië, Australië en op de NAC in Cuijk. Tijdens mijn studie ben ik tutor en mentor geweest van eerstejaars studenten. Gedurende mijn PhD was ik drie maal onderwijsassistent bij het vak Sterrenkundig Praktikum I, en was ik lid van de onderwijscommissie. In het begin van 2012 zijn mijn piano en ik naar Bonn verhuisd, en heb ik mijn carrière in de sterrenkunde vervolgd op het Argelander-Institut für Astronomie in de groep van Peter Schneider.

Dankwoord

In de afgelopen vier jaar heb ik van vele kanten, en op vele vlakken, hulp mogen ontvangen, waar ik erg dankbaar voor ben. Om te beginnen wil ik mijn collega's bedanken van de zwaartekrachtslens groep in Leiden. The lensing group in Leiden is definitely the coolest research group at the Sterrewacht (simulators schmimulators)! Malin, we were once asked whether we were twins, and one could say in a sense we are, since we shared our youth in science. It was great to find out that I was not alone in not understanding a word the grown-ups said (only in the very beginning, clearly). Tim, you've been a great colleague and friend, and I am very excited that you also moved to Bonn. I am looking forward both to working together again and a little bit of partying like we did in the old days! Elisabetta, I have greatly enjoyed your positiveness and your happy view on life has been an inspiration for me! Let us find many excuses to continue collaborating! Stefania, Remco (volgend jaar gaan we winnen!), Merijn, Berenice, thank you for making our group such a great one!

Ruim negen jaar heb ik op de Sterrewacht doorgebracht. Dat dit instituut bijzonder is op velerlei vlakken, zoals de bijzonder aangename algemene sfeer, de vanzelfsprekende gemakkelijke contacten tussen alle lagen, de vele lezingen en borrels, en het jaarlijkse voetbalfestijn, dat weet iedereen die hier tijd heeft mogen doorbrengen. Ik ben dan ook alle Sterrewachters dankbaar voor hun bijdrage aan het instituut, en ik hoop dat de huidige geest van de Sterrewacht nog lang zal blijven rondwaren. In particular I would like to thank our coffee buddies Freeke & Craig, Daniel, Jesse, Steven, and party-friends Edith, Shannon, Ben O. and Simone for the many well-deserved and very-much needed breaks. To all my former office mates, and in particular Lars, Nikta, Adam, Jayne, and Markus, thanks for making the office such a great and pleasant place to be! Jeanette, sharing an office with you was quite dangerous careerwise as we spent more time chatting than working, but it was also the start of a dear friendship. Heren van de sigarenclub, te weten Jan, Frank, Maarten, Franco, Jelle, Rowin en Remco, wanneer prikken wij onze volgende rokerige afspraak om de wereldproblematiek eindelijk voorgoed op te lossen? Mannen van Humboldt: dank voor menig diner ende borrel op niveau! Verder gaat mijn dank uit aan Jeanne, Liesbeth, Anita, Erik, David, Tycho en Aart: ontzettend bedankt voor het feit dat jullie altijd paraat staan en alles op de Sterrewacht zo soepel laten verlopen.

Ik zou een ongelukkig mens zijn zonder mijn goede vrienden. Hungwah, Kai (no touchy), Wai, Anita en HoMing, bedankt voor alle gezelligheid, etentjes, drankjes, flessen wijn, North End, kolonisten en namenspel. Jullie worden gemist in Bonn! En vergeet niet: er gaat nog een dag komen dat ik zal winnen met kolonisten (waarschijnlijk dezelfde dag dat Anita verliest met namenspel...). Johan, Jaap, Geert, Thomas, Matthijs, en de andere huis- en clubgenoten: ik kijk uit naar de volgende borrel! Arielle, heel erg bedankt voor de vele inspirerende muzikale uren achter de piano! Jouw lessen hebben peper en zout aan mijn spel toegevoegd, en ik hoop maar dat ik een nieuwe docent kan vinden waar ik even veel van kan leren. Redmar en Dominique, ik weet niet hoe ik jullie kan bedanken voor wat jullie voor mij betekenen, maar ik weet dat jullie weten wat ik bedoel en het me zullen vergeven dat ik een gênante poging dit onder woorden te brengen nalaat.

DANKWOORD

Aan mijn lieve ouders: jullie hebben voor een groot deel bepaald hoe ik ben (meer dan jullie wellicht denken), en daarmee mogelijk gemaakt dat ik hier nu ben gekomen. Daar ben ik jullie ongelooflijk dankbaar voor! Jullie ontoombare interesse in alles wat ik doe, en jullie trots voor wat ik heb bereikt, is een onmisbare steun voor mij. Allon, brohim, dank voor de vele gezellige avondjes! Het is hoog tijd voor je volgende squashles! Afgezien daarvan: nu rest er nog een... Iris, lief zusJE (haha, nu staat het hier zwart-op-wit!), laat je niet gek maken, en zet die luie broertjes van je eens wat meer aan het werk! Wouter, dank voor alle heerlijke biertjes (het is alweer een tijdje geleden, eigenlijk...) en gezelligheid! Ik kan niet wachten tot de volgende bijeenkomst!!! Jullie zijn me onbeschrijflijk dierbaar, en ik ben zo trots op jullie allemaal!

My last and most important words are for Hoda.

هدی عزیزم ، زبان ساده من رو ببخش چرا که نمیتوانم آنچه را که
میخواهم به قلم بیاورم. یافتن تو مانند پیدا کردن زیباترین گل در گندم زار
است. مطمئن هستم که هیچ باغبانی خوشحال تر از من وجود ندارد. بی
صبرانه در انتظار سپری کردن لحظه های خوش با تو هستم.

Edo van Uitert, April 2012